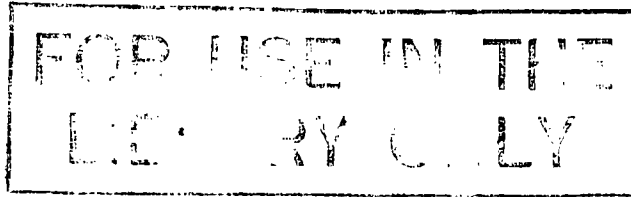


X 8215102



1237329 X

THE APPLICATION OF LASER MEASUREMENT TECHNIQUES TO
THE PNEUMATIC TRANSPORT OF FINE PARTICLES

by

A. Birchenough, B.Sc.

Thesis submitted for the degree of Doctor of Philosophy
under the conditions for the award of higher degrees
of the Council for National Academic Awards.

Theses

531.
163
BIR

School of Mechanical Engineering,
Thames Polytechnic,
London

September, 1975

ABSTRACT

The application of laser anemometry techniques to the measurement of local velocities and turbulence intensities is now well established for gas and liquid flows. In these situations, light from a low powered laser is scattered by seeding particles in the fluid which are small enough to follow the flow. The resulting Doppler shift of the scattered light is proportional to the velocity of the particles and hence, to the velocity of the fluid.

When solid particles are conveyed pneumatically, for example in transport chemical reactors, in drag reducing flows, and in certain heat transfer processes, the particles are generally much larger than the usual seeding particles, and thus do not travel at the same velocity as the carrier fluid. During this investigation, local particle velocity and axial turbulence intensity measurements using a laser anemometer have been made in an upward flowing gas-solid suspension and some of the limitations of the method have been found. The measured velocity profiles were used to evaluate the mean solids velocity and these mean values were compared with the results obtained using a technique developed by the author, which measures the mean solids velocity directly. Solids loading ratios up to 2.0, and conveying velocities up to 56 m/s, have been analysed and it has been confirmed that all the alumina particles (size range 5 to 45 microns) contributed to the analysed signal.

Measurements have also been made of the particle velocity in the wall region of the two-phase flow, using a back-scattered light collection method. The pneumatic conveying rig imposed an upper limit

on the loading ratio of 4 for these experiments. However, the measuring system itself suffers no such restriction. The results of the "back-scatter investigation" are discussed by reference to particle wall velocity curves, which can be used to indicate that 'choking' is imminent. ' .

Further work examined the 'clean' air velocity and axial turbulence intensity profiles obtained by seeding the flowing air with sub-micron particles of titanium dioxide.

Finally, measurements of axial pressure gradient in the fully developed region of the gas-solid flow were made simultaneously with the particle velocity measurements.

—

iii

ACKNOWLEDGEMENTS

The author gratefully acknowledges the guidance and enthusiasm of Dr. J.S. Mason and the support of the School of Mechanical Engineering at Thames Polytechnic. Much of the construction work was carried out by the School's technicians under the supervision of Mr. W.S. Churchill and Mr. R. Davis; Mr. W. Bush deserves special mention.

Other departments at the Polytechnic to whom the author is indebted are the School of Biology and the Central Services Unit.

The technical staff from D.I.S.A. have been most helpful throughout and thanks are also due to Cambridge Consultants and General Survey and Instrument Company for the loan of their laser anemometry equipment.

Finally, the author would like to thank Mrs. Ann Follis for typing the thesis.

Financial support was provided by the Science Research Council.

—

AUTHOR'S NOTE

All the work in this thesis is the sole and original work of the author, except where stated otherwise by acknowledgement or reference.

Large parts of the thesis have already been presented at conferences or prepared for publication at the time of binding, and further publications are planned. Details are given in section 1.4 and Appendix A.4.

CONTENTS

	<u>Page No.</u>
Abstract	i
Acknowledgements	iii
Author's note	iv
1. <u>OUTLINE OF THE STUDY</u>	
1.1 Introduction	1
1.2 Industrial interests	2
1.3 Outline of the main contents of the Thesis	4
1.4 Publication policy	5
2. <u>THEORETICAL REVIEW OF PARTICLE MOTION IN A FLOWING FLUID</u>	
2.1 Introduction	7
2.2 Single spherical particle in a turbulence free fluid of infinite extent	7
2.3 Single spherical particle in a turbulent fluid of infinite extent	9
2.4 The effect of particle shape	10
2.5 Boundary effects	11
2.6 Multi-particle system interactions	12
2.7 Electrostatic effects	14
3. <u>PNEUMATIC CONVEYING PLANT DESIGN</u>	
3.1 Design specification	15
3.2 Description of pneumatic conveying plant	16
3.2.1 Air alone circuit	16
3.2.2 Solids feed circuit	18
3.2.3 Gas-solids circuit	19
3.2.4 Platform	21
3.3 Commissioning of plant	22
3.4 Suggestions for improvement	24

4.	<u>CALIBRATIONS AND POWDER PROPERTIES</u>	
4.1	Introduction	36
4.2	Orifice plate calibration	36
4.2.1	Calibration procedure	36
4.2.2	Treatment of results	37
4.2.3	Results and discussion	39
4.3	Screw feeder calibration	40
4.3.1	Calibration procedure	40
4.3.2	Results and discussion	41
4.4	Load cell calibration	42
4.4.1	Calibration procedure	42
4.4.2	Results and discussion	43
4.5	Powder properties	43
4.5.1	Alumina powder	44
4.5.2	Titanium dioxide powder	45
5.	<u>LASER ANEMOMETRY</u>	
5.1	Introduction	61
5.2	Literature survey	61
5.3	The Doppler shift of scattered light; application to the laser anemometer	73
5.3.1	Basic equation	74
5.3.2	Application to the reference beam mode	74
5.3.3	Application to the differential Doppler mode	76
5.3.4	Application to the one beam mode	77
5.3.5	Derivation of the Doppler shift equation from fringe considerations	78
5.4	Light source requirements	79
5.5	Transmitting optics	81
5.6	Probe volume	82

5.7	Signal detection	84
5.8	Measurement volume	87
5.8.1	Fringe mode measurement volume	88
5.8.2	Reference beam mode measurement volume	88
5.9	Application to turbulence intensity measurements	89
5.9.1	Velocity gradient broadening	91
5.9.2	Disc broadening	91
5.9.3	Broadening correction equation	92
5.10	Signal to noise ratio considerations	92
5.11	Laser anemometry equipment	94
6.	<u>CLEAN GAS VELOCITY AND TURBULENCE INTENSITY MEASUREMENTS</u>	
6.1	Introduction	106
6.2	Seeding arrangements	106
6.2.1	Smoke injector method	106
6.2.2	T _i O ₂ particle injection	106
6.3	Air circuit	107
6.4	Laser anemometer arrangement	107
6.5	Results and discussion	108
7.	<u>OBSERVATIONS WITH LARGE SCATTERING CENTRES</u>	
7.1	Introduction	115
7.2	Probe length investigation	115
7.2.1	Experimental	116
7.2.2	Results and discussion	117
7.3	Signal strength and visibility	118
7.3.1	Experimental	120
7.3.2	Results and discussion	121

8.	<u>LOCAL PARTICLE VELOCITY AND AXIAL TURBULENCE INTENSITY MEASUREMENTS</u>	
8.1	Introduction	136
8.2	Literature survey	136
8.3	Particle velocity profiles, $\theta = 0$	143
8.3.1	Experimental procedure for local particle velocity measurement	144
8.3.2	Results and discussion	144
8.3.3	Confirmation that the $1/e^2$ probe volume has physical significance	149
8.3.4	Results and discussion	150
8.4	Particle velocity and axial turbulence intensity profiles, $\theta = 45^\circ$	151
8.4.1	Experimental procedure	151
8.4.2	Results and discussion	152
9.	<u>MEAN PARTICLE VELOCITY MEASUREMENT</u>	
9.1	Introduction	176
9.2	Literature survey	176
9.3	Laser anemometry arrangement	177
9.4	Experimental procedure	178
9.5	Results and discussion	179
10.	<u>PARTICLE WALL VELOCITY MEASUREMENTS</u>	
10.1	Introduction	187
10.2	Particle wall velocity measurement technique	188
10.3	Experimental procedure	189
10.4	Results and discussion	190
11.	<u>PRESSURE DROP MEASUREMENTS</u>	
11.1	Introduction	198
11.2	Literature survey	198
11.3	Experimental	203
11.4	Results and discussion	204

	<u>Page no.</u>
12. <u>CONCLUSIONS</u>	212
13. <u>SUGGESTIONS FOR FURTHER WORK</u>	216

APPENDICES

- A.1 Nomenclature
 - A.2 List of figures
 - A.3 References
 - A.4 Publications
-

CHAPTER 1

OUTLINE OF THE STUDY

1.1 Introduction

The study of flowing gas-solid suspensions has, in recent years, received a great deal of attention [1,2,3,4] . Examples of such two phase flows which occur in nature are sand and snow storms, and the windborne conveyance of plant pollen, whilst man-made gas-solid flow phenomena include the dispersion of soot particles from factory chimneys, the scattering of radioactive fallout and the emission of solid particles from rocket exhausts.

The earliest harnessing of gas-solid systems for industrial use was associated with pneumatic transportation, but the field is now quite diverse, covering nuclear reactor coolants, transport chemical reactors, coal-seeded natural gas pipelines, and so on. All of these applications are generally concerned with turbulent flow and involve flow accelerations and geometry variations. The fact that the turbulent motion of the gaseous phase alone cannot adequately be described [5], in a statistical manner, precludes any precise description of the particulate motion. Rigorous experimentation is thus essential in order to further our understanding of the mechanics of gas-solid flows.

Numerous measurement techniques have been devised to examine the mean flow properties of such flows, some of which give questionable results; but there are very few measurement techniques which can adequately deal with local flow properties. It is these detailed measurements, however, which are necessary for a more satisfactory explanation of the behaviour of flowing suspensions.

The application of laser anemometry techniques to the measurement of local velocities in gas and liquid flows is now well established.

In these situations, light from a low power laser is scattered by seeding particles in the fluid which are small enough to follow the turbulent velocity fluctuations of the fluid. The resulting Doppler shift of scattered laser light is proportional to the velocity of the particle and, hence, the fluid velocity. Since scattering particles exist, by definition, in gas-solid flow situations, laser anemometry would seem a tractable method of obtaining the appropriate particle velocity information without some of the limitations of other techniques, such as flow disturbance, the need for calibration, and so on.

The objectives of this investigation were to assess the advantages and limitations of laser anemometry when applied to gas-solid flows, and to acquire useful particle velocity and turbulence intensity information.

1.2 Industrial Interests

The earliest full-scale developments of gas-solid systems were in the pneumatic handling of grain [6] and pneumatic conveyors are now used extensively in flour mills. Some of the advantages of this type of bulk solids handling are high standards of hygiene, uniformity of processing, easy adaptation to automation and reduced labour costs. The energy requirements are, however, high in comparison to other transport methods.

A novel application of pneumatic conveying reported recently [7] was the unloading of fish from trawlers with only minimal product degradation.

Problems arising from gas-solid suspension flows include saltation

in horizontal pipes and choking in vertical pipes. These two phenomena are associated with a lowering of the conveying velocity to some critical value and must be avoided from a plant stoppage and production loss standpoint. Increasing the conveying velocity, however, increases the energy consumption and can introduce other problems such as particle attrition and bend wear with consequent product contamination. These features require designers to have some knowledge of pressure losses, electrostatic charge transfer effects, mean slip velocity data, and so on, in order to design efficient plant. In addition, the risk of explosion must always be considered and some powders, such as sulphur, cannot be conveyed pneumatically for this reason alone.

For the past twenty years the fluidised bed reactor has been preferred to the transport reactor for the completion of chemical processes involving solid particles and gases. However, the increasing diversification of requirements in the chemical industry has meant that a great variety of finer chemicals, previously made only in small quantities, are now needed. The transport reactor is well suited to these operations, allowing more intimate contact between the particles and the gas than is possible with the bubble formation in fluidised beds. It has the disadvantage, on the other hand, that long reactor lengths are necessary when the chemical reaction is slow. Examples of transport reactors are to be found in the gasification of coal and in the petroleum industry where the concept was first pioneered for the cracking and reforming of hydrocarbons.

There is some interest in the use of gas-solid flows for certain heat transfer processes. The relatively high thermal capacity of

the solid particles can enhance the heat transfer coefficient of gas-solid flows to a level comparable with liquid coolants. However, in nuclear reactors, liquids can cause corrosion and need to be used under pressure to avoid phase change by boiling.

The phenomenon of drag reduction may result in a considerable saving of energy for some industrial processes since, by the addition of small amounts of solid particles to the gaseous phase, the pressure drop can be reduced below that for the gas alone. A possible application is the transport of natural gas seeded with coal dust, resulting in a transport cost saving and a high calorific value fuel.

The research reported here was carried out with the above industrial interests in mind, in the hope that some improvement in the existing "rule-of-thumb" design methods commonly employed in industry [8] might result. The introduction of laser anemometry to the field is also expected to be beneficial.

1.3 Outline of the Main Contents of the Thesis

In chapter 2, a brief review of the theory of fluid-particle interactions is presented.

In chapter 3, the design and construction of the pneumatic conveying rig is described.

In chapter 4, the calibration of the orifice plate, load cell and the screw feeder are presented, together with an analysis of the powders used in the study.

In chapter 5, conventional laser anemometry is discussed in detail and the Doppler shift equations are derived. This chapter includes a description of the laser anemometry equipment.

In chapter 6, "clean" air velocity and axial turbulence intensity profile measurements are described.

In chapter 7, the experiments illustrate the feasibility of using the laser anemometer for the velocity measurement of "large" particles.

In chapter 8, particle velocity profile and axial turbulence intensity measurements are presented.

In chapter 9, it is shown that the laser anemometer can be used to measure mean particle velocity.

In chapter 10, a back-scatter technique for the measurement of particle wall velocity is described.

In chapter 11, pressure drop measurements in the test section are presented.

1.4 Publication Policy

The following research papers have arisen from this research :-

1. "The Application of a Laser Anemometer in Measuring Parameters Required in the Design of a Pneumatic Conveying System" - presented by the author at "Powtech '75" Conference, Harrogate, February 1975.
2. "The Application of Laser Measurement Techniques to the Pneumatic Transport of Fine Alumina Particles" - presented by the author at "The Engineering Uses of Coherent Optics" Conference, Strathclyde University, April 1975.
3. "Local Particle Velocity Measurements with a Laser Anemometer in an Upward Flowing Gas-Solid Suspension" - submitted to "Powder Technology" in December 1974.
4. "Velocity and Axial Turbulence Intensity Measurements in a Titanium Dioxide Seeded Airstream Flowing Through a Vertical Pipe" - submitted to "Particulate Matter", June 1975.

Paper 1 is based on chapter 9, whilst paper 2 is derived mainly from chapter 7. The first half of chapter 8 is the subject of paper 3, and paper 4 is taken from chapter 6.

In addition to the above, it is intended to submit a paper based on chapter 10 to the forthcoming "Pneumotransport III Conference", whilst chapter 11 and the second half of chapter 8 will be the subject of a paper to be submitted to an "International Powder and Bulk Solids Handling and Processing Conference" to be held in Chicago in May 1976.

CHAPTER 2

THEORETICAL REVIEW OF PARTICLE MOTION
IN A FLOWING FLUID

2.1 Introduction

A brief outline of the fundamentals of particle motion in fluids and related aspects is presented in this chapter. Any proposed theory for gas-solids turbulent pipe flow must take into account, not only the behaviour of a single spherical particle in an infinite turbulent fluid, but the results of deviations from sphericity, the consequences of constraining boundaries, the effects of multiparticle behaviour and interactions with both the fluid and other particles, electrostatic effects, and so on. Up to the present time, exact solutions for the gaseous phase alone are non-existent for turbulent pipe flow, so that the difficulties in attaining even an approximate mathematical explanation of two-phase pipe flow are overwhelming. Recourse is usually made to dimensional analysis and experimentation, resulting in semi-empirical expressions [9,10], or to a continuum mechanics approach [11,12]. It must not be supposed, however, that since exact solutions to the diversity of phenomena which constitute a gas-solids flow are not available, that it is wasteful to consider them analytically. They provide a valuable insight into the compound problem.

2.2 Single Spherical Particle in a Turbulence Free Fluid of Infinite Extent

In 1851, Stokes [13] produced the first known solution to the Navier-Stokes equation for the resistance of an aerodynamically smooth sphere moving with creeping motion through an infinite, incompressible, viscous fluid. For such conditions, inertia terms can be neglected and the Navier-Stokes equation has the form:-

$$\rho \frac{D\bar{u}}{Dt} = \rho \bar{g} - \text{grad } p + \mu_f \nabla^2 \bar{u} , \tag{2.1}$$

where $\frac{D\bar{u}}{Dt}$ is the total time derivative of the velocity vector \bar{u} , this becomes:

$$\text{grad } p = \mu_f \nabla^2 \bar{u} \tag{2.2}$$

giving a drag force on the sphere of :

$$F_D = 3\pi d \mu_f U_\infty \quad (2.3)$$

where U_∞ is the velocity of the approaching fluid relative to the particle.

It can be shown that two thirds of F_D is due to shear and the remaining one third is due to the pressure distribution.

The drag coefficient, defined by:

$$C_D = \frac{F_D}{\frac{1}{2} \rho U_\infty^2 A_p} \quad , \quad (2.4)$$

where A_p is the cross sectional area of the particle, thus becomes, from Stokes' law:

$$C_D = \frac{24}{Re_p} \quad , \quad (2.5)$$

where Re_p is the particle Reynolds' number defined by:

$$Re_p = \frac{\rho U_\infty d}{\mu_f} \quad (2.6)$$

The Stokes' law regime holds for Re_p up to about 1.0, and this solution of the Navier-Stokes equation represents the only successful purely theoretical derivation for the drag force on a particle moving with respect to a fluid. For particle Reynolds' numbers above unity, analytical treatment becomes difficult, since the inertia terms, neglected by Stokes, are of increasing importance. Moreover, separation of the boundary layers occurs at about $Re_p = 10$, so that a stationary vortex ring is formed at the rear of the sphere and the symmetrical flow pattern no longer holds.

Oseen [14], approximated the Navier-Stokes equation by considering the inertia terms to be important only in the flow field away from the particle, giving :

$$C_D = \frac{24}{Re_p} \left(1 + \frac{3}{16} Re_p \right) \quad (2.7)$$

This expression is approximately applicable for $Re_p < 5$.

Goldstein [15] , in 1929, gave a complete solution for the Oseen approximation with the series expansion :

$$C_D = \frac{24}{Re_p} \left(1 + \frac{3}{16} Re_p - \frac{19}{1280} Re_p^2 + \frac{71}{20480} Re_p^3 - \dots \right) \quad (2.8)$$

which agrees to within 20% of experimental data for particle Reynolds' numbers below 10.

Other investigators who have used Oseen's approximation in order to solve the Navier-Stokes equation are Tomotika and Aoi [16] , Pearcy and McHugh [17] and Stewartson [18] . For Re_p above 10, Kawaguti [19] , employed the Galerkin method, which required the assumption of various functional terms for the stream function, found from experimental data.

2.3 Single Spherical Particle in a Turbulent Fluid of Infinite Extent

The conditions of a turbulence free fluid are not found in pneumatic conveying systems. The turbulent motion of the fluid causes the particle motion to be unsteady. If the particle is large in comparison to the scale of turbulence it will follow only the slower large scale turbulent motions of the fluid. If the particle is small compared to the smallest scale of turbulence, it will respond to all the turbulence components of the fluid and the resistance of the particle with respect to the surrounding fluid will be viscous. Most theoretical studies of a particle suspended in a turbulent fluid are confined to particle Reynolds' numbers less than unity, so that Stokes' drag law applies and then assume that the particle diameter is smaller than the micro-scale of turbulence, but large enough to be unaffected by Brownian motion [20, 21, 22] . Basset [20] , showed that the velocity of a sphere in a stationary viscous fluid of infinite extent could be represented by:

$$\frac{\pi d^3}{6} \left(\rho_p + \frac{1}{2} \rho_f \right) \frac{dV}{dt} = -3d^2 \rho_f V - \frac{3}{2} d^2 \rho_f \sqrt{\frac{\pi \mu_f}{R}} \int_{t_0}^t \frac{dV/d\xi}{\sqrt{t-\xi}} d\xi \quad (2.9)$$

where V is the velocity of the sphere and t is time.

The term on the left in equation (2.9) is the force necessary to accelerate the sphere and the $\frac{1}{2} \rho_f$ term arises from the added mass of the entrained fluid, whilst the final term is the Basset history integral. If the relation is assumed to hold for a particle within a turbulent eddy, and if $V = (u_f - u_p)$, then equation (2.9) becomes, [23] :

$$\frac{\pi d^3}{6} \rho_f \frac{du_p}{dt} = 3\pi \mu_f d(u_f - u_p) + \frac{\pi d^3}{6} \rho_f \frac{du_f}{dt} + \frac{1}{2} \frac{\pi d^3}{6} \rho_f \left(\frac{du_f}{dt} - \frac{du_p}{dt} \right) + \frac{3}{2} \frac{d^2}{f} \sqrt{\frac{\pi \mu_f}{\rho_f}} \int_{t_0}^t d\xi \left[\frac{du_f}{d\xi} - \frac{du_p}{d\xi} \right] / \sqrt{t - \xi} \quad (2.10)$$

The term, $\frac{\pi d^3}{6} \rho_f \frac{du_f}{dt}$, arises because the acceleration of the fluid adds a pressure force on the sphere. The equation is not exact, however, and its shortcomings are discussed by Corrsin and Lumley [24]. Tchen [25] generalised equation (2.10) for systems where both the particle and the fluid were undergoing acceleration, but the forces involved are then complex functions of the particle Reynolds' number, as well as of the acceleration. Other attempts to predict the behaviour of a spherical particle in a turbulent fluid for $Re_p < 1$ are by Hjelmfelt and Mockros [23] and Pearcey and Hill [26]. For particle Reynolds' numbers above unity, little or no theoretical work exists, which is unfortunate since the findings of this research cover particle Reynolds' numbers up to 20, depending upon particle size. The simpler case of a cylinder has, however, been investigated by Payne [27] at Re_p 's of 40 and 100.

2.4 The Effect of Particle Shape

Because of the difficulties in Stokes' analysis, the effect of non-spherical particle shapes can only be considered in simple cases

such as cylinders, [27, 19, 28] and perhaps ellipsoids. However, Irani and Callis [29] suggested that, provided the ratio of the maximum to the minimum dimensions does not exceed 4, Stokes' law may be used, equation (2.3), with d replaced by an effective diameter, d_e , that is:

$$F_D = 3\pi\mu_f d_e (u_f - u_p) \quad (2.11)$$

Similarly, Hawksley [30], suggested the approximation that the equivalent diameter should be equated with the diameter of a sphere having the same external surface area as the particle.

2.5 Boundary Effects

When the entraining fluid is contained by solid boundaries then, because of the 'no-slip' condition which exists between the fluid and the boundary, velocity gradients are created. Velocity gradients and particle-boundary impacts impart a rotational motion to the particle. At low particle Reynolds' numbers the friction force of the rotating sphere induces entrainment of the fluid, which adds to the velocity on one side of the particle and decreases it on the other. This phenomenon is known as the Magnus effect, [31, 32], and it tends to exert a force perpendicular to the plane of the boundary. A comprehensive understanding of the Magnus effect is not yet available, but Maccoll [33] expressed the lift force as :

$$\text{lift force} = \frac{\pi C_L d^3 \rho_f U_f^2}{8} \quad (2.12)$$

where C_L is the coefficient of lift.

Alternatively, Rubinow and Keller [34] gave the form :

$$\text{lift force} = \frac{\pi d^3 \rho_f \omega U_f}{8} + \text{terms which are small if } Re_p \text{ is small} \quad (2.13)$$

where ω is the angular velocity of the sphere. It is of interest to note that the lift force is independent of the fluid viscosity. Soo and Tien [35], found that by extending Stokes' method to a fluid bounded by an infinite fixed wall, the presence of the wall significantly affected the intensity of motion of the particles in the mean stream of a two-phase duct flow. They found that the intensity of particle motion increased towards the wall, a result obtained here experimentally in section 8.4.

2.6 Multi-Particle System Interactions

Inter-particle collisions are usually ignored from analyses as having little effect on the overall mechanics of the flow. [36,37] For example, if the particle number density is small enough, the momentum exchange caused by collisions and the force resulting from them is small in comparison with the viscous resistance to particle motion. Alternatively, if the particles are of a uniform size, then they have very nearly the same velocity relative to the gas and, consequently, have little tendency to collide. It has already been shown, however, that when particles are conveyed by a fluid constrained to move within a solid boundary, forces exist which cause motion having a component normal to the mean flow. Thus, even for light solids loadings, neither of the above two conditions are satisfied and the effect of particle-particle collisions must be accounted for in any complete theoretical description of a gas-solids flow. When the particles in the gas cover a wide size distribution, each size slips at its own appropriate rate, with the consequence of collisions. For conditions where the flow field interference between particles can be ignored and for a perfectly elastic collision, Marble [38] derived the momentum increase in the axial direction of a spherical particle of radius

$d_1/2$ due to a single collision to be :

$$m_1 [U_{p1}'' - U_{p1}'] = \frac{2m_1 m_2}{m_1 + m_2} [U_{p2}' - U_{p1}'] \cos^2 j \quad (2.14)$$

where m_1 and m_2 are the masses of the colliding particles,
 U_{p1}' , U_{p2}' are their initial axial velocity components,
 U_{p1}'' , U_{p2}'' are their final axial velocity components,
 and j is the angle of contact.

The force per unit volume acting between two particle clouds of two different sizes is thus given by:

$$\text{Force} = \pi n_1 n_2 \left(\frac{d_1}{2} + \frac{d_2}{2} \right)^2 \left(\frac{m_1 m_2}{m_1 + m_2} \right) |U_{p1} - U_{p2}| (U_{p2}' - U_{p1}') \quad (2.15)$$

where $|U_{p1} - U_{p2}|$ is the absolute value of the mean difference velocity between each cloud

and n_1 , n_2 are the number of particles in each cloud.

Marble also showed that the interparticle collision forces for such a system could be of the same order as the gas viscous forces.

In addition to aspects of momentum exchange, particle-particle impacts must always be associated with agglomeration in the flowing suspension. The degree of particle cohesion is obviously dependent upon the material circulated and it is likely to be dependent upon the flow conditions. Thus, small agglomerates of particles may be formed as a consequence of such collisions and if the cohesive forces are sufficiently small, the agglomerates may be sheared apart later by the fluid motion, thereby furthering the complexity of analysis.

Some factors influencing the formation of agglomerates are : London - Van der Waals forces, humidity, surfaces, time of contact, static electricity, viscous surface coatings and temperature. These are discussed by Corn [39] and Pietsch [40] .

Particle interactions also include interactions with the solid boundary, which may result in the particle adhering to the wall or at least giving up some of its kinetic energy. This results in the necessity for the air stream to supply more energy to enable the particle to accelerate to its former steady state velocity.

In addition, fluid dynamic interaction effects will prevail, which arise on account of the distortion of the flow field around the particle influencing the flow fields of adjacent particles [2]. When two particles move through an extensive viscous fluid, each of them helps the other forward so that the drag of the fluid on either particle is less than if the other particle were absent. The reduction in drag for a pair of spheres was first investigated by Smoluchowski [41] and Faxen [42]. Even at ten diameters apart, the reduction in drag for spheres of the same size was about 7%, and at two diameters was about 25%

2.7 Electrostatic Effects

Electrostatic effects are always a prime suspect where there is a lack of agreement between the results of different investigators and they have been reported to have increased the measured pressure drop by a factor of up to ten [43]. Contact charging has been reviewed by Montgomery [44] and discussed by Soo [2].

The electrostatic charging of suspended particles occurs when they are brought into contact with the flow boundaries by impingement. When in contact, charge transfer takes place due to the initial difference in Fermi levels of the two materials. The Fermi levels equalise and rapid separation of the two bodies leaves one body positively charged and the other, formerly the one with the higher Fermi level, negatively charged. It is still not possible, however, to analytically predict the effect of charge transfer on the pneumatic conveying process and further work is necessary.

CHAPTER 3

PNEUMATIC CONVEYING PLANT DESIGN

3.1 Design Specification

The pneumatic conveying plant was designed according to the following criteria:

(a) The principal requirement was to produce a gas-solids flow in a vertical pipe, with the possibility of adaptation, at a later date, to horizontal flow. Since laser anemometry techniques were to be used for particle velocity measurement, the vertical pipe - or at least that section where measurements were to be taken, had to be transparent. Moreover, the pipe had to be sufficiently long for the establishment of fully developed flow and the two phases completely mixed at the plane of measurement.

(b) Both air mass flow rate and solids mass flow rate were to be metered, so that the air Reynolds number and the solids loading ratio could be determined. In addition, the solids loading ratio was to be variable over a range appropriate for use with the laser anemometer.

(c) The cost of the powder determined that the solids should be recirculated in a 'batch' manner. Recirculation was also expected to be beneficial, since it is known that the particle size distribution stabilises after only a few circuits, [45], resulting in an accurately reproducible powder flow rate.

(d) Apart from requiring that the pneumatic conveying rig should be of industrial pilot plant dimensions in order to yield realistic information, it was necessary for the time of flow of each batch of powder to allow a required number of measurements to be taken. Thus, the feed hopper had to be large enough to store a reasonable amount of powder.

(e) Efficient separation of the two phases, after leaving the test section, was necessary, clean air being exhausted to atmosphere.

(f) The air supply had to be oil free so as to ensure no contamination of the particulate phase, and in sufficient quantities to produce realistic conveying velocities in the test section.

(g) A degree of temperature regulation was desirable in order to control some of the flow properties.

(h) The test section would need to be vibrationally isolated from the rest of the system to avoid any vibrations adversely influencing the operation of the laser anemometer. Also, any supporting arrangements for the laser anemometry equipment should be rigid and similarly vibrationally isolated.

The above requirements resulted in the line diagram shown in fig. 3.1. Apart from a few minor modifications, this diagram closely represents the actual system.

3.2 Description of Pneumatic Conveying Plant

Schematic diagrams of the conveying system are shown in figs. 3.2 and 3.3, whilst general views are shown in figs. 3.4 and 3.5. The system consists basically of three parts:-

- (i) air alone circuit,
- (ii) solids feed circuit, and
- (iii) gas-solids circuit

3.2.1 Air Alone Circuit

The 'air alone' circuit includes the air blower, heat exchanger, air flow meter and the air control valve. The circuit joins the solids feed line at the air-solids mixing unit.

Air is supplied to the system by a Roots positive displacement rotary piston air blower. It delivers oil free air at a nominal maximum rate of 200 s.c.f.m. ($5.66 \text{ m}^3/\text{min}$) and 12.5 p.s.i.g. (880 cm w.g.). The blower is driven by a 20 h.p. motor and its operating speed is 2860 r.p.m., so the effect of pulsations on the flow is minimised. The blower assembly is mounted on anti-vibration mountings and is housed, together with the heat exchanger, in a soundproof room.

The heat exchanger is a shell-and-tube once-through type, made by Serck Heat Transfer, and it is positioned directly above the air blower. The cooling water is drawn from the main laboratory supply line and passes over the aluminium-brass heat exchanger tubes before being exhausted to a nearby drainage system. In practice, only a small flow is required to maintain a constant air temperature of between 20°C and 28°C .

The physical geometry of the powder handling laboratory required that a major part of the air supply line was above head height and this posed problems of supporting heavy mild steel gas pipe. The inclusion of a heat exchanger, however, reducing the air temperature from well above 100°C at the blower outlet, allowed rigid plastic piping to be used without fear of temperature distortion. This air supply piping is of 3 inch bore p.v.c. manufactured by Le Bas, and all joints are air tight cemented. The flow control valve is a ball type and has the approximate characteristics shown in fig. 3.6. The air mass flow is metered by an orifice plate, section 4.2., designed to B.S. 1042, with ample upstream and downstream straight lengths. This portion of the air line, which has an overhead location, is well supported by square section steel tubing. Before entering the gas-solids mixing chamber, the air line undergoes a reduction from

3 inches to 1 inch diameter, in order to increase the air velocity for better mixing. At the lowest point of the air line, a drain cock enables collected water to be purged from the system.

Thermistor temperature gauges enable the air temperature to be found at exit from the heat exchanger, and at entry to the gas-solids mixing chamber.

3.2.2 Solids Feed Circuit

The solids feed system includes a storage hopper, feed hopper and metering screw feeder.

After leaving the test section, the two-phase flow enters a 50 ft³ capacity hopper which acts as both cyclone separator and storage hopper. Fines are collected as the air passes through the bag filter, (section 3.2.3), which is situated above the storage hopper.

The storage hopper is pivoted about two support points, and rests on a load cell at a third support point. The weight of powder in the hopper is determined from the calibrated load cell reading (section 4.4). The weight of the hopper and its contents can be removed from the load cell using a lifting screw. This facility is necessary in order to prevent damage to the load cell when shaking the filter bags. The hydraulic load cell and dial, made by Hydracell Limited, was found to have ample capacity for the amount of powder in use. The makers quote an accuracy of $\pm 1\%$ full scale deflection.

A 6 inch diameter hand-operated butterfly valve separates the storage hopper from the 10 ft³ capacity feed hopper. The two hoppers, both of mild steel, share a valve controlled pressure balance pipe, the purpose of which is to equalise the pressure in the two hoppers before discharging powder from the storage to the feed hopper. The

feed hopper, which includes a 12 inch diameter access hatch for loading purposes, is fitted with a Simon's bin activator. The bin activator is essentially a vibrating conical baffle, driven by a 1/8 h.p. vibrator motor and its function is to prevent problems such as bridging and rat-holing, which would invalidate the screw feeder calibration and produce a non-uniform gas-solid flow.

Powder from the feed hopper enters the trough of a metering screw feeder. A sectional view of the screw feeder is shown in fig. 3.7, which includes the air-solids mixing unit, and an external view is shown in fig. 3.8. The feeder was slightly modified, following commissioning trials, from its original form (section 3.3). The 1 27/32" diameter stainless steel screw is driven through a Carter hydraulic variable speed gear unit, by a 1/2 h.p. motor. A speed control wheel incorporates a graduated dial which can be suitably calibrated in terms of powder discharge rate (section 4.3). A vibrator motor, which provides constant intensity vibration, is situated beneath the feeder trough. The vibrating action contributes to the accuracy of the feeder, which the makers quote as $\pm 1 - 2\%$ on a minute to minute basis. The screw feeder unit is mounted on a flexibly supported base. Bearing support for the feed screw flight is achieved at the discharge end by incorporating an extension piece to span the gas-solids mixing chamber as shown in fig. 3.7. The extension piece is found to wear in practice, (section 3.3) because of the constant abrasive action of the fluidised powder, and so the design allows for easy replacement.

3.2.3 Gas-Solids Circuit

The metering screw feeder discharges powder into the mixing unit, where it is fluidised by the incoming turbulent air jet. The mixing

unit dimensions are similar to those of Mason, [45] having a 1 inch diameter air inlet and a 2 inch diameter two-phase outlet. It is constructed of mild steel sheet and the top and bottom plates are removeable. In practice, the arrangement results in an evenly dispersed flow in the measurement plane of the test section.

A pressure equalising line joins the mixing chamber to the feed hopper, in order to provide 'zero' pressure differential between these two positions, thus simulating the conditions under which the screw feeder was calibrated (section 4.3). The two phase flow leaves the mixing unit through 2 inch diameter mild steel pipework and the 7 inch radius bends in the two-phase flow circuit are designed to minimise problems of bend erosion caused by the abrasive action of the flowing suspension [46] .

Vibrations emanating from the powder feed and air supply systems are effectively damped by the inclusion of a length of heavy rubber piping at each end of the vertical test section. Also included in this part of the pipework is a smoke injection point, whose function is described in chapter 6. This short section of piping is firmly anchored to the concrete floor, thus enhancing the effect of the rubber piping.

The series of bends following the mixing unit is designed to enable a sufficient vertical length of test section for established flow to prevail at the plane of measurement, whilst enabling the plane of measurement to be sufficiently below roof height. A 3 m length of 50 mm nominal bore Q.V.F. glass pipe, with sealed flange connections at each end, forms the test section. The actual bore, measured at the upper end of the tube, was found to be 49.4 mm. Pressure tappings were introduced into the glass pipe for some of the work in this thesis and these are described in section 3.3. The test section,

which precedes a 2 inch bore perspex section having facility for pitot-static traverse tests, (section 4.2) is supported throughout its length by a triangular framework of square section steel tubing, and is further supported by tie-bars at the top of the section. These are attached to overhead cross members. The perspex section and the test section supporting framework can be seen in fig 4.2.

Separation of the two phases is achieved partly in the storage hopper, due to the reduction in air velocity there, whilst fines are collected by a venting unit which utilises 100 ft² of washable cotton filter pads. Powder which becomes entrained in the filter pads is dislodged by means of a mechanical shaking mechanism, which is activated by a $\frac{1}{4}$ h.p. motor only under static air conditions. The powder falls into the storage hopper ready for recirculation. Clean air leaves the filter via an extraction duct which terminates on the outside of the laboratory. A lightly sprung flap at the end of the duct prevents ingress of rain. The auxiliary filter unit shown in fig 3.4 (section 3.3), was used for the work outlined in chapter 6.

3.2.4 Platform

The laser anemometer and ancillary equipment are housed on a rigid supporting platform. This has no physical contact with any part of the pneumatic conveying system and rests on four rubber pads. It is capable of supporting two operators in addition to the measuring equipment, and is constructed of various substantial steel sections and a wooden floor and work-top. The height of the worktop allows laser anemometry measurements at about 50 pipe diameters above the inlet to the glass test section. A white screen is provided for use with the laser equipment and the worktop provides placement for an ample plugboard and emergency knock-off switches for the whole plant.

3.3 Commissioning of Plant

Many unforeseen problems, which could not be predicted at the 'drawing board' stage, became apparent very soon after construction of the pneumatic conveying rig was completed. Modifications to manufacturers' products, routine maintenance problems and additions for specific purposes were required. Modifications to the metering screw feeder were found necessary in order to achieve an evenly mixed flow in the test section. The original design of the screw feeder utilised a screw in the form of an open helix, the conveyed material passing through the central core and discharging directly into the perpendicular flowing air-stream. Inspection of the two-phase flow which resulted from this arrangement revealed that the powder flowed in short bursts rather than in a continuous, evenly mixed manner. In addition, the feeder became unstable at the higher solids feed rates due to the open helix providing an easy path for the air to short-circuit through to the feed hopper. This was resolved by introducing a central shaft into the helix and slightly shortening the helix at the discharge end. Shortening the helix allowed a small build up of powder at the discharge end and this, together with the inclusion of a central shaft, increased the path resistance to air influx.

The first attempt to attain a more uniformly distributed gas-solid flow, by increasing the air velocity at the air/solids interface using a venturi insert was, however, a failure. At low solids feed rates the two-phase flow was satisfactory, but at higher solids feed rates a pulsating flow was generated. Redesigning the air/solids intersection point to its present form resulted in satisfactory flow conditions for all feed rates obtained. The improvement is attributed to the turbulent eddies associated with the sudden enlargement at entry to, and sudden contraction at exit from, the mixing chamber.

The mixing chamber design necessitated the use of an extension piece to the central shaft of the feed screw for bearing support purposes, see fig. 3.7. Erosion of the extension piece resulted in several attempts being made to reduce the wear rate by protecting the extension piece with materials such as soft rubber, stellite weld and a tight hard nylon sleeve. Hardened silver steel was also used. Although some reduction in wear rate was achieved at the lower conveying velocities, particularly with the nylon sleeve, there was little improvement at the higher velocities. A selection of extension piece specimens is shown in fig. 3.9.

Wear also necessitated occasional replacement of bends in the gas-solids circuit and, for this reason, it was the policy to 'back' the bends in an attempt to prolong their working life. Two examples of worn bends are shown in fig. 3.10., where virtually all the wear occurred at the outer radius.

The work described in chapter 6 required sub-micron titanium dioxide particles to be injected into the air flow in order to measure air velocities and turbulence intensities. It was considered that contamination of the pneumatic conveying system with T_iO_2 was undesirable and, since the normal cotton filter bags were unsuitable for such fine particles, an auxiliary filter was incorporated into the rig. For this investigation the T_iO_2 seeded air flow passed from the test section directly to the auxiliary filter through rubber piping. The filter, shown in fig. 3.4, utilises 100 ft² of polypropylene filter pads capable of retaining sub-micron particles. As with the main filter, the pads are removeable and can be shaken to dislodge any adhered powder. However, in this case the filter has its own removeable particle collecting container.

The work discussed in chapter II required the measurement of pressure drop along the vertical pipe and facilities for earthing or not earthing the glass test section. The difficulty of drilling through glass pipe to produce a clean hole on the inner surface was overcome by using a diamond tipped core drill and a liberal supply of industrial cutting fluid. This gave a fast passage through the pipe wall and chipping of the glass at breakthrough was avoided by positioning a shaped backing plate against the inner pipe surface. A thin layer of beeswax was melted between the backing plate and the inner surface of the glass pipe, and the wax-coated backing plate was held in position by a specially designed jack clamp. Holes for static pressure measurements were drilled along the length of the test section and connected to an inclined multi-tube manometer.

Aluminium foil strip was taped to the outer surface of the glass tube to provide a conducting path for the current generated by charge transfer caused by the solid particles passing through the glass tube. Insulated wire connected to the foil conducts the current to earth through a heavy duty switch: The current being measured by a calibrated charge amplifier (section 8.4)

3.4 Suggestions for Improvement

The addition of solids to a given air mass flow rate increases the pressure drop per unit length of pipework and thus increases the compressor blow-off valve opening. In order to obtain a constant air mass flow rate for different solids feed rates, it is necessary to adjust the air flow control valve for each solids feed rate. It may be seen from the valve characteristics, fig. 3.6, that the existing valve has a non-linear characteristic which makes small adjustments difficult. Thus, a control valve having a linear characteristic,

and which can be automatically regulated by variations in orifice plate differential pressure, would be most desirable.

In chapter 10 it was found possible to measure particle wall velocity, using a back-scatter technique for solids loading ratios up to 5. The limit of loading ratio was due to the pneumatic conveying plant having reached its maximum solids feed rate, and not the laser anemometer. In order to achieve a solids loading ratio of 5, only low air flow rates could be used. A more comprehensive range of results would have been obtained with a larger screw feeder.

It would have been useful to have examined the change in particle velocity profile along the axial length of the test section.

However, the series of pipe bends preceding the glass pipe induce an initial spiral flow condition and some rearrangement of the pipework at entry to the test section would be advantageous.

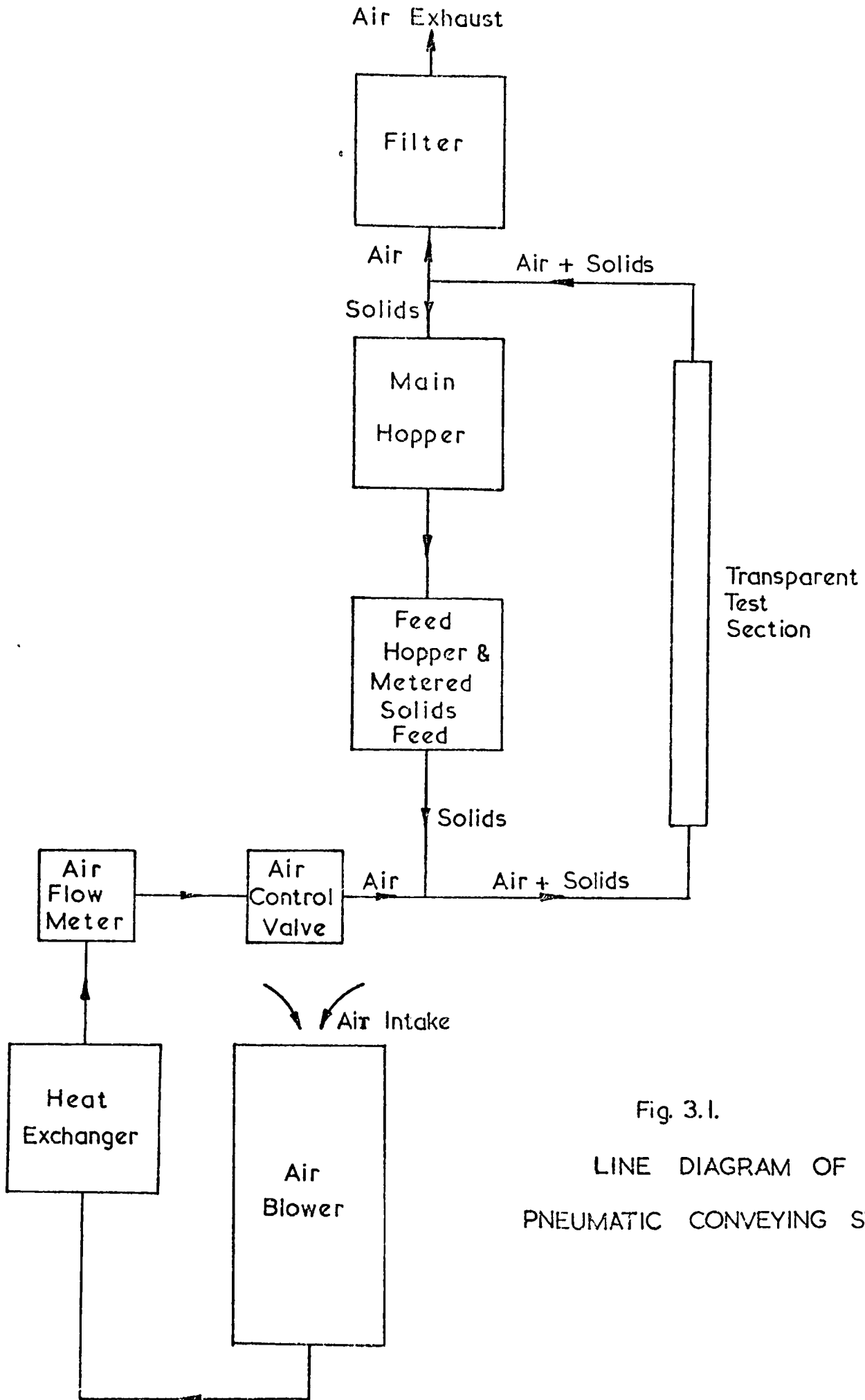
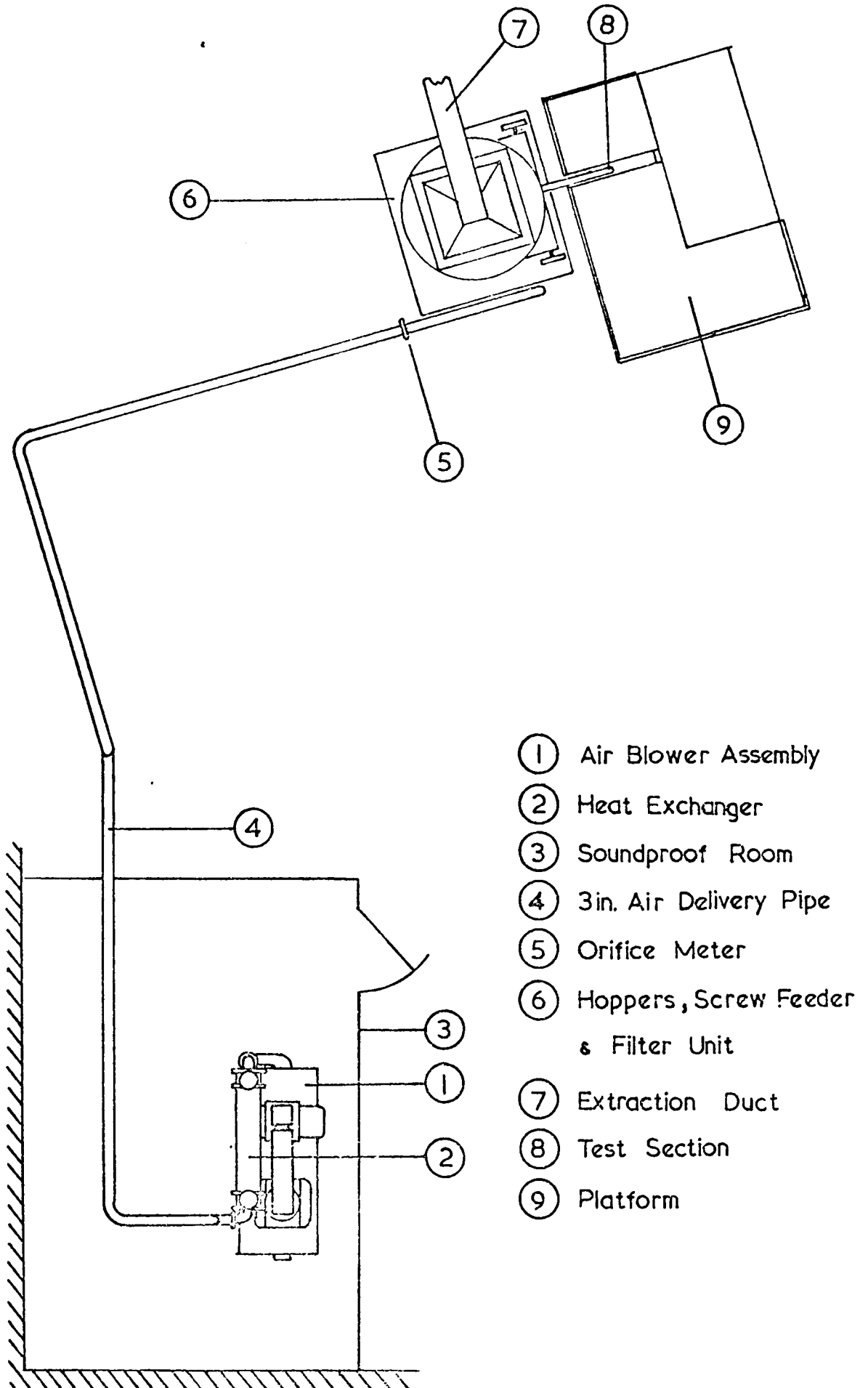


Fig. 3.1.
LINE DIAGRAM OF
PNEUMATIC CONVEYING SYSTEM

Fig. 3.2. PLANT LAYOUT (plan view)



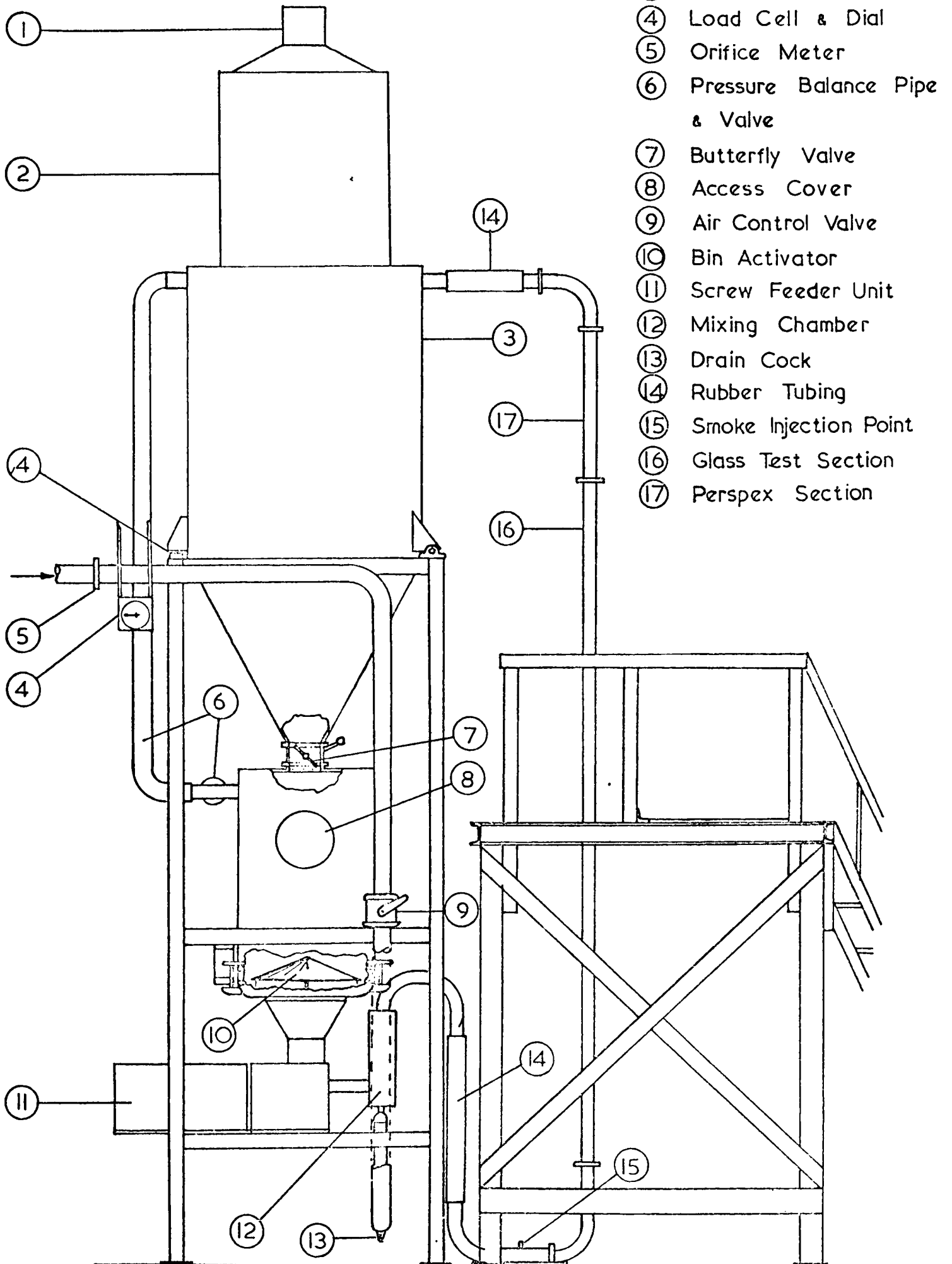


Fig. 3.3. PLANT LAYOUT (elevation)



FIG. 3.4. PNEUMATIC CONVEYING PLANT

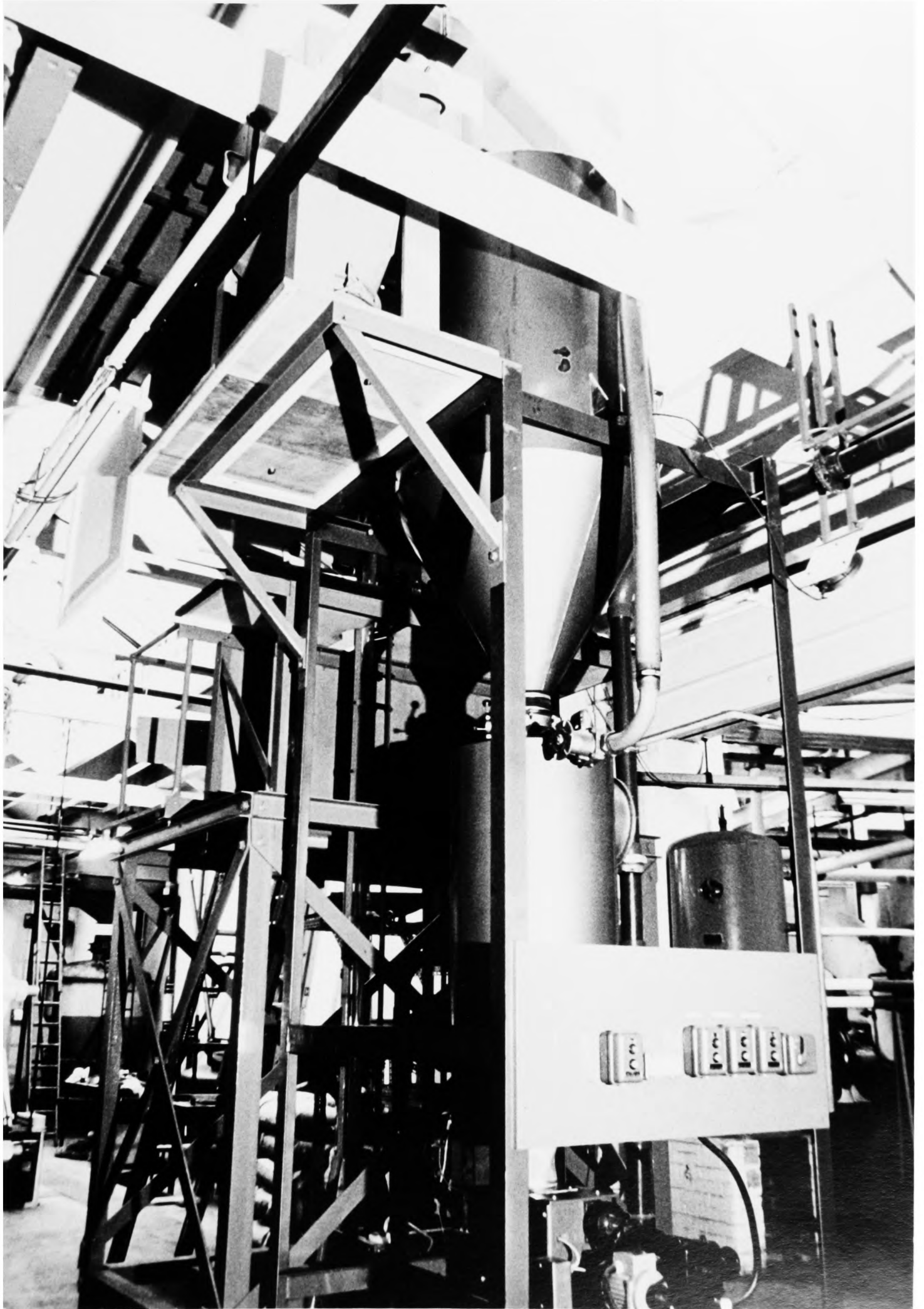




FIG. 3.5. PNEUMATIC CONVEYING PLANT



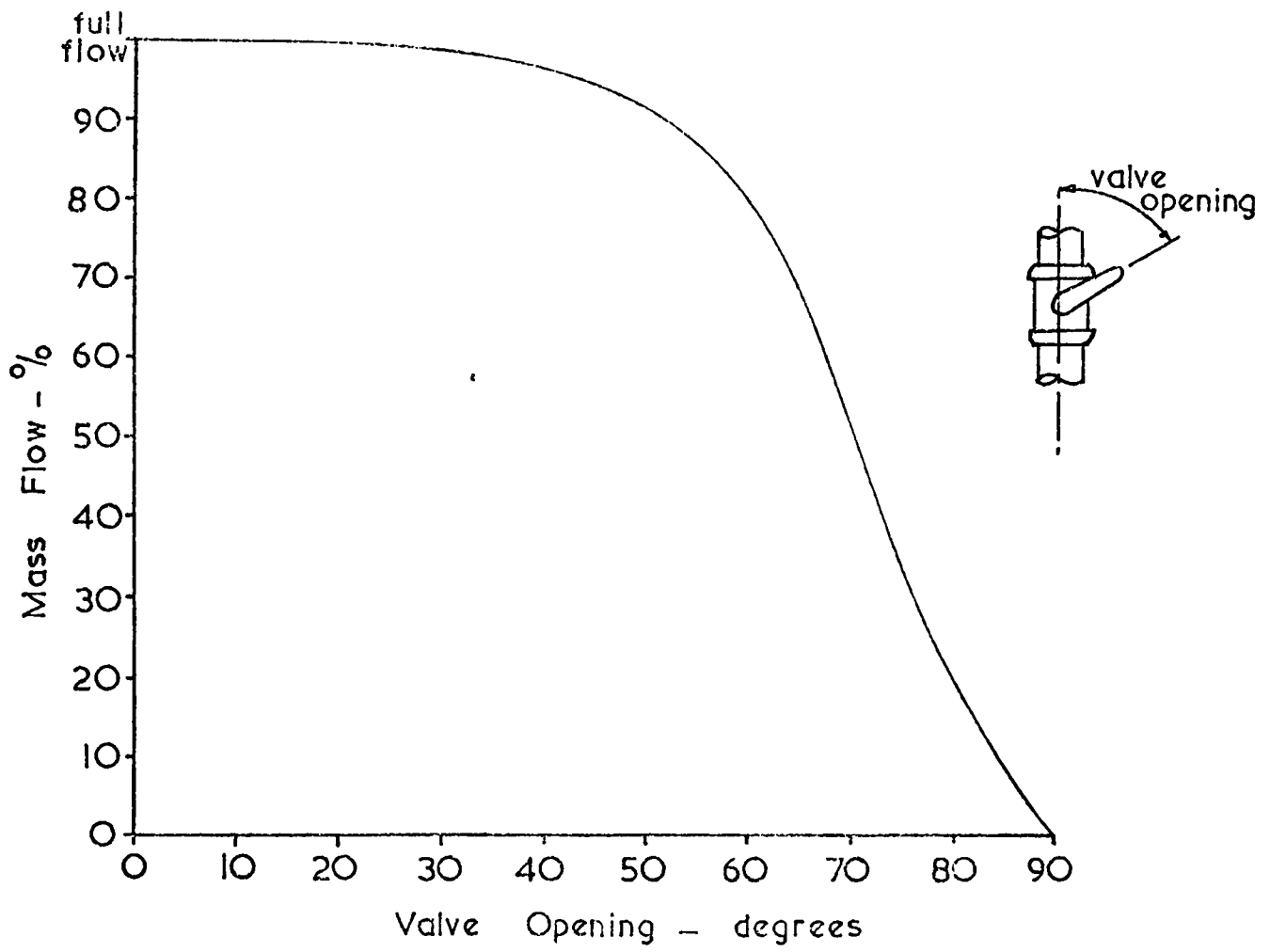


Fig. 3.6. BALL VALVE CHARACTERISTICS

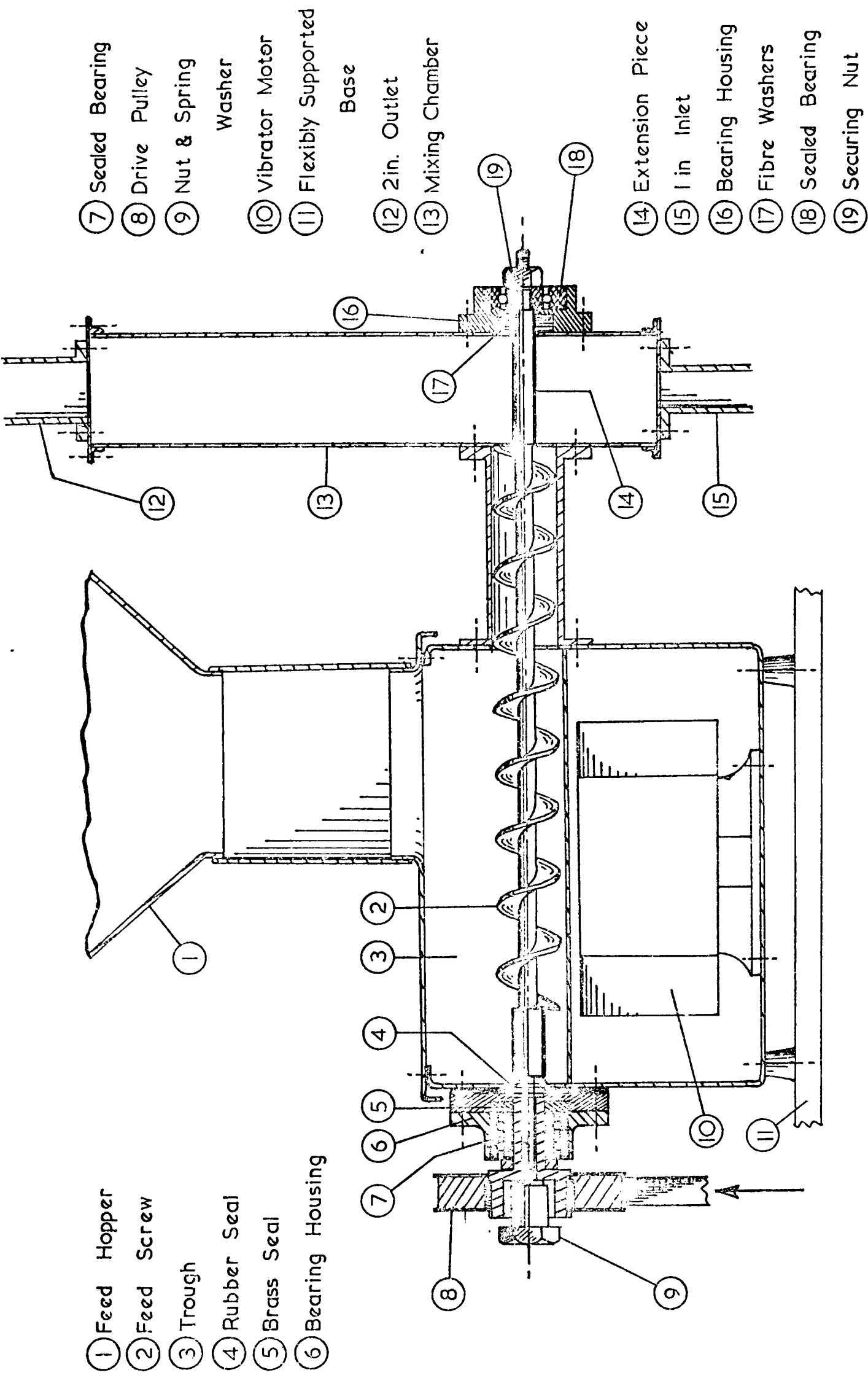


Fig. 3.7 SCREW FEEDER

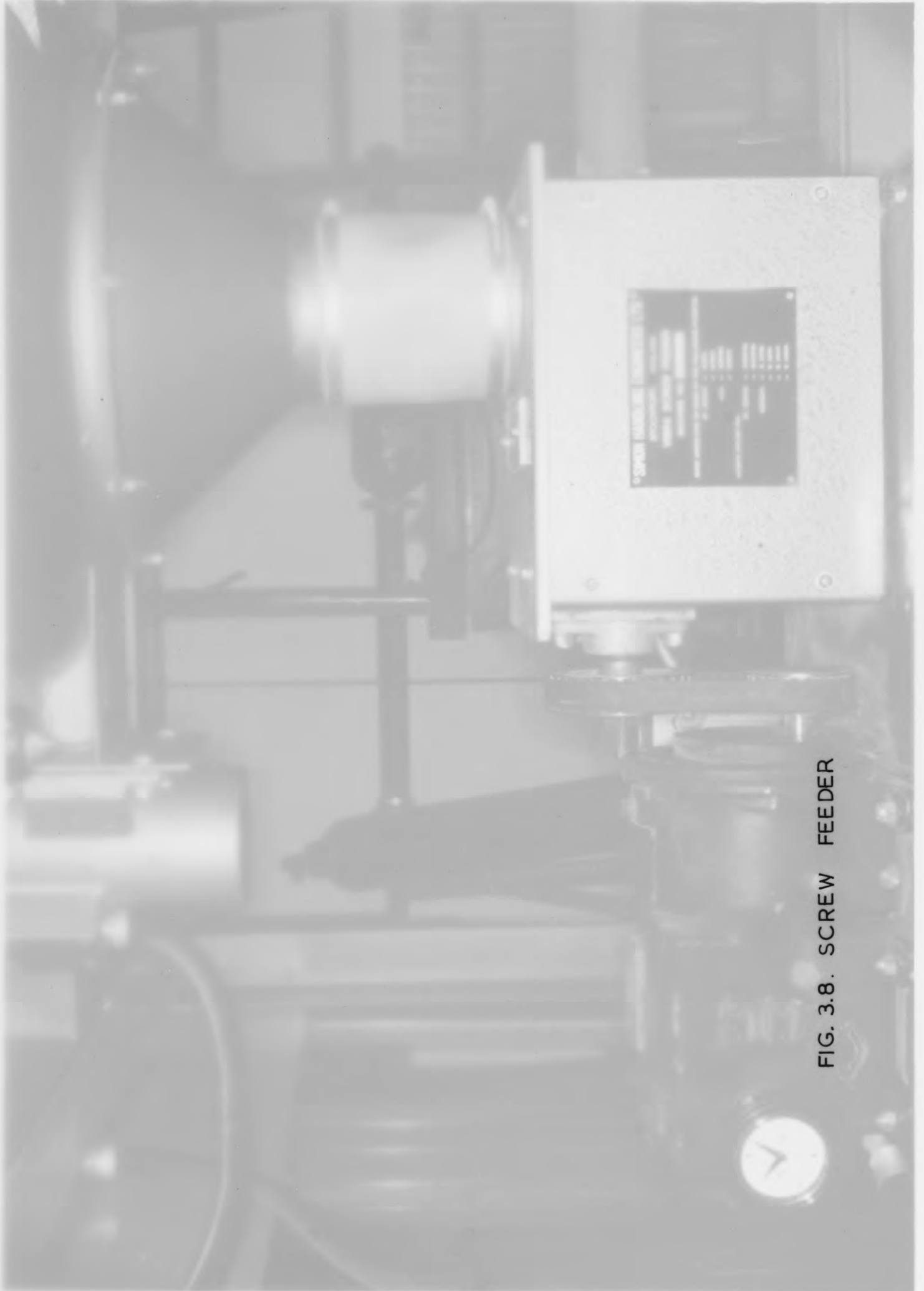


FIG. 3.8. SCREW FEEDER

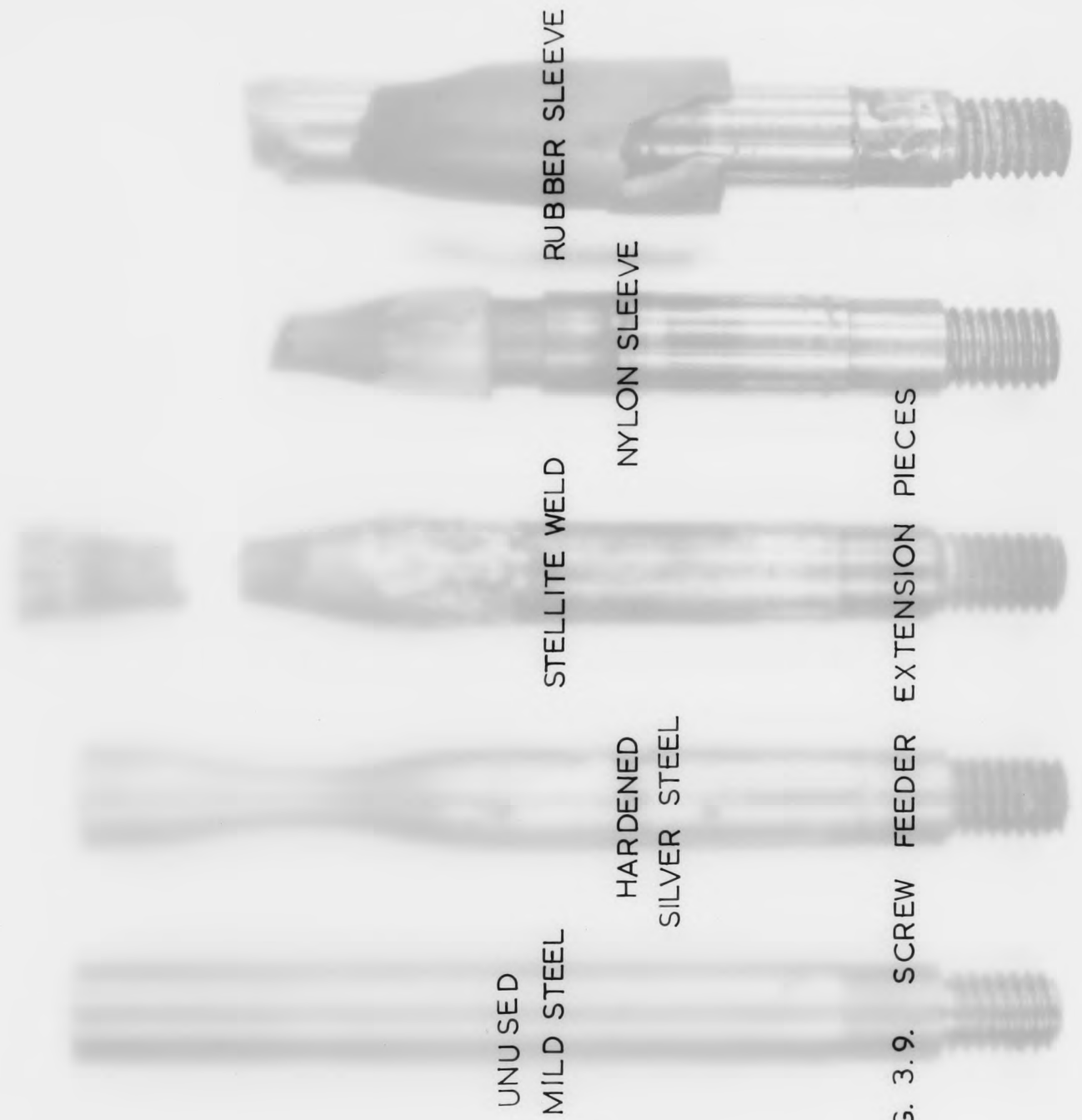
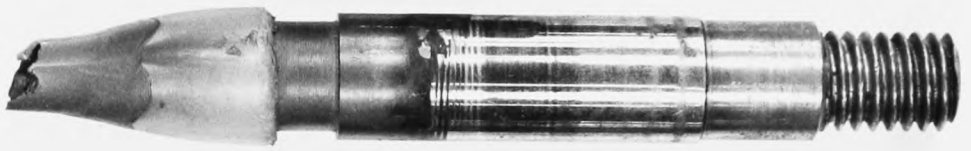
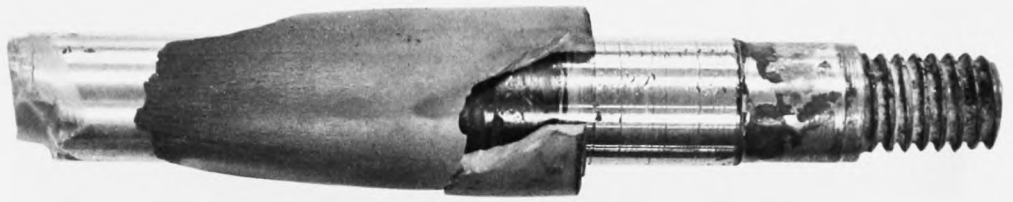


FIG. 3.9. SCREW FEEDER EXTENSION PIECES



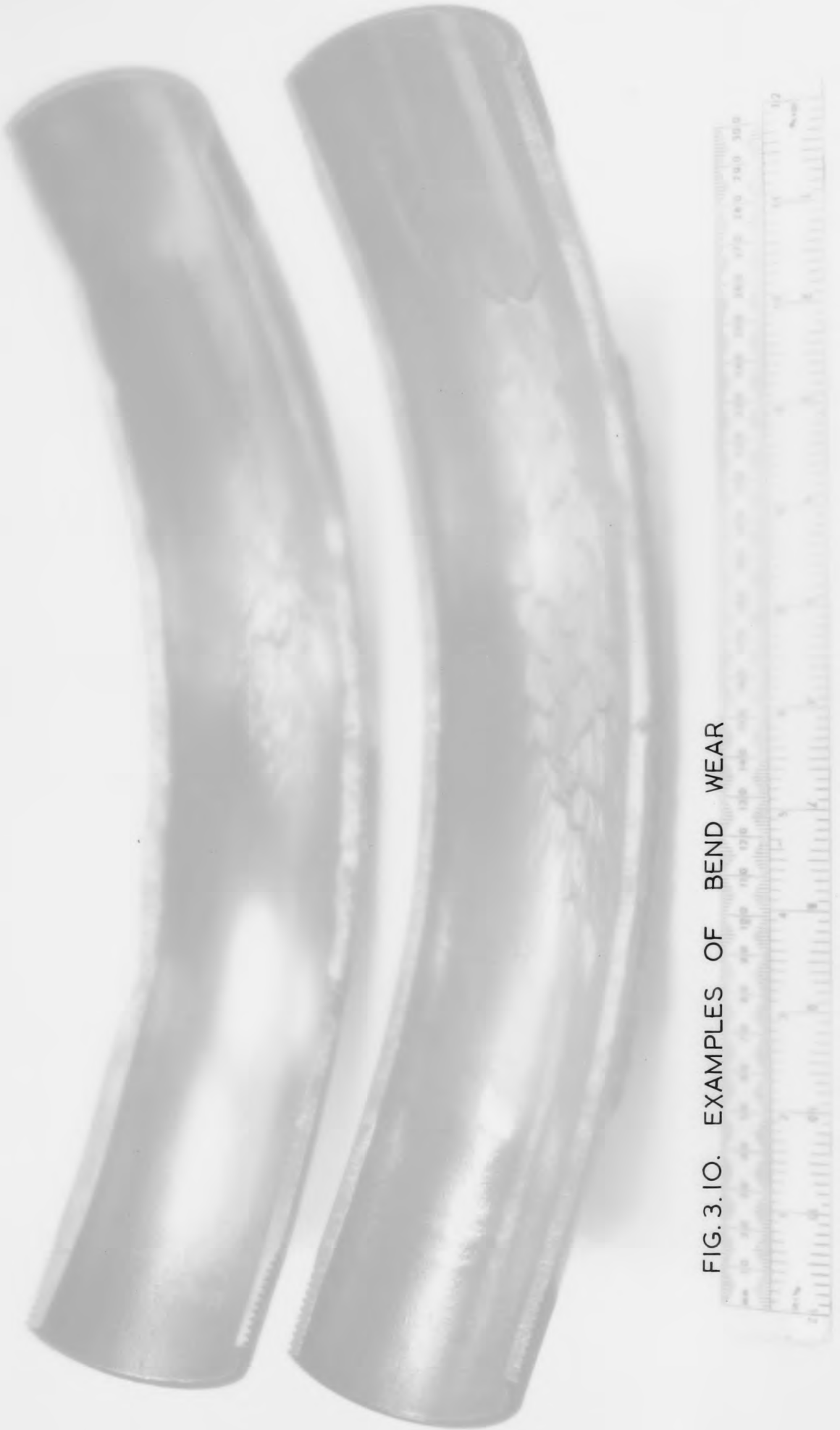


FIG. 3.10. EXAMPLES OF BEND WEAR



CHAPTER 4

CALIBRATIONS AND POWDER PROPERTIES

4.1 Introduction

Calibration of the various metering devices is most important if good accuracy of both direct and derived quantities is to be achieved.

Details of the orifice plate calibration, the screw feeder calibration, and the load cell calibration are given here. The readings from these meters enable the air mass flow rate, the solids mass flow rate, the air superficial velocity, the air Reynolds number and the solids loading ratio to be evaluated.

Powder properties are also discussed in this chapter. Two powders were used, namely Titanium dioxide (chapter 6), and 360 mesh alumina, the latter being used in all the two-phase flow investigations.

4.2 Orifice Plate Calibration

The air mass flow rate was metered with an orifice plate, manufactured according to B.S. 1042, see Fig. 4.1, and having "D and D/2" static pressure tappings. The mass flow rates obtained with the calibrated orifice plate were compared to those predicted by B.S. 1042 and the variation in air mass flow rate values justified calibration.

4.2.1 Calibration Procedure

Calibration was performed by traversing a 2.34 mm diameter pitot static tube across two perpendicular diameters of the 5.08 cm bore perspex section, see figs. 3.3, 4.2. The traverse section is situated some 60 pipe diameters above entry to the glass test section. An inclined manometer was used in conjunction with the pitot static tube, and a thermistor temperature gauge immediately prior to entry to the gas-solids mixing chamber was used to measure the air temperature.

The pressure drop across the orifice plate, ΔH , was measured using a U-tube manometer and the upstream pressure tapping also provided for measurement of the absolute pressure for British Standards mass flow calculations. [47]

After an initial warm-up period, the air temperature was stabilised by adjusting the heat exchanger water flow and the air temperature and orifice plate differential readings, ΔH , were recorded at frequent intervals and mean values were determined. The air temperature did not vary by more than 1.5°C during any test. The pitot static tube pressure difference readings were taken at diametral intervals of 1 mm.

4.2.2 Treatment of Results

From reference [47], the error in assuming that the flow is incompressible for Mach numbers, M , less than 0.2 is less than 1%. That is, from Euler's equation,

$$\frac{P_s - P}{\frac{1}{2}\rho U_a^2} = \left[1 + \frac{M^2}{4} + \frac{(2-\gamma)}{24}M^2 + \dots \right] \quad (4.1)$$

where P_s is the stagnation pressure of the air stream,

P is the static pressure of the air stream,

ρ is the density of the air

U_a is the axial air velocity

and γ is the ratio of the specific heats, (=1.4 for air)

The maximum air velocity expected with the flow rig was 60 m/s, or $M = 0.18$, so that the second term in equation 4.1 becomes 0.0081, whilst the third and successive terms are negligible. Thus, the error in neglecting terms involving M is small and equation 4.1 can be reduced to:-

$$P_s - P = \frac{1}{2}\rho U_a^2 = \text{pressure difference recorded by pitot static tube manometer} \quad (4.2)$$

A general expression for the pressure differential registered by an inclined tube manometer has the form:

$$\Delta h = l \left(\sin\alpha + \frac{d}{A} \right) \quad (4.3)$$

where $\Delta h = \frac{P_s - P}{\rho_m}$ is the vertical height of manometer fluid,
 ρ_m is the manometric fluid density,
 l is the manometer fluid column length at inclination α to the horizontal,
 a is the cross-sectional area of the manometer tube,
and A is the reservoir cross-sectional area.

In this calibration the reservoir was a sealed container and its internal dimensions could not be ascertained. However, an approximation showed the area ratio to be about 0.005. At the angle of inclination used, $\alpha = 20^\circ$, this ratio is small in comparison with $\sin \alpha$ and the error involved in neglecting it is less than 1.5%. Hence, equation(4.3) becomes

$$\Delta h = l \sin \alpha \quad (4.4)$$

Combining equations(4.2)and(4.4)gives

$$U_a = \sqrt{2 \frac{\rho_m}{\rho_a} l \sin \alpha} \quad (4.5)$$

Equation(4.5)was used to calculate the axial air velocity at each traverse position.

The airdensity, ρ_a , was found from the Equation of State:

$$\rho_a = \frac{P_a}{R T_a} \quad (4.6)$$

where P_a is the absolute pressure of the air at the test section,
 R is the gas constant, (= 0.287 kJ/kg^oK)
and T_a is the air temperature

Knowledge of the axial air velocity at each pitot static tube traverse position enabled calculation of the total volumetric air flow rate, \dot{V}_a , from the equation:

$$\dot{V}_a = 2\pi \int_0^{D/2} U_a r dr \quad (4.7)$$

where r is the distance from the axial centre line of the pipe
and D is the pipe diameter

Mass flow rate, \dot{M}_a , is then readily found by multiplying \dot{V}_a by ρ .

4.2.3 Results and Discussion

A typical set of results is shown in table 4.1 and it can be seen that the pitot static tube pressure differential has been averaged over the two diameters before substitution into equation(4.5.)

Fig. 4.3 shows axial air velocity plotted against traverse distance and compares the results with the velocity profile obtained from the power law relationship [48] . The correlation is good, which is surprising since the variation in bore of the perspex and glass tubes is from 5.08 cm to 4.94 cm respectively.

Originally, the connection between the two sections was inherently non-smooth, but the abrasive action of the flowing suspension during commissioning trials rectified this situation.

Fig. 4.4 is a plot of $U_a r$ against r , and integration of each curve enabled equation(4.7) to be evaluated. Integration was performed using the mid-ordinate rule and the mean \dot{V}_a of the two curves was used to calculate \dot{M}_a .

A total of twenty-one calibration points were obtained, see table 4.2, and fig. 4.5. The mean air temperature varied between 27.5°C and 22.5°C, as shown in table 4.2, and the absolute pressure at the test section ranged from 74 cm Hg to 78.3 cm Hg. The absolute pressures were governed primarily by the prevailing barometric conditions, these varying from 73.2 cm Hg to 77.09 cm Hg. Thus, the calibration was carried out over a workable range of conditions.

The points may be conveniently represented by three equations, as follows:

$$(i) \quad \Delta H < 7.4 \text{ cm H}_2\text{O} \quad \dot{M}_a = \frac{\log_{10} \Delta H}{18.9} \quad (4.8)$$

$$(ii) \quad 7.4 \text{ cm H}_2\text{O} \leq \Delta H \leq 15.15 \text{ cm H}_2\text{O} \quad \dot{M}_a = \frac{\log_{10} \Delta H - 0.26}{13.31} \quad (4.9)$$

$$(iii) \quad \Delta H > 15.15 \text{ cm H}_2\text{O} \quad \dot{M}_a = \frac{\log_{10} \Delta H - 0.62}{8.15} \quad (4.10)$$

A comparison between these equations and the experimental air mass flow rates is given in table 4.2. The maximum percentage deviation of the experimental points from these equations is 3.91% and the average deviation is 1.66%.

Also shown in table 4.2 is a comparison between the mass flow obtained from the pitot static tube traverses and the air mass flow calculated according to B.S. 1042. It can be seen that the experimental points deviate by large amounts from those predicted by the standard, the deviation for test 1 being 30.5%. However, at the 'design point', 25.4 cm H₂O, the standard gives a fair approximation. In view of the poor comparison above, calibration of the orifice plate was justified.

4.3 Screw Feeder Calibration

Details of the screw feeder construction are given in chapter 3 and the screw flight has the following details:

Shaft diameter	1/2 inch
Flight diameter	1 27/32 inches
Screw length	17 9/16 inches
Screw pitch	2 inches
Flight thickness	1/8 inch
Material	stainless steel

The calibration gave the relationship between the powder discharge rate, the variable drive speed setting and the rotational speed of the screw flight.

4.3.1 Calibration Procedure

To carry out the calibration it was necessary to remove the bottom cover plate of the mixing chamber and allow the feeder to discharge into a bin of known weight. The weight of powder discharged in a given time was then determined. The head of powder above the feed point ranged from 50 kg to 275 kg and the time of each test varied between 90 and 600 seconds. The screw flight rotational speed was

obtained with a tachometer and all tests were carried out using the screw feeder vibrator facility, but not the vibrating bin activator. Before readings were taken, the powder was circulated around the gas-solids conveying plant several times in order to stabilise the powder size distribution. [45].

4.3.2 Results and Discussion

The results of the calibration are shown in table 4.3 and in Fig. 4.6. In this table, the 'head of powder' column refers to the weight of powder in the feed hopper at the commencement of each test. Fig. 4.6 shows the experimental points of discharge rate, \dot{M}_p , plotted against calibration dial setting, which has a linear relation with the screw feeder rotation rate. It can be seen that the discharge rate is independent of the head of powder.

The line through the experimental points, found by a 'least squares' estimate, has the equation :

$$\text{discharge rate (kg/min) } \dot{M}_p = (1.25 \times \text{calibration wheel revolutions}) + 0.16 \quad (4.11)$$

and the percentage differences between the experimental points and this line are also given in table 4.3. Only the first five results have excessive deviation from equation(4.11). The remainder of the results lie within 5%, and 80% of these results lie within 2%. Exclusion of the first 1.25 dial revolutions results in an average remaining percentage deviation from the calibration line of 1.3%.

The calibration was carried out entirely under atmospheric conditions, the feed hopper loading hatch being open throughout. Thus, zero pressure differential existed between the feed hopper and the screw feeder. In order to maintain these conditions when discharging into the flowing air, a pressure balance pipe was introduced between the mixing chamber and the feed hopper. Some of the powder inevitably

escaped through the balance pipe back to the feed hopper, but the amount was negligible.

4.4 Load Cell Calibration

The purpose of the load cell is to provide a check on the screw feeder discharge rate. During a normal two hour test, fluctuations in the screw feeder output or a malfunction in its operation were possible. Observation of the calibrated load cell enabled these problems to be avoided and gave confirmation of the solids feed rate obtained from the screw feeder calibration.

It has been found in practice that deviations from the expected weight of powder in the main hopper, detected by keeping a check on the load cell, often indicated a fault somewhere in the system; for example, a fractured extension piece, a loose screw flight lock nut, wet powder, or a starved screw feeder trough.

4.4.1 Calibration Procedure

Two methods were used to calibrate the load cell:

- (i) Various weights were placed above the filter unit. These were positioned centrally between the pivots and the load cell, so as to simulate powder in its mean position in the storage hopper. These readings gave a load cell calibration which is independent of the screw feeder.
- (ii) The bulk of the calibration data was found by pneumatically conveying powder from the screw feeder to the storage hopper for a known time. This method gave an indication of the consistency of the screw feeder under conditions of varying feed rate, discharge time and air mass flow rate.

4.4.2 Results and Discussion

Tables 4.4 and 4.5 show the data obtained from the two methods outlined above and fig. 4.7 includes both sets of data plotted as the weight of powder, Mp, against load cell gauge divisions. The circular points indicate the first calibration method of table 4.4, whilst the crosses are for table 4.5. The line through the points of fig. 4.7 was obtained by a 'least squares' method, and is given by:

$$\text{weight of powder, Mp (kg)} = 0.57 \times \text{Load Cell Divisions} \quad (4.12)$$

The average deviation of the calibration points from the calibration line is 5.54% and, although 16.67% of the points have a deviation greater than 10% from the line, 83.4% lie within 9% of it.

Relatively poor repeatability of load cell calibration was expected, since the centre of mass of the powder could not always be expected to act through the same line. Indeed, it was observed that the load cell needle moved in jerks rather than smoothly, due to the powder sliding down the conical sides of the main hopper in a random manner.

The wide range of conditions under which powder discharge from the screw feeder was tested during calibration of the load cell, indicates that the screw feeder calibration holds for varying air flow rates. Only when there was very little powder above the screw flight did starvation make itself apparent.

4.5 Powder Properties

Two powders were used in this study, namely titanium dioxide and alumina. The titanium dioxide powder was used to obtain air velocity profiles and turbulence intensities, (chapter 6). It was chosen for this purpose because of its nominally sub-micron size range, whereas

the new alumina powder was quoted by the manufacturers to have a size range of between 11 and 45 microns.

4.5.1 Alumina Powder

Three samples of 360 mesh alumina powder were obtained by passing a collecting vessel several times beneath the screw feeder discharge. Particle size analyses were carried out on new powder, powder which had been circulated several times and powder regularly used over a period of several months, (samples 1, 2 and 3 respectively). The purpose of taking three samples was to assess the effects of transportation on the size distribution.

For this powder, size analyses were carried out by the School of Biology on an Industrial Model D Coulter Counter, equipped with a 200 micron diameter aperture tube. The dispersant used was Glycerol and the calibration factor was found to be 13.9. The resulting size distributions, in terms of both percentage number frequency and percentage weight, are shown in fig. 4.8. It can be seen that samples 2 and 3 give virtually the same size distributions, which are slightly different from those of the unused powder. That is, after a slight variation in size distribution over a few circuits of the pneumatic conveying rig, the alumina was characterised by a distribution which did not significantly change during several months of use. It is seen that the number of fines in samples 2 and 3 is greater than that of sample 1. In addition, the peak of the percentage weight curve for used powder has shifted to a slightly lower value. These two observations suggest that the sharp corners have been removed from many of the particles, creating more fines and thus slightly lowering the mean size. The phenomenon has been previously observed by Mason [46]

From the data given by the Coulter Counter analysis, the size distributions for the three samples are as follows :-

	LOWEST RECORDED SIZE (MICRONS)	MEAN SIZE PERCENTAGE WEIGHT (MICRONS)	MEAN SIZE PERCENTAGE NUMBER (MICRONS).	HIGHEST RECORDED SIZE (MICRONS)
Sample 1	4.46	22.77	9.57	75.46
Sample 2	4.46	19.99	8.03	75.46
Sample 3	4.46	20.31	8.10	75.46

The colour of the powder changed from white to grey, which was probably caused by the particles becoming contaminated with paint from the interior of the two hoppers.

The density of the alumina was found, by specific gravity bottle, to be 3870 kg/m^3 and the bulk density was 2010 kg/m^3 .

4.5.2 Titanium Dioxide Powder

The Coulter Counter cannot be used for size analysis of sub-micron particles and so the samples of titanium dioxide powder were analysed with an electron microscope in the School of Biology. The micrograph shown in fig. 4.9 has a magnification of 25,714. The samples were collected on a prepared grid by injecting the powder at the bottom of the test section, (chapter 6) and allowing it to issue from a pressure tapping at the top of the test section. Since the particles are seen to be non-spherical, an 'equivalent diameter' was assessed for each particle considered and a total of 144 particles were used to construct the histogram of fig. 4.10. The data collected gave a size distribution between 0.04 microns and 0.6 microns, with a mean diameter of 0.274 microns.

The density of the T_iO_2 was found to be $4,200 \text{ kg/m}^3$.

Table 4.1. SPECIMEN PITOT-STATIC TUBE TRAVERSE RESULTS

pressure difference across orifice plate = 17.65 cm.H₂O

test section absolute pressure = 74.75 cm.Hg

air temperature = 27°C

manometer inclination = 20°

TEST N° 10

traverse distance (cm)	pipe radius - r (cm)	pressure differential			axial air velocity - U _a (m/s)	U _a x r (cm. m/s)
		diameter 1 (cm H ₂ O)	diameter 2 (cm H ₂ O)	mean (cm H ₂ O)		
.116	2.424	12	11.1	11.55	25.88	62.72
.216	2.324	13.8	13.15	13.475	27.96	64.97
.316	2.224	14.95	14.3	14.625	29.07	64.65
.416	2.124	15.9	15.6	15.75	30.24	64.22
.516	2.024	16.7	16.5	16.6	31.02	62.79
.616	1.924	17.5	17.15	17.325	31.71	60.99
.716	1.824	18.35	17.9	18.125	32.45	59.19
.816	1.724	18.95	18.85	18.9	33.13	57.11
.916	1.624	19.5	19.3	19.4	33.6	54.55
1.016	1.524	20.05	19.85	19.95	34.03	51.83
1.116	1.424	20.8	20.45	20.625	34.61	49.28
1.216	1.324	21.3	21.15	21.225	35.16	46.53
1.316	1.224	21.85	21.75	21.8	35.57	43.53
1.416	1.124	22.45	22.3	22.375	36.04	40.52
1.516	1.024	22.9	22.85	22.875	36.43	37.32
1.616	.924	23.45	23.3	23.375	36.82	34.02
1.716	.824	24.05	23.8	23.925	37.27	30.71
1.816	.724	24.35	24.25	24.3	37.57	27.19
1.916	.624	24.75	24.65	24.7	37.87	23.63
2.016	.524	25.2	25.15	25.175	38.23	20.03
2.116	.424	25.45	25.5	25.475	38.46	16.31
2.216	.324	25.65	25.8	25.725	38.64	12.51
2.316	.224	25.8	26	25.9	38.77	8.684
2.416	.124	25.95	26.2	26.075	38.9	4.825
2.516	.024	26.05	26.35	26.2	39.01	.936
2.616	.076	26.05	26.4	26.225	39.02	2.965
2.716	.176	25.95	26.4	26.175	38.98	6.863
2.816	.276	25.8	26.3	26.05	38.88	10.73
2.916	.376	25.55	26.2	25.875	38.75	14.56
3.016	.476	25.3	26	25.65	38.62	18.39
3.116	.576	24.9	25.65	25.275	38.3	22.07
3.216	.676	24.55	25.35	24.95	38.06	25.72
3.316	.776	24.1	25	24.55	37.75	29.29
3.416	.876	23.6	24.55	24.075	37.37	32.74
3.516	.976	23.1	24.1	23.6	37.01	36.12
3.616	1.076	22.55	23.55	23.05	36.58	39.36
3.716	1.176	22	23	22.5	36.14	42.5
3.816	1.276	21.55	22.5	22.025	35.77	45.63
3.916	1.376	20.8	21.9	21.35	35.22	48.46
4.016	1.476	20.3	21.4	20.85	34.79	51.36
4.116	1.576	19.7	20.65	20.175	34.27	54
4.216	1.676	19	20.05	19.525	33.65	56.4
4.316	1.776	18.4	19.4	18.9	33.13	58.85
4.416	1.876	17.9	18.8	18.35	32.63	61.24
4.516	1.976	17.25	18.25	17.75	32.09	63.42
4.616	2.076	16.45	17.55	17	31.42	65.22
4.716	2.176	15.7	16.8	16.25	30.71	66.85

test N ^o	pressure drop across orifice plate (cm H ₂ O)	absolute pressure at test section (cm Hg)	air temp. (°C)	air mass flow rate from pitot traverse (Kg/s)	air mass flow rate from BS 1042 (Kg/s)	% diff. ^{ce} between BS 1042 & pitot traverse	air mass flow rate from equations 4.8, 4.9 & 4.10 (Kg/s)	% diff. ^{ce} between eqns. 4.8, 4.9 & 4.10 & pitot traverse
1	3.925	75.07	23.25	.0308	.0402	30.5	.0314	1.91
2	6.625	75.07	23	.0434	.0517	19.1	.0435	.23
3	8.725	75.26	22.5	.0491	.0609	24	.0511	3.91
4	9.975	75.1	26	.0558	.0631	23.3	.0554	.722
5	11.6	77.45	25	.0586	.0680	13.81	.0605	3.14
6	13.3	74.95	26	.0649	.0726	11.89	.0648	.154
7	13.8	77.5	25	.0674	.0745	9.53	.0661	1.97
8	14.68	74	27.5	.0666	.0751	12.75	.0681	2.2
9	15.5	74	26.5	.0704	.0775	9.15	.0700	.571
10	17.65	74.75	27	.0742	.0831	10.7	.0769	3.51
11	19.65	77.89	24.75	.0834	.0871	4.25	.0826	.969
12	22.98	77.75	26.6	.0930	.0921	9.76	.0910	2.2
13	25	77.85	26.5	.0970	.0939	3.1	.0954	1.68
14	25.72	77.27	24.5	.0977	.0940	3.94	.0969	.826
15	29.3	77.91	26	.1051	.0970	8.35	.1040	1.06
16	32.42	77.16	26	.1101	.1002	9.88	.1092	.824
17	34.8	78.15	26	.1150	.1017	13.1	.1131	1.68
18	37.45	77.19	27	.1182	.1041	13.51	.1169	1.11
19	39.9	78.3	25.25	.1221	.1070	14.1	.1203	1.5
20	43.74	77.3	26.75	.1240	.1103	12.4	.1252	.956
21	47.23	77.93	26	.1257	.1133	10.91	.1293	2.78

Table 4.2. ORIFICE PLATE CALIBRATION DATA

Table 43. SCREW FEEDER CALIBRATION DATA

speed setting (dial revs)	head of powder (kg)	discharge time (secs)	weight of powder (kg)	actual discharge rate (kg/min)	discharge rate from eqn. 4.11 (kg/min)	% difference
0.25	275	600	3.31	0.331	0.473	30
0.5	275	360	3.96	0.66	0.785	15.9
0.75	275	600	9.86	0.986	1.097	10.1
1.0	265	120	2.42	1.21	1.41	14.2
1.25	262	420	11.86	1.551	1.723	10
1.5	250	360	12.14	2.023	2.035	.59
1.75	275	480	18.42	2.303	2.347	1.89
2.0	255	120	5.24	2.62	2.66	1.5
2.25	249	180	9.02	3.007	2.973	.825
2.5	239	360	20.08	3.347	3.285	1.885
2.75	219	300	18.19	3.638	3.597	1.13
3.0	200	120	7.8	3.9	3.91	.256
3.25	192	300	21.84	4.368	4.223	3.44
3.5	170	300	23.4	4.68	4.535	3.2
3.75	147	240	19.75	4.938	4.848	1.86
4.0	127	120	10.4	5.2	5.16	.774
4.25	117	240	22.82	5.705	5.473	4.25
4.5	94	240	23.7	5.925	5.785	2.42
4.75	70	210	21.4	6.114	6.098	.271
5.0	49	120	13.07	6.535	6.41	1.95
5.25	275	240	27.29	6.823	6.723	1.495
5.5	275	210	25.22	7.205	7.035	2.42
5.75	275	270	33.0	7.333	7.347	.197
6.0	275	120	15.56	7.78	7.66	1.565
6.25	275	180	23.96	7.987	7.923	.182
6.5	275	180	24.94	8.313	8.285	.338
6.75	250	180	25.94	8.647	8.598	.570
7.0	224	120	17.9	8.97	8.91	.673
7.25	206	180	27.78	9.26	9.223	.407
7.5	178	150	24.11	9.644	9.535	1.145
7.75	154	150	24.06	9.624	9.847	2.27
8.0	130	120	20.54	10.27	10.16	1.08
8.25	110	150	25.85	10.34	10.472	1.27
8.5	84	120	21.64	10.82	10.785	.325
8.75	62	120	21.82	10.91	11.097	1.69
9.0	275	120	22.95	11.475	11.41	.569
9.25	275	120	23.05	11.525	11.722	1.68
9.5	275	90	17.87	11.913	12.035	1.01
9.75	275	120	24.19	12.095	12.347	2.04
9.9	275	120	24.95	12.475	12.535	.478

Table 4.4.

LOAD CELL CALIBRATION DATA

load cell divisions	weight (Kg)	weight from eq. 4.12 (Kg)	% difference
25	13.08	14.26	8.3
45	26.18	25.62	2.18
85	50.63	48.5	4.4
130	75.05	74.1	1.28
151	92.3	86	7.33
188	107.3	107.1	.187
235	138.3	134	3.2
287	165.05	163.8	.765
372	219.2	212	3.4

Table 4.5.

LOAD CELL CALIBRATION DATA

screw feeder speed setting (revs)	pressure drop across orifice plate (cm.H ₂ O)	discharge time (mins)	load cell reading			actual weight of powder (Kg)	weight of powder from eqn.4.12 (Kg)	% difference
			initial	final	N ^o of divisions			
3	40.5	15	0	90	90	58.65	51.4	14.1
3	28.6	15	115	210	95	58.65	54.1	8.4
2	39.6	16	0	48	48	42.56	27.4	55.2
5	14	15	65	222	157	96.15	89.5	7.43
5	32.2	7.5	245	326	81	48.075	46.2	4.05
4	6.75	15	40	160	120	77.4	68.4	13.15
6	25.2	18.5	130	371	241	141.7	137.4	3.13
7	36.5	20	0	296	296	178.2	168.8	5.57
8	37.05	15	0	260	260	152.4	148.2	2.83
9	31.4	15	0	261	261	171.15	148.9	14.95
3.5	32.7	45	0	363	363	204.08	207	1.41
2.5	40.75	26	0	140	140	85.41	79.8	7.04
4.5	38.5	22	165	399	234	127.27	133.3	4.52
5.5	38.2	34	0	419	419	239.19	239	.079
5	40.2	22.5	0	230	230	144.22	131	4.27
3	32.6	30	0	200	200	117.5	114	3.07
4	22.9	33	0	281	281	170.28	160	6.4
4	22.9	43	0	384	384	221.88	219	1.31
6	22.8	6	0	76	76	45.96	43.3	6.14
6	22.8	8	0	104	104	61.28	59.3	3.34
6	10	10	0	153	153	76.6	87.2	12.1
6	36.8	17	0	220	220	130.22	125.3	4.71
6	36.8	19	0	246	246	145.54	140.2	3.8
6	36.8	23	0	300	300	176.18	171	3.03
6	39.5	26	0	350	350	199.16	199.6	.22
6	39.5	30	0	410	410	229.8	233.8	1.71
6	37.3	32	0	438	438	245.12	249.8	1.88
6	37.6	33	STARVATION					
8.5	32	10.5	0	175	175	111.563	99.8	11.8
8.5	17.8	11.5	0	202	202	122.19	115.1	6.15
8.5	8.72	2	230	260	30	21.25	17.1	24.2
8.5	36.5	18	0	322	322	191.25	183.5	4.23
8.5	10.3	23.5	0	431	431	249.69	245.9	1.54
8.5	36.5	24.5	0	450	450	260.31	256.3	4.6

Fig. 4.1. ORIFICE PLATE DETAILS

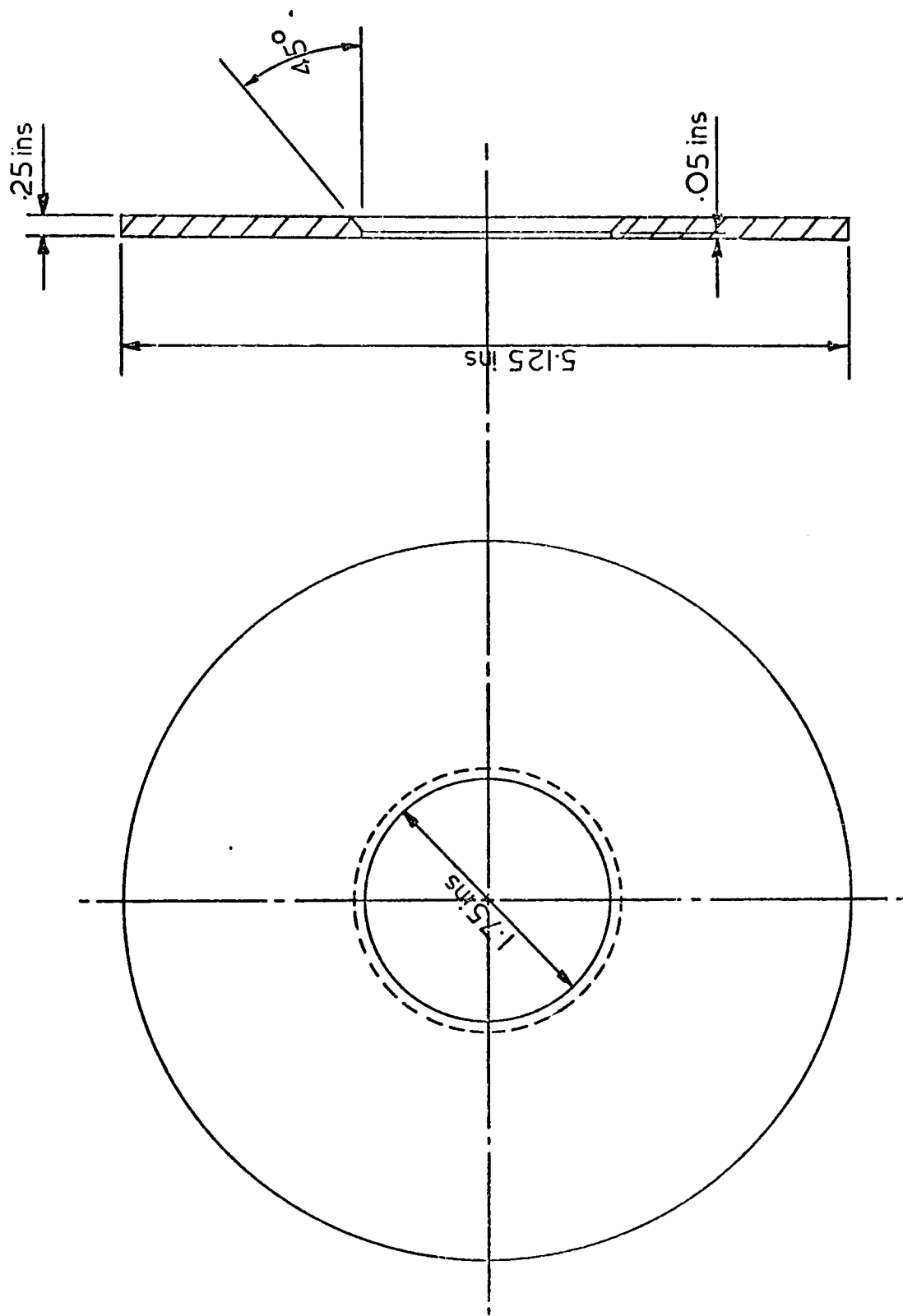
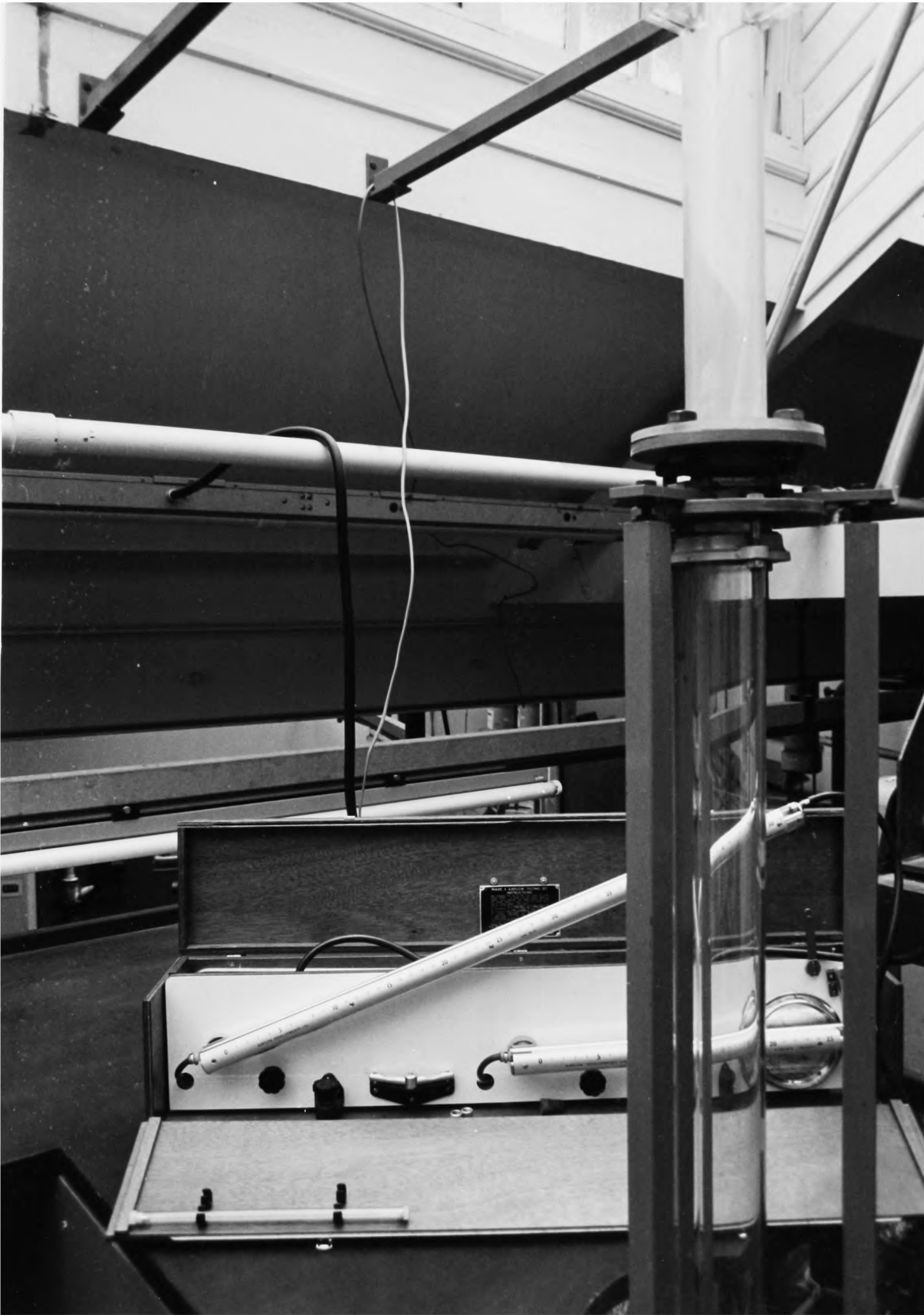




FIG. 4.2. PITOT-STATIC TUBE TRAVERSE SECTION



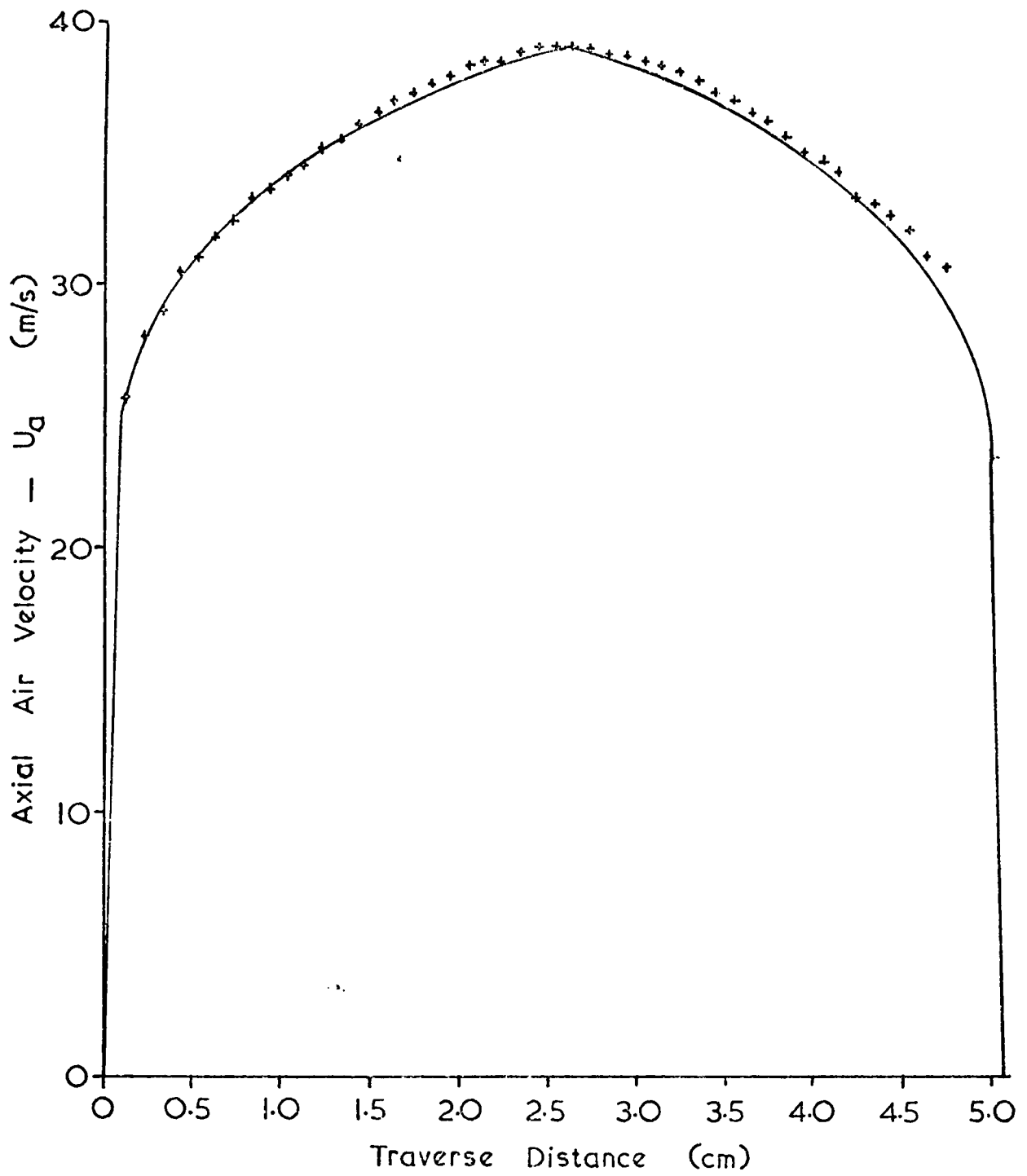


Fig. 4.3.

PITOT-STATIC TUBE TRAVERSE RESULTS FOR
TEST No 10

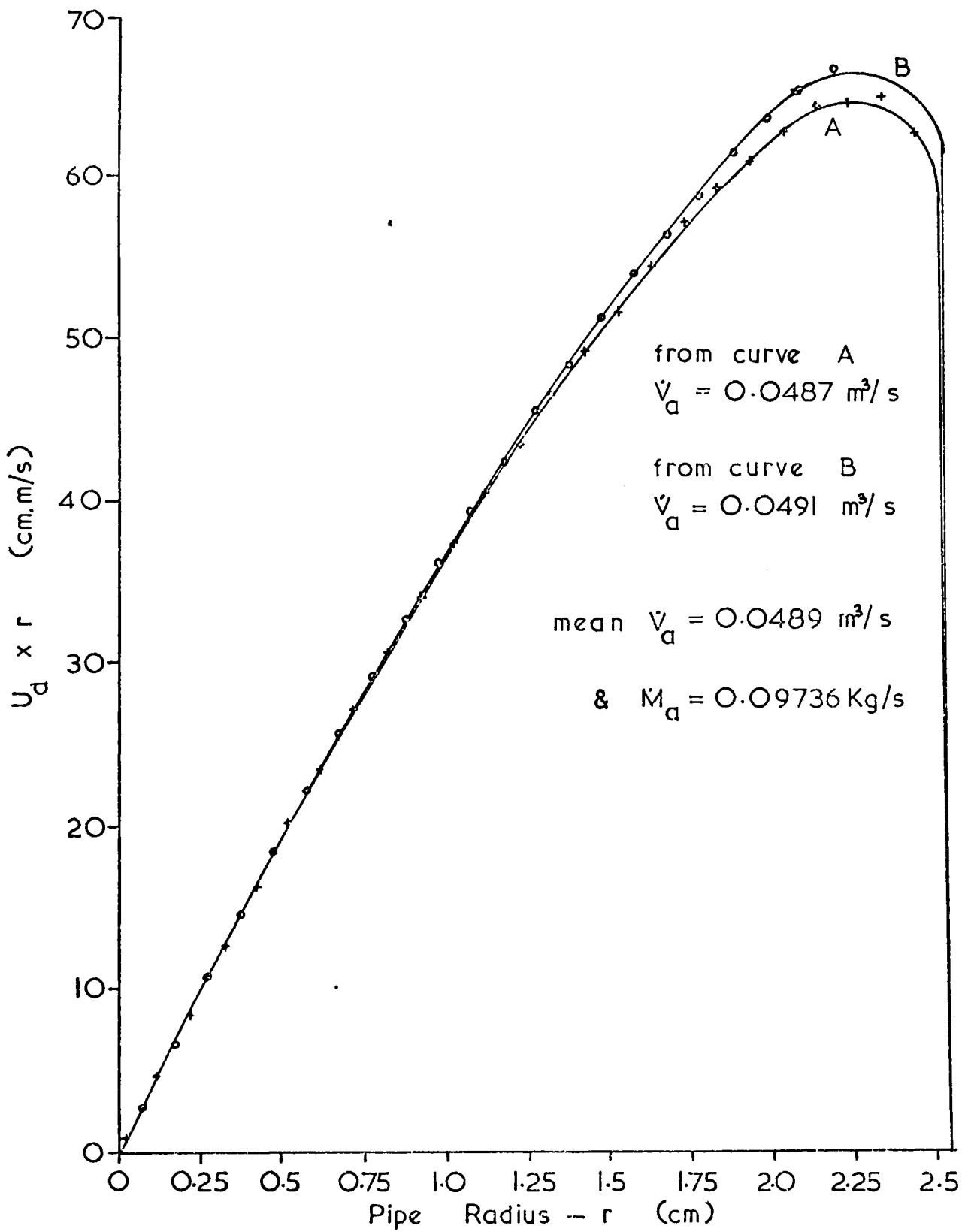


Fig.4.4. GRAPHICAL ANALYSIS OF PITOT-STATIC TRAVERSE FOR TEST No 10

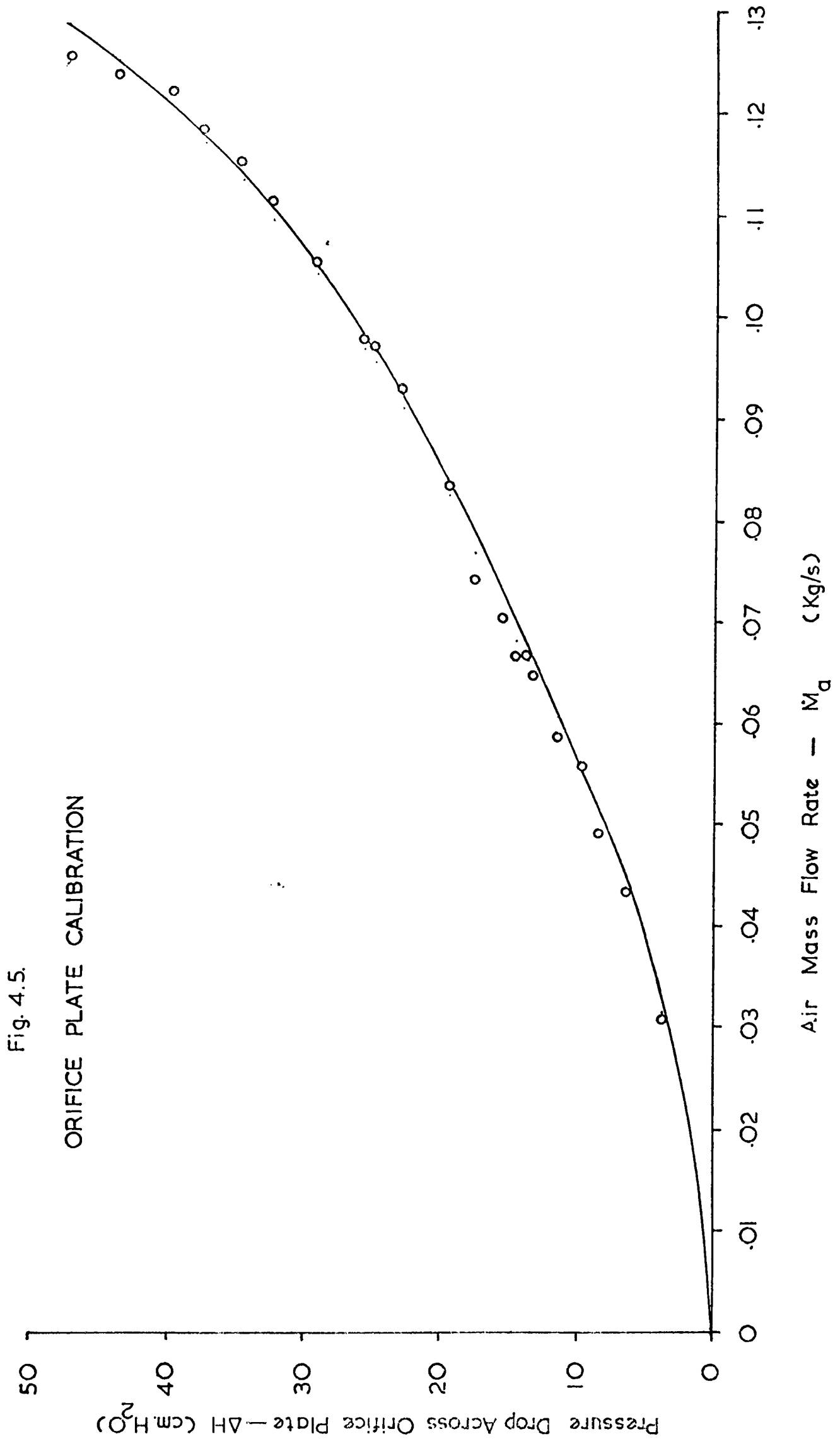


Fig. 4.6.

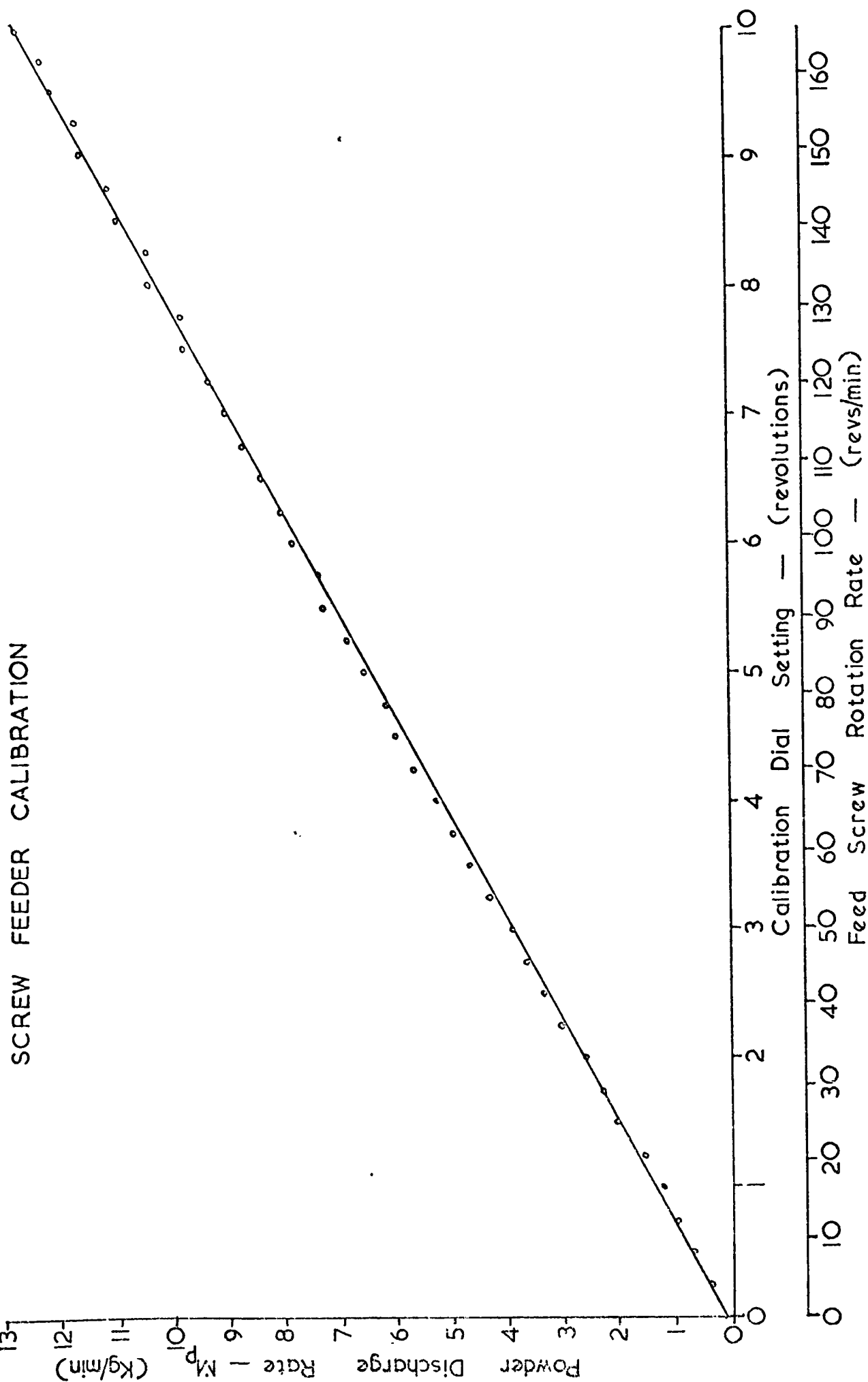
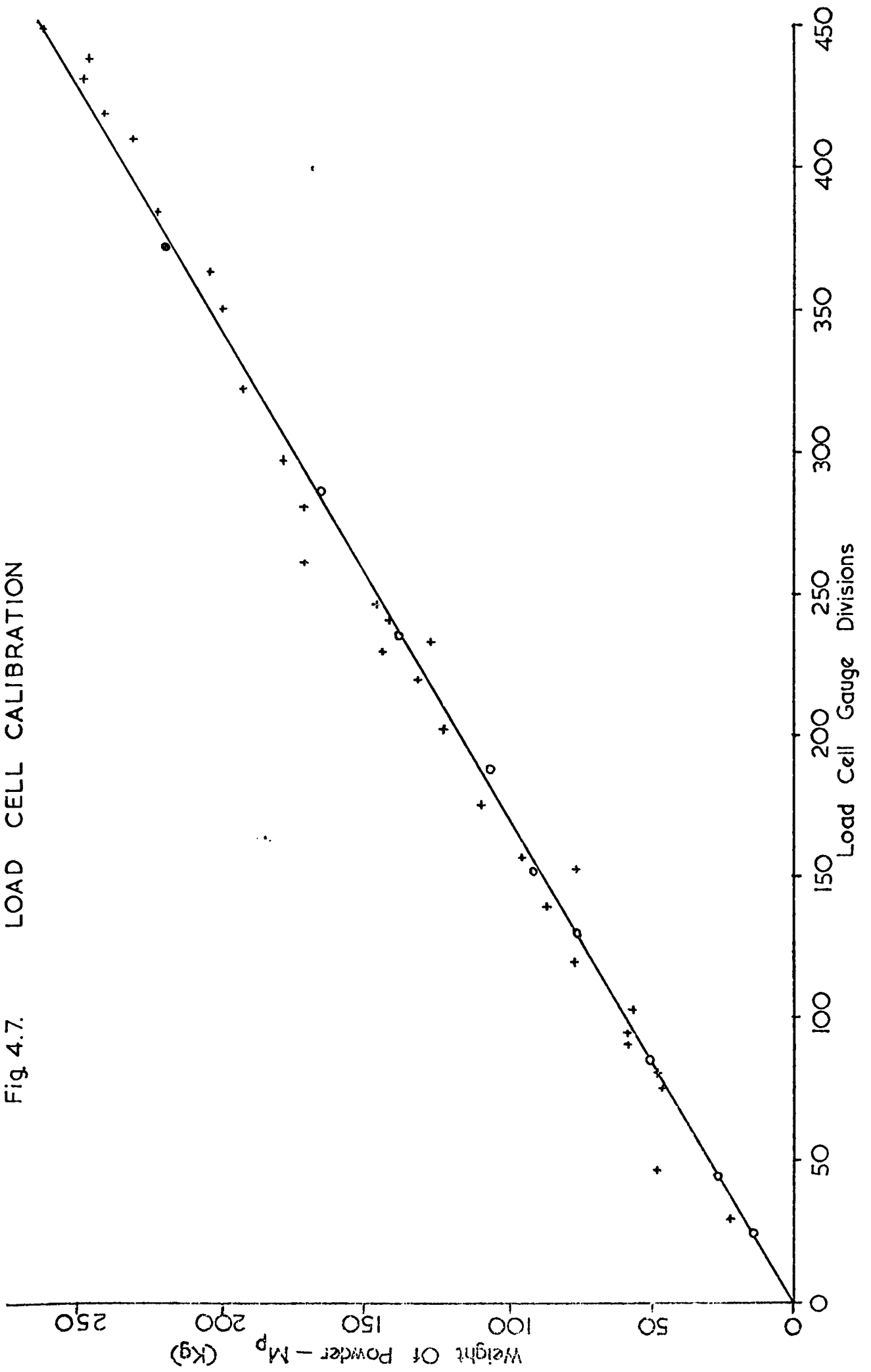
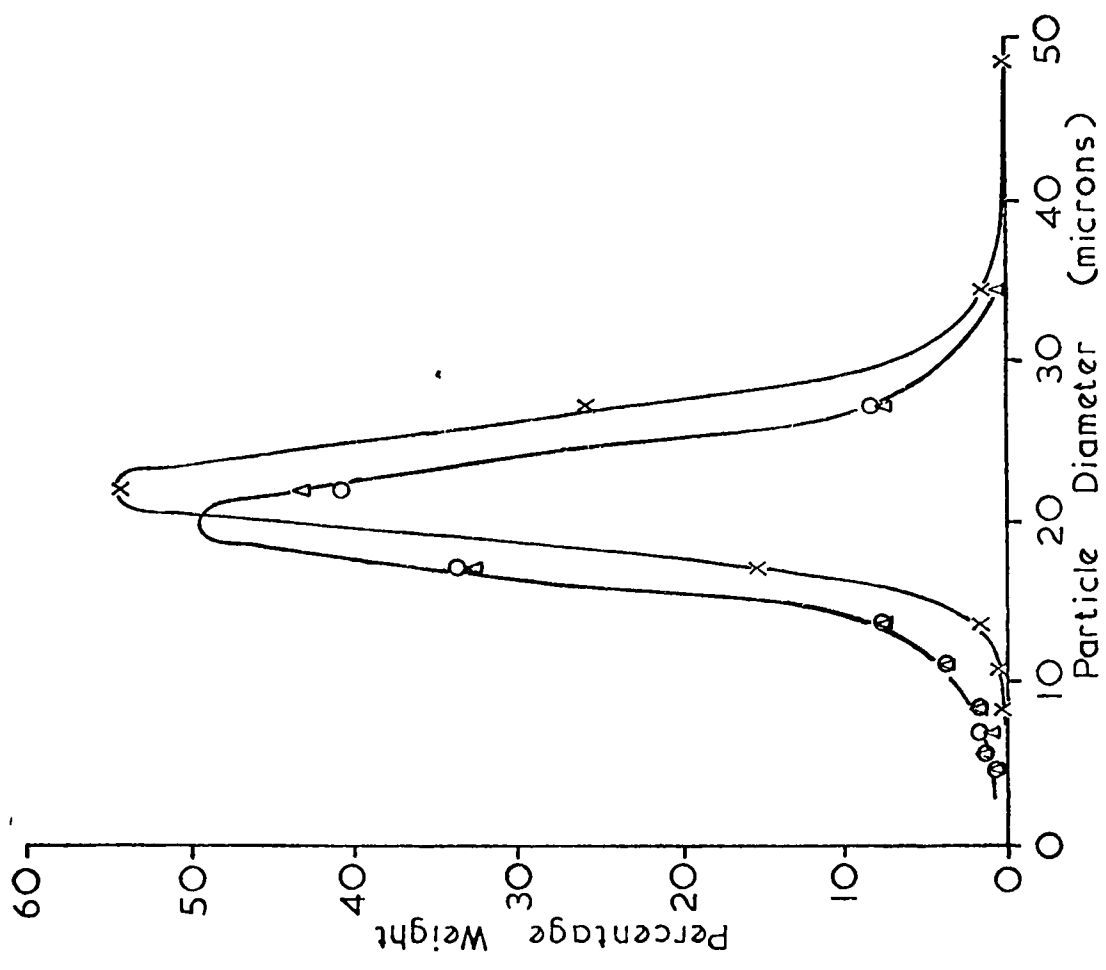


Fig 4.7. LOAD CELL CALIBRATION





- x sample 1
- o sample 2
- Δ sample 3

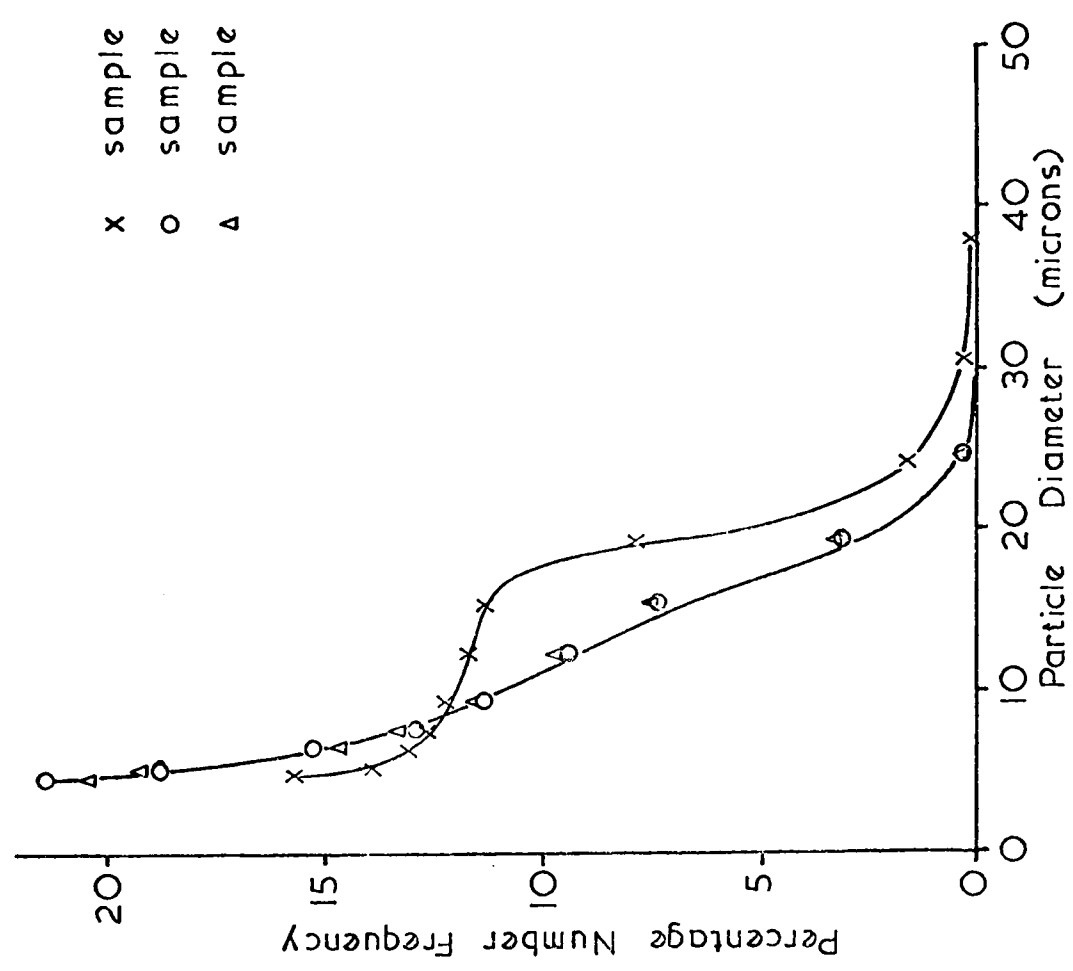


Fig. 4.8. ALUMINA SIZE DISTRIBUTION



FIG. 4.9. ELECTRON MICROGRAPH OF TiO_2 PARTICLES



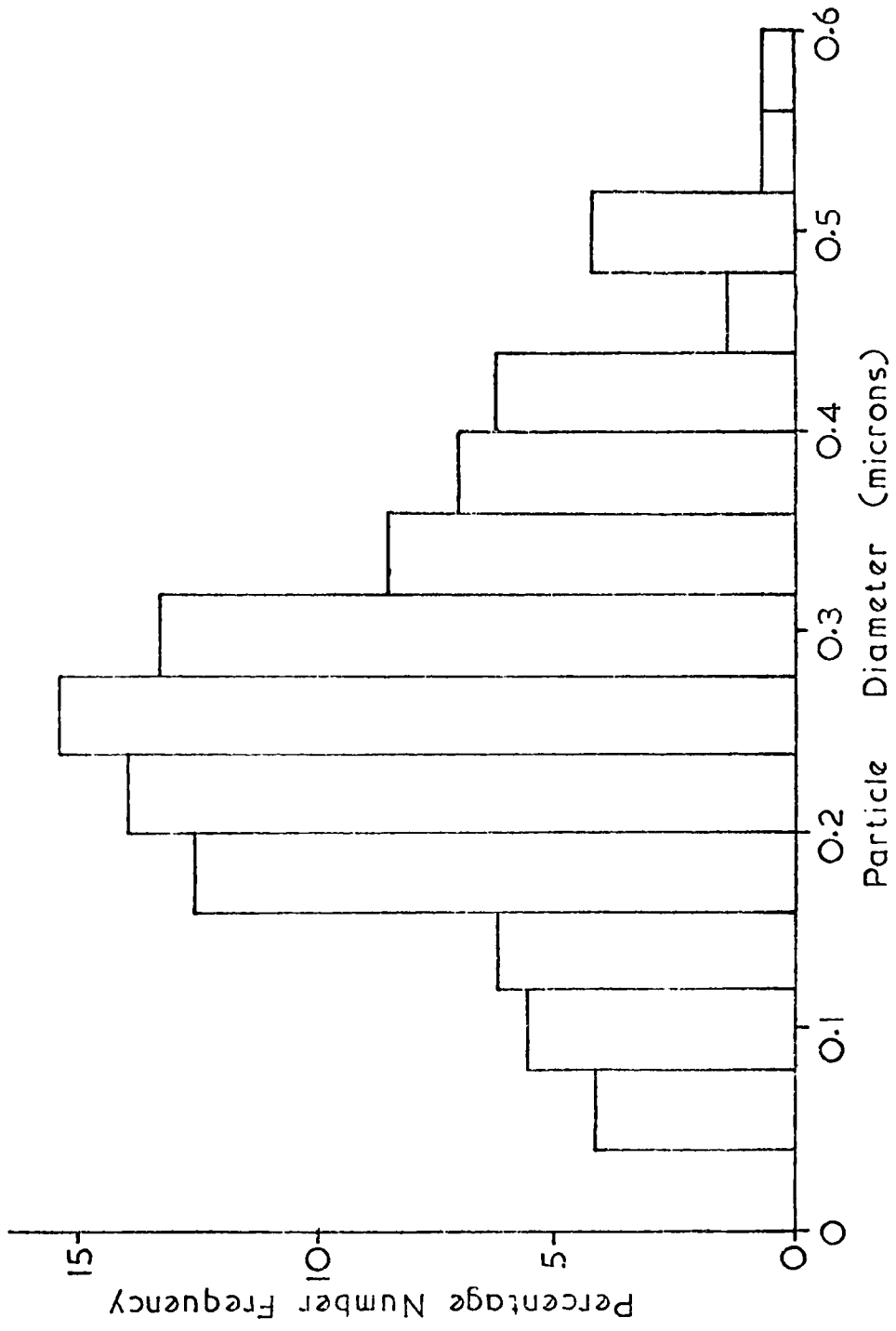


Fig. 4.10. TITANIUM DIOXIDE SIZE ANALYSIS

CHAPTER 5

LASER ANEMOMETRY

5.1 Introduction

In this chapter the equation which governs the Doppler shift of scattered light is derived and applied to the three laser anemometry modes; these are the reference beam mode, the differential Doppler or fringe mode, and the one beam mode. The probe volume is discussed and the application of the laser anemometer to turbulence measurements is outlined. The laser anemometry equipment is also described, but signal appearance is not discussed until sections 7.2 and 7.3.

5.2 Literature Survey

Since the introduction of laser anemometry to fluid flow by Yeh and Cummins [49], literature on the subject has become extensive. Early users of the laser anemometer employed the reference beam technique, which found application in a wide range of situations. Foreman, George and Lewis [50] were the first to use the laser anemometer in smoke contaminated gas flows, for velocities up to 144 cm/s, whilst Foreman, Lewis, Thornton and Watson [51] demonstrated that this means of measurement could be used in tap water, where natural contaminant particles were sufficient to cause light scattering. A more comprehensive paper by Foreman, et al [52] described measurements in both gas and liquid flows. The gas flow took place in a high speed wind tunnel and velocities up to 458 m/s were observed, whilst laminar water flow profiles in a 2.21 cm bore tube were found where the centre line velocity was only 5.35 cm/s. Lewis, Foreman, Thornton and Watson [53] described measurements in the transition region and in the turbulent region of an unseeded tap water flow and, apart from producing a velocity profile which agreed well with the Prandtl velocity distribution, they were able to estimate the instantaneous velocity deviation from the mean. However, they presented no explanation of possible frequency broadening effects.

Developing laminar flow in a square duct was studied by Goldstein and Kreid [54] using a reference beam configuration. The authors found that, with both reference and scattering beams passing through the flow, the most critical adjustment was in ensuring accurate beam intersection. Contributions to the broadened spectrum analyser signal were discussed. Their flow was seeded with sub-micron polystyrene particles and, with mean flow velocities between 0.65 and 3.62 cm/s, the velocities near the axis were found to be within 0.1% of the values predicted by theory. Using the same optical arrangement, Goldstein and Hagen [55] studied mean turbulent velocities and velocity probability functions for a seeded water flow. By subtracting the spectrum analyser line width in laminar flow from that in turbulent flow, they were able to find the fluctuating component of velocity with favourable results.

Welch and Tomme [56] measured mean velocities and local velocity distribution functions in a turbulent liquid flow. They developed an electronic system capable of measuring the frequency distribution functions directly and, from these, local velocity distributions were obtained for Reynolds' numbers from 4605 to 9301. Comparison with Nikuradse's data was good, but measurements close to the flow boundary were not achieved.

Centre line turbulent velocities in a 13 mm diameter glass tube at water flow rates between 2.5 and 75 cm³/s were measured by Pike et al [57]. The flow was seeded with milk and wave analysers were used to determine the beat frequency produced at the photomultiplier. The concept of a 'cone of coherence' was introduced as a criterion for strong optical beating between the reference and scattered beams. An explanation for the broadening of the frequency spectrum was given in terms of ambiguity broadening and a derived ambiguity broadening equation was reinforced

with experimental observations in laminar flow. Turbulence intensity measurements with the laser anemometer were found to differ by only about 0.5% from those produced by a hot wire anemometer.

In an analytical paper Davis [58] discussed reference beam Doppler shift detection by deriving an equation for the phototube current produced by similarly polarised beams with constant phase relation. Davis showed that decreasing the focussing lens focal length to reduce the beam waist diameter also reduced system accuracy and he discussed the effect of finite scattered and reference beam solid angles on frequency broadening.

James, Babcock and Seifert [59] used back-scattered light in reference beam mode operation to measure the velocities of particles issuing from a nozzle. The Doppler frequency was analysed using a Fabry-Perot scanning plate interferometer linked to the horizontal movement of an oscilloscope display. Broadening of the frequency envelope was attributed to particle collisions. A particle counting technique based on the number of frequency envelopes received was developed and several types and size ranges of particles were used.

An alternative and equivalent model to that described by the Doppler effect was proposed by Rudd [60] which explained the photodetector signal as arising from intensity fluctuations caused when particles crossed a real or virtual fringe system set up by the laser beams. Rudd explained the spread in the Doppler frequency as being caused by the finite size of the fringe system; only a finite number of signal cycles are received at the detector, giving rise to an uncertainty in the Doppler frequency. The explanation is similar to the finite scattered angle or finite receiving aperture interpretation.

Angus, Morrow, Dunning and French [61] investigated liquid flows seeded with 0.15 micron polystyrene spheres using a reference beam technique. They measured developing laminar profiles in a 22 cm bore tube and centre line velocities at several axial positions which compared well with theory. Fully developed laminar flow in a duct was also studied and the maximum velocity at various flow rates differed from theory by an average of only 0.24%. The minimum velocity measured was 9.5×10^{-3} cm/s. An estimate of the probe diameter was obtained from diffraction theory and found to be 39 microns. In addition, an investigation into the nature of the laminar sub-layer in a fully developed turbulent flow was carried out at a Reynolds' number of 8200. By allowing the probe length to straddle the flow boundary so that an estimated 10 microns remained in the flow, the authors were able to monitor velocity fluctuations in the laminar sub-layer at this close proximity to the wall.

Berman and Santos [62], using a reference beam configuration, investigated developing laminar water flows for Reynolds' numbers of 16.5, 47, 108 and 460. The flow was seeded with 0.5 micron diameter polystyrene spheres and the authors estimated velocity accuracy, based on the accuracy of the spectrum analyser, was $\pm 1\%$. The scattering volume was calculated to be less than 10^{-7} cm³.

A three-dimensional laser anemometer was developed by Huffaker, Fuller and Lawrence [63] for the measurement of velocity phenomena in a subsonic turbulent jet. They discussed heterodyning at the photomultiplier and the conditions for a high a.c. component of photocurrent. The spatial resolution of the anemometer was assessed and an electronic data processing system described.

Mazumder and Wankum [64] outlined the differences between the reference beam mode and the differential Doppler mode with respect to frequency broadening. In the former, both transmitting and receiving solid angles contribute to the frequency spread, whereas there is no spread in frequency due to the collection solid angle in differential Doppler operation. Thus, the differential Doppler mode removes the major contribution to frequency broadening.

Tangential and axial velocities in a swirling pipe flow were measured by Thew and Bedi [65] using a reference beam technique. Their results were slightly inaccurate, however, because of the optical arrangement used and the two components of velocity were not found simultaneously.

Brayton [66] developed a reference beam configuration which utilised 'self aligning' optics. The beam splitting component was an accurately produced parallel surface flat, or two such flats giving path length equalisation, which could produce two parallel beams. A focussing lens was then used to collimate the beams which automatically had true intersection. The transmitting optics could be translated for velocity profile traverse purposes, whilst the receiving optics remained fixed. Perhaps the major contribution of this work was in defining the probe volume as an ellipsoid, hence the '1/e' ellipsoid, formed within the $1/e^2$ boundaries of the two intersecting beams. Several variations to the basic configuration were also explained.

In a later publication, Brayton and Goethert [67] analysed the differential Doppler technique and again proposed an ellipsoidal probe volume. Both $1/e$ and $1/e^2$ ellipsoids were analysed, the latter probably having the more significance. The authors verified the probe volume dimensions experimentally and photographed oscilloscope displays of particles passing through the cross-over region at various planes.

They also pointed out that the differential Doppler mode was well suited to sparsely seeded flows, whilst the reference beam mode should be used for higher seeding densities.

The laser anemometer has been used to measure wind velocity remotely at a distance of 100 ft. by Bourke and Brown [68]. They used a 5 mW He-Ne laser and very small intersection angles, producing only about 15 frequency cycles for each air borne dust particle. However, the signals depicted were remarkably clear considering that the fringes oscillated in a random manner. The authors predicted that velocity measurements at 500 ft would be possible with an Argon laser.

Velocity measurements in pulsating laminar flows were made by Denison, Stevenson and Fox [69]. A 30 ft long, 0.75 inch bore, glass tube comprised the test section and a distilled water filled glass compensator box was used to maintain a constant refractive index across the tube diameter. An analysis of frequency broadening showed that velocity gradient broadening was a dominant factor. A tracking filter was used for frequency analysis, but it only allowed accurate velocity measurements to be taken at radii up to 60% of the tube radius. The flow was seeded with 0.5 micron diameter polystyrene particles.

Adrian and Goldstein [70] derived an expression for the photocurrent on a circular detector by considering the contributions of light scattered from both reference and scattering beams. They also accounted for the Gaussian intensity distribution of the beams and for the attenuation due to many particles passing through the entire reference beam. The authors discussed frequency broadening in terms of ambiguity, laser band width and instrument broadening, and commented upon refraction effects at the test section wall.

Prior to the introduction of the laser anemometer, most measurements of two point velocity correlation functions required the use of hot wire anemometers. In some cases it was necessary to place one probe in the wake of an upstream probe, so that corrections had to be made for interference. Morton and Clark [71], however, used two laser anemometers for such measurements in a 0.9 m long, 0.025 m bore glass tube. They argued that broadening due to finite particle transit time was independent of frequency and demonstrated this feature experimentally. Their measurements of both lateral and longitudinal correlation coefficients compared favourably with the work of other authors.

Durst and Whitelaw [72] compared the potential of the laser anemometer to established velocity measurement techniques used in recirculating flows. They proposed a one beam mode of operation in which a single focussed beam was used and light was collected from two scattering directions. The resulting signal was shown to be free from broadening due to scattering angle variations because of the convergence of the incident beam. Nine different optical geometrics were investigated both experimentally and theoretically by Durst and Whitelaw [73] in an attempt to optimise these arrangements to the particular application. The authors investigated fringe, Doppler shift and combined anemometer systems. They derived expressions for the light intensity in the probe volume and found that some configurations were more affected by vibrations than others. In addition, it was discovered that for fringe anemometers the intensities of the two beams should be the same for maximum signal to noise ratio.

A major contribution to the design of laser anemometry systems was made

by Durst and Whitelaw [74] when they conceived an integrated optical unit which contained a beam splitter and director, focussing lens and beam separation adjustment in one robust casing. The optical unit they designed could be used in all three modes of operation and it made possible laser anemometry measurements outside the laboratory. In addition, it enabled research workers to investigate each mode of operation easily, since rapid and simple setting up of the unit for a given mode was possible. The authors also carried out velocity and turbulence intensity measurements in a duct water flow to illustrate the capabilities of the optical unit.

By considering the signal received at a detector from several particles in a fringe system, Drain [75] derived equations which showed that the signal was due to two mechanisms - (i) the intensity modulation caused by particles passing through the light and dark fringes, and (ii) the coherent mixing of light scattered from different particles. Drain called the former mechanism non-coherent, since it did not require coherent beating between different particles, and the latter coherent. The coherent mechanism imposed a limitation on the detector aperture. He pointed out that the presence of fringes was not always necessary for the existence of a non coherent signal, as was the case with a one beam anemometer. Coherent beating usually required the use of a reference beam. The author's analysis showed that, with a small number of scattering particles in the measurement volume, a non-coherent mode was appropriate; however, when a large number of scattering particles were involved, a coherent mode and the use of a reference beam was more satisfactory.

Bourke, Brown and Drain [76] measured Reynolds' shear stress in a 2.35 cm internal diameter glass tube, using two frequency tracking units to simultaneously follow the Doppler shifted light scattered in two directions from one point. The optical arrangement utilised a single scattering beam and two reference beams symmetrically situated about the scattering beam. The three beams converged to a point in the flow. The tracked frequencies were fed to a correlator, which gave the time averaged product of the sum and difference of the two tracker outputs, enabling the Reynolds shear stress to be found. The shear stresses obtained were compared to values derived from pressure drop data and showed a standard deviation about the latter of 5%.

An investigation into the application of laser anemometry for use in a supersonic wind tunnel was carried out by Pfeifer and vom Stein [77]. They used a differential Doppler technique and a one watt Argon laser with about 12 fringes in the probe volume, the distance between the fringes being 70 microns. A spectrum analyser was used for signal analysis. Natural atmospheric impurities, which were found to be sub-micron, sufficed as scattering particles, whereas ice particles in the wind tunnel were undesirable. The velocity of the flow was 502 m/s and the authors were able to measure the velocity across a shock wave to an accuracy which agreed to within 1% of theory.

The light source requirements for laser anemometry have been discussed by Durst and Whitelaw [78]. An optical unit with facility for path length equalisation was proposed and the dimensions of the probe volume to give a predetermined accuracy were outlined. The light source power requirements were found to be strongly dependent on the velocity to be measured, the particle diameter and the probe diameter.

Melling [79] and Melling and Whitelaw [80] pointed out the importance of correctly seeding the flow, both with regard to particle characteristics and seeding concentration. The ability of the suspended particles to follow the turbulent fluctuations of the flow was assessed from the Bassett equation and the authors concluded that a mean particle diameter of approximately one micron was suitable for most purposes, with a turbulence energy below 1 kHz. Various methods of particle generation and determination of particle size distribution were explained.

The flow of water through a right angle bend in a rectangular channel was investigated by Humphrey, Melling and Whitelaw [81]. The bend had a mean radius of 93 mm, a 40 mm x 40 mm cross section and the Reynolds' number of the flow was 42,000. Velocity and turbulence information was obtained from which velocity and turbulence intensity contours were plotted. Using the intensity of scattered light as a measure of concentration, simultaneous measurements of velocity and concentration were found in a fully developed pipe air flow.

Only four publications relating laser anemometry to gas-solid pipe flows are known to the author. Although some velocity measurements were reported, two of these investigations were mainly concerned with the development of a laser anemometer for such flows.

Barker, Reithmuller and Ginoux [82] developed a fringe laser anemometer for the velocity measurement of 100 micron and 500 micron spherical glass particles. At the development stage it was found more convenient to simulate the two phase flow using a rotating plexiglass disc on which the solid particles were randomly attached with a transparent spray. Using a fringe mode of operation because of its ease of setting up, the clarity of the signals from the simulation wheel was not satisfactory.

The lack of clarity was attributed to reflections and refractions from the wheel and the adhesive spray. In an attempt to improve signal simulation, small wires were used instead of particles, these requiring no retaining disc. The resulting signals were found to be most satisfactory; for example, the quality of signal produced by a 300 micron wire in a 35 micron fringe spacing was greater than that predicted by small particle scattering theory. This was thought to be due to only a small portion of wire being illuminated as it traversed the fringe pattern, thereby acting as a small particle. Observation of various signals from the simulation wheel showed that signal amplitude decreased with increase in velocity and that more accurate velocity information was obtained with a larger number of fringes in the probe volume. Velocity measurements taken of particles issuing from a nozzle gave good accuracy when compared with Stokes' predictions, even though some distortion of the fringe pattern was observed when an adjacent wind tunnel was in operation, thereby reducing the clarity of the frequency information.

The laser anemometer designed as above was used by Reithmuller and Ginoux [83] to measure particle velocity in a horizontal gas-solids pipe flow. A fringe spacing of "18.986 microns" giving 13 fringes in the $1/e^2$ probe volume, was used for 500 micron particles flowing through a 4.2 cm diameter glass pipe. The authors claim to have used the system at gas velocities from 3 m/s to 25 m/s and solids loading ratios up to 15, the latter being determined with a Venturi tube. However, the paper only included results for solids loading ratios up to 3. A 1 mW He-Ne laser was used and the receiving optics were displaced from the optical axis. A period counting device was used

to process the signal, thus an output of both particle velocity and particle number density was obtained from which the particle flow rate distribution across the pipe was derived.

The work of Carlson [84] was primarily devoted to the development of a laser anemometer for the measurement of particulate phase velocities. An interferometric interpretation, drawing an analogy with a modified Michelson interferometer, was used to derive the scattered light frequency for various aspects of the anemometer design. Functional relationships between the scattered light intensity and particle size were developed and Carlson found that for a symmetrical two beam anemometer, the optimum position for the receiving optics for maximum scattered light intensity was along the bisector of the two beams. A variable width slit was incorporated into the design, this being positioned in front of the photosensitive surface of the photomultiplier. The slit acted as an optical filter which could discriminate against particles of a given size. Analysis of the Doppler signal was by counting circuitry. The two phase flow test section was a 3 inch x 3 inch duct having an optical window and mean gas velocities of 37.6 and 39.1 m/s were measured. Spherical glass particles of diameters 44 and 214 microns were used at solids loading ratios of less than unity. Examination of the velocity profiles revealed considerable slip between the phases. At the flow centre-line a slip velocity of about 10 m/s was noted for the 214 microns particles for a Reynolds' number of 202,000, and of about 2 m/s for the 44 micron particles at a Reynolds' number of 194,000. Particle turbulence intensities measured for the 214 micron particles showed that the particle intensity at the core of the flow was greater

than the clean air turbulence intensity there. It was not made clear how the air turbulence intensity was measured, however, but the greater particle turbulence was attributed to the size distribution of the particles.

Experiments reported by Arundel [85] used a laser anemometer for particulate phase velocity measurements in a vertical pipe. The range of particle size was from 15 to 150 microns and particle flow velocities varied from zero to 3 m/s, which are unfortunately well below velocities of industrial interest. The Reynolds' number was kept below 4,000 and the solids loading ratio was described merely as dilute. It was found that the slip velocity of the smaller particles at the wall was greater than large ones and this observation was made possible by a specially developed electronic frequency analysing system. The reason for the apparent difference in slip velocity was attributed to wall electrostatic effects. In the centre of the flow, the small particles were observed to slip less than the larger ones, which is to be expected.

5.3 The Doppler Shift of Scattered Light - Application to the Laser Anemometer

The basic equation relating the scattered light frequency to the particle velocity is derived. A heuristic, nonrelativistic approach is used and the result is identical to that obtained relativistically [86]. This equation is applied to the three laser anemometry modes and a second derivation in terms of interference fringes is included as an alternative approach. This explanation is usually applied to the differential Doppler mode, which has consequently become known as the fringe mode.

5.3.1 Basic Equation

Consider a beam of laser light with unit direction vector \mathbf{k} illuminating a small particle, P, as shown in fig. 5.1. The coherent light has a wavelength $\lambda_i = \frac{c}{\nu_i}$ where ν_i and c are respectively the light frequency and velocity in the surrounding medium. The particle, moving with velocity $\bar{\mathbf{v}}$, has a component $\bar{\mathbf{v}}\mathbf{k}$, in the direction of the incident radiation, so that the velocity of light observed by P is $(c - \bar{\mathbf{v}}\mathbf{k})$. The rate at which wavefronts strike and are scattered by the particle is given by :

$$\nu_p = \frac{(c - \bar{\mathbf{v}}\mathbf{k})}{\lambda_i} \quad (5.1)$$

Now consider light scattered by the particle towards an observation point, O, which lies in the direction of unit vector, \mathbf{l} . After scattering a wavefront, the particle moves towards that wavefront with velocity, $-\bar{\mathbf{v}}\mathbf{l}$, so that the scattered light has wavelength λ_{sc} , where:

$$\lambda_{sc} = \frac{(c + \bar{\mathbf{v}}\mathbf{l})}{\nu_p} = \frac{(c + \bar{\mathbf{v}}\mathbf{l})}{(c - \bar{\mathbf{v}}\mathbf{k})} \lambda_i \quad (5.2)$$

This gives the frequency seen by an observer at O :-

$$\nu_{sc} = \frac{c}{\lambda_{sc}} = \frac{c}{\lambda_i} \frac{(c - \bar{\mathbf{v}}\mathbf{k})}{(c + \bar{\mathbf{v}}\mathbf{l})}$$

or

$$\nu_{sc} = \nu_i \left[\frac{1 - \frac{\bar{\mathbf{v}}\mathbf{k}}{c}}{1 + \frac{\bar{\mathbf{v}}\mathbf{l}}{c}} \right] \quad (5.3)$$

Equation (5.3) expresses the Doppler shifted frequency of scattered light in the direction of \mathbf{l} , in terms of the original laser frequency and the particle velocity.

5.3.2 Application of Equation (5.3) to the Reference Beam Mode

For the configuration shown in fig. 5.2, equation (5.3) for the

scattering beam becomes :

$$\nu_{sc} = \nu_i \left[\frac{1 + \frac{\bar{v}}{c} \cos \delta_1}{1 + \frac{\bar{v}}{c} \cos \delta_2} \right] \quad (5.4)$$

The sign in the numerator of equation (5.4) has changed from that of equation (5.3), since the direction of \bar{v} now has a component in the negative direction of the scattering beam. Heterodyning the scattered light of frequency ν_{sc} , with reference beam light of original laser frequency, ν_i , results in the difference frequency, or Doppler shift, ν_D , where :

$$\begin{aligned} \nu_D &= \nu_{sc} - \nu_i \\ &= \nu_i \left[\frac{1 + \frac{\bar{v}}{c} \cos \delta_1}{1 + \frac{\bar{v}}{c} \cos \delta_2} \right] - \nu_i \end{aligned}$$

i. e.
$$\nu_D = \frac{1}{\lambda_i} \left[\frac{\bar{v}(\cos \delta_1 - \cos \delta_2)}{1 + \frac{\bar{v}}{c} \cos \delta_2} \right] \quad (5.5)$$

It is normally required to find the vertical component of velocity of P, that is v . This requires that δ_1 and δ_2 are rotated to the Y - axis, giving :

$$\begin{aligned} \cos \delta_1 &= \cos (90 - \theta) = \sin \theta \\ \cos \delta_2 &= \cos (90 + \theta) = - \sin \theta \end{aligned}$$

so that,

$$\nu_D = \frac{1}{\lambda_i} \left[\frac{2 v \sin \theta}{1 - \frac{v}{c} \sin \theta} \right] \quad (5.6)$$

For conditions where $v \ll c$, equation (5.6) becomes :

$$\nu_D = \frac{2 v \sin \theta}{\lambda_i} \quad (5.7)$$

Equation (5.7) expresses the detected frequency in terms of θ and, in so doing, it selects only that component of velocity which is normal to the bisector of the reference and scattering beams. The reference

beam is usually reduced in intensity to "match" that of the scattered beam [87] . It will be noted that, with the reference beam mode of operation, the angle of observation is fixed by the angle, θ , of the reference beam.

5.3.3. Application of Equation (5.3) to the Differential Doppler Mode

In the differential Doppler mode of operation, the receiving optics collect light scattered from two different scattering beams as shown in fig. 5.3. Each scattered beam undergoes its own frequency shift and heterodyning the two scattered beams results in a difference frequency, ν_D . Consider the scattered light from beam 1, fig. 5.3 :

from equation (5.3)

$$\nu_{sc_1} = \nu_i \left[\frac{1 + \frac{\bar{v}}{c} \cos \delta_1}{1 + \frac{\bar{v}}{c} \cos \delta_3} \right] \quad (5.8)$$

Scattered light from beam 2 similarly gives :

$$\nu_{sc_2} = \nu_i \left[\frac{1 + \frac{\bar{v}}{c} \cos \delta_2}{1 + \frac{\bar{v}}{c} \cos \delta_3} \right] \quad (5.9)$$

Subtracting equation (5.9) from equation (5.8) to give the difference frequency:

$$\begin{aligned} \nu_D &= \nu_{sc_1} - \nu_{sc_2} \\ &= \frac{\bar{v}(\cos \delta_1 - \cos \delta_2)}{\lambda_i(1 + \frac{\bar{v}}{c} \cos \delta_3)} \end{aligned} \quad (5.10)$$

To obtain the vertical component of velocity, v , and for $v \ll c$, equation (5.10) becomes:

$$\nu_D = \frac{2v \sin \theta}{\lambda_i} \quad (5.11)$$

This expression is identical to equation (5.7), where θ is the half angle between the two incident beams. However, unlike equation (5.7) in which θ defines the collecting angle, equation (5.11) for the

differential Doppler mode does not include the observation angle .
Thus, the difference frequency, ν_D , is independent of the observation angle and may, therefore, be selected for convenience.

5.3.4 Application of Equation (5.3) to the One Beam Mode

The one beam mode utilises a single scattering beam and scattered light is collected from two different directions. Heterodyning, by directing the two scattered beams onto the photodetector, again produces the difference frequency ν_D . Consider the configuration shown in fig. 5.4:

For scattered beam 1,
$$\nu_{sc1} = \nu_i \left[\frac{1 + \frac{\bar{v}}{c} \cos \delta_2}{1 + \frac{\bar{v}}{c} \cos \delta_3} \right] \tag{5.12}$$

and for scattered beam 2,
$$\nu_{sc2} = \nu_i \left[\frac{1 + \frac{\bar{v}}{c} \cos \delta_2}{1 + \frac{\bar{v}}{c} \cos \delta_1} \right] \tag{5.13}$$

Subtracting (5.13) from (5.12) gives:

$$\begin{aligned} \nu_D &= \nu_{sc1} - \nu_{sc2} \\ &= \frac{\bar{v}}{\lambda_i} (1 + \frac{\bar{v}}{c} \cos \delta_2) \left[\frac{\cos \delta_1 - \cos \delta_2}{(1 + \frac{\bar{v}}{c} \cos \delta_3)(1 + \frac{\bar{v}}{c} \cos \delta_1)} \right] \end{aligned} \tag{5.14}$$

In order to obtain ν , the vertical component of \bar{v} , $\delta_2 = 90^\circ$, so $\cos \delta_2 = 0$, $\cos \delta_1 = \sin \theta$ and $\cos \delta_3 = -\sin \theta$

hence,

$$\nu_D = \frac{\bar{v}}{\lambda_i} \left[\frac{2 \sin \theta}{(1 - (\frac{\bar{v}}{c})^2 \sin^2 \theta)} \right] \tag{5.15}$$

For normal conditions where $v \ll c$, then,

$$\nu_D = \frac{2 v \sin \theta}{\lambda_i} \tag{5.16}$$

Again, the expression for the change in frequency is identical to (5.7)

and (5.11). The one beam mode of operation has not been used in this work

and it is therefore not discussed further. It is hoped that its usefulness

for gas-solid flows will be investigated at a later date. Information on

this mode can be found in ref. [72].

5.3.5 Derivation of the Doppler Shift Equation from Fringe
Considerations

The fringe model for laser anemometry is often useful and offers an alternative to the Doppler shift explanation. The model is in 'complete' agreement with the Doppler shift interpretation and the fringes can be 'real', as in the differential Doppler mode and some reference beam mode arrangements, or 'virtual', as in the one beam mode and other reference beam mode arrangements, [60]. However, when utilising two incident beams of equal intensity, as in the differential Doppler mode, the fringes are well defined and the method of operation is sometimes referred to as the fringe mode. The following derivation assumes such conditions.

Consider two beams of laser light intersecting as shown in fig. 5.5a. For simplicity it is assumed that the wavefronts are plane, which is approximately true in the waist region of a focussed beam. The diagram is an instantaneous representation, so that positive wavefronts (full lines) and negative wavefronts (dotted lines) are stationary. Where positive wavefronts meet and where negative wavefronts meet there is reinforcement, resulting in regions of maximum intensity, which are represented by the full circles. The open circles define regions of zero intensity resulting from encounters between positive and negative wavefronts. Thus, the instantaneous picture shows regions of maximum and zero intensity extending into the diagram, the intensity varying continuously between them.

From figure 5.5b, the distance between two like regions in the Y-direction is given by:

$$\delta = \frac{\lambda_i}{2\sin\Theta} \quad (5.17)$$

Now consider the wavefronts in motion, travelling along their propagation axes with velocity of light, c , it is apparent that the intersection points move in the x -direction. Moreover, the velocity of movement makes individual maximum intensity regions and zero intensity regions indistinguishable, thus producing the fringe appearance of fig. 5.6.

For a small particle, P , which has a velocity, \bar{V} , it is evident that P will scatter more light when situated in a highly illuminated region than it will in a low intensity region. Thus, in passing through the fringe system, the scattered light will undergo an intensity modulation, the frequency of which depends upon the fringe spacing, δ , and the particle velocity component perpendicular to the plane of the fringes, v . This frequency is ν_D , where

$$\nu_D = \frac{v}{\delta} = \frac{2v \sin\theta}{\lambda_i} \quad (5.18)$$

This equation is the same as equation (5.11) and it is apparent that the observed frequency is independent of the angle of observation. The mechanism is analogous to a light source being moved past a fence; obviously, the number of flashes per unit time is the same when viewed from any direction.

5.4 Light Source Requirements

The light source for laser anemometry must fulfill both coherence and intensity requirements. Temporal coherence, or frequency stability, is of importance in the light source when small frequency shifts due to the Doppler effect are to be detected. Laser light is highly monochromatic in comparison with conventional light sources, but unless precautions are taken the laser can operate in several modes simultaneously, giving more than a single frequency. Heterodyning between the two beams is still possible since they originate from the same source and variations

in the laser frequency affect both beams equally, so that the beat frequency is unaffected. However, the appearance of many modes reduces the laser's effective coherence length, so that arrangements must be made to equalise path lengths in laser anemometry systems. The effect of increasing path length differences and of increasing axial modes is to reduce the strength of the signal from the light scattering region of the anemometer [88] .

Lasers for anemometry applications are generally designed to operate only in the simplest transverse mode, TEM_{00} , which produces an axially symmetrical beam with a Gaussian intensity distribution across its diameter. Conventionally, this is achieved by inserting a suitable diaphragm in the laser cavity, which introduces losses in the off-axis modes. Single mode operation is thus generally at a very much lower power than that obtained with multimode operation.

The power requirements for laser anemometry are strongly dependent upon the velocity of the seeding particles, since the number of photons scattered is proportional to the residence time of the particle in the beam cross-over region. The number of photons is also related to the particle diameter. Thus, a 'large', slow moving particle will require less laser power for its velocity determination than a small, fast one. Durst and Whitelaw [78] illustrate a means of evaluating the laser power requirements for a typical laser anemometry system and they recommend that the laser power $> 5 \times 10^{-6}$ W/m/s for their system. However, the requirements for gas-solid flows are more severe and any analysis must take into account the solids loading ratio of the system. Light scattered from the cross-over region must penetrate through the surrounding flow before reaching the detector. One of the objectives of the present investigation is to determine experimentally the limits of usefulness of the laser anemometer with respect to loading ratio.

5.5 Transmitting Optics

The prime functions of the transmitting optics are to divide the single laser beam into two mutually coherent beams and to define a region in space over which velocity measurements may be taken. Two beams are required in order to provide both reference and scattering beams in the reference beam mode, and for the formation of interference fringes in the fringe mode. In order to provide a high illuminating intensity in the measurement region, it is necessary to focus the beams to a 'point' in the flow. Thus, for fringe and reference beam anemometers, the transmitting optics comprise a beam splitter, some means of causing the beams to become parallel, and a suitable focussing facility. In addition, it is often desirable to be able to adjust the separation distance between the beams prior to focussing.

Beam splitting is usually accomplished with a bi-prism or splitter plate, from which the beams do not necessarily emerge parallel. Parallelism is required in order to ensure proper intersection of the beams at the focal plane of the focussing lens. To achieve parallel beams, correction to one or both of the beam paths is normally effected with surface mirrors. The inclusion of surface mirrors has, in some cases, provided a facility for path length equalisation and can also be used as a means of beam separation adjustment by translation. For some reference beam arrangements, two beams at entry to the test section are not necessary, [56, 53, 62] , so that pre-focussed parallelism is not necessary. However, the arrangements in which the beams are crossed in the fluid are now the most common since they enable easy adjustment of the photocathode and help define more clearly the probe volume. Some beam splitting devices automatically provide parallel beams at exit [66, 67] .

In order to focus the two beams to a point in the flow, some arrangements have used separate focussing lenses for each beam. This type of

layout is, however, sensitive to vibrations [73] and most modern arrangements utilise a single focussing lens. The choice of focal length for the focussing lens is an important consideration, since it affects the probe volume dimensions, (see section 5.6), and the illuminating intensity of the probe volume. Also, for a given beam separation, prior to focussing, the lens focal length determines the angle of beam intersection and thus affects the Doppler frequency.

For reference beam operation, "matching" the intensity of the reference beam to that of the scattered light is essential for optimum signal-to-noise ratio. Hence, the intensity of the reference beam must be reduced and a neutral density filter overcomes this problem effectively.

Before the introduction of integrated optical units to laser anemometry [74] it was inconvenient to use more than a single mode of operation because of the difficulty of re-aligning the individual optical components. Thus, comparison between the application of various modes was not widely undertaken. Moreover, systems in which the optics are not fixed with respect to each other are sensitive to vibrations and cannot, therefore, readily be used outside the laboratory. In this study, vibrations emanating from the pneumatic conveying system were always present, even though steps were taken to minimise them, and comparison between the reference beam and fringe modes was considered desirable. Hence, integration of the transmitting optics was also essential (see section 5.11).

5.6 Probe Volume

The volume of the beam cross-over region from which frequency envelopes of appropriate quality may be generated is called the probe volume and its dimensions can be derived solely from the dimensions of the focussed beams. However, the volume from which measurements are taken may be

modified by the receiving optics, the analysing electronics, or by the particles themselves (see section 7.2). A distinction is therefore made here between the probe volume and the volume of measurement, (see section 5.8). In many cases the two volumes are identical, but sometimes the probe volume can be excessive and must be modified by the receiving optics. On the other hand, the measurement volume can be larger than the probe volume if the particles of interest are large.

The light intensity across the diameter of the laser beam follows a Gaussian distribution, see fig. 5.5a, given by:

$$I = I_0 e^{-\frac{1}{2} \left[\frac{4x}{2b} \right]^2} \quad (5.19)$$

where I_0 is the maximum intensity at the beam centre, and x is the radial distance.

The beam diameter, $2b$, is defined where the light intensity, I , has diminished to $1/e^2$ of its maximum value. For a laser beam focussed by a lens of focal length, f_l , the diameter of the beam at the waist is given by [67] :

$$2b_0 = \frac{4f_l \lambda_i}{\pi 2b} \quad (5.20)$$

where $2b$ is the unfocussed beam diameter.

A definition of the probe volume based upon equation (5.20) is "that volume within which a small scattering particle will produce photo-multiplier signals larger than $1/e^2$ of those produced by a scattering particle located in the centre of the volume". The volume thus defined is applicable to both reference beam and fringe modes and has the form of an ellipsoid [67]- see fig. 5.6, thus :-

$$X^2 + Y^2 \cos^2 \Theta + Z^2 \sin^2 \Theta = b_0^2 \quad (5.21)$$

where:

$$\Delta X = 2b_0 \quad (5.22)$$

$$\Delta Y = \frac{2b_0}{\cos \Theta} \quad (5.23)$$

$$\Delta Z = \frac{2b_0}{\sin \Theta} \quad (5.24)$$

and the volume is given by:

$$\text{volume} = \frac{\pi (2b_0)^3}{3 \sin 2\Theta} \quad (5.25)$$

The dimensions ΔY and ΔZ are of particular importance. For an arrangement in which the measurement volume equals the probe volume, ΔZ is the major dimension normal to the flow and, if ΔZ is large, results can be misleading. Combining equations (5.17), (5.20) and (5.24), gives:

$$\Delta Z = \frac{8f_1 \delta}{\pi 2b} \quad (5.26)$$

It is evident that ΔZ can be reduced by having a more powerful lens, a large value of $\sin \Theta$ (that is, small δ) and a large initial beam diameter.

The error of frequency determination is of the order of $(t\tau)^{-1/2}$ [75] where t is the time available for measurement and τ is the time taken for the particle to cross the probe volume. t is usually fixed for the analysing system, so that for a given velocity it is necessary that ΔY should not be so small as to appreciably reduce accuracy. Unfortunately, any attempt to reduce ΔZ by changing any of f_1 , λ_i or $2b$, also reduces ΔY ; thus ΔY and ΔZ are interdependent and a compromise becomes inevitable. In reference [89] about 100 fringes are recommended for good accuracy. The number of fringes in the $1/e^2$ probe volume is given by:

$$N = \frac{8f_1 \sin \Theta}{\pi 2b \cos \Theta} \quad (5.27)$$

5.7 Signal Detection

Consider the superposition (optical beating or heterodyning) of two beams of different frequency on a square law detector. The two beams correspond to the reference and scattered beams in the reference beam mode, or the two scattered beams in the differential Doppler or fringe mode. The square law detector may be a photoconductive solid state detector (photodiode)

or a photomultiplier. Let the electric fields be represented by:

$$e_1 = E_1 \cos (\omega_1 t + \beta_1) \quad (5.28)$$

$$e_2 = E_2 \cos (\omega_2 t + \beta_2) \quad (5.29)$$

where E is the amplitude, ω the circular frequency ($=2\pi\nu$), and β an arbitrary phase for each beam. The waves are assumed plane polarised and monochromatic for simplicity, so that their interaction with a square law detector will produce an output current :

$$i \propto (e_1 + e_2)^2 \quad (5.30)$$

by substitution, this yields:

$$i \propto \frac{E_1^2}{2} + \frac{E_2^2}{2} + \frac{E_2}{2} \cos 2(\omega_2 t + \beta_2) + \frac{E_1}{2} \cos 2(\omega_1 t + \beta_1) \\ + E_2 E_1 \cos [(\omega_2 + \omega_1)t + \beta_2 + \beta_1] + E_2 E_1 \cos [(\omega_2 - \omega_1)t + \beta_2 - \beta_1] \quad (5.31)$$

Typical square law detectors are unable to follow frequencies above several hundred mega-hertz, so that terms involving ω_1 , ω_2 , and $(\omega_1 + \omega_2)$ average to zero. Equation (5.31) thus reduces to:

$$i \propto \frac{E_2^2}{2} + \frac{E_1^2}{2} + E_1 E_2 \cos [(\omega_2 - \omega_1)t + \beta_2 - \beta_1] \quad (5.32)$$

Thus, the output current from the detector is composed of a d.c. term and a term involving the difference frequency, $(\omega_2 - \omega_1)$. The difference frequency is, in this instance, the Doppler shift, $\nu_D = \omega_D / 2\pi$. Equation (5.32) is only an approximation to the actual heterodyning process, since the wavefronts striking the detector are usually neither plane nor linearly polarised [70].

The choice of detector is dependent upon the level of illumination. Photodiodes are known to be superior for heterodyning applications at high light levels, but the photomultiplier is preferable at lower levels

and generally has been used in most investigations.

In this work the two incident light beams focus onto the photocathode of the photomultiplier through a pinhole, the purpose of which is to prevent any undesired light from hitting the photomultiplier tube during measurement. Thus, the pinhole should be large enough to accept light only from the $1/e^2$ probe volume. The incoming beams are made parallel by means of a lens of focal length f_2 , see fig. 5.7 after which they are focussed onto the pinhole using a lens of focal length f_3 . The diameter of the pinhole in the receiving optics was fixed at d_{ph} , so that the diameter of view of the pinhole at the plane of the cross-over region, $2b_w$, is found by successive application of equation (5.20) to be:

$$2b_w = \frac{f_2}{f_3} \cdot d_{ph} \quad (5.33)$$

Provided that $2b_w$ is greater than the image of the $1/e^2$ probe volume seen by the photodetector, then the measurement volume equals the probe volume, ignoring effects due to the analysing electronics, see section 5.8.

In the fringe mode of operation, where the frequency derives from intensity modulations in the scattering volume, the received frequency is independent of the scattering angle, so that the solid angle of light collection is not restricted. For reference beam mode operation, however, the solid angle of light collection must be restricted [75, 87] For example, consider two plane wavefronts striking a photodetector surface which has an effective diameter D . The two wavefronts may be considered to be due to a scattered wave from a scattering particle, P , in the probe volume and a wavefront generated by the reference beam which is assumed to be aligned with the detector surface and emanating

from a point source at the probe centre, as shown in fig. 5.8. If the phase between the wavefronts varies by more than half a wavelength, then the signals from different parts of the detector tend to annul one another. Hence, the condition for a strong signal may be derived as follows - see fig. 5.8 :

For large m and small d , $\Psi_1 \approx \Psi_2 = \Psi$ (5.34)

and so, $s \approx \frac{d}{2} \sin \Psi$

For total variation of phase less than $\lambda/2$, that is, for $2s < \lambda/2$

then $\frac{2d}{2} \sin \Psi < \lambda/2$

that is, $\frac{2d}{4} \frac{D}{m} < \lambda/2$, since $\sin \Psi \approx \frac{D}{2m}$

or $dD < m\lambda$ (5.35)

In equation (5.35), d represents the diameter of the probe volume and, for the system used in this study, m represents the distance to the collecting lens and D represents the diameter of the beams at the collecting lens. In order to ensure that equation (5.35) is obeyed, it is necessary to include an adjustable aperture stop in the system for the correct value of D to be realised, see fig. 5.7.

It may be noted that equation (5.35) also implies a cone, called the "cone of coherence", [57].

5.8 Measurement Volume

As indicated in section 5.6, a distinction is made between the probe volume and the measurement volume. In the fringe mode of operation, since the angle of view is not restricted, the measurement volume is affected by both the pinhole diameter and the position of the viewing optics with respect to the optical axis of symmetry. For reference

beam mode operation, the angle of view is fixed and the measurement volume is changed only by pinhole diameter alterations.

5.8.1 Fringe Mode Measurement Volume

Consider the fringe mode arrangement shown in fig. 5.7, in which the angle between the viewing optics and the optical axis of symmetry is θ . Thus, the portion of the $1/e^2$ ellipsoid 'seen' by the photomultiplier will be as shown in fig. 5.9, where $2b_w$ is given by equation (5.33). If $\Delta Y < 2b_w$, the effective measurement volume is that shown in fig. 5.10, and for large θ it is approximately a cylinder of diameter $2b_0$ and length $\frac{f_2}{f_3} d_{ph}$. For a shallow angle, θ , the length of the cylinder will approach ΔZ .

5.8.2 Reference Beam Mode Measurement Volume

In the reference beam mode, viewing is along the axis of the reference beam and so the dimension of the $1/e^2$ probe volume seen by the viewing optics is $\Delta Y'$, as shown in fig. 5.11, whilst ΔX is unaltered. The $\Delta Y'$ dimension may be derived as follows:

$$\text{For an ellipse, } y = \sqrt{b^2 - \frac{x^2}{a^2} b^2} \quad (5.36)$$

and the position x, y at which the reference beam is tangential to the ellipse is given by:

$$\frac{dy}{dx} = - \frac{xb}{a^2 \sqrt{1 - (\frac{x}{a})^2}} = \tan \theta \quad (5.37)$$

from which:

$$y = \frac{b}{\sqrt{(\frac{a}{b})^2 \tan^2 \theta + 1}} \quad (5.38)$$

and

$$x = \frac{a^2 \tan \theta}{b \sqrt{(\frac{a}{b})^2 \tan^2 \theta + 1}} \quad (5.39)$$

c and e can be evaluated from x and y such that:

$$c = \frac{b}{\cos\theta \sqrt{\left(\frac{a}{b}\right)^2 \tan^2\theta + 1}} \quad (5.40)$$

and

$$e = \frac{a^2 \tan\theta \sin\theta}{b \sqrt{\left(\frac{a}{b}\right)^2 \tan^2\theta + 1}} - \frac{b \tan\theta \sin\theta}{\sqrt{\left(\frac{a}{b}\right)^2 \tan^2\theta + 1}} \quad (5.41)$$

thus, $\Delta Y'$ can be found from

$$\begin{aligned} \Delta Y' &= 2(c + e) \\ \text{giving } \Delta Y' &= \frac{2}{\sqrt{\left(\frac{a}{b}\right)^2 \tan^2\theta + 1}} \left[\frac{b}{\cos\theta} + \tan\theta \sin\theta \left(\frac{a^2}{b} - b \right) \right] \end{aligned} \quad (5.42)$$

Substitution of the conditions $b = \frac{b_0}{\cos\theta}$ and $a = \frac{a_0}{\sin\theta}$ from equations (5.23) and (5.24) yields:

$$\Delta Y' = \frac{2b_0}{\sqrt{2}} \left[\frac{1}{\cos^2\theta} + 1 - \tan^2\theta \right] \quad (5.43)$$

Rationalisation and making a trigonometrical substitution gives the result:

$$\Delta Y' = \sqrt{2} 2b_0 = \sqrt{2} \Delta X \quad (5.44)$$

That is, $\Delta Y'$ is constant and independent of θ , the half angle between the two beams. The design of the DISA system used here assumed that $\Delta Y' = \Delta Y$ in calculating the pinhole diameter, d_{ph} . In consequence, d_{ph} is $\sqrt{2}$ smaller than that required for acceptance of the $1/e^2$ probe volume. Thus, the measurement volume on this basis is not an ellipse. The pinhole accepts light scattered from a truncated ellipse which retains its ΔY , ΔX and ΔZ values.

5.9 Application to Turbulence Intensity Measurements

The frequency tracking unit, see section 5.11, produces a voltage output that is directly proportional to the tracked frequency, which is itself related to fluid velocity. Hence, the turbulence characteristics of the flow may be analysed by obtaining the velocity fluctuations about the

mean by processing the tracking unit output with an R.M.S. voltmeter. The R.M.S. voltmeter then gives $\sqrt{(\nu_D')^2}$, that is, the root-mean-square of the frequency fluctuations. Unfortunately, this does not represent $\sqrt{(v')^2}$, the root-mean-square of the velocity fluctuations, since there are contributions to the frequency other than those produced by the velocity fluctuations alone. These contributions are normally termed "frequency broadening" and their origin can be shown by implicitly differentiating equation (5.7), to give:

$$d\nu_D = \frac{2 \sin \Theta}{\lambda_i} dv + \frac{2v \cos \Theta}{\lambda_i} d\Theta - \frac{2v \sin \Theta}{\lambda_i^2} d\lambda_i \quad (5.45)$$

The first term in equation (5.45) is usually referred to as "velocity gradient broadening" and it arises from the finite dimensions of the probe volume. The second term is due to the finite scattering angles involved. The converging laser beams will have finite angles within the probe volume, causing variation in the fringe spacing and there is also a spread in the scattering angle at the collecting aperture, so that the term is often called "aperture broadening". Aperture broadening is equivalent to "finite transit time broadening" as shown by reference [90], which derives its name from the uncertainty in the measured frequency due to the limited duration of the frequency burst. It is usually expressed by an equation of the form [57] :

$$\frac{\delta \nu_{Dt}}{\nu_D} \approx \frac{c}{v_i} \cdot \frac{\cotan 2\Theta}{2\Delta Y} \quad (5.46)$$

where $\delta \nu_{Dt}$ is the spread in frequency due to finite transit time broadening and ν_D is the mean Doppler frequency. Whilst "finite transit time" or "ambiguity broadening" and "aperture broadening" are treated as equivalent, [89, 65] some authors have treated them as separate entities [58, 69, 84].

The final term in equation (5.45) is negligible since the laser produces a line spectrum with virtually no frequency spread. However, another broadening term, not indicated by equation (5.45), is that due to the noise produced by the analysing electronics, photomultiplier shot noise and so on. These are referred to as "instrument broadening". In this study instrument broadening and finite aperture broadening have been obtained as a single value, using a rotating disc. The combination will be called "disc broadening" for brevity.

5.9.1 Velocity Gradient Broadening

For pipe flow in the axial y-direction, the first term in equation (5.45) can be expressed as:

$$\delta V_{D_{vg}} = \left[\frac{\partial v}{\partial x} \delta x + \frac{\partial v}{\partial y} \delta y + \frac{\partial v}{\partial z} \delta z \right] \frac{2 \sin \Theta}{\lambda_i} \quad (5.47)$$

or in cylindrical co-ordinates:

$$\delta V_{D_{vg}} = \left[\frac{\partial v}{r \partial \delta} r \delta \delta + \frac{\partial v}{\partial y} \delta y + \frac{\partial v}{\partial r} \delta r \right] \frac{2 \sin \Theta}{\lambda_i} \quad (5.48)$$

For fully developed, axi-symmetric flow, equation (5.48) reduces to:

$$\delta V_{D_{vg}} = \frac{2 \sin \Theta}{\lambda_i} \frac{dv}{dr} \delta r \quad (5.49)$$

In equation (5.49) $\frac{dv}{dr}$ represents the slope of the velocity profile at the radial station considered and δr is the length of the measurement volume as given by either equation (5.24) or (5.33), depending upon the position of the viewing optics.

5.9.2 Disc Broadening

Disc broadening was assessed using the arrangement shown in fig. 5.12.

For a constant rate of rotation of the disc there would be a zero reading on the R.M.S. voltmeter, were it not for the broadening effects.

There can be no velocity gradient broadening if the radius of measurement is very much larger than the ΔY dimension. Hence, for a given configuration in the real flow situation, the various broadening effects can be found by reproducing that configuration, in back-scatter as shown, using a rotating disc to give the same frequency, aperture size, fringe spacing, and so on. Thus, the resulting R.M.S. voltmeter reading gives the broadened frequency, δv_{Dd} .

5.9.3 Broadening Correction Equation

The root-mean-square velocity fluctuations can be found by subtracting the broadening contributions from the R.M.S. voltmeter reading, as follows:

$$\frac{\sqrt{(v')^2}}{v} = \frac{\sqrt{(v'_D)^2}}{v_D} - \frac{\delta v_{Dd}}{v_D} - \frac{2 \sin \Theta}{\lambda_i} \cdot \frac{dv}{dr} \delta r \quad (5.50)$$

5.10 Signal to Noise Ratio Considerations

Several expressions for the signal to noise power ratio are to be found in the literature for a laser anemometer, [82, 66, 75]. However, perhaps the most comprehensive expression is that derived by Buchhave [87], which is given as:

$$\text{SNR}_{\text{power}} = \frac{\frac{2\eta\epsilon^2 P_1 P_2}{h\nu}}{2K\Delta f(P_1 + P_2 + P_B + \frac{h\nu}{\eta e'} i_D) + \frac{4h\nu k T \Delta f}{G^2 e^2 \eta R_L}} \quad (5.51)$$

where $h\nu$ is the energy of a quantum of radiation of frequency ν ,

e' is the electron charge,

η is the quantum efficiency of the detector

Δf the bandwidth of the detector circuitry

i_D the cathode dark current,

ϵ^2 is the heterodyning efficiency

$4kTR_L\Delta f$ is the mean square thermal noise voltage created when the anode current is further amplified by an electronic amplifier with an effective resistive load R_L ,

G is the photomultiplier gain,

K is a measure of the average gain per dynode of the photomultiplier,

and P_R is the background light power contribution.

The terms P_1 and P_2 are the light power of the two incident beams. For reference beam mode, if P_1 is the scattered light power and P_2 the reference beam power, then for small background illumination, P_B , high photomultiplier gain, G , and negligible i_D , equation (5.51) becomes:

$$SNR_{power} = \frac{\eta \epsilon^2 P_1 P_2}{K \Delta f h \nu (P_1 + P_2)} \quad (5.52)$$

It is evident from this expression that high SNR can be obtained if $P_2 \gg P_1$. However, an upper limit on P_2 exists of about $5P_1$ [87] and thus equation (5.52) becomes:

$$SNR_{power} = \frac{5 \eta \epsilon^2}{6 K \Delta f h \nu} P_1 \quad (5.53)$$

For fringe mode operation, both beams striking the photocathode are scattered beams of power P_1 , so that for similar considerations to the reference beam mode case, equation (5.52) becomes:

$$SNR_{power} = \frac{\eta \epsilon^2 P_1}{2 K \Delta f h \nu} \quad (5.54)$$

Thus, for fringe mode operation and scattered light power P_1 from each beam, the signal to noise ratio is only 60% of the signal to noise ratio of a reference beam anemometer having similar scattered light power.

However, fringe mode operation does not require a restricted aperture as does the reference beam mode, so that the scattered light power in the former mode may be many times greater than that of the reference beam mode. Thus, the fringe mode has potentially the higher overall signal to noise ratio.

A high signal to noise ratio is essential in laser anemometry, since poor SNR signals require more sophisticated electronic circuitry for analysis. An obvious way to increase the SNR is by a reduction in the detector bandwidth, Δf . It must be remembered, however, that this also restricts the velocity fluctuations which can be measured by the system.

5.11 Laser Anemometry Equipment

The laser anemometry equipment used throughout this study, with the exception of chapter 10, consisted of a D.I.S.A. 55L system, as shown in figs. 5.13 and 5.14.

A 5 mW He-Ne gas laser, ($\lambda_l = 0.6328$ microns), provided the coherent light source. The laser, operating in the TEM₀₀ mode, had a beam diameter of 0.65 mm at the $1/e^2$ points and a divergence of 1.7 milliradians. Beam splitting and focussing was achieved with an integrated optical unit utilising a biprism and traversable surface mirror for beam separation adjustment. The beam which passed directly through the biprism could be slightly directionally adjusted in the horizontal and vertical directions in order to obtain perfect beam intersection. This was achieved by means of two glass wedge plates, having their taper directions at right angles to each other, which could be rotated. Three interchangeable focussing lenses were provided for use with the optical unit, these having focal lengths of 130 mm, 300 mm and 600 mm. An adjustable filter enabled one of the beams to be intensity damped by up to 99% for reference beam operation. The optical unit housing was capable of rotation through 360°, so that any velocity component could be measured.

The photomultiplier tube and receiving optics were intergrated into a single unit. Three collecting lenses were provided of focal length 200 mm, 333 mm, and 600 mm, so that combinations of these provided matching focal lengths to those of the transmitting optics, that is

$$\frac{1}{\frac{1}{200} + \frac{1}{333}} \text{ mm} = 125 \text{ mm}, 333 \text{ mm and } 600 \text{ mm for the } 130,$$

300 and 600 mm focussing lenses respectively.

A collimating lens of 105 mm focal length was used to focus the collected light onto the photocathode through a variable diameter aperture and a 0.15 mm pinhole aperture having positional adjustment. A built-in shutter protected the photocathode from exposure during setting-up procedures. Alignment of the pinhole with the focussed scattered light was facilitated with the use of a viewfinder mounted with the receiving optics.

The photomultiplier was an EMI type 9658B having a cathode voltage range of 500 to 1400 volts negative and a maximum anode current of 1 mA. The high voltage was supplied to the photomultiplier by a 250 to 2000 V, negative polarity D.I.S.A. 55L15 high voltage supply.

Analysis of the signal from the photomultiplier was effected by a D.I.S.A. 55L20 Doppler signal processor, which comprised a "frequency compressive feedback" system. Although a detailed description of the signal processor is available elsewhere, [91, 92] , a brief outline is included here.

Fig. 5.15 shows a block diagram of the tracking unit which follows a signal preamplifier. The incoming Doppler signal, which is inherently amplitude modulated, is multiplied with the output of a voltage controlled oscillator, VCO, at the mixer stage shown. The output from the mixer stage is composed of components containing the sum ($\nu_{osc} + \nu_D$) and difference frequencies ($\nu_{osc} - \nu_D$). Filter IF/A is a band pass filter with centre frequency, ν_0 , and band width QA. This filter rejects most of the noise inherent in the mixer signal and removes the sum frequency ($\nu_{osc} + \nu_D$). In the steady state, the output frequency ($\nu_{osc} - \nu_D$) will be equal to the centre frequency of IF/A, Limiter 1 reduces the amplitude modulated signal to a square waveform of frequency equal to its input frequency ($\nu_{osc} - \nu_D$). The signal

then passes to a frequency discriminator which consists of a second filter, IF/B, limiter 2 and a phase comparator. IF/B senses only the sinusoidal component of the incoming square wave, $(\nu_{osc} - \nu_D)$ and has a centre frequency, ν_0 , and bandwidth Q_B . IF/B is arranged so that its output lags its input by an angle ξ . If $(\nu_{osc} - \nu_D) = \nu_0$, then $\xi = 90^\circ$; if $(\nu_{osc} - \nu_D) < \nu_0$, then $90^\circ > \xi > 0$; and if $(\nu_{osc} - \nu_D) > \nu_0$, then $90^\circ < \xi < 180^\circ$. The phase comparator merely performs a multiplication of the original square waveform with the square wave from limiter 2. Thus, the square wave from limiter 2 resembles that from limiter 1 except for the phase difference, ξ . If $\xi = 90^\circ$, i.e. if $(\nu_{osc} - \nu_D) = \nu_0$, the output from the phase comparator is a rectangular wave at twice the IF centre frequency. The d.c. level of this wave, obtained by subsequent smoothing, is zero. Thus, the smoothed voltage output, u , of the frequency discriminator, varies linearly between a positive maximum, g , through zero to a negative maximum, $-g$, depending upon whether $(\nu_{osc} - \nu_D) < \nu_0$, $(\nu_{osc} - \nu_D) = \nu_0$, or $(\nu_{osc} - \nu_D) > \nu_0$, respectively. Thus:

$$u = -\frac{2g}{\pi} \xi + g \frac{2g}{\pi} \left[\frac{\pi}{2} - \xi \right] \quad (5.55)$$

The smoothed voltage, U , given by equation (5.55) is amplified and, since it is directly proportional to $(\frac{\pi}{2} - \xi)$, and hence ν_D , it can be applied to a meter graduated directly in terms of Doppler frequency.

U is also required to drive the VCO, reducing ν_{osc} when it has a negative value and increasing ν_{osc} when it has a positive value; that is, negative feedback. In this way, the difference frequency $(\nu_{osc} - \nu_D)$ always attempts to be maintained at ν_0 , so that U is always proportional to ν_D .

The acceptance bandwidth of IF/A, QA, is variable in order to suit different signal to noise conditions, whilst Q_B is fixed. ν_0 can be adjusted to

seven values in the range 1.5 kHz to 1.5 MHz, thereby giving a tracker frequency range, ν_D , of 2.25 kHz to 15 MHz. The analogue voltage, U , is available at two outputs for processing on a DISA RMS voltmeter, or averaging on a DISA digital voltmeter.

.

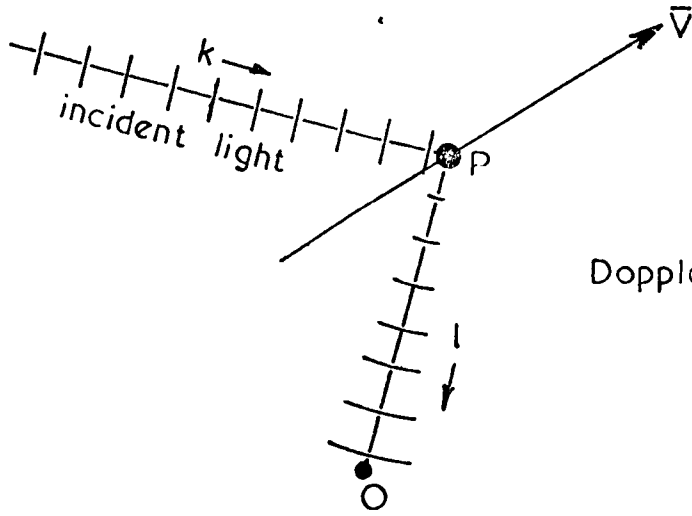


Fig. 5.1.

Doppler shift of scattered light

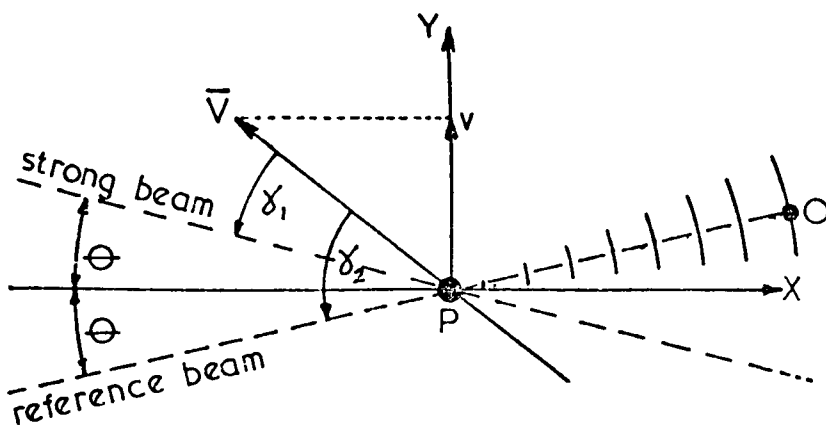


Fig. 5.2.

Analysis of reference beam mode

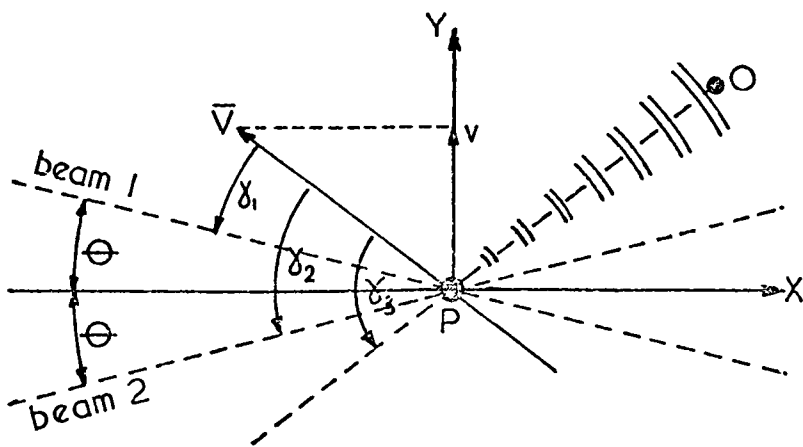


Fig. 5.3.

Analysis of differential Doppler mode

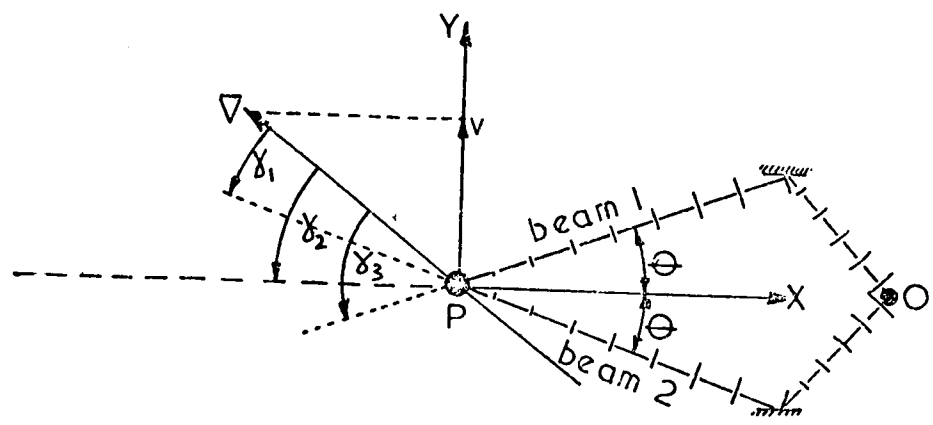


Fig. 5.4.
Analysis of
one beam
mode

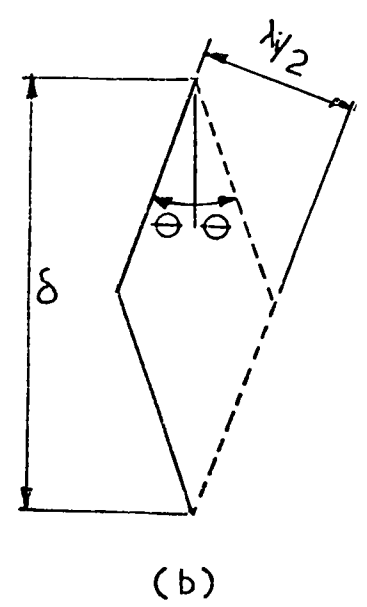
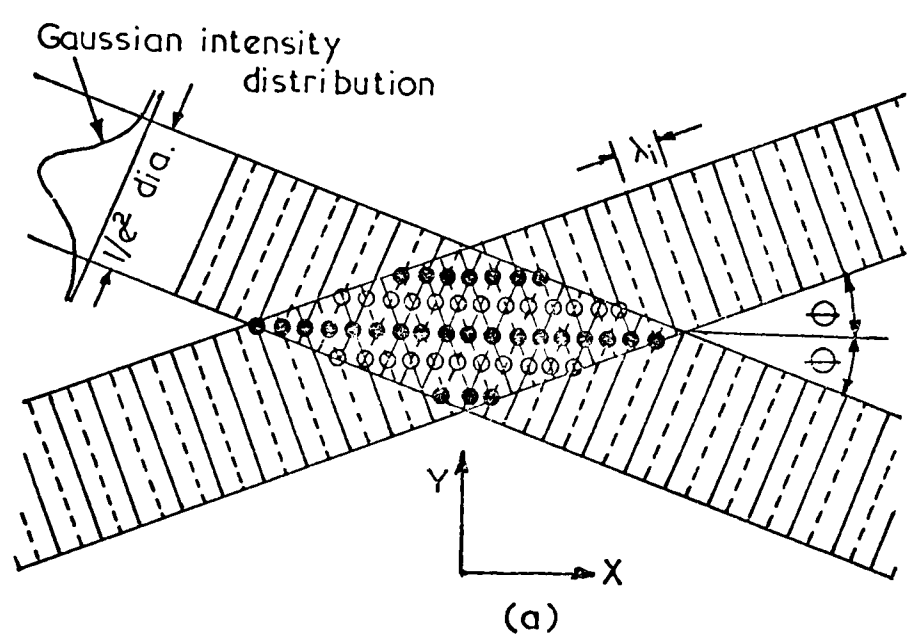


Fig. 5.5. Intersection region

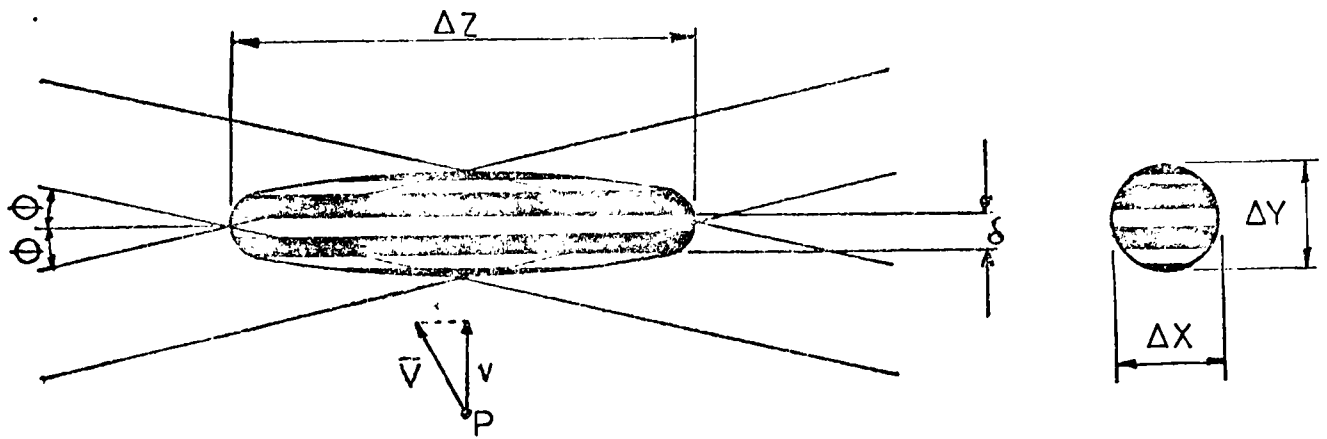


Fig.5.6. Fringe formation in the $1/e^2$ ellipsoid

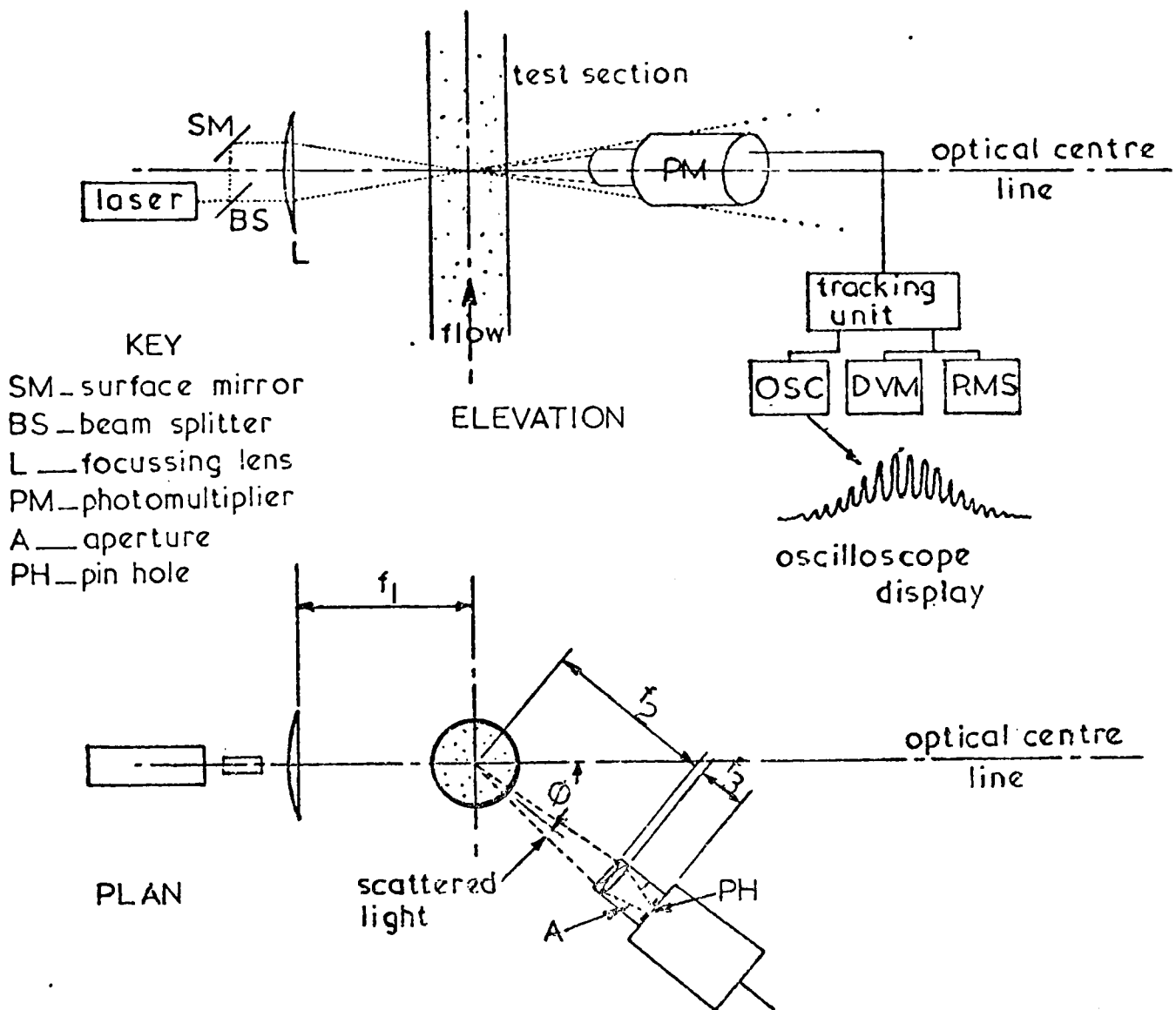


Fig. 5.7. Laser anemometry arrangement for fringe mode

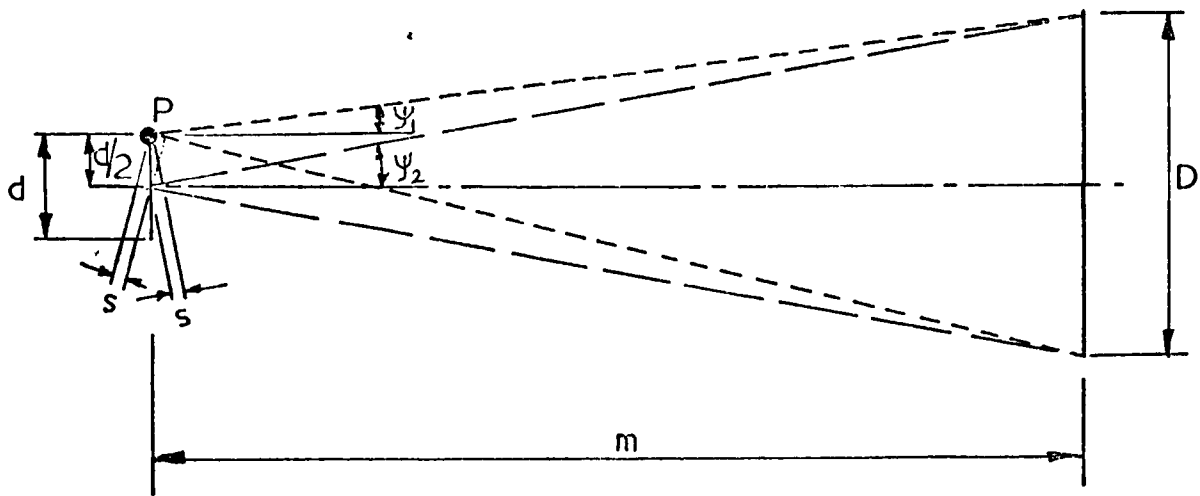


Fig 5.8. Reference beam mode coherence condition

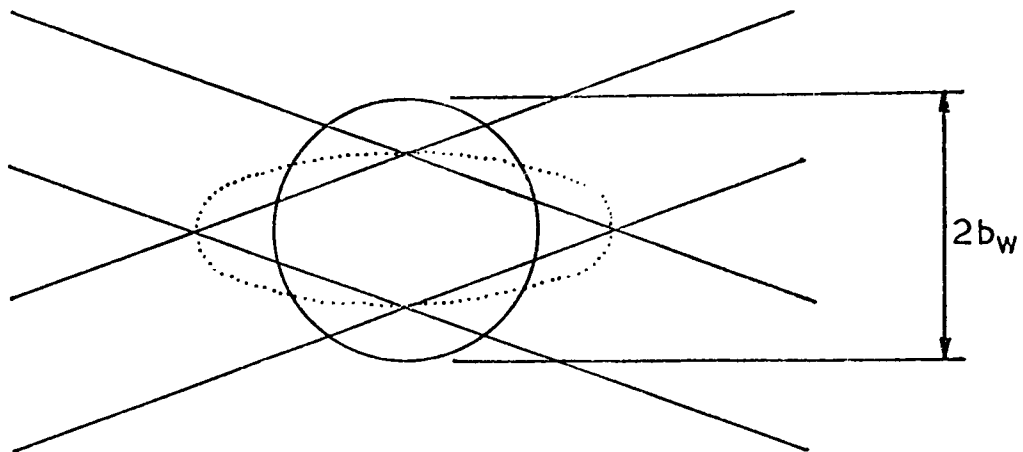


Fig. 5.9. View from photomultiplier pinhole

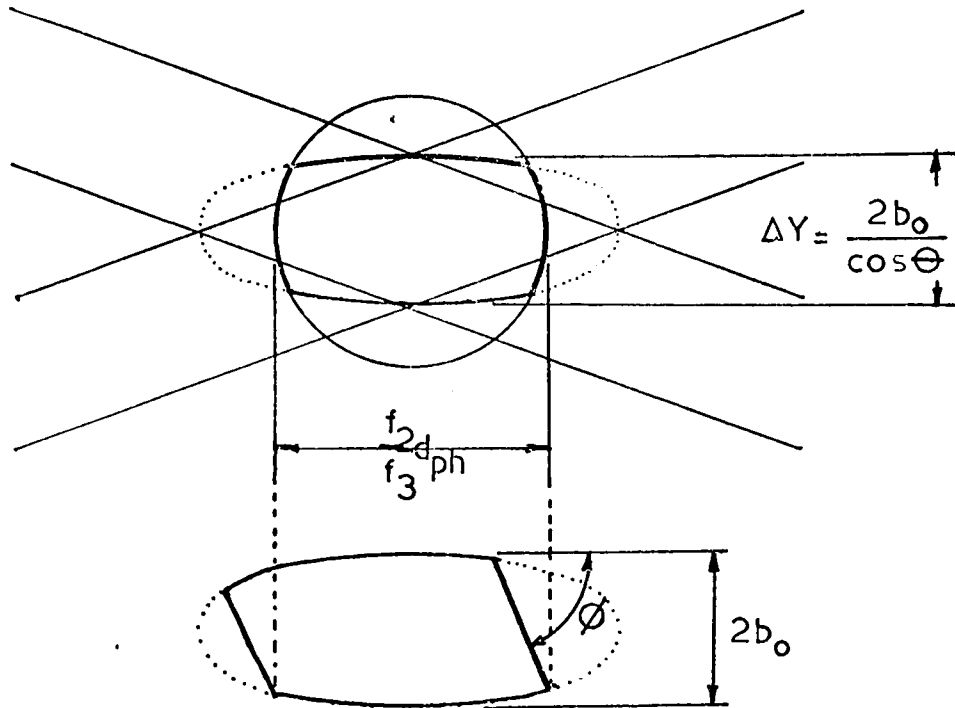


Fig.5.10. Measurement volume — fringe mode

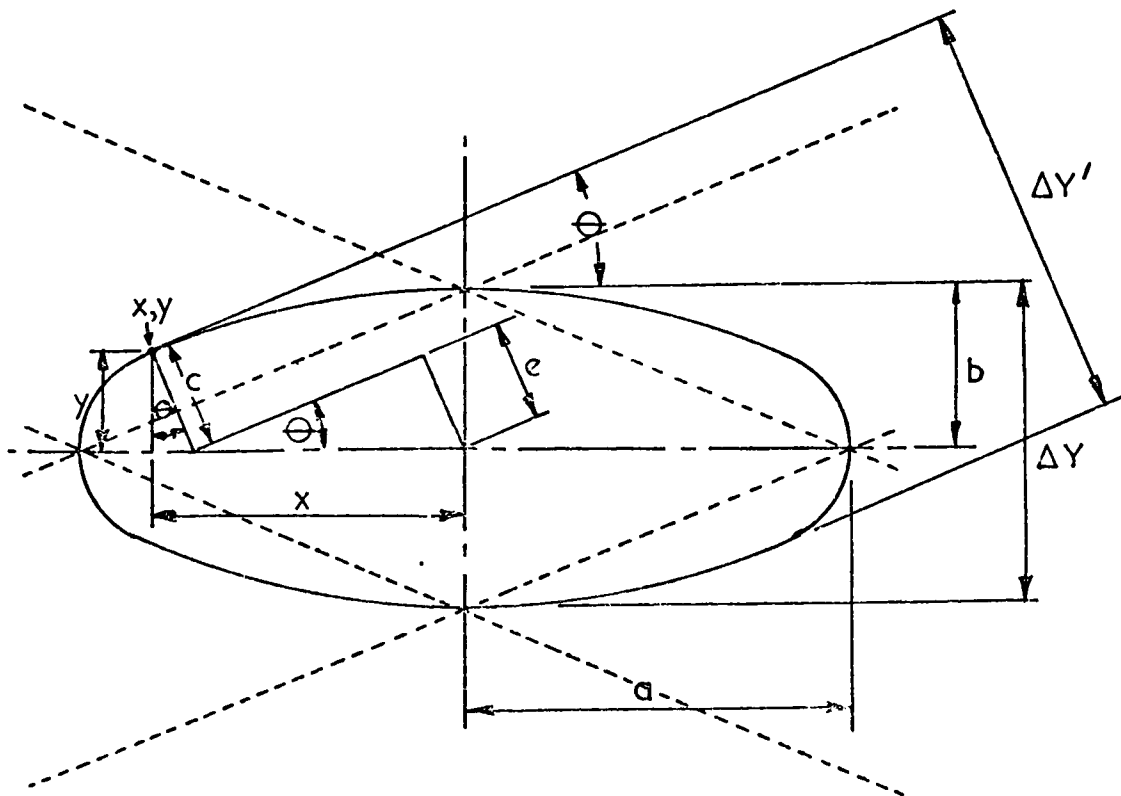


Fig.5.11. Measurement volume — reference beam mode

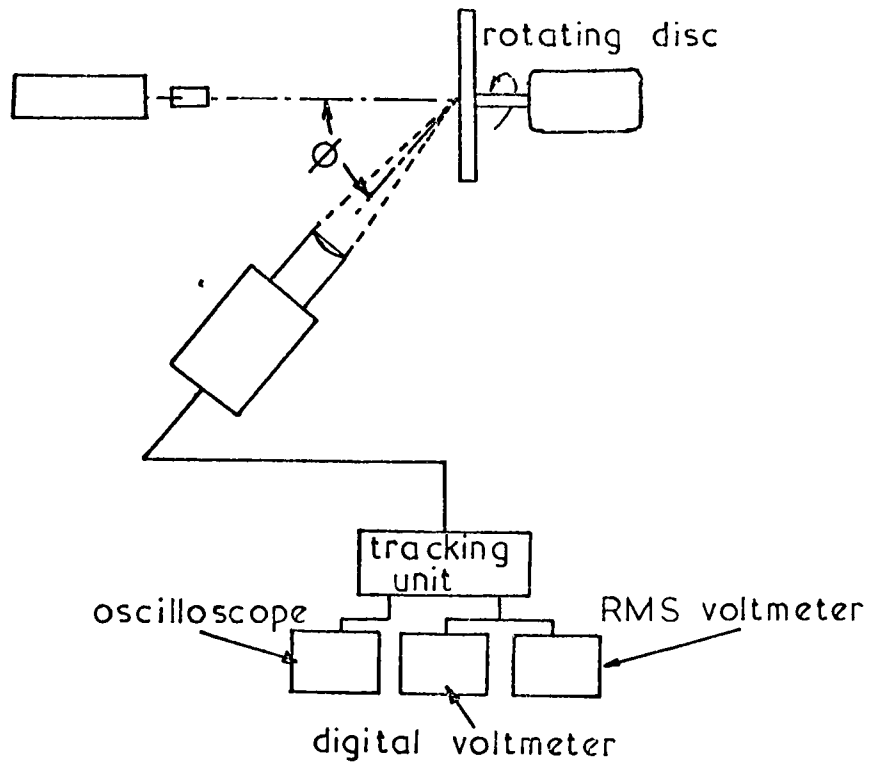


Fig. 5.12. Broadening determination

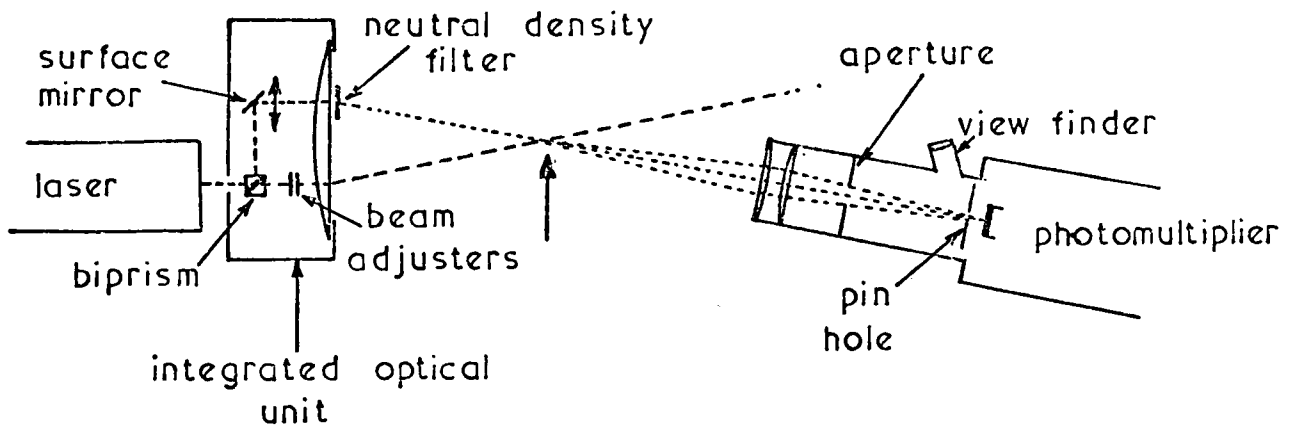


Fig. 5.13. Reference beam mode arrangement



FIG. 5.14. LASER ANEMOMETRY EQUIPMENT



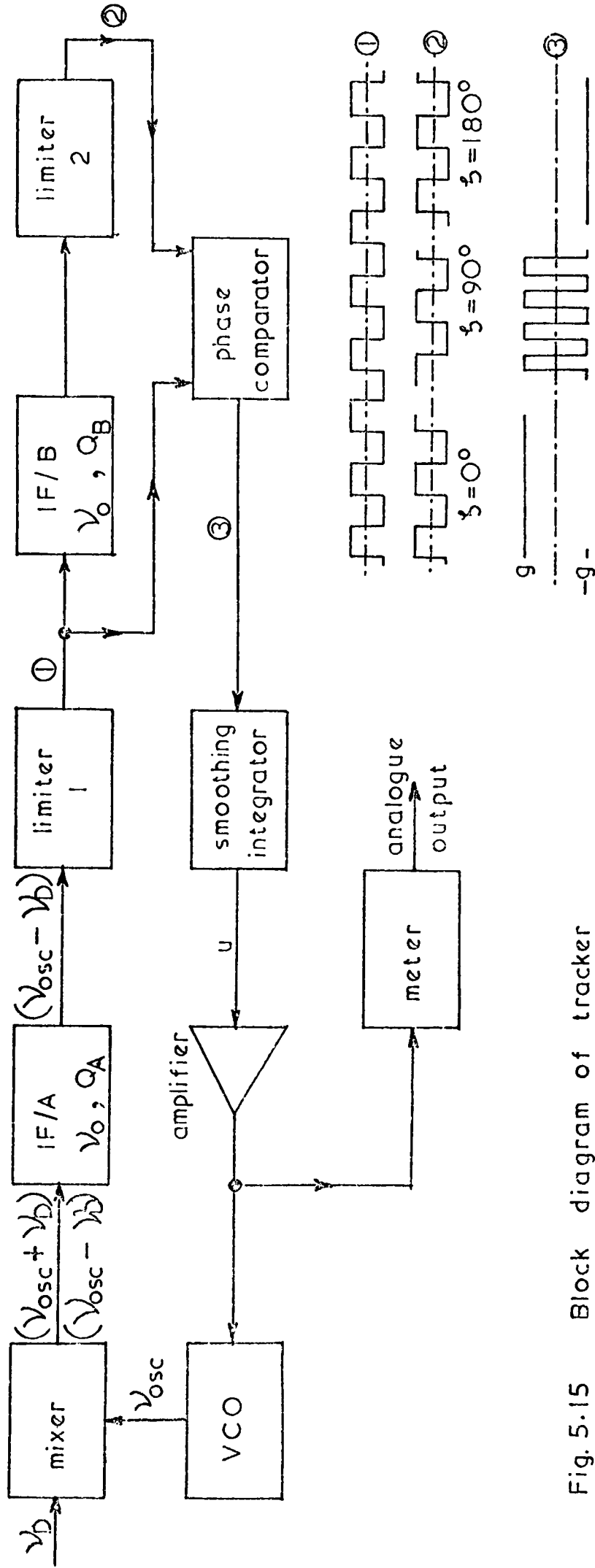


Fig. 5.15 Block diagram of tracker

CHAPTER 6

'CLEAN' GAS VELOCITY AND TURBULENCE INTENSITY MEASUREMENTS

6.1 Introduction

In this chapter, local velocity and axial turbulence intensity measurements for the flow of air only through the glass test section, using the laser anemometer, are described. The measurements required the flow to be seeded with suitable light-scattering particles which were small enough to follow the air velocity fluctuations [80]. The resulting 'clean' air velocity profiles enabled the calculation of mean air velocities and hence comparison of the laser anemometry measurements with the orifice plate calibration curve.

6.2 Seeding Arrangements

Two methods of seeding the flow were used in this investigation :-

6.2.1 Smoke Injector Method

Three sets of local velocity results in the lower velocity range were obtained using a smoke generator, (C.F. Taylor Co., model 3020). The atomised paraffin oil was introduced into the test section at the smoke injection point shown in fig. 3.3., using CO₂ gas at a pressure of 40 p.s.i.g. from a 500 p.s.i.g. bottle. This method was found to be unsatisfactory for the higher velocity measurements and for turbulence intensity measurements. Droplet size was assessed under the microscope to be within the range 2 to 5 microns.

6.2.2 TiO₂ Particle Injection

The greater part of this work was carried out using titanium dioxide seeding particles. These particles had a mean diameter of about 0.27 microns, but they did agglomerate and the size distribution of the flowing particles varied from 0.04 to 0.6 microns. An electron-micrograph of a sample of the powder taken at the measurement position is shown in fig. 4.9. Injection of the particles into the air flow system was accomplished with a fluidising unit similar to that described in [80]

and shown in fig. 6.1.

Air from the system drain cock, see fig. 3.3, passed through a small drying chamber in which silica gell removed any moisture. The silica gell could itself be dried using a heating element. Limited control of the amount of air passing into the fluidising unit was available by adjusting the drain cock opening. The air then passed through the T_iO_2 , entraining some of the particles, which were drawn off into the flow system. This was achieved by incorporating a venturi section into the main flow system. The pressure at this point was thus reduced sufficiently for the entrained particles to be drawn into the flow. This method of seeding was found to be satisfactory, though not ideal, for the entire range of air flow rates. Furthermore, no external gas supply was required to introduce the particles.

6.3 Air Circuit

The air flow circuit was similar to that described in sections 3.2.1 and 3.2.3, except that the flow was diverted finally into an auxiliary filter, (section 3.3), for T_iO_2 particle removal. The arrangement is therefore essentially as shown in fig. 6.2.

6.4 Laser Anemometer Arrangement

The laser anemometry arrangement used for these measurements was the fringe mode configuration shown in fig. 5.7, in which the angle θ was 45° . The range of fringe spacings used was from 3.7 to 10 microns, depending upon the velocity. The mean local flow velocity was calculated from equation (5.18) and the turbulence intensity was assessed using equation (5.50).

6.5 Results and Discussion

The 'clean' air velocity profiles for all eight sets of results are shown in fig. 6.3. The experimental points compare well with the curves, which are power law representations given by:

$$\frac{U_a}{U_{a_{\max}}} = \left[\frac{Y}{R} \right]^{1/n} \quad (6.1)$$

where n is dependent upon the air Reynolds' number and has been estimated from Schlichting [48], $U_{a_{\max}}$ is the centreline velocity, R the pipe radius and Y the distance from the pipe wall.

Paraffin oil seeding was used for Reynolds' numbers of 57,110, 71,490, and 82,570. Some difficulty was experienced in obtaining these results since oil was found to form a deposit on the inside of the glass test section, destroying the fringe system within one or two minutes.

Cleaning of the tube was facilitated by using the pneumatic conveying system to convey alumina powder through the test section to remove the oil film. At higher Reynolds' numbers the pressure in the air flow system became too great for the smoke injector to function properly and, in addition, the short time period available for measurement did not allow R.M.S. voltmeter readings to be taken.

The remainder of the air velocity profiles, covering a range of Reynolds' numbers from 72,020 to 169,390 were obtained using the sub-micron T_iO_2 particles and the fluidising unit. This was found to function well, but the fixed inlet-to-throat pressure ratio produced by the venturi section caused the seeding particle density to increase with increase in superficial air velocity and so a variable venturi section is desirable. Thus, for lower velocities the seeding density was less than optimum whilst the converse applied for higher velocities.

Again, with the titanium dioxide particles, a deposit formed on the pipe interior; the length of time in which this occurred was dependent upon the seeding density and thus on the air flow rate. Generally, the test section had to be purged clean after ten minutes, but this merely required a short burst of alumina particles from the main pneumatic conveying rig.

The titanium dioxide particles seemed to be inefficient scatterers of light, since, with the high voltage supply to the photomultiplier at its maximum value, the anode current was only about 5 microamps compared with the recommended 40 microamperes [91] but fortunately the tracking unit functioned satisfactorily. Higher scattering intensity could have been observed for $\theta = 0^\circ$, [84], but this would have caused the measurement length to be increased, with a consequent increase in velocity gradient broadening.

Since the power law relationship gave good agreement with the experimental points, the equation:

$$U_{a\text{mean}} = U_{a\text{max}} \frac{2n^2}{(n+1)(2n+1)} \quad (6.2)$$

which is readily derived from the power law relationship of equation (6.1), was used to obtain the mean air velocity, $U_{a\text{mean}}$, thus enabling calculation of the air mass flow rate.

Fig. 6.4 shows a comparison between the orifice plate calibration curve obtained from a pitot-static tube traverse in two perpendicular directions (section 4.2), and the results obtained from the laser anemometer single diameter traverse. The latter points deviate from the calibration curve by an average of about 4%, which is very satisfactory considering that only one traverse plane was used.

Fig. 6.5. shows the turbulence intensity, $\sqrt{(u'_q)^2} / U_q$, experimental points for the five sets of results utilising titanium dioxide particles. These have been corrected using equation (5.50). The curves are compared with Ower's interpretation [47] of Laufer's results [93], for a Reynolds' number of about 40,800, which is below the range considered here. It can be seen that, in the core of the flow, the turbulence is slightly greater than that given by Laufer. The high core value is probably enhanced by the blower pulsations and the complicated pipework prior to entry to the test section.

Velocity gradient broadening, $\delta v_{D_{vg}} / v_D$, was estimated using equation (5.49), to be from about 0.1% in the flow core and up to 4% near the wall, on account of the steep profile slope there. $\delta v_{D_d} / v_D$ on the other hand, was found to be approximately constant over a wide range of frequencies for a given configuration, provided that the tracking unit filter range remained unaltered.

The thickness of the buffer layer, that is where $5 < \frac{Y U_\tau}{\nu} < 70$ [48] was estimated to be $Y = 0.046$ cm for the highest Reynolds' number and $Y = 0.122$ cm at the lowest Reynolds' number. Thus, the measurements taken (Y minimum = 0.07 cm) were just in the buffer layer. However, the laminar sublayer was not penetrated at all, since its thickness was estimated to be between 0.0033 cm and 0.0087 cm at the upper and lower Reynolds' numbers respectively. The buffer layer and laminar sublayer from Laufer's results can similarly be estimated to be 0.165 cm and 0.0115 cm respectively, so that the relative penetration of Laufer's measurements was greater. This explains the greater turbulence intensity of Laufer's results in the wall region compared with the results obtained here.

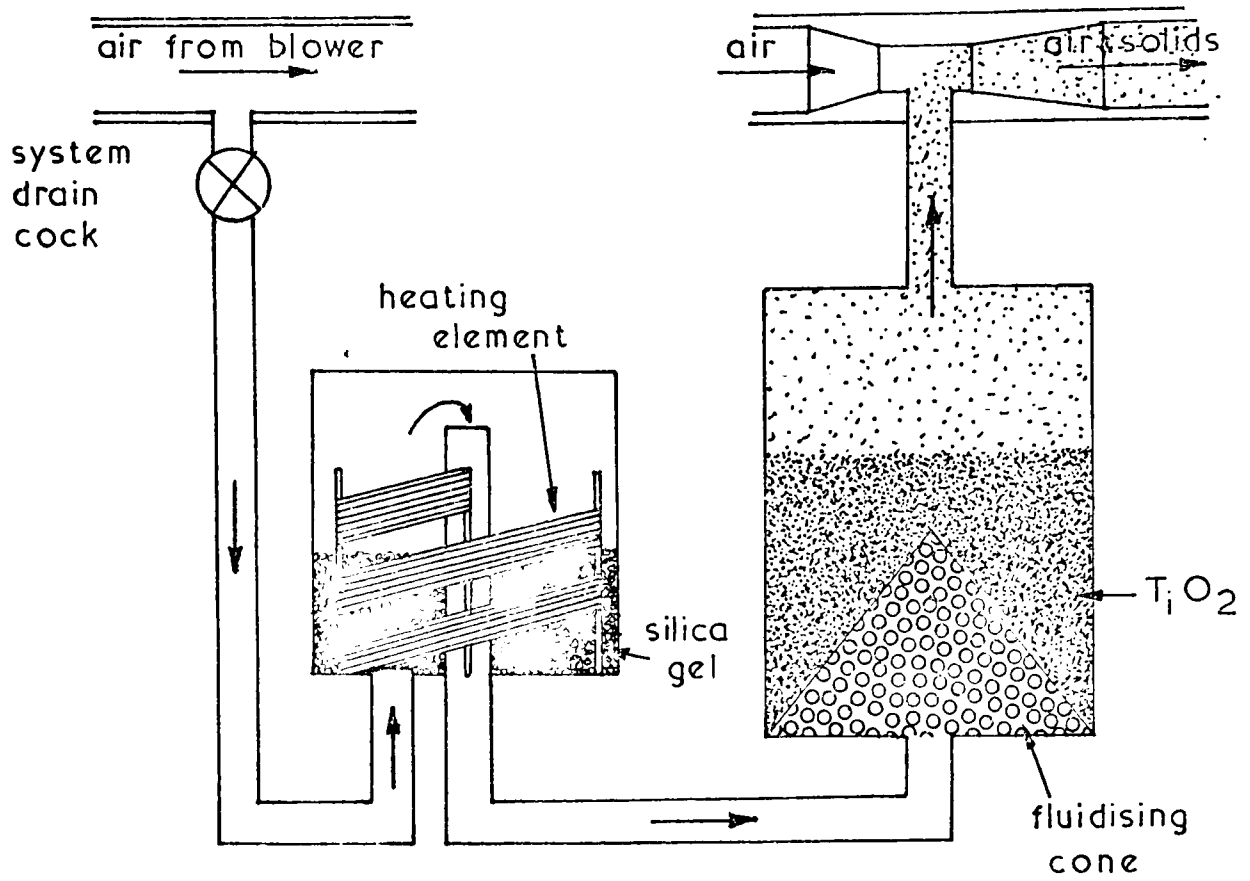


Fig. 6.1. TiO_2 fluidising unit

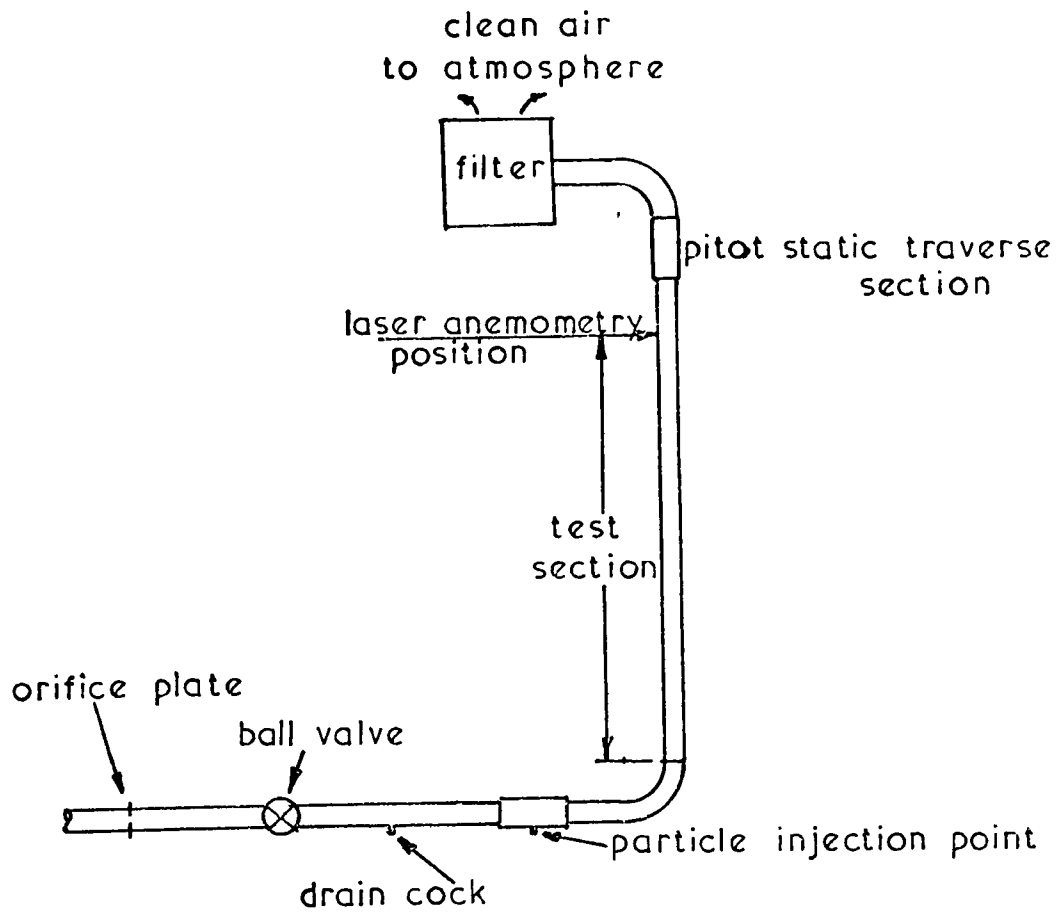


Fig. 6.2. 'Clean air' circuit

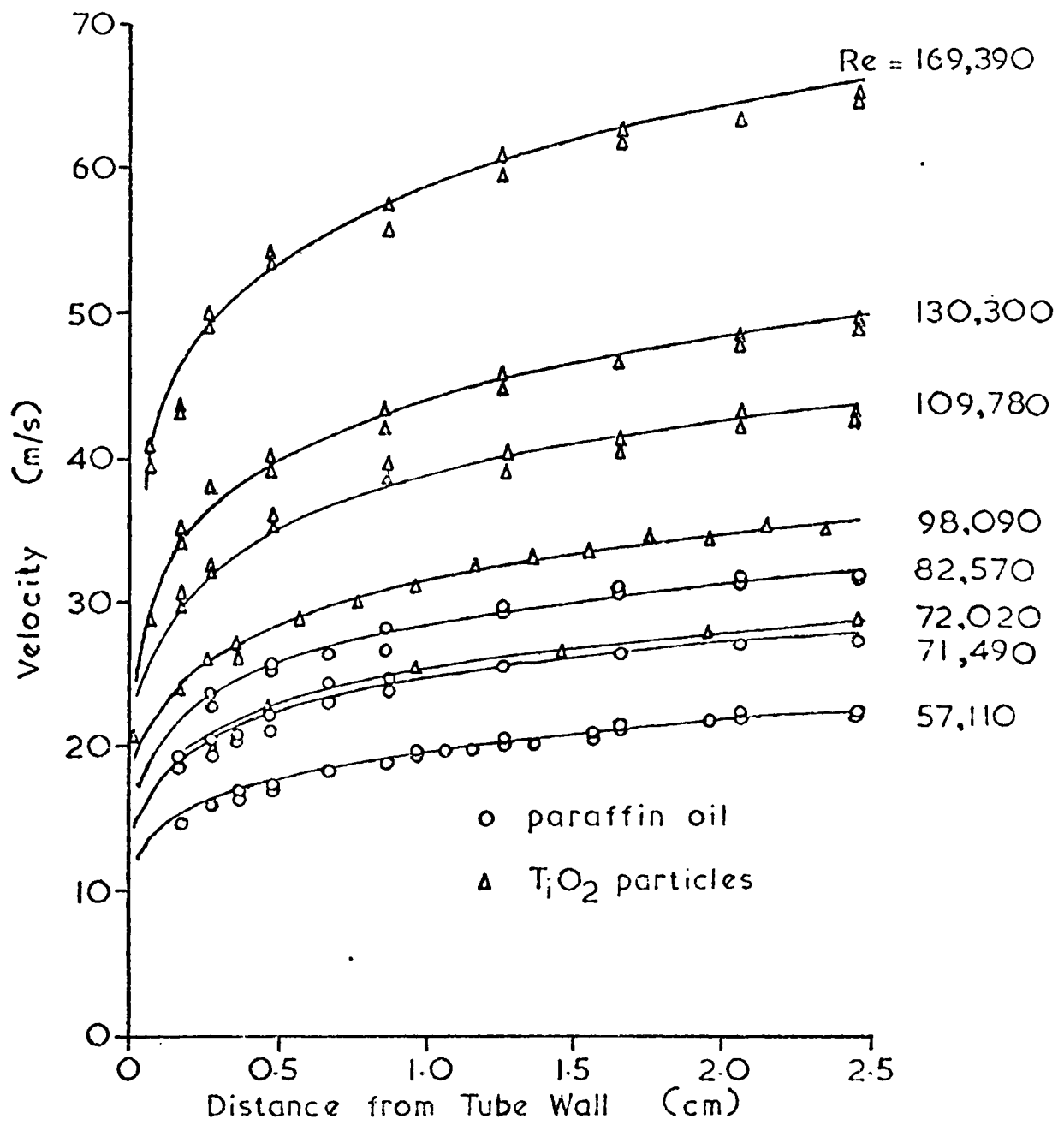


Fig.6.3. Air velocity profiles

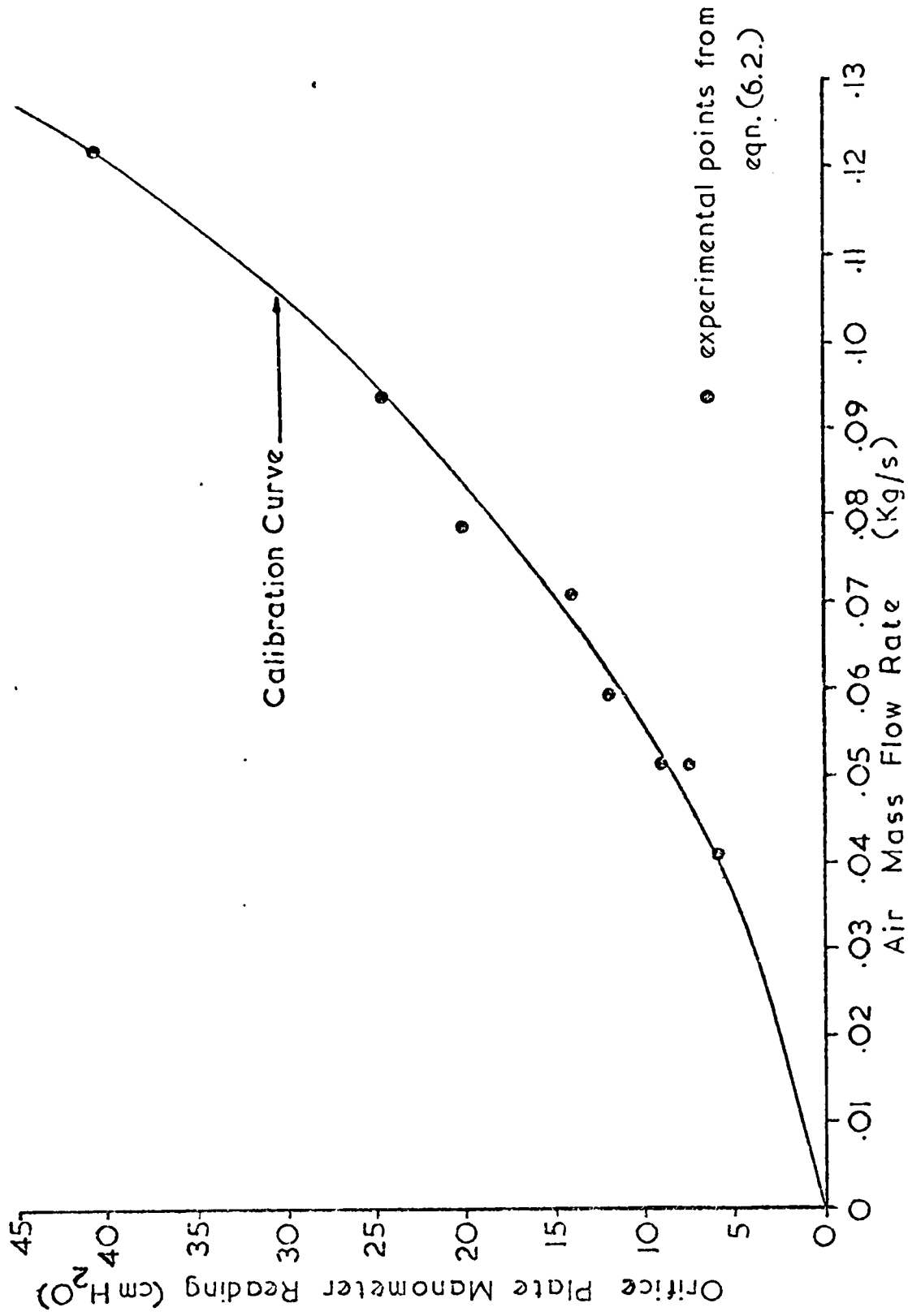


Fig.6.4. Comparison between experimental points and orifice plate calibration curve

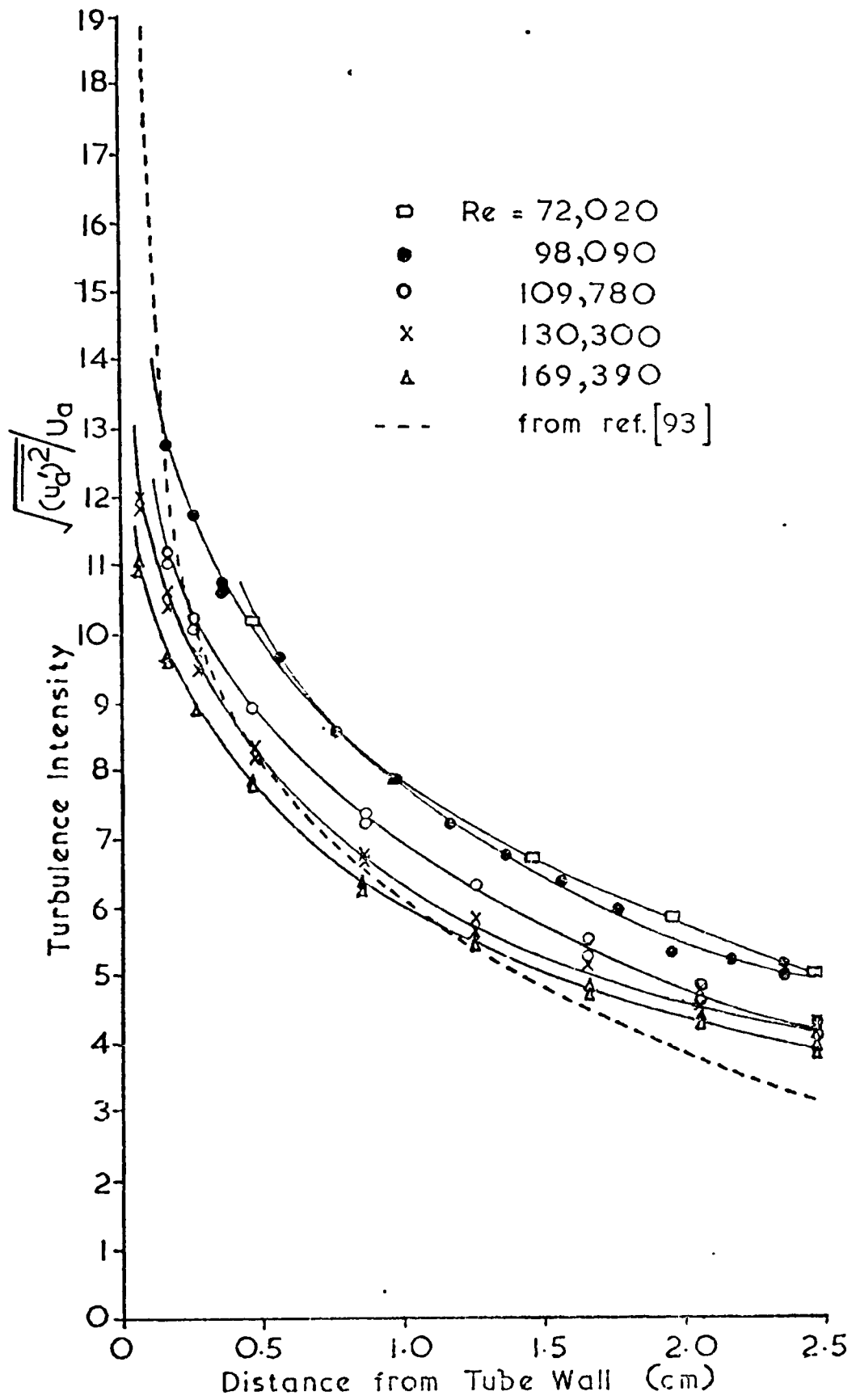


Fig.6.5. Axial turbulence intensity profiles

CHAPTER 7

OBSERVATIONS WITH LARGE SCATTERING CENTRES

7.1 Introduction

The use of laser anemometry for the velocity measurement of particles larger in size than the usual seeding particles requires modifications to conventional laser anemometry guidelines. Two aspects of 'large' (greater than about 5 microns) particle velocity measurement are considered in this chapter. The definition of the probe volume given in section 5.6 refers to a small scattering particle and the equations describing the probe volume dimensions were independent of particle size. In this chapter, the effect of the scattering particle diameter on the probe length, ΔZ , is considered.

It has been suggested in the literature [89] that the Doppler frequency component of the signal burst reduces in amplitude with increase in particle diameter for a given fringe spacing. For large diameter particles it was proposed that no signal would be detectable. Thus, an investigation into the quality of signals was required, since with a size range of conveyed particles it was essential to verify that signals were not only generated from the fines in the flowing suspension.

7.2 Probe Length Investigation

A particle passing through the intersection region will generate different signal forms, depending upon its trajectory, as shown in fig. 7.1. For a given particle size, the maximum a.c. component of the signal, ΔI_{max} , occurs when the particle traverses the mid-section of ΔZ . Elsewhere the a.c. component is reduced in amplitude to ΔI . When ΔI has attenuated to $1/e^2$ of ΔI_{max} , the axial position of the particle axis along ΔZ should correspond to that given in equation (5.24). However, this equation is based only on the laser beam dimensions and takes no account of the scattering particle size.

For a small particle whose diameter is of the order of the fringe spacing, δ , it is to be expected that the signal amplitude, for scattering planes along the ΔZ axis, will vary directly with the light intensity profile. This is not so for a larger particle which may occupy several fringes at any one instant and will begin to enter the $1/e^2$ ellipsoid when its central position is $d/2$ outside it, where d is the particle diameter. Thus, the effect of particle size on the probe dimensions is in doubt. Alternatively, the maximum particle size for which the conventional $1/e^2$ volume is suitable needs to be investigated.

7.2.1 Experimental

Both fringe and reference beam mode arrangements, as shown in fig. 5.7 (where $\theta = 0^\circ$) and fig. 5.13, were used, the raw Doppler signal output passing directly to an oscilloscope for analysis. In order to simulate particle signals, single test wires of various diameters were passed through the probe volume, these previously having been carefully aligned with the fringe direction. The wires were fixed onto a slotted gear wheel, as shown in fig. 7.2, which was arranged as part of a gear train. The gear train, driven by a variable speed motor, allowed a slow rate of passage of the test wire through the probe volume, thus providing easy observation of the resulting frequency envelope. The gear arrangement was mounted on a traversing table to facilitate measurement of the position of the test wire in the direction of the probe length. The plane of motion of the test wire was normal to the major axis of the intersection region and the maximum a.c. component of the signal was measured. This procedure was carried out for several longitudinal positions, thus enabling a plot of a.c.

signal amplitude against axial ΔZ position to be obtained. Only one probe volume was considered, but thirteen separate wire diameters were tested, ranging from 5 to 312 microns diameter.

7.2.2 Results and Discussion

The selection of results shown in fig. 7.3 give the a.c. signal amplitude profiles along the probe volume for wire diameters of 5, 12.7, 22.86, 50 and 70 microns in fringe mode operation. The experimental $1/e^2$ probe length was obtained by multiplying the maximum value of the signal amplitude by $1/e^2$ and estimating the width of the curve at that amplitude. For this test a 300 mm focal length focussing lens was used and, since $\lambda_i = 6328\text{\AA}$, $2b = 0.65$ mm and $\sin \theta = 0.0633$, then the $1/e^2$ probe length calculated from equation (5.24) was 5.88 mm. A comparison between this value and the experimentally determined probe lengths is shown in table 7.1.

It is evident that the experimental ΔZ dimensions were always greater than the calculated values. This may be attributed to either a higher than expected a.c. amplitude at the cross-over region extremities or a reduction in the peak signal amplitude. The results are not sufficiently comprehensive to allow definite conclusions about the effect of scattering particle diameter on probe length and any particle size effect will probably depend upon the ratio of particle(wire) diameter, d , to probe length, ΔZ . However, the ratio of particle size to probe length for the experiments described in later chapters was generally less than 1%, so that from table 7.1 the application of equation (5.24), and presumably (5.22) and (5.23), was considered to be sufficiently accurate. These results show that care is essential in the use of the above equations and the possibilities of an increase in probe volume because of large particle scattering has also been noted by Riethmuller and Ginoux [83] .

The signal envelopes from light scattered by a wire or a particle should be similar. For wires having diameters in the range of 5 to 35 microns, the oscilloscope display resembled that of fig. 7.4a. for both modes of operation. However, the 50 micron and larger wire diameters produced a frequency burst with the form shown in figs. 7.4b and 7.4c, using a reference beam technique. The tail of the signal became thinner with increase in wire diameter. The reason for the shape of the latter is elusive, but the shape variation may prove useful in the particle size analyses of flowing suspensions.

In this experiment, the diameter of the wire did not exceed the probe diameter, which was approximately 372 microns. For conditions in which $d > \Delta Y$, a further variation in signal may occur; this can be envisaged by considering the passage of a fibre of length equivalent to d passing through the probe. A frequency burst would be observed as the front end of the fibre passed through the probe, whilst the d.c. level of the signal increased, until the fibre spanned the ΔY dimension. The d.c. level would then remain constant and no a.c. component would be generated until the rear end of the fibre entered the probe, thereby reducing the d.c. value. Thus, two frequency bursts are to be expected, spanned by a constant d.c. level signal.

7.3 Signal Strength and Visibility

The unprocessed frequency burst, as shown on an oscilloscope, consists of both a.c. and d.c. components and its appearance depends upon the particle trajectory through the beam intersection region. A typical signal trace from a single particle is sketched in fig. 7.4a. Two important characteristics of the signal are signal strength and signal

quality or visibility. The signal strength is the a.c. amplitude, $I_{\max} - I_{\min}$, and the signal visibility is the ratio $\frac{I_{\max} - I_{\min}}{I_{\max} + I_{\min}}$, which can be shown to be the ratio of the a.c. component to twice the d.c. component. These two quantities affect the anemometer signal-to-noise ratio and should, therefore, be high [94].

Farmer, [95], using small particle scattering theory, analytically derived the visibility curve for small beam intersection angles of a spherical particle passing through or near the centre of the probe volume in fringe mode situations. To allow for non-uniform particle illumination, the mean illuminating intensity was averaged over the cross-section of the particle. The resulting visibility curve is shown in fig. 7.5. It is evident from this curve that for high signal visibilities the particle size to fringe spacing ratio, d/δ , should be small. Thus, for large particles, the fringe spacing and consequently the probe length, should also be large, resulting in a reduced number of frequency cycles and reduced spatial resolution. A visibility greater than 0.5 for a 20 micron particle would require a fringe spacing of about 28 microns according to this curve. Such a fringe spacing would result in excessive probe length and measured velocities, (for $\theta \simeq 0$), could not be referred to as local.

Barker et al [82], however, found that for particles having a diameter greater than the ΔY dimension, the curve of Farmer was not applicable. Clearly, if the laser Doppler anemometer is to be used to measure local particle velocities in gas-solid flows where the particle diameters are up to, for example, 60 microns, the relationship between fringe spacing and particle diameter must be examined. Consequently, the signal strength

and visibility of three spherical glass "Ballotini" particles of approximate diameters 13.8, 23 and 62 microns, and an irregularly shaped alumina particle with dimensions and orientation shown in fig. 7.6, were investigated. The fringe spacings were varied between 3.5 and 24 microns, using 30 cm and 60 cm focal length focussing lenses, for both differential Doppler and reference beam modes.

7.3.1 Experimental

The two arrangements used are shown in fig. 5.7, with $\theta = 0$, and fig. 5.13, but with the photomultiplier output connected to an avometer in order to determine the anode current. The particles were each mounted by electrostatic force onto clean glass slides which were fixed to a small gear wheel, this being part of the gear train previously referred to in section 7.2.1. The gear train allowed minute manual movement of the particle in the probe volume. The traverse table on which the gear train was mounted allowed the particle to be positioned at any required longitudinal selected value of $\lambda_i / 2 \sin \theta$, that is, δ , and the longitudinal centre of the probe volume was found using a 4 mm projecting lens and noting the appearance of the fringe system on a viewing screen for various longitudinal positions. The particle under examination was positioned in the probe volume so that it was in the focal plane of the projecting lens and in the centre of the fringe system. Fig. 7.7 shows a photograph of a 62 micron spherical glass particle in a 14.4 micron fringe system. The photomultiplier was located as shown in fig. 5.7, $\theta = 0$, for fringe mode operation and the high voltage supply to the photomultiplier was set to 1.3 kV. By slowly moving the selected particle across the central fringes a maximum and adjacent minimum anode current output could be found, these corresponding to I_{max} and I_{min} respectively.

A variable neutral density filter was then placed in the path of one beam and the photomultiplier positioned as shown in fig. 5.13. The neutral density filter was then adjusted to give an anode current of 40 microamps in the absence of the particle, this represented an intensity of about 1.6 % of the strong beam intensity. The anode currents representing I_{max} and I_{min} were again recorded.

7.3.2 Results and Discussion

The results are shown in figs. 7.8 to 7.16, and consist of signal strength and signal visibility curves for both differential Doppler and reference beam modes of operation. It is important to note that all the curves are for particles in the central region of the probe volume. Figs. 7.8a, b, and c show signal strength curves, $I_{max} - I_{min}$, for the 13.8, 23 and 62 micron spherical glass particles respectively in fringe mode operation. As expected, the signal strength is greater for the more powerful lens and increases with increase in particle size due to an increase in the scattering cross-section.

In the reference beam mode, the amplitude of the signal is generally smaller than in the differential Doppler mode, as shown in figs. 7.9a, b, and c. The signal strength never reduces to zero in reference beam mode, unlike that for differential Doppler mode operation, due to the ever present reference beam. Thus, the curves consist of maxima and minima as opposed to the distinct lobes of fig. 7.8. However, the positions of the maxima and minima coincide closely with the maxima and zero positions of the differential Doppler mode curves. The scatter in the results shown in fig. 7.9 is probably due to slight misalignment since the reference beam mode is sensitive to alignment accuracy.

The above curves are of qualitative value only, since the signal a.c. amplitude decreases as the particle velocity through the probe increases [89] . However, they do indicate the form of the signal strength variation with d/δ . In the case of reference beam mode operation the ratio of the intensity of the two beams can be varied continuously for optimisation of the signal, so that fig. 7.9 shows only one family of many possible curves. It can be seen from figs. 7.8 and 7.9 that, for a given intersection angle and focussing lens, there is no detrimental effect on signal strength due to the presence of large particles.

The signal visibility curves for differential Doppler mode operation are shown in figs. 7.10a, b, and c, where the maxima and zero points correspond to those of fig. 7.8. A mean line drawn through these curves, on a base of particle diameter to fringe spacing ratio, is shown in fig 7.11. This curve shows little comparison with Farmer's curve, so it is evident that a different or a number of different mechanisms govern the visibility of the signal for large particles. For this situation, scattering will be governed mainly by reflection, whereas for Farmer's curve the major contribution was by diffraction. There will thus be a transition region in which the emphasis is shared between diffraction and reflection, possibly somewhere between 5 and 10 microns.

There is negligible decrease in the peak visibility of each lobe over the range considered, which infers that good visibility values can be obtained even for small δ and large particle diameter. The choice of fringe spacing is largely irrelevant for the present application from the point of view of signal visibility since, for a polydispersed solids phase, there is no mean tendency for visibility to decrease as particle diameter increases. Thus, it can be assumed that all particles

passing through the measurement volume will register on the electronic equipment.

Similar reasoning can be applied to the curves of figs. 7.12a, b, and c, which show the signal visibility curves in the reference beam mode. The lower signal visibility is to be expected since the "fringes" in this technique are less distinct since they depend upon the ratio of the beam intensities. In addition, signals in this mode arise from coherent beating between the light scattered from particles in the probe volume, an aspect not considered in this analysis [75].

Irregularly shaped particles passing through the probe volume present a more difficult case to explain than spherical particles. An irregular three-dimensional particle may present a wide variation in its scattering cross-section by merely rotating about any axis. In pneumatic conveying situations the particles will have rotation and so their scattering cross-section will vary as they pass through the probe volume. Since the effective cross-section can also be changed by altering the fringe spacing, it becomes difficult to define an equivalent diameter for these particles in terms of laser anemometry.

The reasons outlined above have prevented a graph of signal strength or signal visibility against d/δ from being obtained for irregularly shaped particles. Although only one particle was considered, it was considered reasonable to assume that similar signal visibility curves would be obtained for all such particles.

Fig. 7.13 shows the relationship between signal strength and fringe spacing in fringe mode operation for the irregularly shaped particle and the corresponding visibility curve is shown in fig. 7.14. As in the case of the spherical particle for this mode, the curve consists of a series of lobes, the peak value of which may not vary over a wider range of effective particle diameters than was considered in

these experiments. If it can be assumed that similar curves result from all large irregularly shaped particles, then the electronic equipment will accept signals from these particles, irrespective of their size. This reasoning can also be applied to figs. 7.15 and 7.16, for reference beam mode operation.

Table 7.1.

Wire Diameter d(microns)	$\frac{d}{\Delta Z}$ %	Experimental ΔZ (mm)	% difference from 5.88mm
5	.085	5.93	.842
12.7	.216	5.95	1.19
15.24	.259	6.15	4.59
20.32	.345	6.30	7.14
22.86	.389	6.10	3.74
35	.555	6.30	4.59
50	.850	6.20	5.44
55	.935	6.22	5.51
70	1.19	6.50	10.55
91	1.55	6.70	13.95
100	1.70	6.82	16.00
117	1.99	6.50	10.55
312	5.31	6.30	7.14

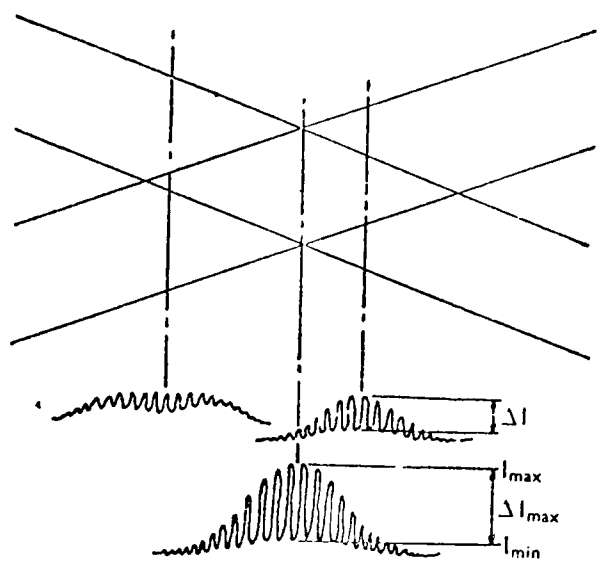


Fig. 7.1. Signal form variation with Z-position

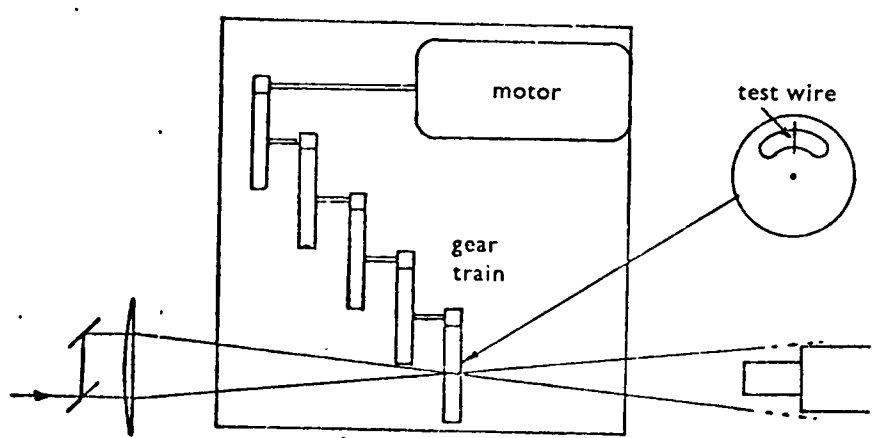


Fig. 7.2. Probe length experiments

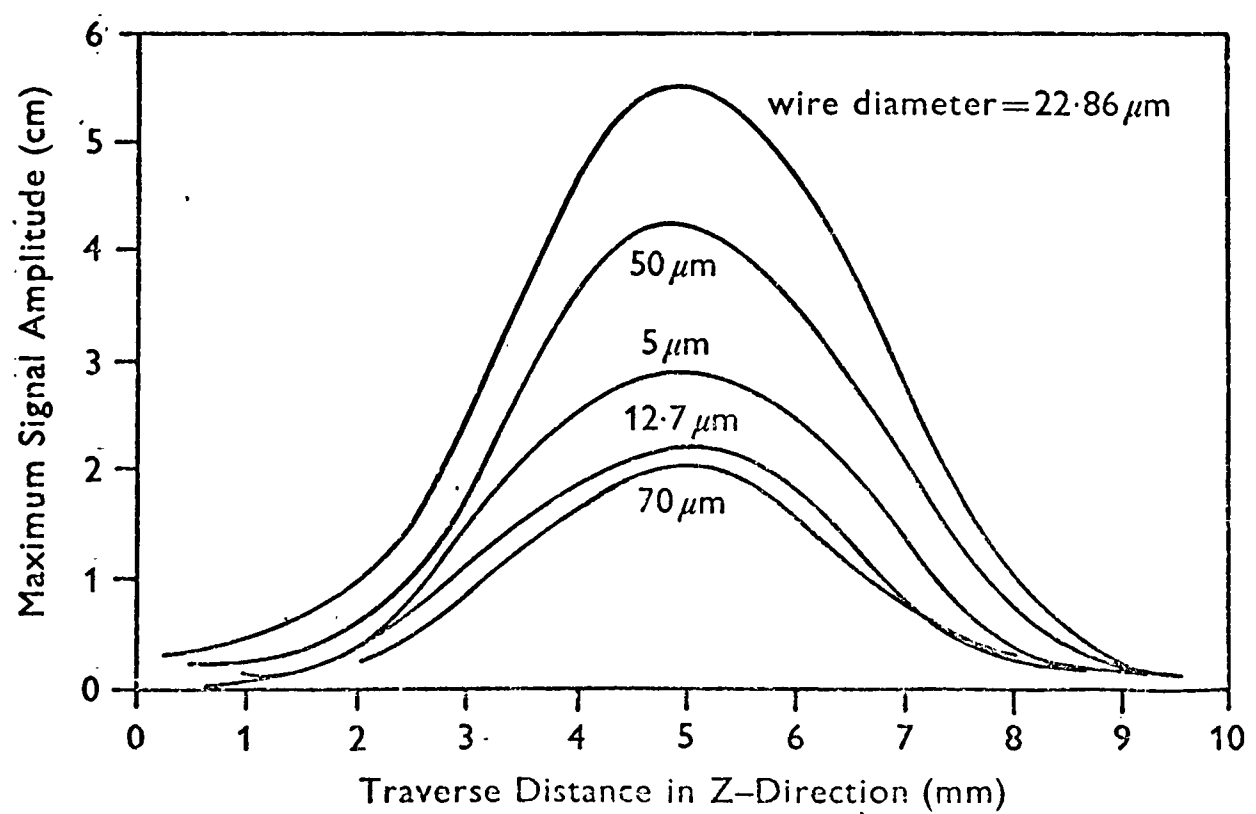


Fig. 7.3. Probe length analysis

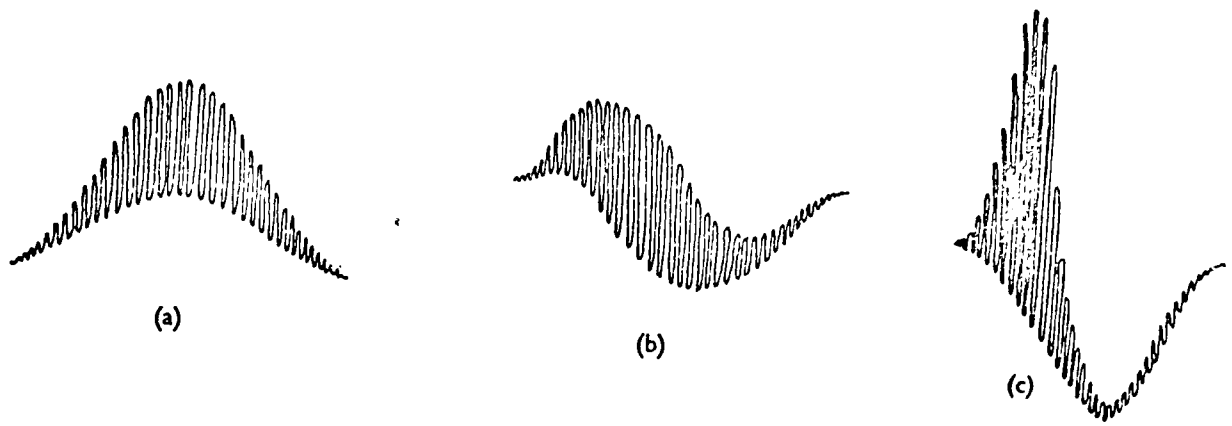


Fig.7.4. Effect of wire diameter on signal forms. (a) Typical fringe mode signal; (b) reference-beam mode signal for $d=50\mu\text{m}$; (c) reference-beam mode signal for $d=312\mu\text{m}$

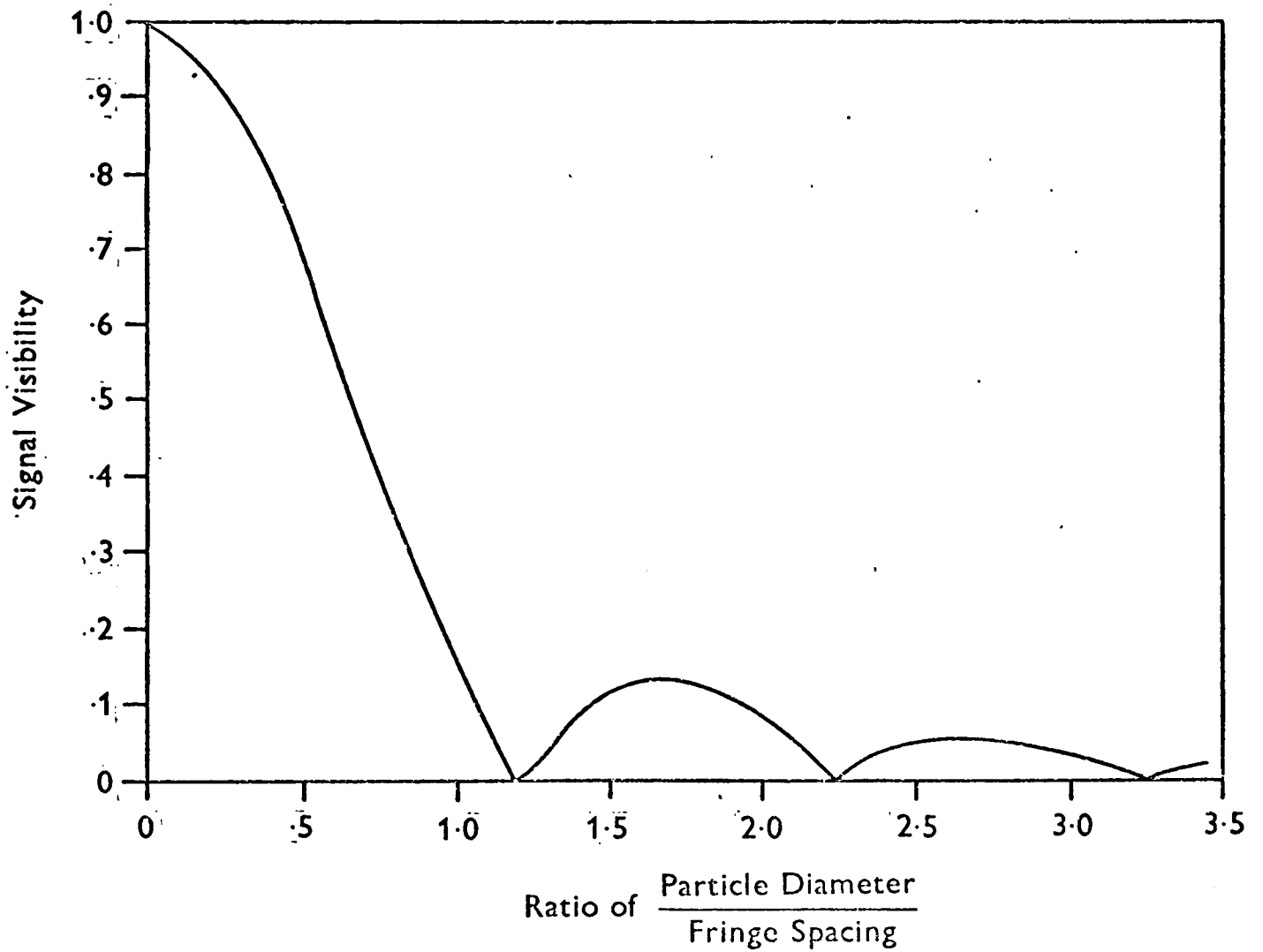


Fig.7.5. Signal visibility curve from reference [95]

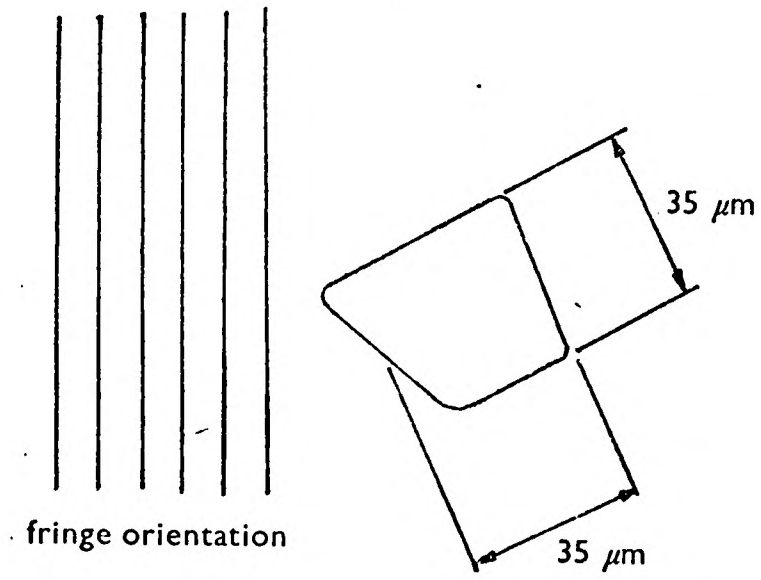


Fig. 7.6. Irregular particle dimensions and orientation

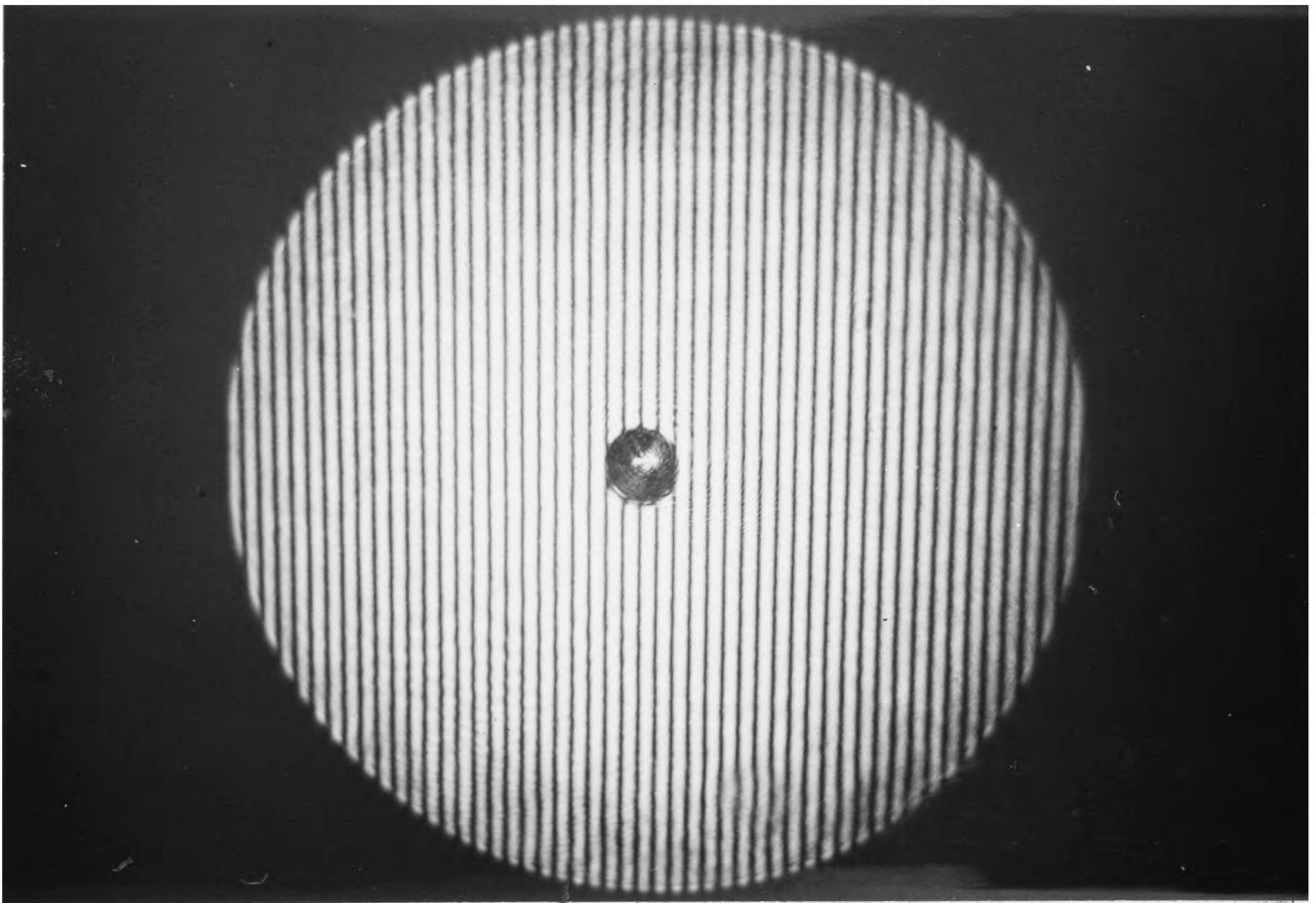


Fig. 7.7. 62 μm particle in 14.4 μm fringe system

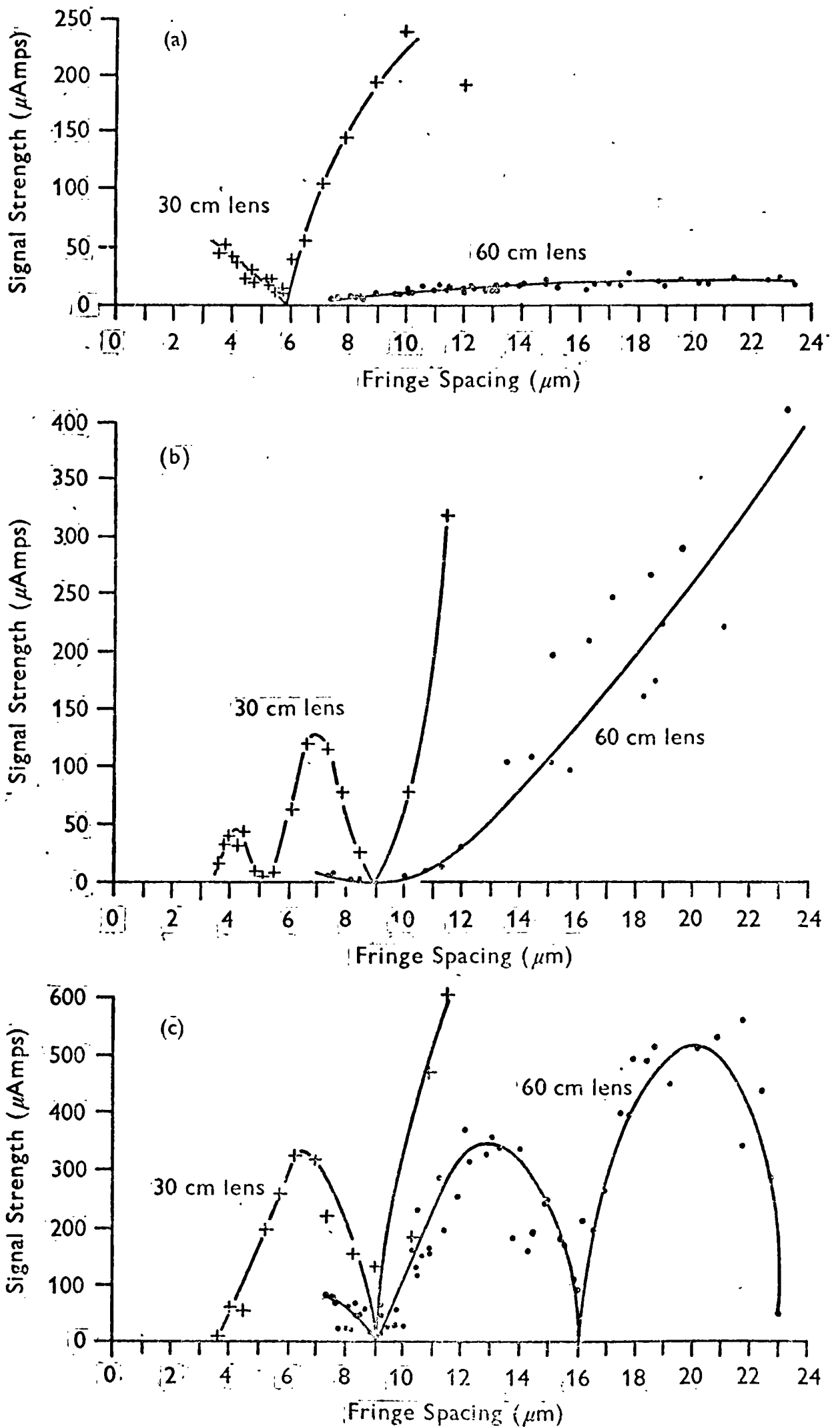


Fig. 7.8. Signal strength curves for spherical glass particles in fringe mode. (a) $d=13.8\mu\text{m}$; (b) $d=23\mu\text{m}$; (c) $d=62\mu\text{m}$.

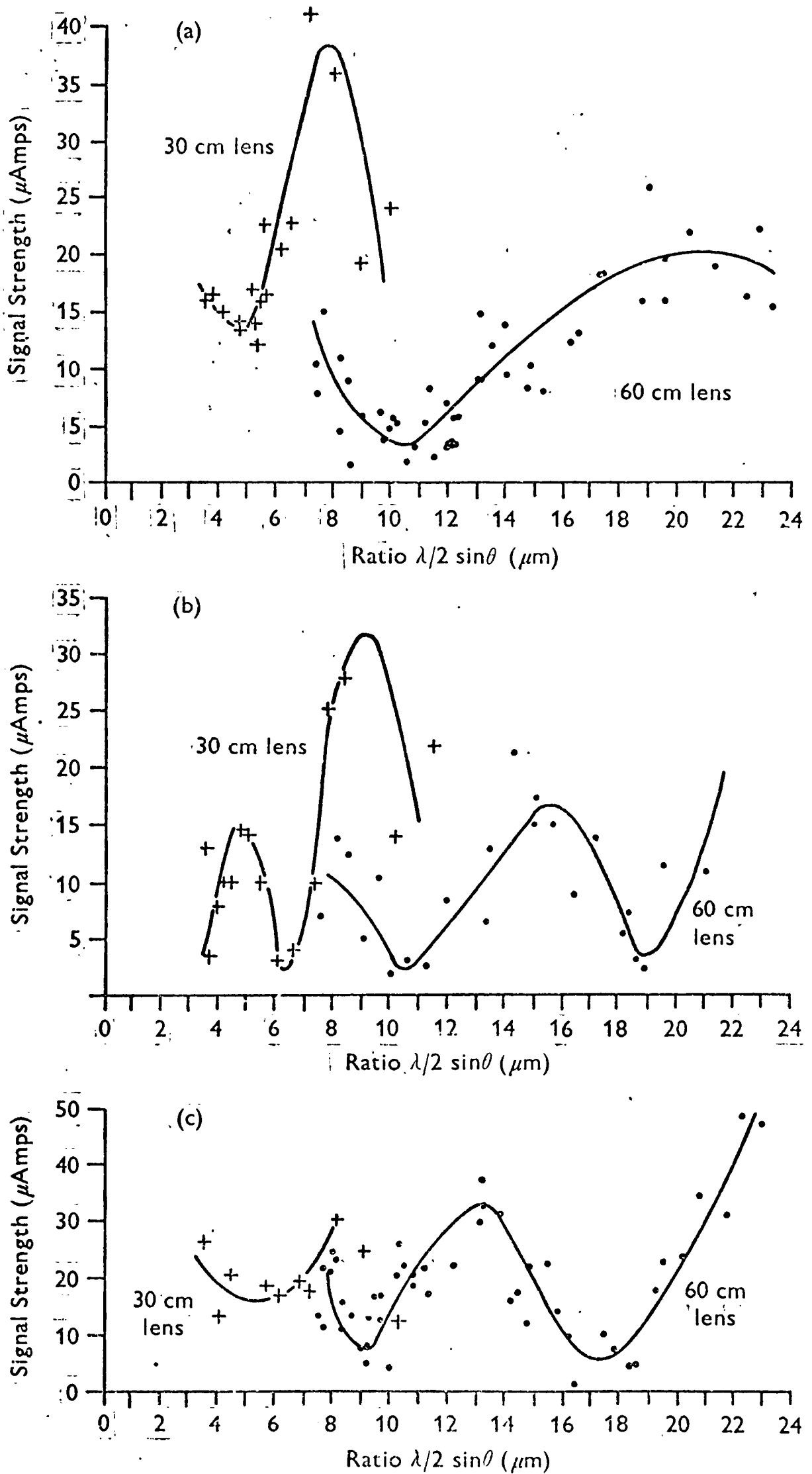


Fig.7.9. Signal strength curves for spherical glass particles in reference beam mode. (a) $d=13.8 \mu\text{m}$; (b) $d=23 \mu\text{m}$; (c) $d=62 \mu\text{m}$.

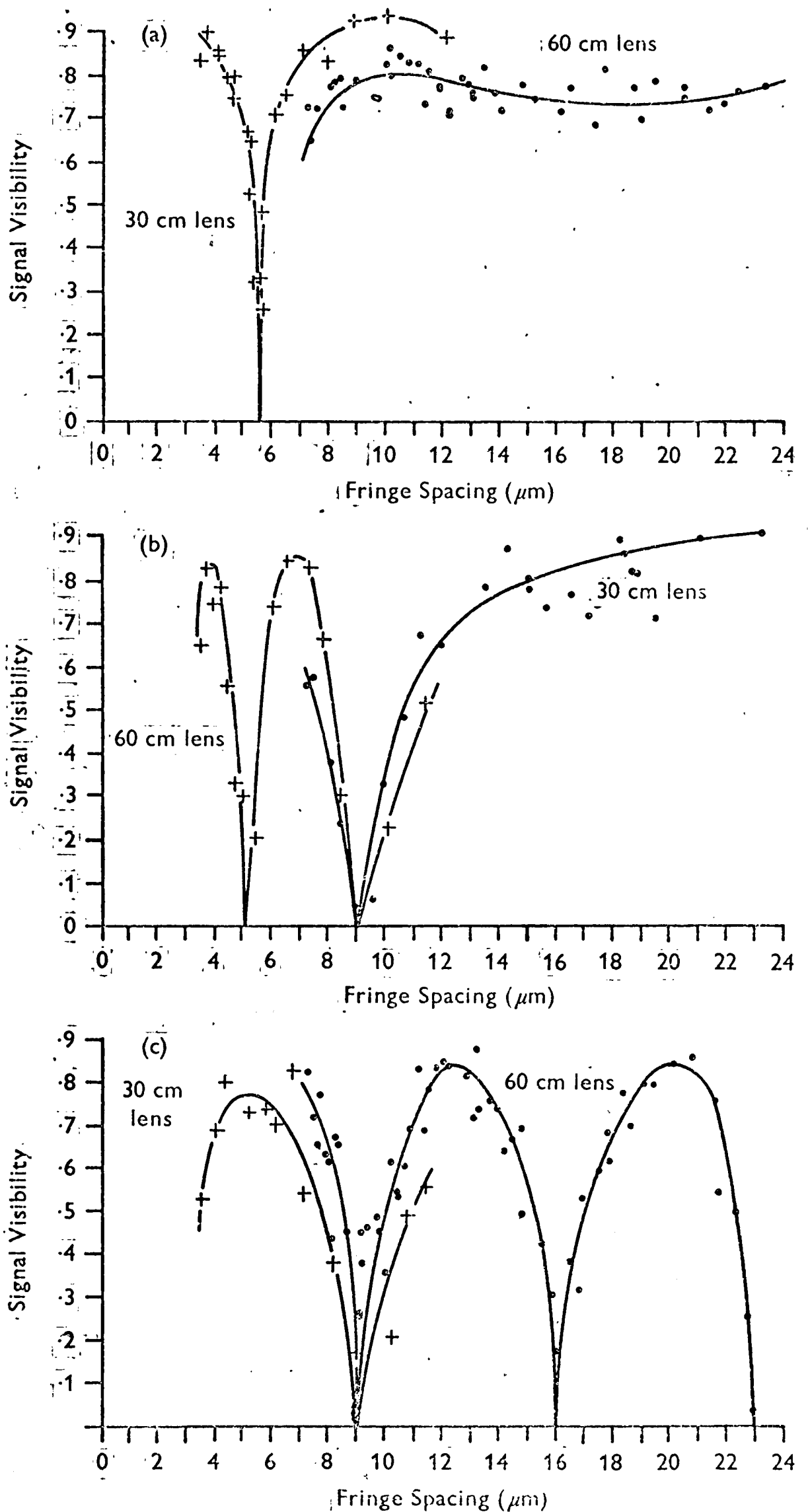
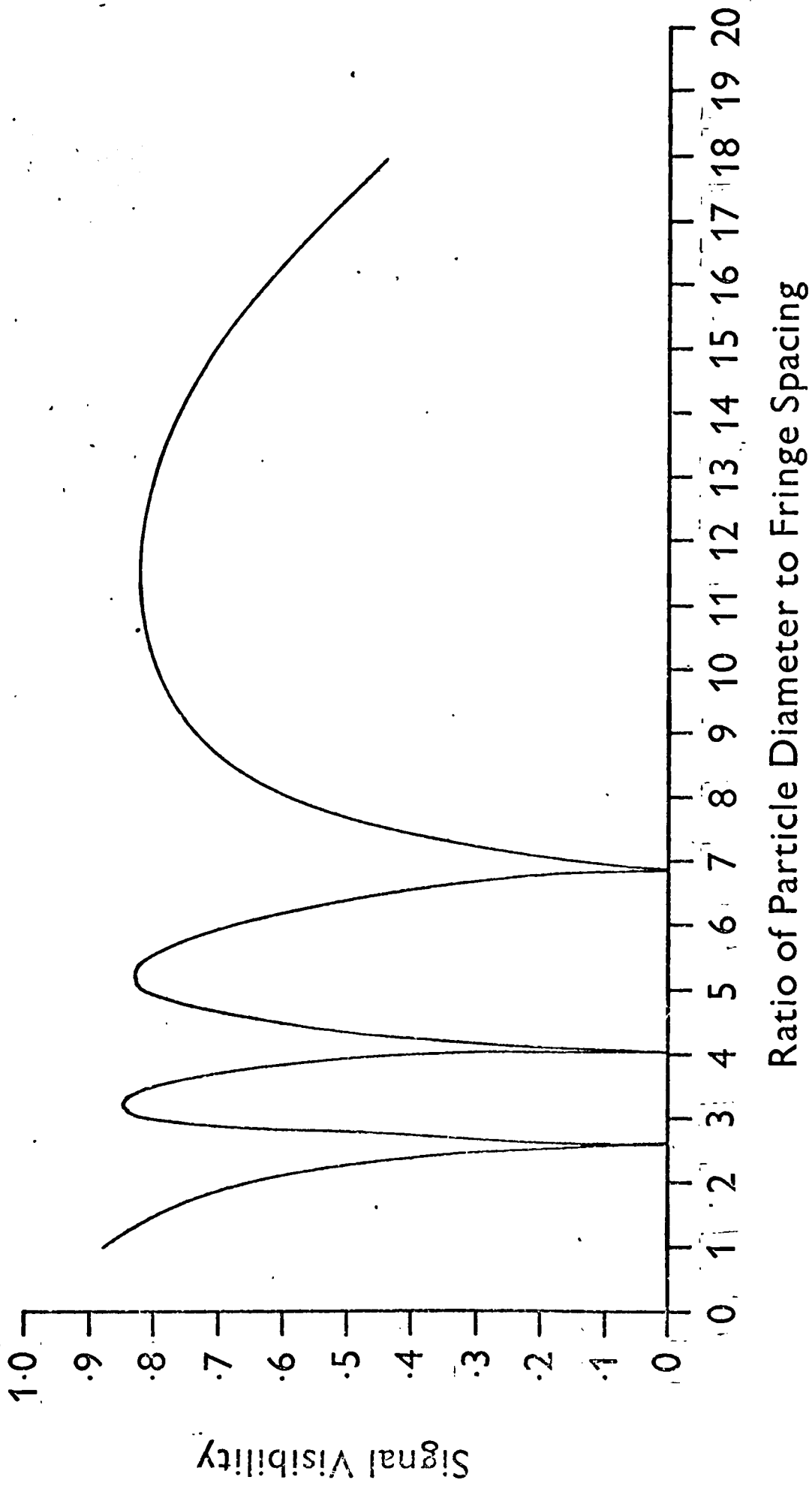


Fig. 7.10. Signal visibility curves for spherical glass particles in fringe mode. (a) $d=13.8\mu\text{m}$: (b) $d=23\mu\text{m}$: (c) $d=62\mu\text{m}$.



Ratio of Particle Diameter to Fringe Spacing

Fig.7.II. Mean experimental signal visibility curve for spherical glass particles in fringe mode.

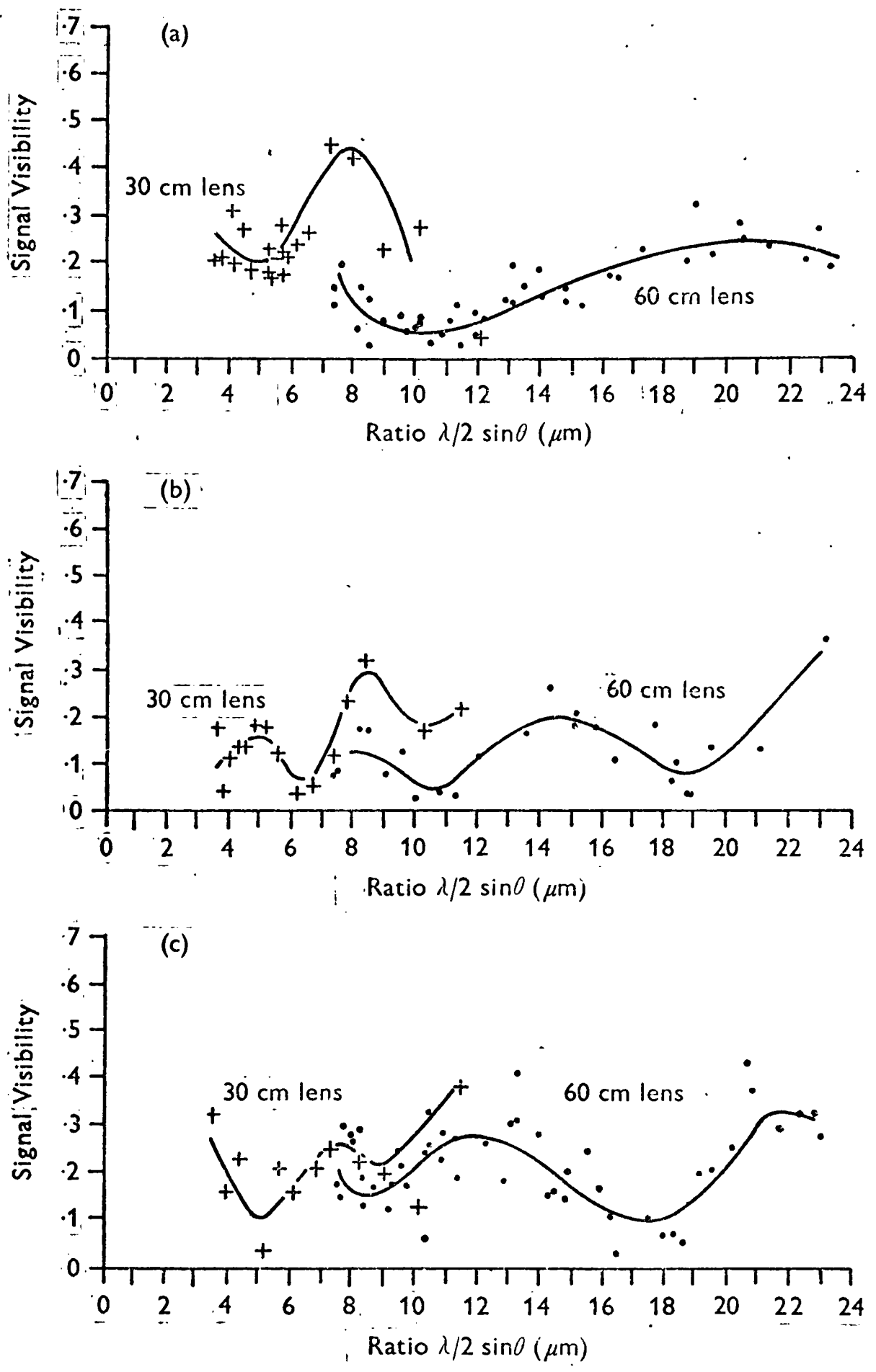


Fig. 7.12. Signal visibility curves for spherical glass particles in reference beam mode. (a) $d = 13.8 \mu\text{m}$; (b) $d = 23 \mu\text{m}$; (c) $d = 62 \mu\text{m}$.

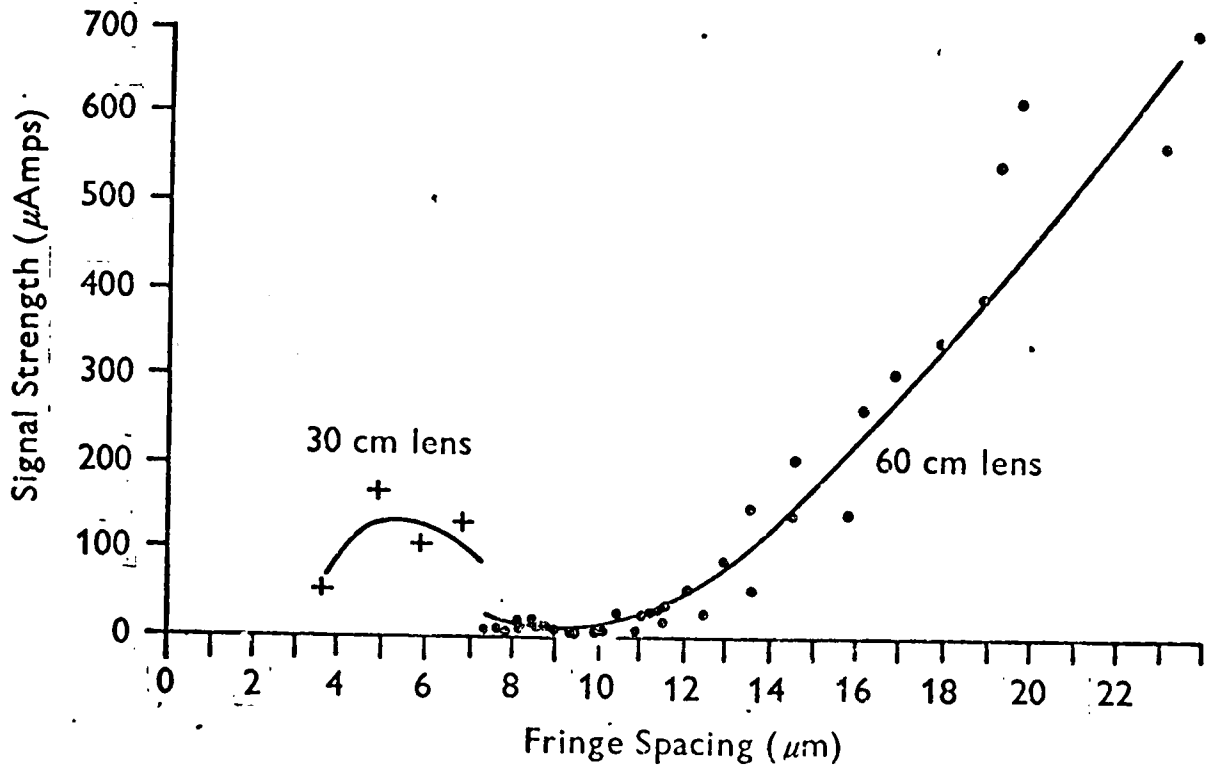


Fig. 7.13. Signal strength curves for irregular alumina particle in fringe mode.

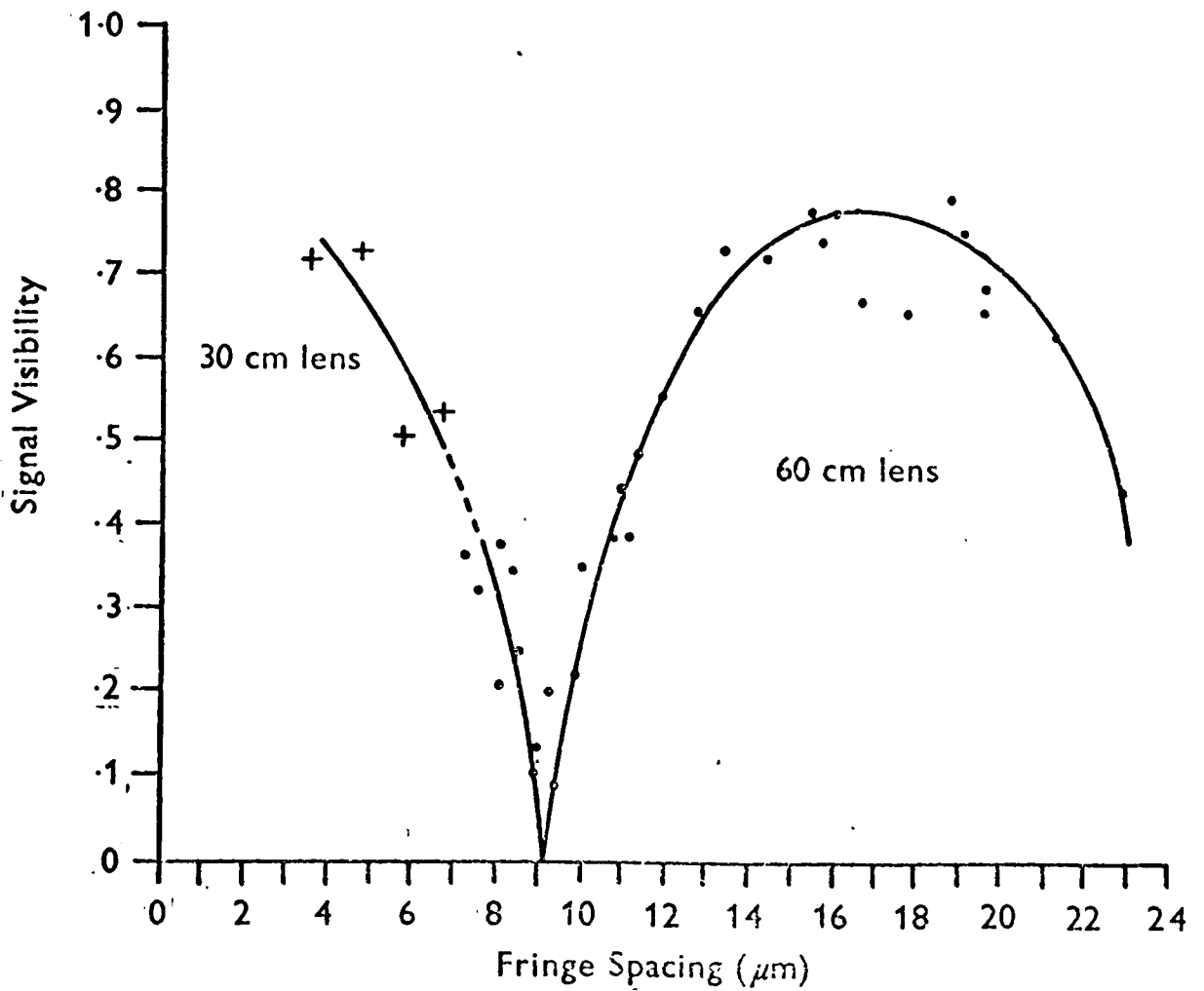


Fig. 7.14. Signal visibility curves for irregular alumina particle in fringe mode

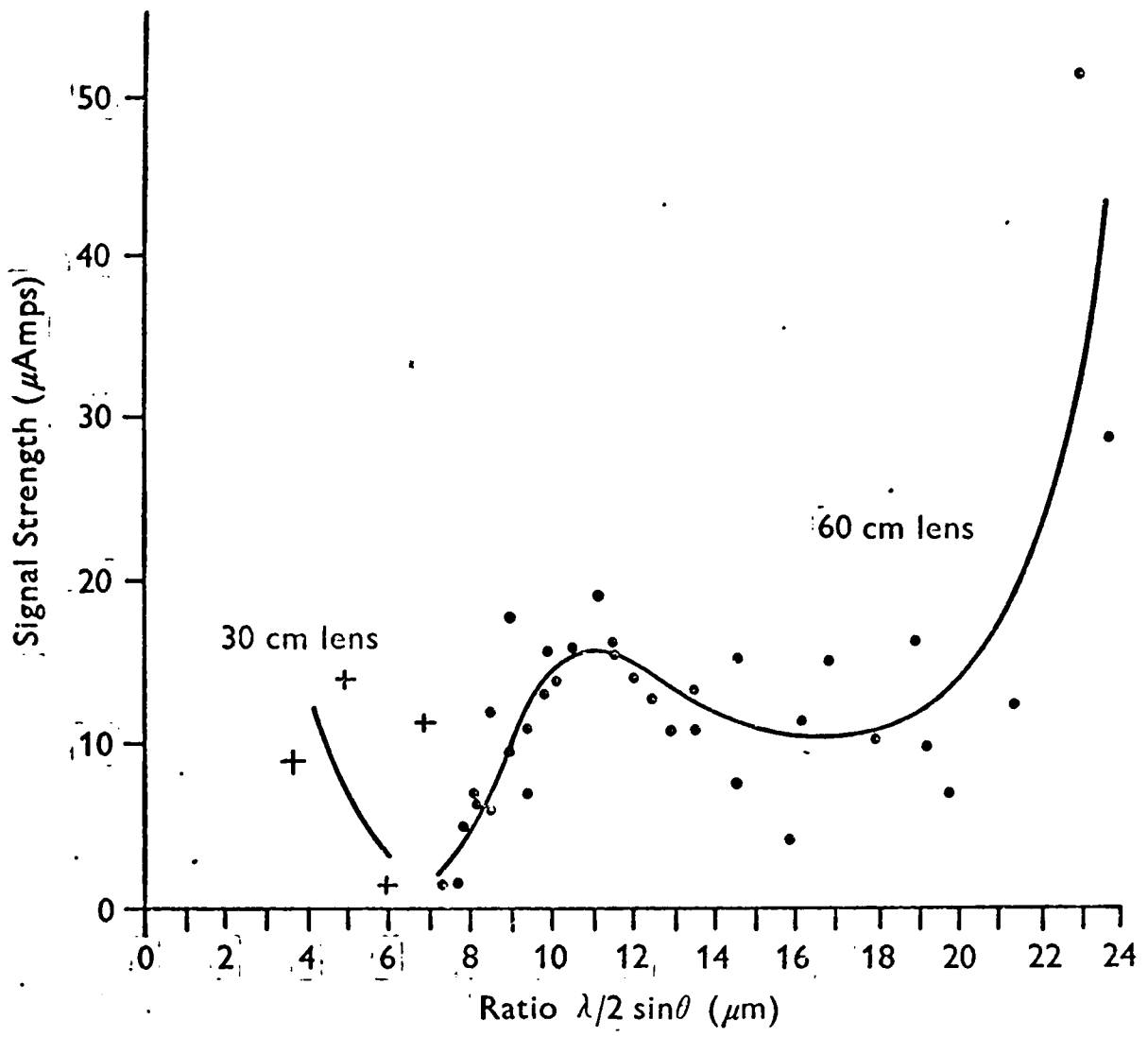


Fig. 7.15. Signal strength curves for irregular particle in reference beam mode.

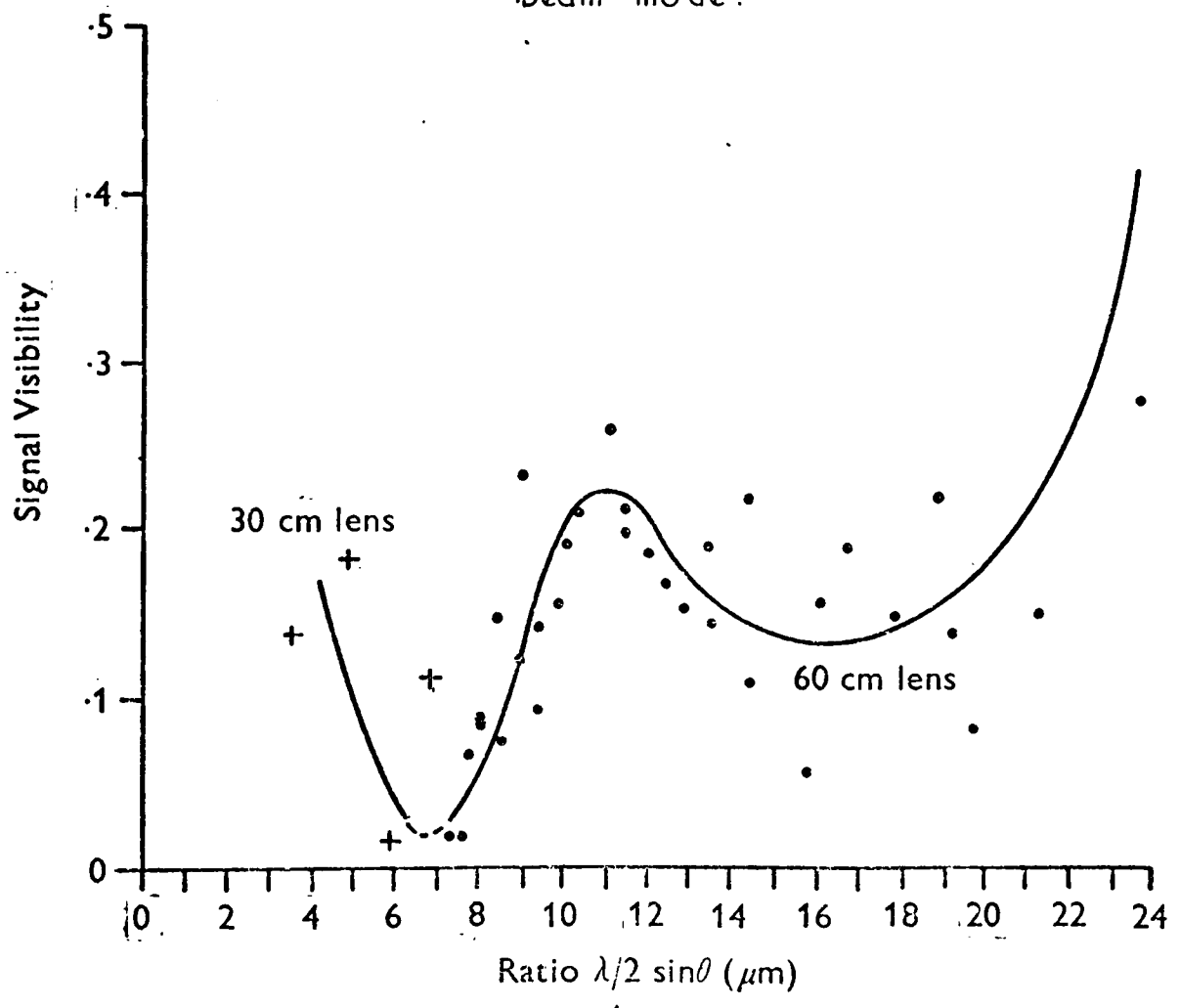


Fig. 7.16. Signal visibility curves for irregular particle in reference beam mode.

CHAPTER 8

LOCAL PARTICLE VELOCITY AND AXIAL
TURBULENCE INTENSITY MEASUREMENTS

8.1 Introduction

The experimental determination of local particle velocities and turbulence intensities in a two phase flow is needed to understand the flow behaviour of such flows, since a rigorous theoretical explanation still eludes us. Solids velocity is normally associated with pressure loss equations [96, 97] since the transfer of energy from the air stream to the particles takes place as a result of the drag force arising from the particle slip velocity. Also, where the conveyed material is abrasive, an estimate of bend and duct wear rates may be predicted more satisfactorily if the particle velocities are known [98] and knowledge of particle velocity may help in the design of plant which will minimise particle degradation.

The scarcity of published information on local particle velocity measurement has been due to the lack of availability of suitable measurement systems. The conventional methods of velocity measurement, such as hot wire anemometry and pitot probes, are not generally suitable since the former suffers from calibration changes due to particle impact, whilst the pitot tube becomes blocked. The insertion of a probe into a hostile environment, such as when the conveyed solids are abrasive, produces rapid erosion of the probe, which must necessarily be robust and thus causes flow disruption.

8.2 Literature Survey

Amongst the researchers who have investigated local particle velocity, van Zoonen [99] used a Prandtl tube for his measurements, in which the orifices were kept clear of the solid catalyst phase by blowing air through them. It was assumed that the pressure differential between the stagnation and static sides of the tube was caused by the solids

phase velocity head, since the gas velocity head was small by comparison. Calculation of the particle velocity required measurement of the local particle dispersed density and this was obtained using a capacitometer. The author found that the resulting particle velocity profile approached a parabolic shape for the 20 to 150 micron particles flowing through the 5 cm diameter riser and he reasoned that the slip between the two phases could not be very much higher than the free fall or settling velocity of a particle in air. This statement is questionable in the light of the present work and of the work of Carlson [84] since the free fall velocity would only be about 0.3 m/s for these particles, whereas far greater slip velocities have been observed.

A method of particle velocity determination which has been used [100, 101] is to measure the local particle dispersed density, ρ_{dp} , and the local mass flux, $\rho_{dp} U_p$, from which the particle velocity may be deduced. Soo et al [100] used a fibre optic local density probe and an electrostatic mass flux probe for measurements in a 5 inch diameter horizontal brass tube through which 50 micron glass particles and 35 micron magnesia particles were transported. Spatial resolution was not good since the measurements were taken over a distance of 0.125 inches and, in order to find the local mass flux, it was necessary to know the particle velocity at some position. A previous theoretical study [102], unsubstantiated by experimentation, had shown that the particle and gas velocities were approximately equal at the pipe centre line. This relationship was used to find the mass flux distribution. The authors found that the resulting particle velocity profile obeyed the approximation:

$$\frac{U_p - U_{pw}}{U_{p0} - U_{pw}} = \left[\frac{y}{R} \right]^{1/m} \quad (8.1)$$

where the subscripts o and w referred to the pipe centre line and wall respectively. The index m varied between 0.81 and 1.504, depending upon the conveyed material and upon the solids loading ratio. The loading ratios considered were from 0.249 to 8.13, whilst the air velocity was kept fairly constant at around 128 to 138 ft/s.

Peskin and Dwyer [101] used fibre optic probes for the measurement of both local particle mass flux and local dispersed phase density in a horizontal 3" x 3" duct through which 80 micron glass spheres were conveyed. The mass flux probe utilised a detection gap of 0.011 inches, improving on the spatial resolution of Soo et al, whilst the dispersed phase density probe was similar to that of Soo et al. From particle inertia considerations it was suggested that the probes did not disturb the particle flow. Loading ratios up to 3 were investigated, whilst the superficial air velocity was 102 ft/s. In order to evaluate particle velocity from the two measurements, it was necessary to assume equal velocity of the phases at the flow centre line, following the example of Soo et al. It is pertinent to note that, if this assumption is incorrect, then a slip velocity of 9 ft/s at a solids loading ratio of 2, as found by Peskin and Dwyer, would be increased by an amount dependent upon the core slip velocity.

Air velocity profiles in the presence of particles were measured by the authors with small pitot tubes and they found that these profiles were identical to those obtained for clean gas flow. This was accounted for by the small particle size and large distance between centres.

The importance of measuring particle velocity directly was realised by

Eichhorn, Shanny and Navon [103], who used two fibre optic probes and timed the flight of particles between them. The fibres were spaced 0.2 inches apart and the gap between transmitters and receivers was 1/32 inches. The probes were located in an aerofoil section which spanned the 3 inch diameter horizontal pipe. It was found that, with 200 micron glass particles being conveyed by an air flow having a superficial air velocity of 170 ft/s, the particle velocity profile was reasonably flat and the mean slip velocity was about 70 ft/s for a loading ratio of 0.35. The technique allowed particle turbulence intensity to be measured and this was found to be about 30% with little variation across the pipe diameter. Number flux was also determined.

The above methods of particle velocity measurement all require the insertion of some kind of probe into the flow stream and the methods of Soo et al and Peskin and Dwyer require calibration and the use of unsubstantiated assumptions. Photographic techniques, however, cause no flow disturbance and, provided that the time between film sequences is known, do not require calibration. Although photographic techniques have been applied to the measurement of particle velocities in rocket exhausts [104] and for application of liquid droplets in air streams [105, 106], only gas-solid pipe flow measurements will be considered here.

McCarthy and Olson [107] used a two flash photographic technique to measure the particle velocities of 65 micron glass and sub-20 micron calcium carbonate particles flowing through a one inch bore pipe. The depth of view of the camera was less than 1/16". Only three radial positions were considered (radius = 0, 0.25" and 0.4") and loading ratios were all less than 0.2. It was found that the velocity in the core of the flow was approximately constant with the radius, there being

only a 10 to 15% deviation from the average particle velocity. The mean solids velocity was calculated from a summation of the 'standard' drags on individual particles and this correlated well with the experimental results. This approach was reasonable in view of the very lean phase flow.

Sterephotogrammetry was used for the velocity measurement of 200 micron diameter spherical glass particles passing up a 10 cm vertical pipe by Reddy, van Wijk and Pei [108]. Two photographs were taken simultaneously from two different camera stations, to give three-dimensional information about the particle flow. Co-ordinates for particle positions had to be computed and the field of view of the camera was from the flow centre to the far pipe wall. The results obtained were compared with those found using a double flash technique for a loading ratio of 0.02 and an air Reynolds' number of 55,000. The particle axial velocity profiles were represented by the law -

$$U_p = U_{p0} \left[\frac{y}{R} \right]^{1/p} \quad (8.2)$$

where $p = 7$, which has little physical meaning since it implies zero particle wall velocity. The average lateral and transverse particle turbulence intensities were found to be about 0.22 m/s, whilst the average axial turbulence intensity was found to be 0.545 m/s from the stereophotogrammetry results. Unfortunately, no turbulence intensity radial profiles were reported.

Reddy and Pei [109] modified Soo's expression, equation (8.1) to account for the finite particle diameter, d , as follows :-

$$\frac{U_p - U_{Rw}}{U_{p0} - U_{Rw}} = \left[\frac{y - \frac{d}{2}}{R - \frac{d}{2}} \right]^{1/m} \quad (8.3)$$

and estimated the "wall" velocity, that is, where $y = d/2$, from :

$$U_{p_w} = U_{p_o} \left[\frac{d}{2R} \right]^{1/p} \quad (8.4)$$

where p was obtained by fitting the experimental velocity profile data to equation (8.2). This procedure seems questionable and would result in a lower value of U_{p_w} than is required for equation (8.3). p was found to lie within $\pm 10\%$ of 7 and this led the authors to believe that m could be expressed solely as a function of $d/2R$. The slip velocity at the centre of the pipe was correlated in terms of the particle terminal velocity and the solids loading ratio.

Chandok and Pei [110] used a three flash photographic technique for their measurements and this provided a clear definition of individual particles so that loading ratios up to 3 could be investigated. Spherical glass particles having mean diameters ranging from 150 to 500 microns were transported through a 10 cm bore vertical pipe at Reynolds' numbers from 58,000 to 100,000. The authors correlated their data using equation (8.2) and found that the value of the index, p , varied from 9 to 32, in comparison with Reddy and Pei's 7. The particle velocity data were also correlated by equation (8.3) and the index, m , showed no significant variation with loading ratio, but was dependent upon the Reynolds' number. Turbulence information was obtained which showed some agreement with the results of Reddy and Pei in that the axial turbulence intensity was greater than the radial components and all intensities were less than the air turbulence components. There was found to be little variation in particle turbulence with radius.

Jotaki and Tomita [111] used slow motion pictures of high speed film marked with a timer at 1/120 second intervals and between 2000 and

6000 scenes per second were filmed. Unfortunately, comparison of their work with the present study is not valid on account of Jotaki and Tominta having used millimetre size particles.

Kramer and Depew [112] found that the streaking method of particle filming, although it gave consistent results, was time consuming and so they used an optical cross-correlation technique for vertical particle velocity measurements. This involved determining the time delay between two photomultipliers, of particle images, using a correlation function computer. Pipe sizes of 0.5, 0.75 and 1 inch, and particle sizes of 62 and 200 microns at Reynolds' numbers between 5,670 and 50,000 were investigated for solid loading ratios up to 5. It was found that the solids loading ratio did not have a significant effect on the slip velocity but, as expected, was greater for the larger particles. The slip velocity across the pipe diameter was variable and could be negative at the wall. The results of these experiments were compared with values obtained from a continuum analysis, but the correlation was not satisfactory. This was attributed to the particle dispersed density being non-uniform and error in the assumed logarithmic air velocity profile near the tube centre.

Kane [113] and Kane, Weinbaum and Pfeffer [114] used the double streak technique to measure the velocity of 10 to 60 micron diameter glass beads flowing through a 2.21 cm diameter vertical pipe at Reynolds' numbers between 12,000 and 25,000 and for loading ratios between 0 and 4. They suggested that the particles had the effect of thickening the air viscous sublayer in an attempt to explain the resulting drag reduction. Their measurements showed that the particles followed the mean velocity profile of the gas fairly closely, except near

the wall where there was negative particle slip. They used equation (8.4) to evaluate particle wall velocities.

Other studies which have been concerned with the measurement of local particle velocity and turbulence intensity have used the laser anemometer and were reviewed in section 5.2.

It is evident from the above literature survey that there is much to be resolved concerning the motion of suspended particles in pipe flow and that there is wide disagreement between some authors. It is difficult to evaluate how much of the disagreement can be attributed to the measurement techniques since the flow situations with regard to particle size distribution, pipe diameter, solids loading ratio, air Reynolds' number and so on have been so diverse. However, many of the measurement techniques reviewed suffer from obvious shortcomings and it is hoped that the laser anemometer, which has good spatial resolution, does not disturb the flow, requires no calibration and is capable of producing a continuous and instantaneous particle velocity output, will provide a useful and versatile local velocity and turbulence intensity measuring instrument for a range of solids loading ratios.

8.3 Particle Velocity Profiles, $\emptyset = 0$

The particle velocity profiles measured in this part of the investigation were obtained using two main procedures. In section 8.3, measurements which utilised both reference beam and differential Doppler mode operation, variable beam intersection angle and the photomultiplier aligned with the anemometer optical axis are described, ($\emptyset = 0$, see fig. 5.7), whilst in section 8.4 the angle of observation was set to 45° and velocity profiles and turbulence intensities were measured in fringe mode operation only.

8.3.1 Experimental Procedure for Local Particle Velocity Measurement

The velocity profiles measured here used a 130 mm focal length focussing lens and typically $\theta = 4^\circ$, so that :

$$\Delta Y \approx \Delta X = 0.161 \text{ mm}$$

$$\Delta Z = 2.31 \text{ mm}$$

Particle velocity profiles were obtained for seven sets of air velocity, each set involving four or five solids loading ratios. At the lowest velocity, both reference beam mode and differential Doppler mode arrangements were used. However, since no obvious advantage became apparent in the use of either mode, the differential Doppler mode was used in all subsequent tests because of its relative ease of setting up. Local particle velocity measurements were made at 2 mm intervals across the test section diameter and the air mass flow rate and air temperature were frequently recorded.

8.3.2 Results and Discussion

The particle velocity profiles obtained are shown in fig. 8.1 and give the mean profile over both halves of the test section diameter. Although wall particle velocities were estimated by extrapolating the profile, it was possible to obtain particle velocity measurements close to the tube wall. In some cases the measurement position was about 0.03 cm from the wall, so that the measured profile covered 95% of the test section diameter. For each set of results the variation in superficial air velocity, with respect to solids loading ratio, was at the worst 5.6%. The profiles were obtained for solids loading ratios up to 1.434 in the lower velocity range, whilst for the highest air velocity the maximum solids loading ratio was 0.726. This reduction in solids loading with increase in superficial air velocity was expected since fast moving

particles scatter fewer light photons than slow ones, thus reducing the amount of information being received by the collecting optics. A more powerful laser would increase the solids loading penetration of the anemometer. The measuring limitation on solids loading at the higher ratios is partly due to the frequency tracking unit, since a frequency trace, indistinct though it was, was still visible on the filtered oscilloscope display at higher solids loadings. Spectrum analysis, which is sometimes useful under conditions where there are few scattering particles, resulting in intermittant signals, could prove useful for "high" solids loading ratios.

The simple power law expression, equation (8.2) cannot realistically be used to correlate the particle velocity profile results, since it implies zero velocity at the tube wall. To take account of the finite wall velocity, Soo [100] suggested the form:

$$\frac{[U_p - U_{p_w}]}{[U_{p_0} - U_{p_w}]} = \left[\frac{y}{R} \right]^{1/m} \quad (8.1)$$

whilst Reddy and Pei [109] realising that the boundary condition "at" the wall actually occurs at $y = d/2$ for particles having diameters of 100 to 270 microns, used the correlation:-

$$\frac{[U_p - U_{p_w}]}{[U_{p_0} - U_{p_w}]} = \left[\frac{y - d/2}{R - d/2} \right] \quad (8.3)$$

For the particles used in this study, however, the error in using equation (8.1) for correlation purposes is negligible, ($d/2 < 0.16\%R$). Logarithmic plots of equation (8.1) did not result in straight lines, see figs 8.2a and b, which respectively portray the conditions for the lowest and highest conveying air velocities. However, linearity does improve with increase

in superficial air velocity, except near the wall where the particle velocity reduces rapidly. The reasons for the difference between the results shown in figs. 8.2a and b and the linear approximation obtained by Soo [100] are difficult to establish. In the present section no account of electrostatic effects has been taken and this was originally thought to contribute to the lower wall velocity compared with an earthed system. Section 8.4 investigated this possibility. In most cases, however, the deviation from linearity occurs well into the core of the flow where electrostatic effects are relatively unimportant. In Soo's investigation an electrostatic ball probe having a 1/8 inch diameter face perpendicular to the flow was used, causing possible flow disturbance and preventing measurements as close to the pipe wall as have been achieved here.

Fig. 8.1 shows a flattening of the particle velocity profile with increase in solids loading due to the particles in the core of the flow being influenced more than the particles away from the axis by the solids loading. That is, the dispersed phase density in the core of the flow probably increases with loading ratio more rapidly than it does near the pipe walls. This flattening is clearly illustrated in fig. 8.3. It was possible to take measurements in flows having higher solids loading ratios by sacrificing spatial resolution. The results shown in fig. 8.4 confirm that the flattening trend continues at higher loading ratios. The plots of fig. 8.4 are not true profiles and used a

ΔZ of 13.9 mm, but they do display the flattening effect and show that care must be taken when choosing the probe length for situations where

$\theta = 0$. A plot of

$$\frac{U_p - U_{pw}}{U_{p0} - U_{pw}} \text{ vs } \frac{y}{R}$$

for approximately constant solids loading ratio and various superficial

air velocities suggested that the velocity profile remains stable with respect to superficial air velocity. This agrees with the work of Kramer and Depew [112] who used 62 micron and 200 micron particles, for loading ratios from 1 to 5. Flattening of the particle velocity profile was noted by Chandok and Pei [110] for 150 to 500 micron particles and loading ratios up to 3.

Throughout this work it was assumed that the air velocity profile was unaffected by the presence of the solid particles. There is some rather limited experimental justification for this assumption [110, 109, 100, 101] but further work is necessary. If the air mass flow rate is known, then the form of the air velocity profile can be computed using a power law expression with a suitable index [48]. Comparison between the assumed air velocity profile and the corresponding particle velocity profile reveals the extent of interaction between the two phases.

Seven air and particle velocity profiles are shown in figs. 8.5a to g, these being for similar loading ratios and are fairly representative of their sets. For the lowest superficial air velocity, fig. 8.5a, the air profile exceeds the particle velocity profile in the central region of the flow. The reverse applies for values of Y generally less than 1.0 to 1.5 cm, this value depending upon the loading ratio. Thus, the particle velocity normally exceeds the air velocity for $1.5 > Y > 0.1$ cm. For $Y < 0.1$ cm, the air profile is greater than the particle velocity until very close to the wall, when the air profile decreases to zero under the normal "non-slip" conditions, whilst the particle velocity remains finite, producing negative slip at the wall. The negative slip condition arises because of the radially outward

movement of relatively high velocity particles from the core of the flow. Fig. 8.5a is similar to fig 8 in [114]. For higher solids loadings, just prior to "choking" the particle velocity at the wall may reduce to zero and particle flow reversal can occur, giving positive slip at the wall (see chapter 10).

The results in fig. 8.5b show no profile interaction until $0.6 \text{ cm} > Y > 0.05 \text{ cm}$, the value of Y decreasing with increasing solids loading. For higher superficial air velocities, figs. 8.5c to g, the two profiles only meet in the vicinity of the pipe wall. The profile interaction point moves nearer to the wall as the superficial air velocity increases and the solids loading increases. Along the axis of the pipe, the slip velocity increased with solids loading, as found by Chandok and Pei [110]. It is interesting to note from figs. 8.5a to g that conditions of zero slip at the core and an unaffected air velocity profile as stated in refs. [100, 101] cannot both hold. Indeed the condition of zero core slip would require a drastic reshaping of the velocity profile in order to attain the same air flow rate. Thus, it may be concluded from the present study that either the air profile remained the same as the clean gas profile and there was substantial particle slip at the core, or there was negligible slip at the core and a dramatic change in the air profile.

The experimental data obtained in this investigation have been presented as mean slip velocities in fig. 8.6. Each set of results shows a linear increase in loading ratio, as illustrated in fig. 8.6 by "least squares" lines. The slope of these lines, ignoring the lowest velocity set of results, shows only slight variation for each air velocity. Kramer and Depew [112] found that the solids loading

ratio had little effect on slip velocity, whereas the increase in mean slip velocity with loading ratio is considered here to be significant. It is always of dubious value to compare the results of different investigations when basic parameters have been very different. However, Peskin and Dwyer [101] using 80 micron particles in 3 inch x 3 inch square section ducting in horizontal flow, found the average slip velocity to be 6.16 ft/s (= 1.88 m/s), at an air Reynolds' number of 132,000 and a loading ratio of 2. This is of the same order as the slip velocity which would be obtained (5.8 m/s) by projecting the least squares line for a superficial air velocity of 38.98 m/s (Re = 123,800) and a loading ratio of 2. It is evident that, if the no slip condition at the core assumed by Peskin and Dwyer does not hold, then the comparison would be improved. Kramer and Depew [112], found slip velocities in the region of 5 ft/s (1.53 m/s) for 62 micron particles at a solids loading ratio of unity and a Reynolds' number of 24,500

8.3.3 Confirmation that the $1/e^2$ Probe Volume has Physical Significance

In section 7.2 the effect of particle size on the ΔZ dimension of the $1/e^2$ probe volume was investigated. This work could have been carried out on the $1/e$ probe volume or some other arbitrarily defined probe volume. It is shown here that the $1/e^2$ probe length is a realistic measure of the region from which suitable signals can be generated.

The probe volumes used in sections 8.3.1 and 8.3.2 were assumed to be small enough to be ignored, so that the profiles obtained were true particle velocity profiles. However, slight correction was made close to the wall where some of the ΔZ lay outside the flow and this was carried out in an identical manner to that described for "finite" probe

lengths in section 8.3.4. The "true" profile was used to calculate the velocity profile which could be obtained for a significantly larger probe length and the resulting profile compared with experimental measurements. If the experimental measurements, utilising a $1/e^2$ ΔZ equal to the assumed value in the calculation, corresponded to the derived curve, then the $1/e^2$ probe length is justified.

8.3.4 Results and Discussion

Figs. 8.7a, b, and c, show the particle velocity profiles identified as curve 'A', for which ΔZ is assumed to be negligible. Fig. 8.7a shows the experimental values of velocity for a $1/e^2$ probe length,

ΔZ , of 1.375 cm. The spatial position of the plotted values is taken at the centre of the effective probe length. However, near the wall, part of the $1/e^2$ probe length lies outside the flow and so these experimental points are plotted to correspond with the centre of the remaining probe length. Since the probe length is finite, a spread of velocities will be encompassed by it for all but a flat velocity profile. The laser anemometer arrangement shown in fig. 5.7, with $\theta = 0$, measures the mean velocity of all particles passing through the probe volume. If velocity gradients in the ΔY direction are ignored, curve 'B' can be obtained by finding the average velocity over lengths of 1.375 cm at intervals across the profile. Thus, a probe length of 1.375 cm was decided upon without reference to the $1/e^2$ values and curve 'B' was obtained. It can be seen that when Y is greater than 1.375/2 cm there is good agreement between the deduced $\Delta Z = 1.375$ cm profile and the $1/e^2$ $\Delta Z = 1.375$ cm experimental points. Therefore, for this portion of the curve the $1/e^2$ dimension of equation (5.24) is a realistic value of the length from which suitable signals can be generated. Where part of the probe length lies outside the flow boundary, that is when $Y < 1.375/2$ cm,

the experimental points deviate from the calculated curve. Thus, although velocities in these situations may still be measured, the spatial accuracy is uncertain. It is probable that the position of the recorded velocity is dependent upon the distribution of fringes within the remaining probe length and upon the velocity gradient. Figs. 8.7b and c show similar trends to fig. 8.7a.

8.4 Particle Velocity and Axial Turbulence Intensity Profiles: $\theta = 45^\circ$

In this section measurements of local particle velocity and axial turbulence intensity are described, both for the test section being earthed and not earthed, in order to assess the effect of electrostatic charge on the flow.

8.4.1 Experimental Procedure

The glass test section was earthed through a make-or-break switch, as described in section 3.3 and the current generated by particle charge transfer under earthed conditions was collected from the top 600 mm of the test section. The amount of current was measured on a charge amplifier which was calibrated using a 'Duracell' 1.5 volt battery and various resistors. Laser anemometry measurements were taken using the fringe mode configuration shown in fig. 5.7, with the observation angle, $\theta = 45^\circ$. Under these circumstances the measurement volume can be represented by a cylinder, as described in section 5.8, and for the lens and beam intersection angle used, the cylinder had the dimensions:

$$\begin{aligned} \text{diameter, } 2b_o &= \frac{4f_1 \lambda_i}{\pi 2b} = 0.161 \text{ mm} \\ \text{length, } \frac{f_2}{f_3} d_{ph} &= 2b_w = 0.1786 \text{ mm} \end{aligned}$$

Turbulence intensity measurements were taken according to section 5.9 and equation (5.50) was used to correct the observed frequency.

Recordings were taken at 4 mm intervals in the core of the flow and

at 2 mm intervals and then 1 mm intervals as the wall was approached. Velocity and axial turbulence intensity measurements were taken first with the system unearthed. The earth contact was then made and the measurement repeated. Orifice plate differential pressure, air temperature at entry to the test section, barometric pressure and wet-and-dry bulb temperatures were taken throughout.

8.4.2 Results and Discussion

The particle velocity profiles and axial turbulence intensity profiles obtained by the above method are shown in figs. 8.2a to e. It was observed throughout this work that the velocity and turbulence intensity profiles were not noticeably affected by either earthing or unearthing the test section, so that only a single set of profiles per run was necessary. This was a surprising result, since the effect of electrostatic charge transfer has been reported to have caused an increase in pressure drop in some cases [96] so that perhaps a lowering of particle velocity in the wall region was expected. However, this was not the case, even though large "sparks" were seen to cross the gap as the earth switch was closed, indicating that substantial charge transfer was present. The charge amplifier calibration curve is shown in fig. 8.9. By considering the number of particles per unit volume of the flowing suspension, which may be shown to be :

$$N/\text{unit volume} = \frac{M_p}{M_a} \cdot \frac{\rho_a}{w_p} \cdot \frac{\bar{U}_a}{\bar{U}_p} \text{ per unit volume} \quad (8.5)$$

where w_p is the weight of one particle, it is possible to estimate the charge per kilogram, assuming that all particles contribute to the observed current, I_p .

The number of particles passing through the measurement length of the test section, L , is:

$$N/\text{second} = \frac{M_p}{M_a} \cdot \frac{\rho_a}{w_p} \cdot \frac{\bar{U}_a}{4} \cdot \pi D^2 \text{ per second} \quad (8.6)$$

and therefore the charge per particle is:

$$Q/\text{particle} = I_p \cdot \frac{\dot{M}_a \cdot w_p}{\dot{M}_p \rho_a} \cdot \frac{4}{\bar{U}_a \pi D^2} \quad \text{coulombs} \quad (8.7)$$

so that the charge per kilogram is:

$$Q/\text{kg} = I_p \cdot \frac{\dot{M}_a}{\dot{M}_p} \cdot \frac{4}{\rho_a \pi D^2 \bar{U}_a} \quad \text{coulombs} \quad (8.8)$$

Equation (8.8) enables the charge per kilogram to be estimated to be between 0.051×10^{-4} and 0.010×10^{-4} coulombs/kg, depending upon velocity, loading ratio and ambient humidity. However, this gives an underestimate, since not all particles in the length considered will contribute to the observed current. The actual charge to mass ratio may thus be several times higher. It must be pointed out that the work carried out here on electrostatic effects is by no means intended to be exhaustive. The object was merely to see if any change in velocity or turbulence intensity could be observed by earthing the unearthed system. Electrostatic effects are discussed in the literature by Duckworth, [115], Doig and Roper, [116], and Soo [2].

The velocity profiles in figs. 8.8a to e confirm the results shown in fig. 8.1., obtained with $\theta = 0$. When $\theta = 45^\circ$, the spatial resolution is improved and this enables measurements to be taken as close as 0.02 cm from the pipe wall with none of the measurement volume being outside the flow. However, this configuration has disadvantages since the solids loading ratio penetration is substantially lower, due to the forward scattered light intensity being greater than that at the side, and it is difficult to focus the photomultiplier onto the sometimes faint cross-over region. This must be compared with focussing the pinhole onto the two bright beams before blocking them out, when $\theta = 0$. Thus, a reduction in loading ratio from 0.726 to 0.510 occurred at the higher

superficial air velocity and 1.434 to 0.909 at the lower velocities.

Figs. 8.8a to e also show the particle turbulence intensity profiles obtained as explained in section 5.9. The turbulence profiles for the clean gas, section 6.5, are also included for similar Reynolds' numbers. It may be seen that the turbulence intensity of the particles is in some cases less than, and in some cases greater than, that of the air. The phenomenon appears to be strongly dependent upon loading ratio and the loading ratio at which the particle intensity becomes greater than the air turbulence intensity is seen to be lower at the higher velocities. It may also be noted that in the wall vicinity the air turbulence profile slope is always greater than that of the particles and that the turbulence intensity of the air is generally greater there. The true picture of the air velocity fluctuations cannot be assessed from the results found in this study since they may be affected by the presence of the solids phase. Turbulence suppression near the wall has been found, for example, by tracer diffusion experiments in a flowing suspension [117] although the air turbulence in the core of the flow was found not to differ significantly from that of the clean gas.

Particle velocity fluctuations about the mean may be attributed to five contributory factors:

(i) Air turbulence intensity; the particle motion is primarily caused by the turbulent motion of the conveying gas and, in fully developed flow, the particle turbulence intensity for a monodispersion of particles should be less than the gas intensity. Only in the limiting case of particles approaching molecular size can the particles be expected to follow the turbulent fluctuations of the gas. Depending upon the frequency of the turbulent motion, however, particles of around 1 micron should be able to match the gas turbulence with reasonable accuracy, [80] .

(ii) Particle size distribution; for a polydispersion of particles extending well above 1 micron in effective diameter, the ability of individual particles to follow the motion of the conveying gas will decrease with increase in size. Thus, if it were possible to convey particles in a laminar gas flow in which there was a wide particle size distribution, apparent turbulence of the solid phase would still be observed because of the variation in individual particle velocities. Obviously, this term becomes more significant for a large particle size spectrum and reduces for a monodispersion of particles.

(iii) Non-axial particle trajectories; no particle, in passing through the test section, moves entirely parallel to the pipe axis, since its mean path is affected by a series of collisions with the walls of the pipe, and with other particles, resulting in a loss of kinetic energy. These collisions direct the particle along trajectories having a component normal to the mean flow [118]. Since all particle trajectories will be different, the axial component of velocity of each particle at a given radial position will be different and hence, this phenomenon will contribute to the overall turbulence level.

(iv) Particle collisions; where a variation in velocity is attributed to trajectory variations on account of particle collisions, the collisions themselves will cause interchanges of momentum between particles and between particles and the wall. Both terms (iii) and (iv) are strongly dependent upon loading ratio.

(v) Local dispersed solids density fluctuations; temporal fluctuations in the particle concentration will always be present in any gas-solids flow and will have a complex effect on the turbulence measurement. For example, a sudden brief reduction in particle dispersed density will

cause a slight reduction in interactions and cause an increase in the velocity of the particles since the instantaneous loading ratio has been reduced, see section 8.3.2, and fig. 8.6. In addition, particularly with laser anemometry equipment, the instrumentation may be affected, for example, by the sudden brief reduction in scattered light. It is impossible to predict how this phenomenon will affect the results.

Fig. 8.10 is a plot of particle axial turbulence intensity along the centre line of the pipe versus solids loading ratio. The turbulence intensity for the particles appears to lie within a narrow band, although this cannot be substantiated since the number of results decreases with increase in loading ratio. However, by projecting the band to the particle turbulence intensity axis, it is seen that the resulting intensity is always less than that of the air, which may be assumed to remain essentially the same in the presence of particles [117]. At low values of loading ratio, contributions (iii), (iv) and (v) are small and may be neglected as $\frac{M_p}{Ma} \longrightarrow 0$. Thus, it may be assumed that the turbulence contributions of (i) and (ii) are less than the air turbulence. Turbulence of the particles above this level can only be attributed to contributions (iii), (iv) and (v). Hence, if density fluctuations are small, the increase in particle turbulence above that of the gas in figs 8.8a to e is due directly and indirectly to particle/particle and particle/wall collisions.

Close to the wall a similar plot to that of fig. 8.10, but with very much less correlation, reveals that for $\frac{M_p}{Ma} \longrightarrow 0$, the air turbulence is much greater than contributions (i) and (ii), showing that the level of turbulence exhibited by the air here is much too great for the particles to follow and is only approached by an increase in contributions (iii), (iv) and (v); see fig. 8.8b for a loading ratio of 0.909.

Finally, in an attempt to explain why the increase in air velocity causes the particle turbulence intensity to become greater than that of the air at a lower loading ratio than for lower velocities, it can only be supposed that the collisions become more severe and more erratic as a result of the increased kinetic energy of the particles. Thus, contributions (iii) and (iv) depend not only upon the loading ratio, but also upon the air velocity.

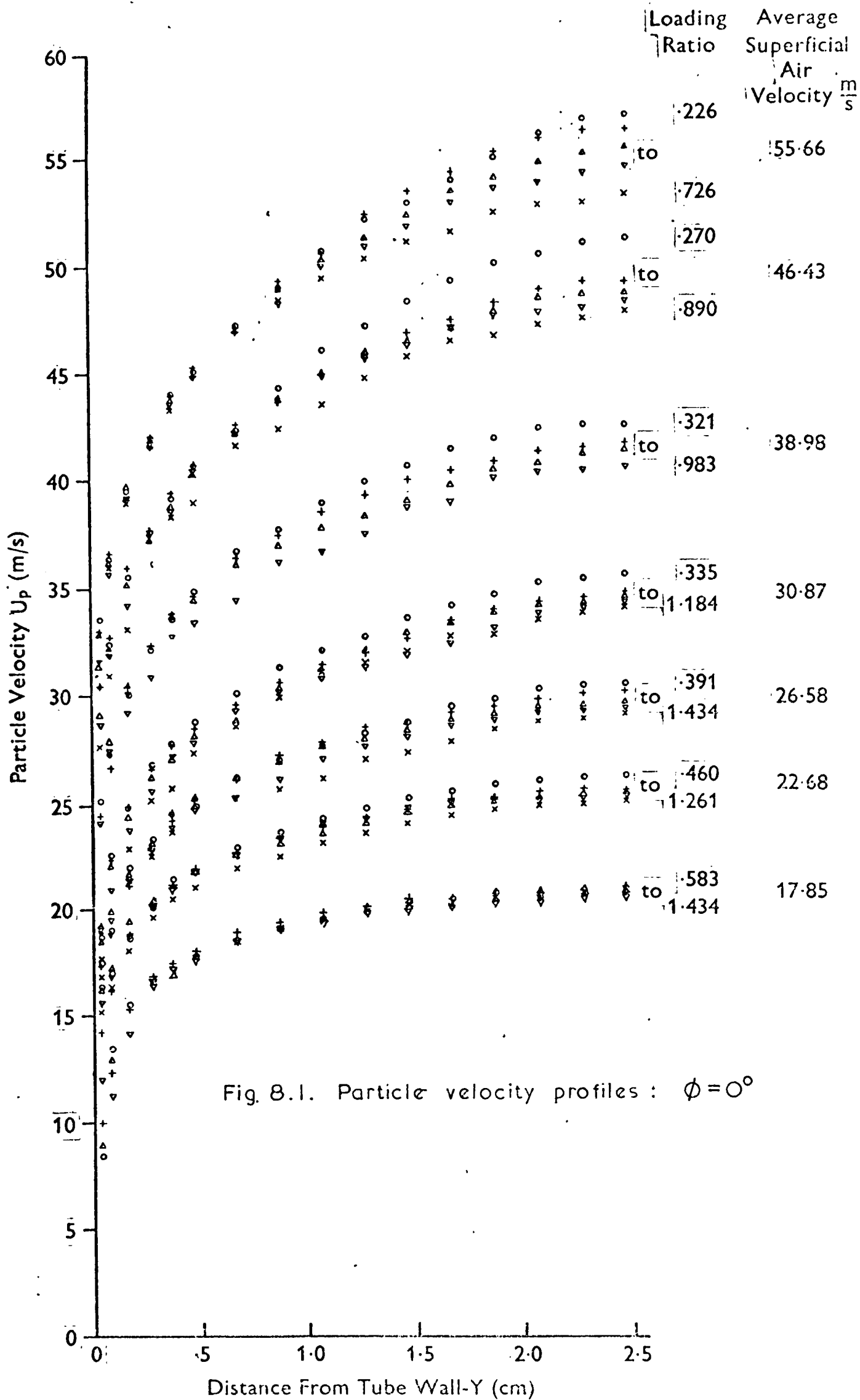
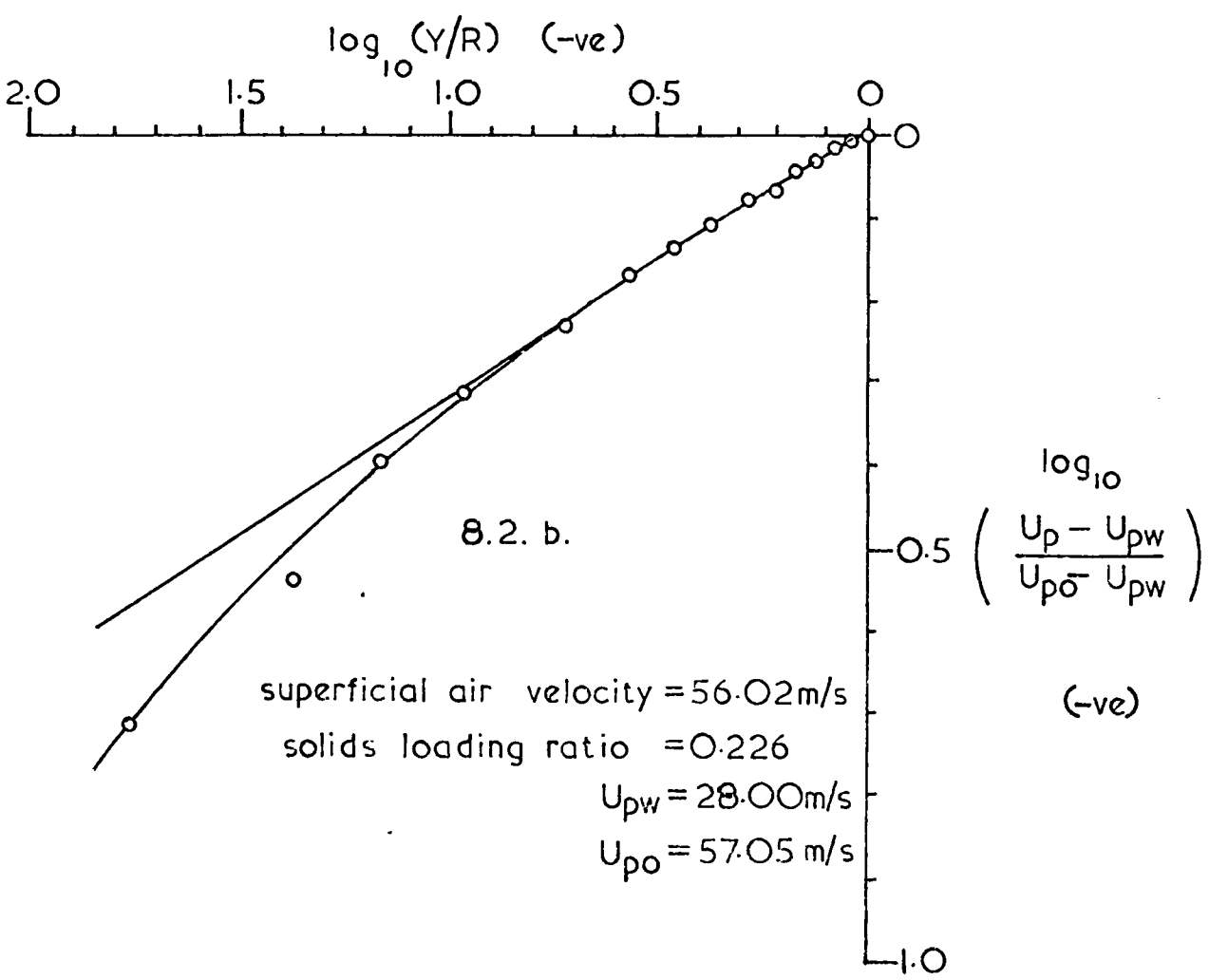
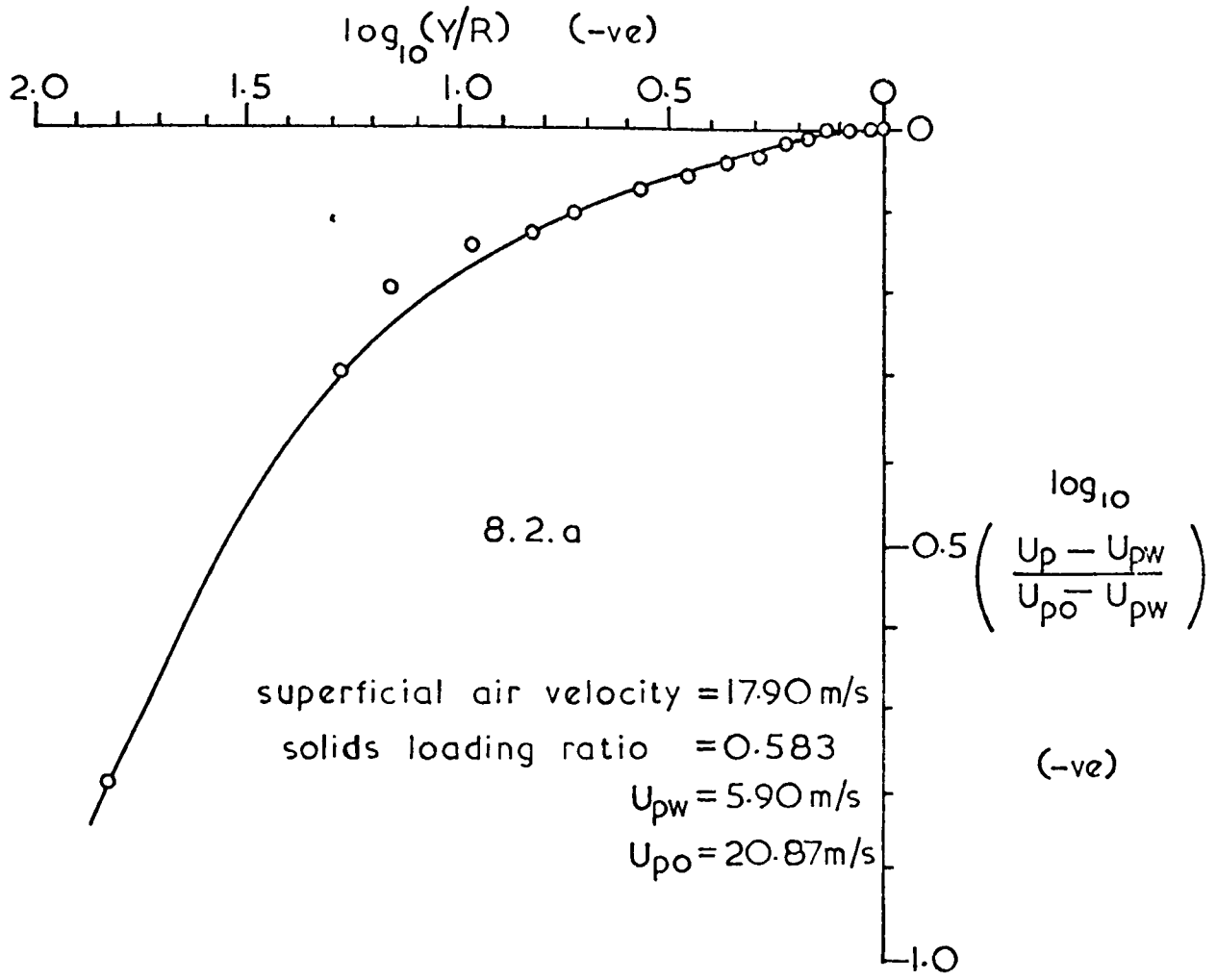


Fig. 8.1. Particle velocity profiles : $\phi = 0^\circ$

Fig.8.2. Log. plots of dimensionless particle velocity vs. dimensionless distance from the wall



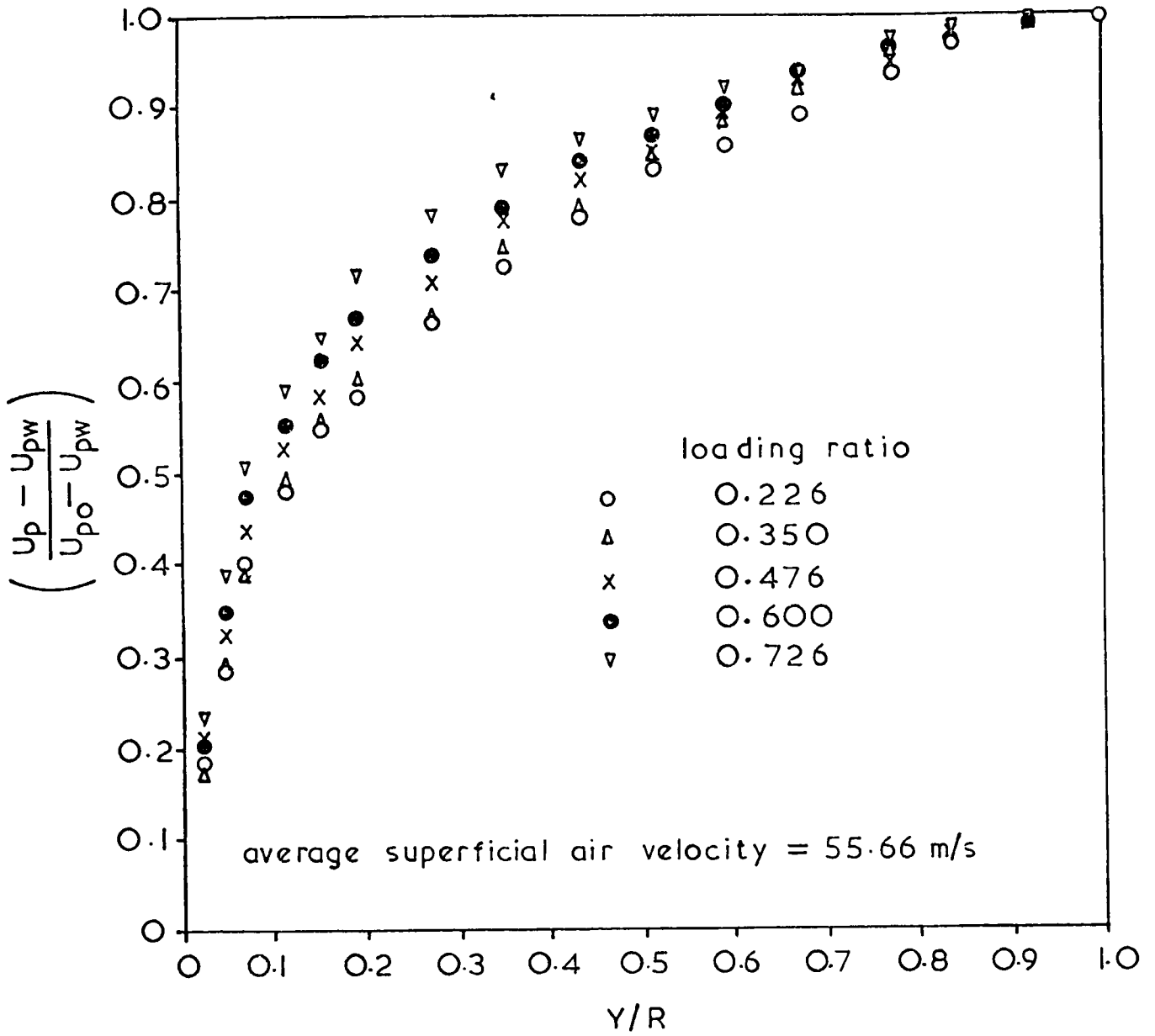


Fig.8.3. Effect of solids loading on particle velocity profile

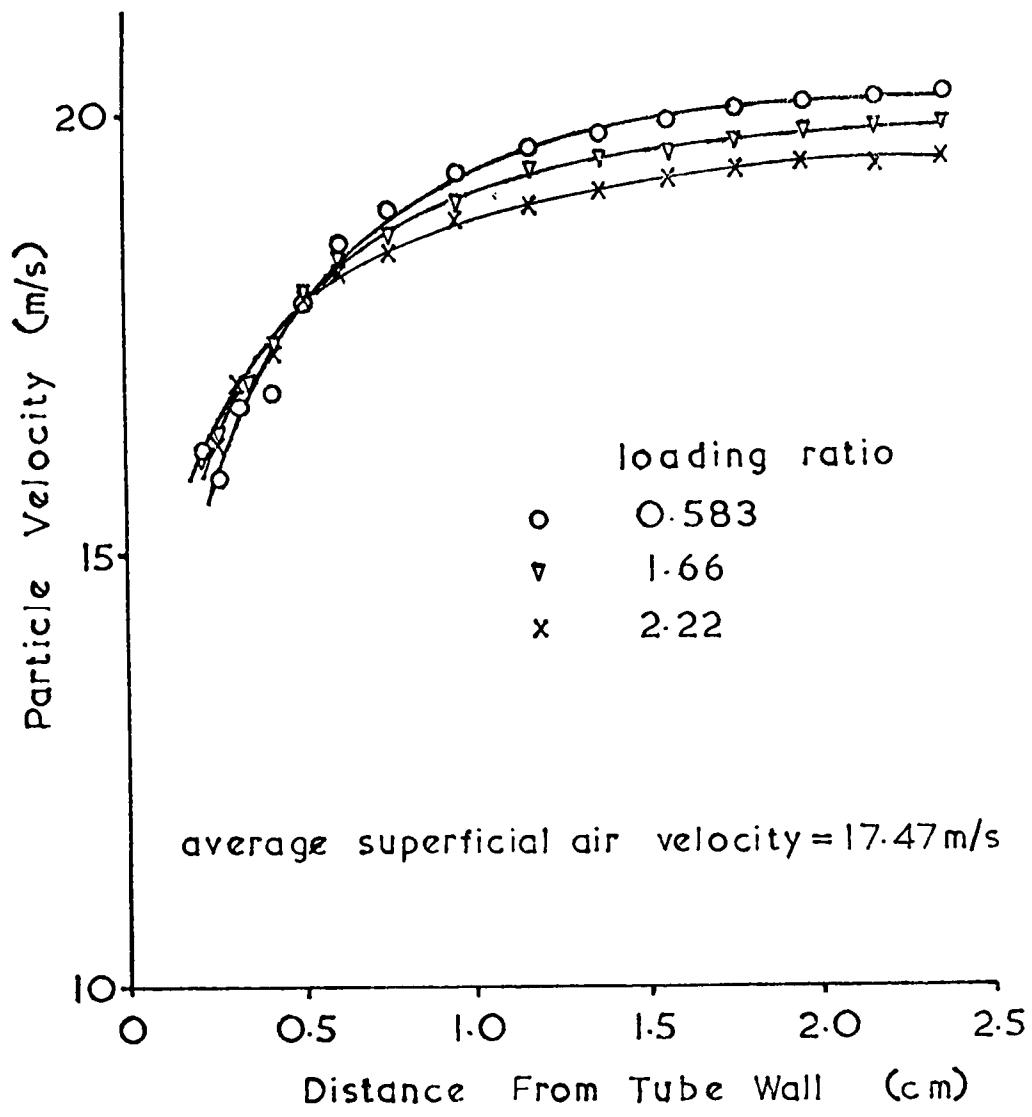


Fig. 8.4. Particle velocity profiles for $\Delta Z = 13.9$ mm

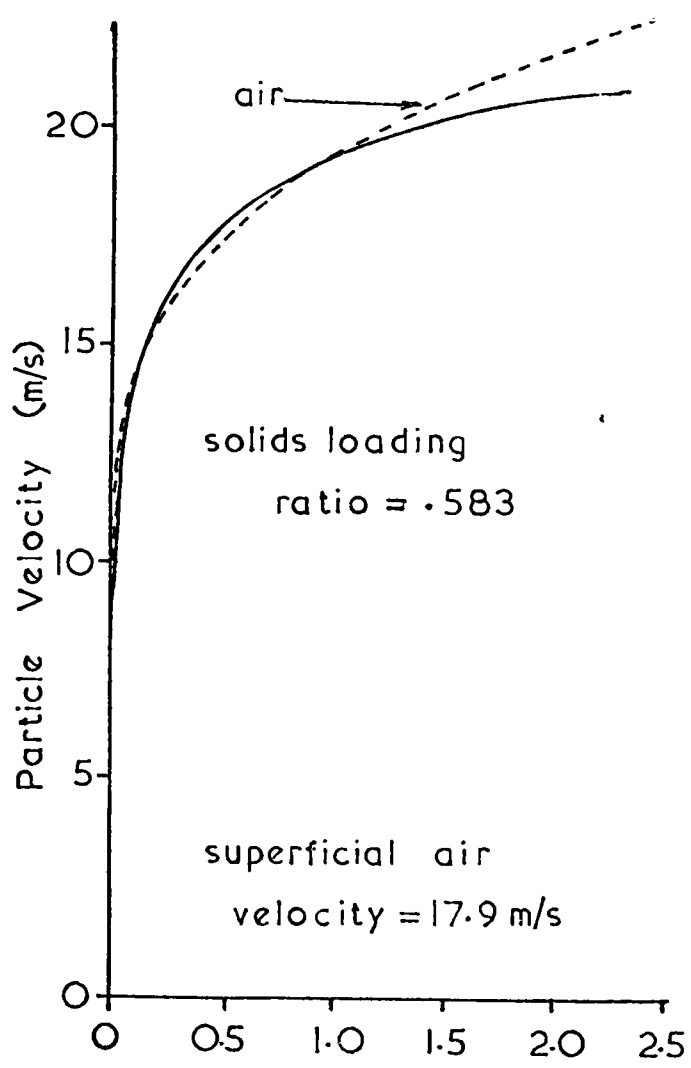


Fig. 8.5. a.

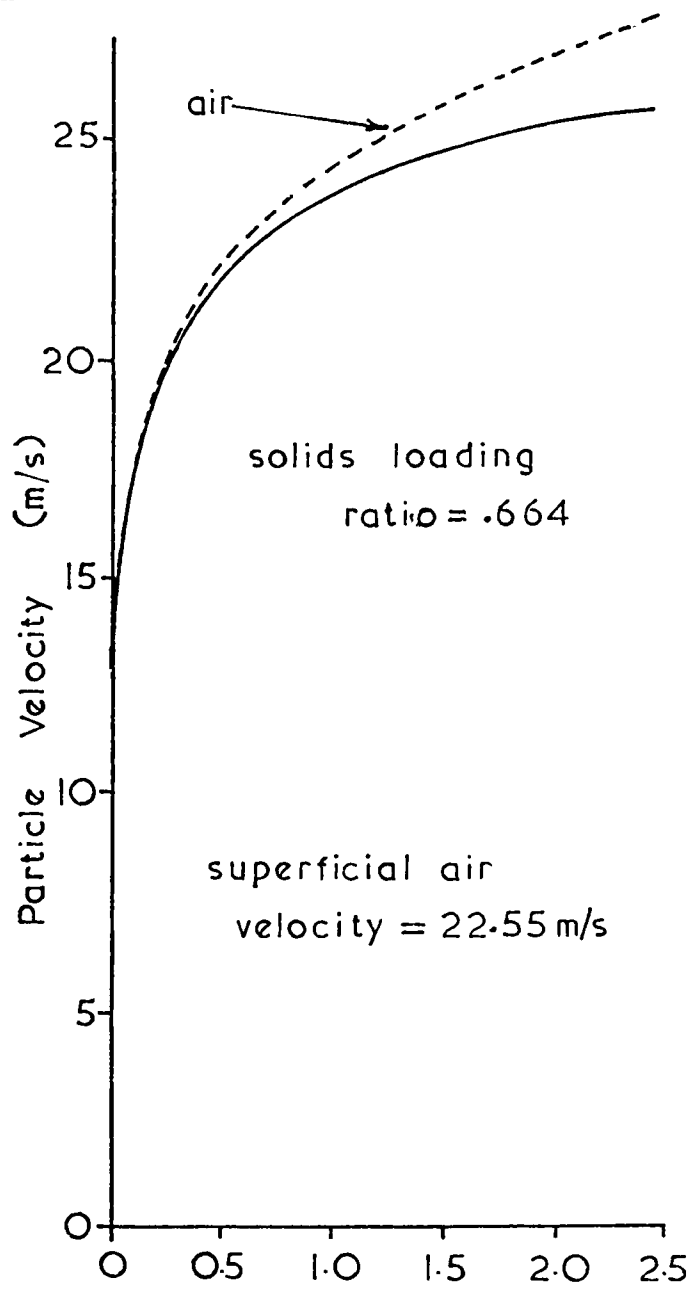


Fig. 8.5. b.

Particle and clean air velocity profile comparisons

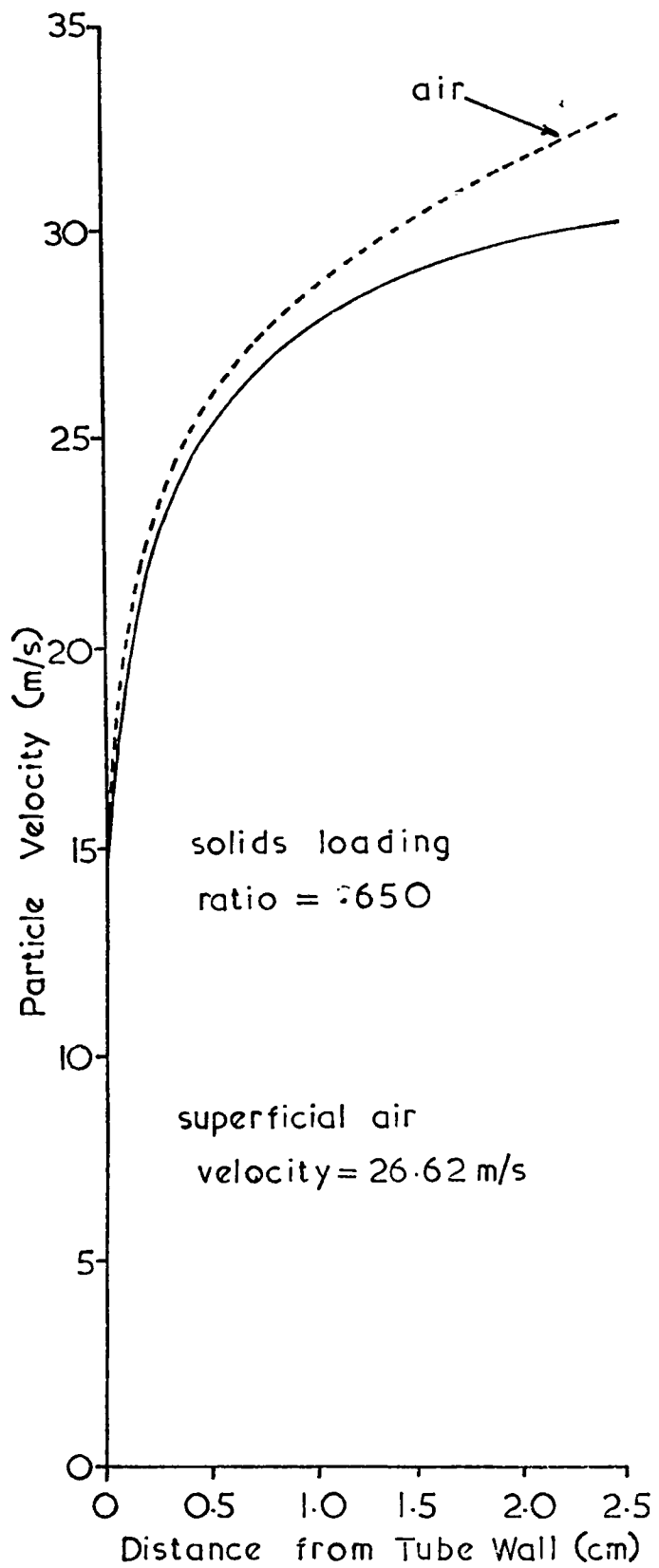


Fig. 8.5.c.

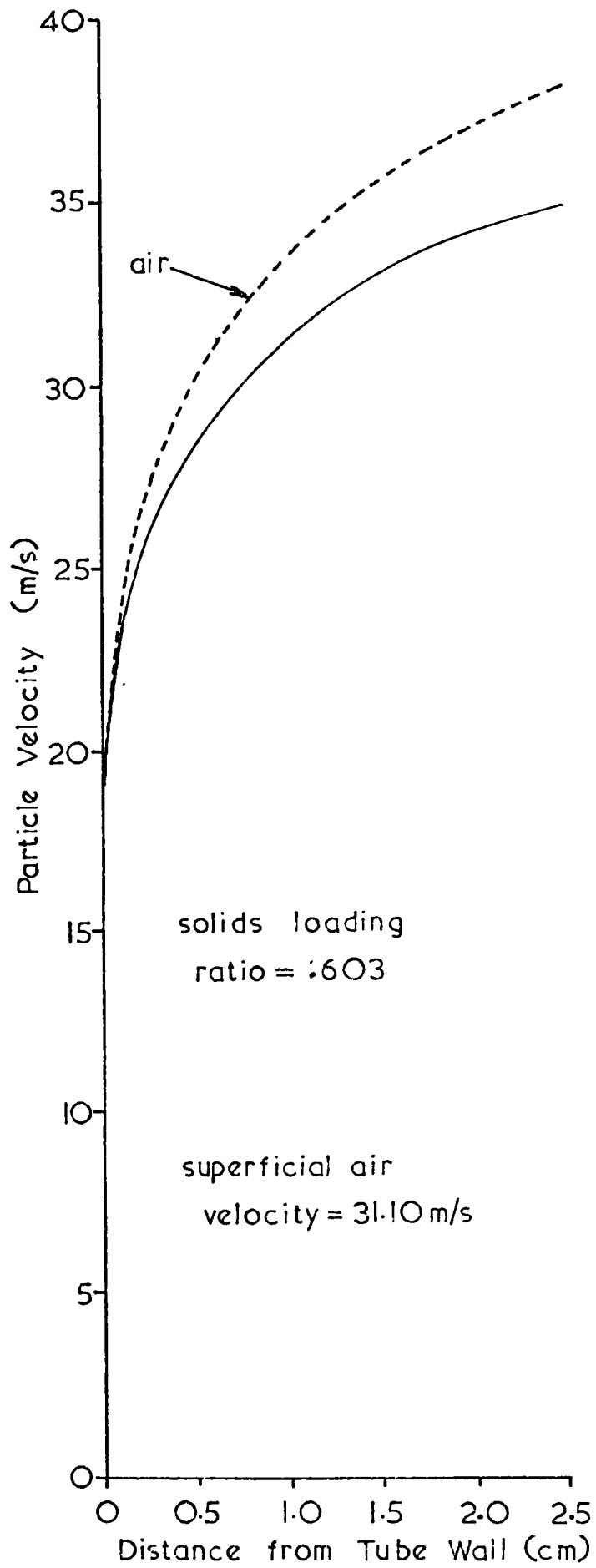


Fig. 8.5.d.

Particle and clean air velocity profile comparisons

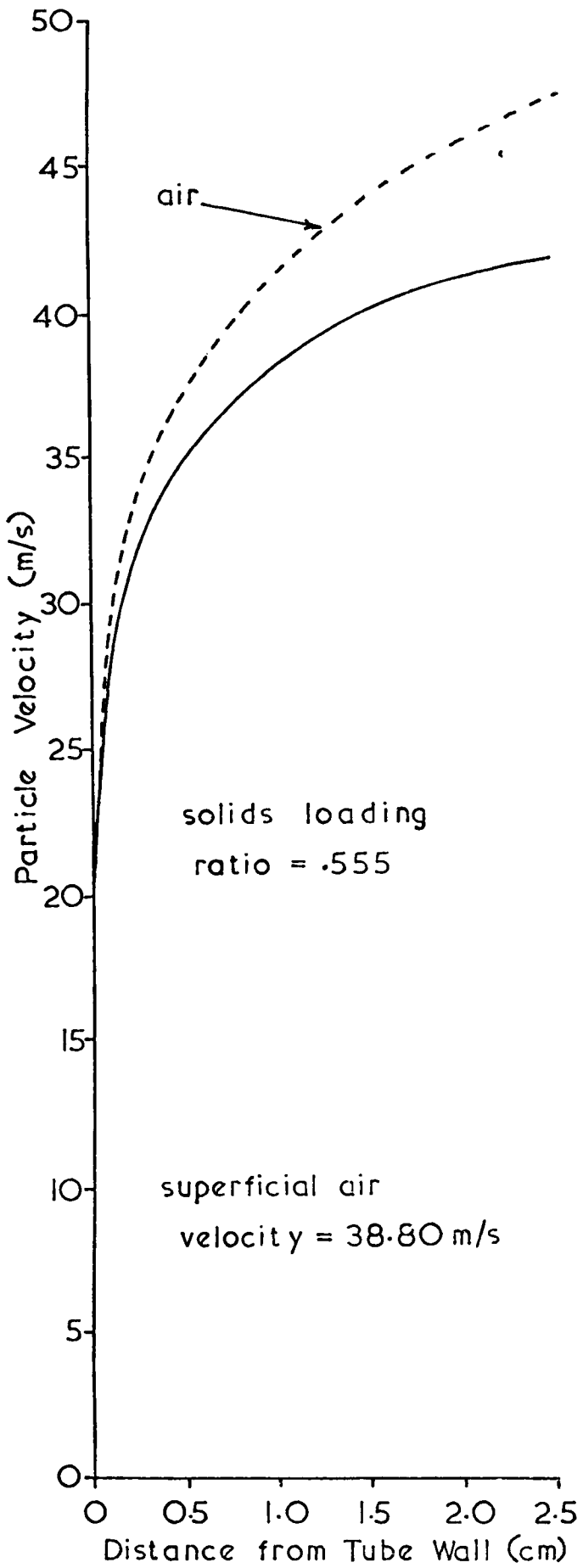


Fig. 8.5. e.

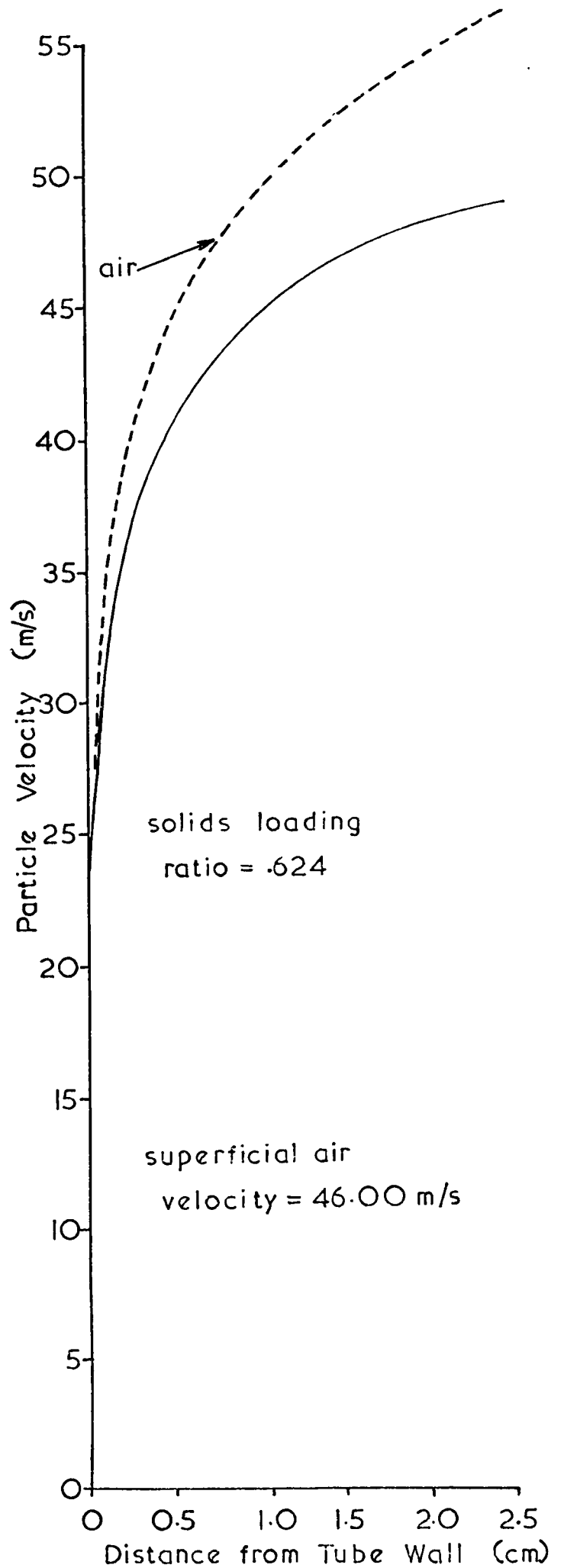


Fig. 8.5. f.

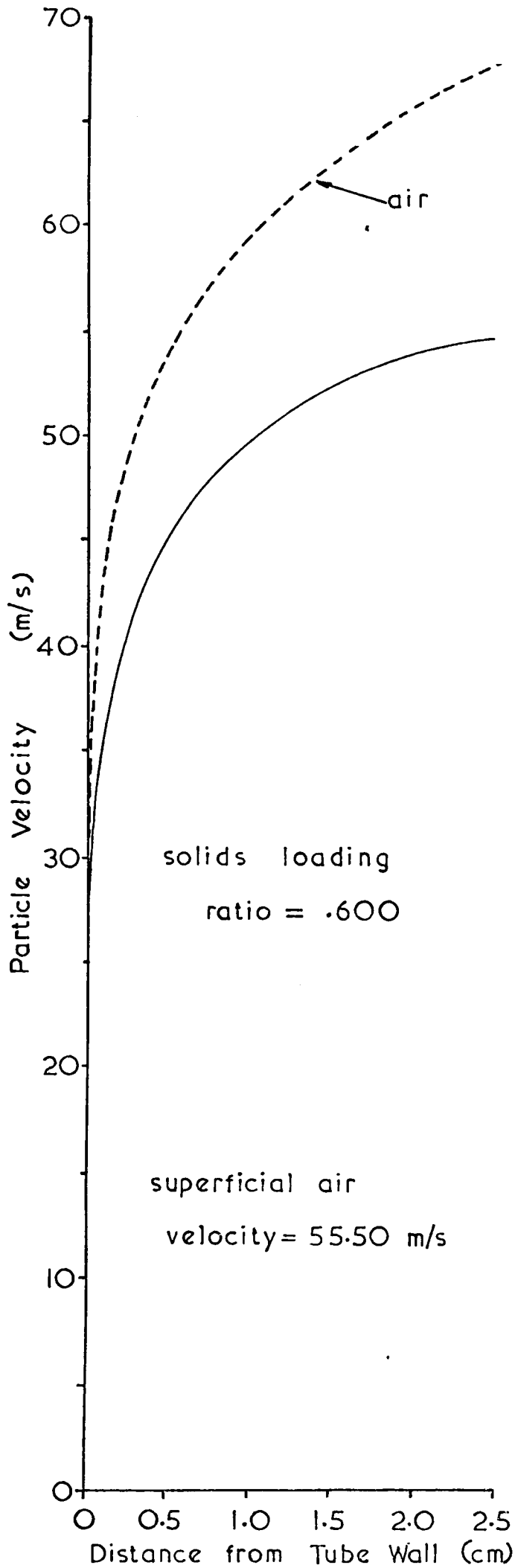


Fig. 8.5. g.
Particle and clean air
velocity profile comparison

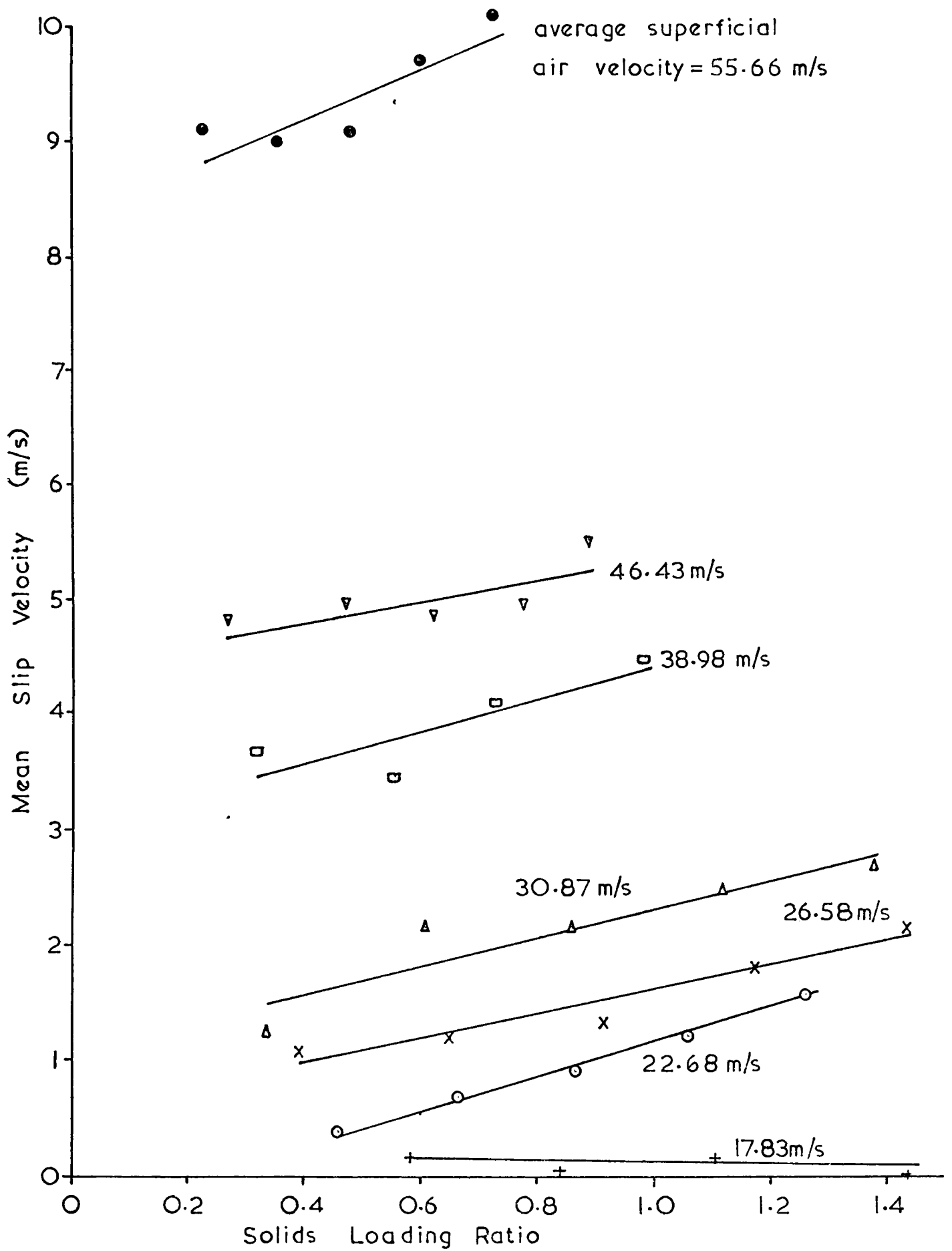
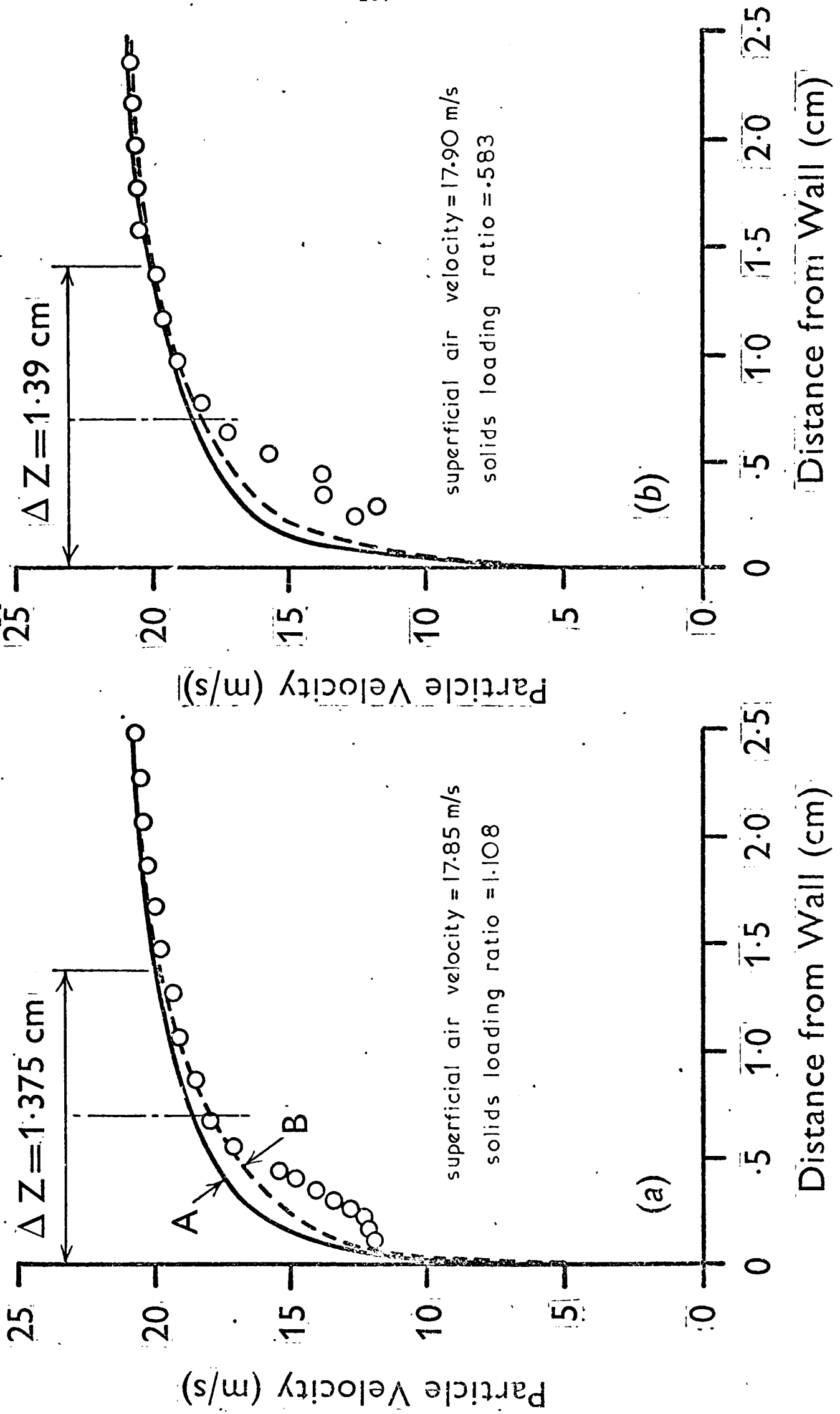


Fig 8.6. Mean Slip Velocities Derived from Fig.8.1.

Fig. 8.7. Comparison of the $1/e^2$ and the measured probe lengths



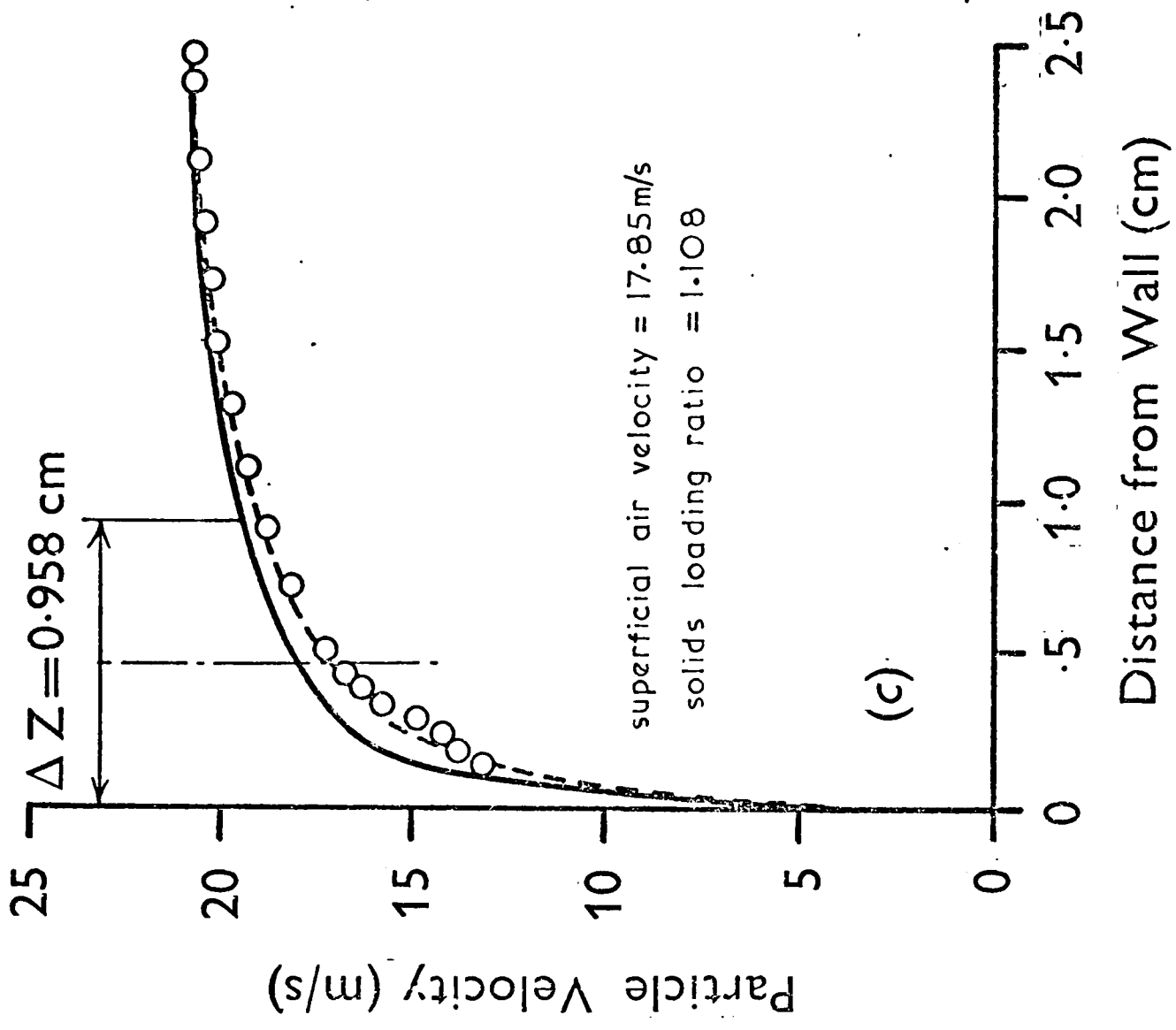


Fig.8.7. Comparison of the $1/e^2$ and the measured probe lengths

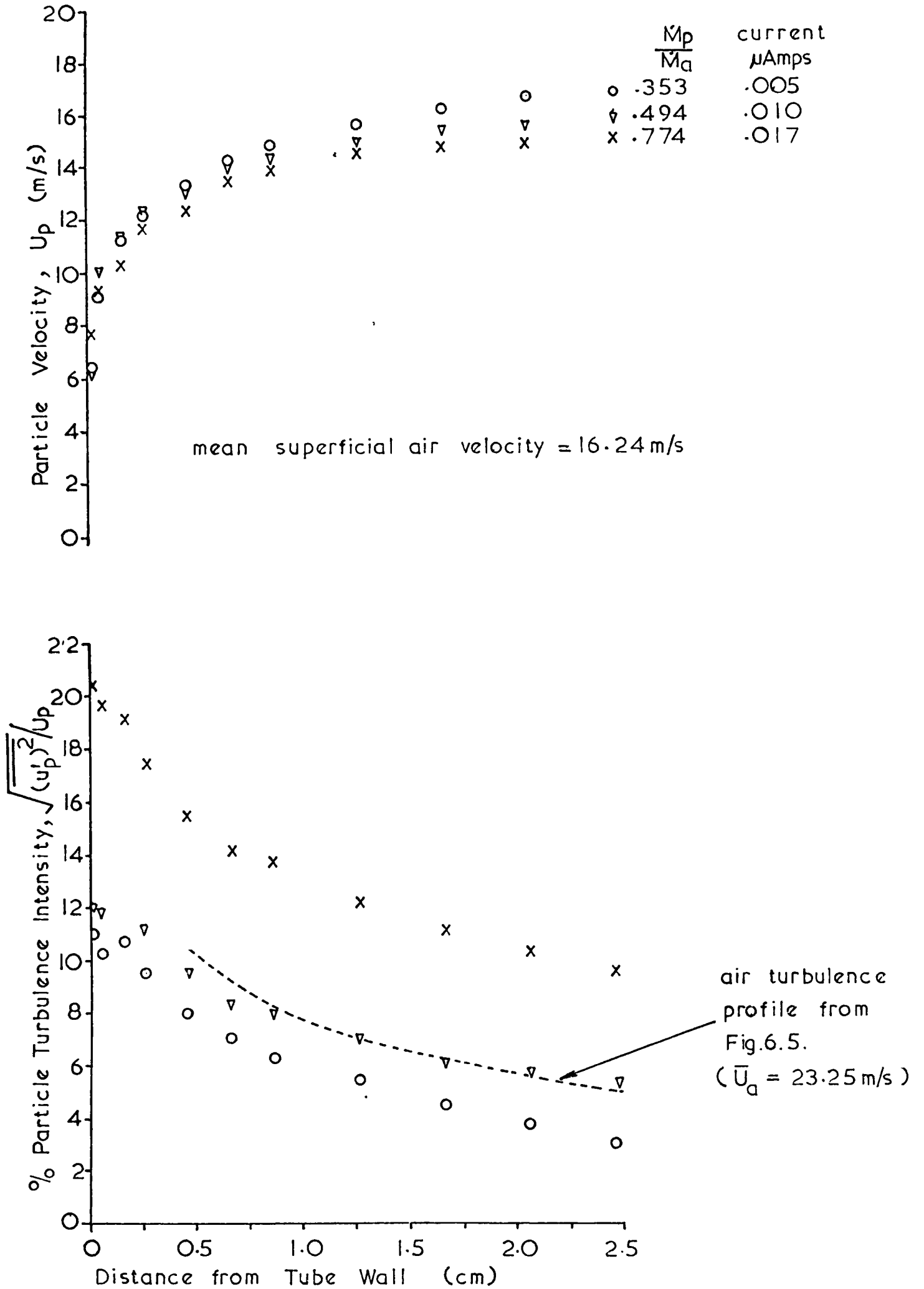


Fig.8.8.a. Particle velocity and axial turbulence intensity profiles

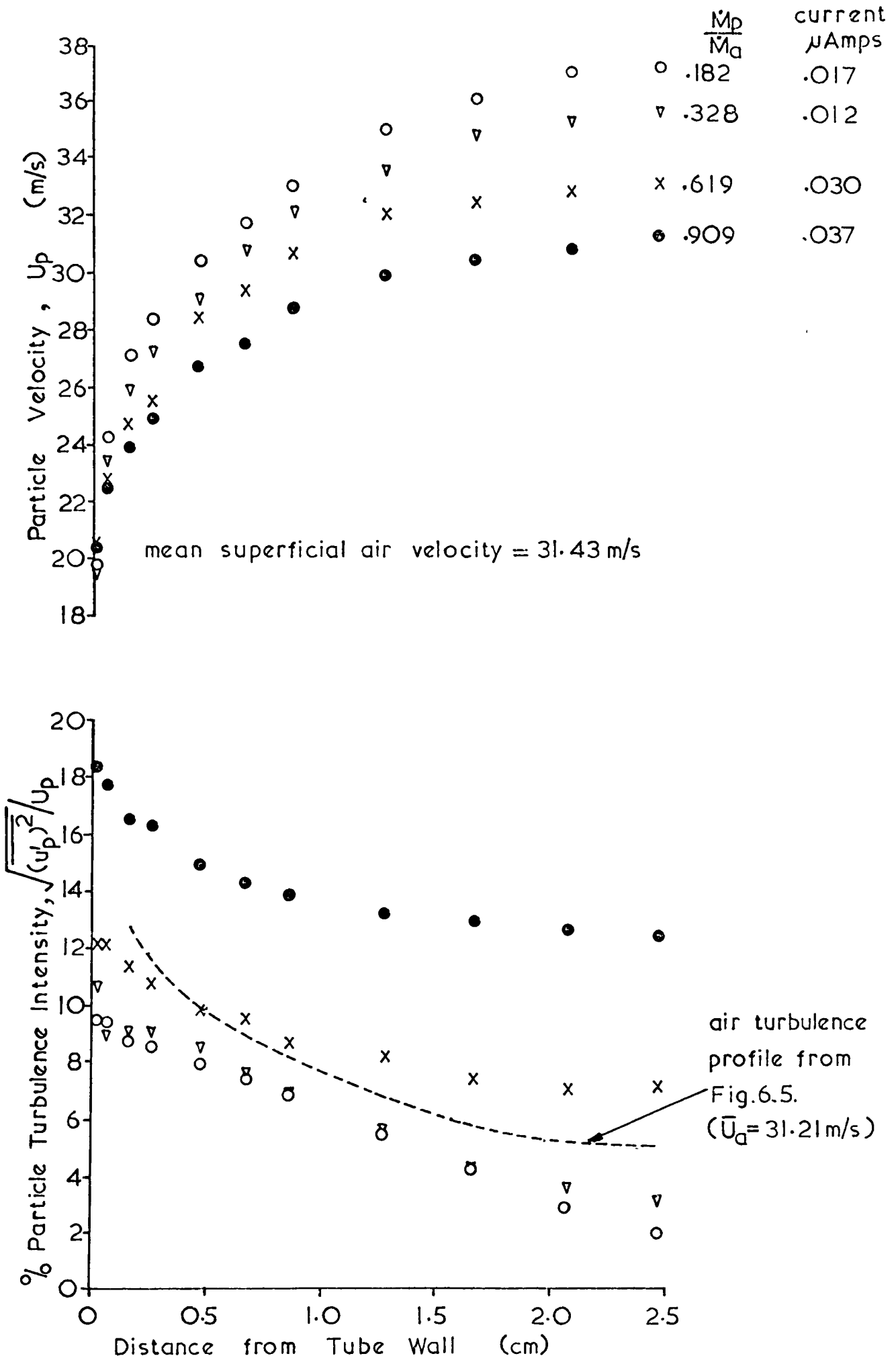


Fig.8.8.b. Particle velocity and axial turbulence intensity profiles

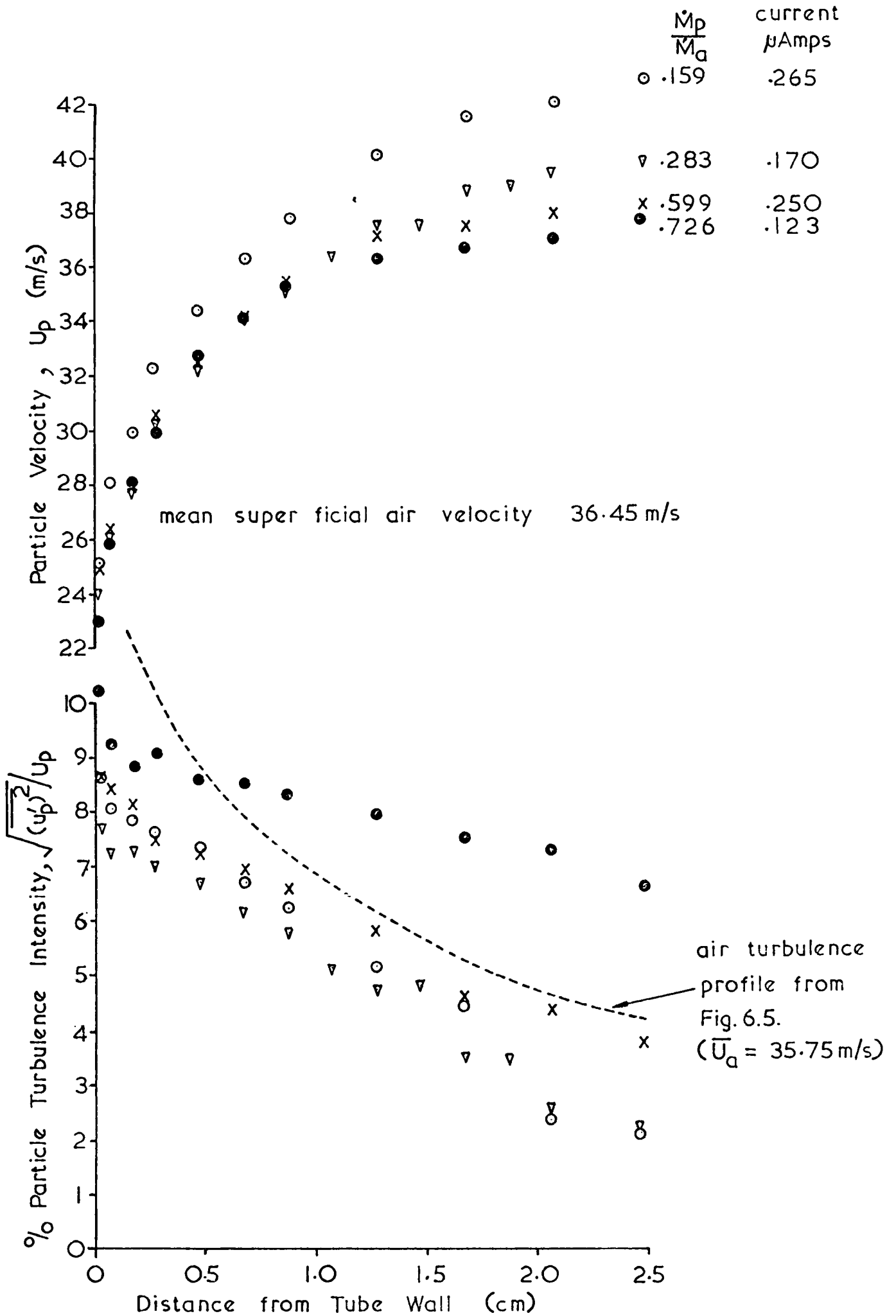


Fig.8.8.c. Particle velocity and axial turbulence intensity profiles

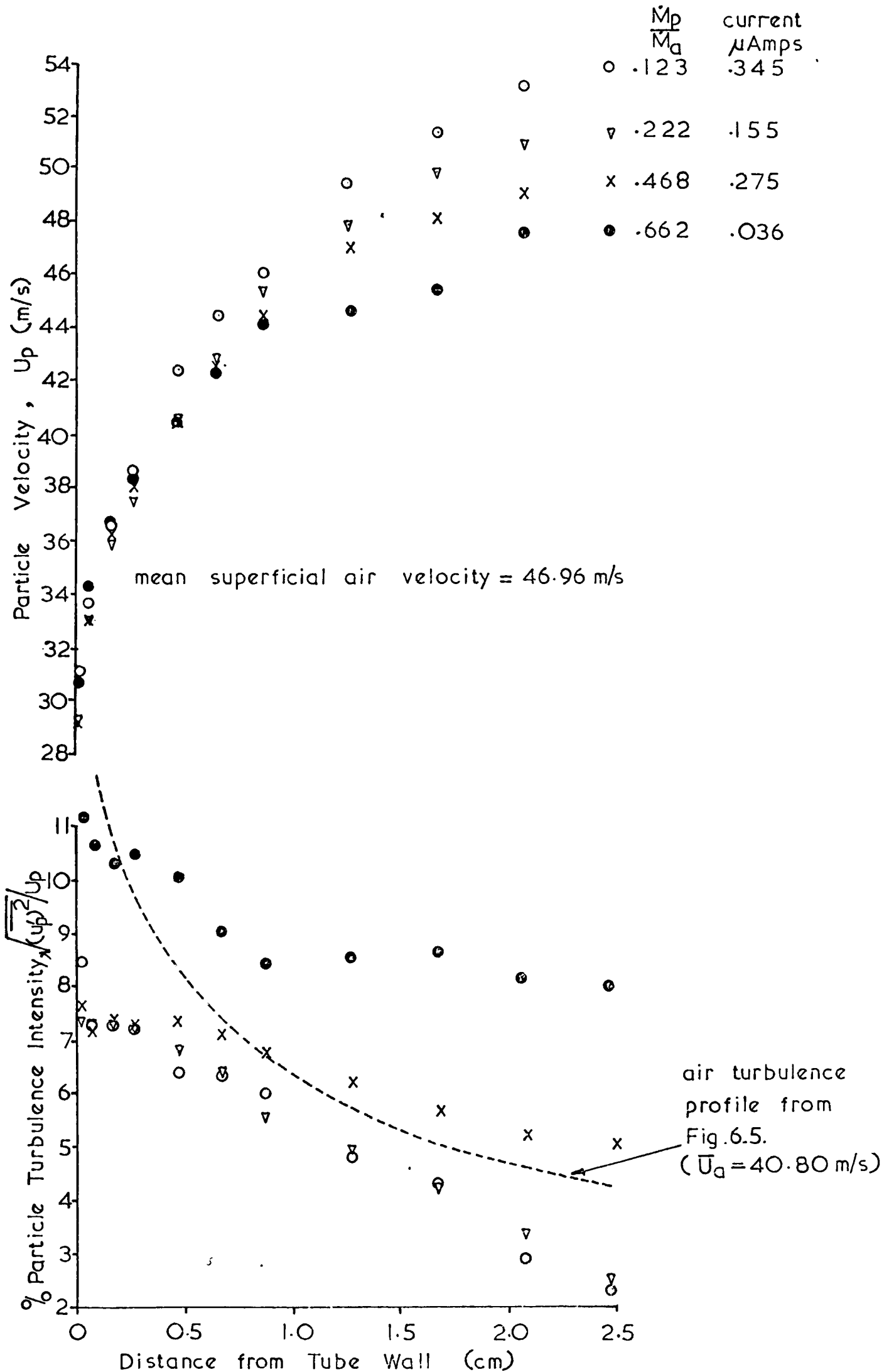


Fig.8.8.d. Particle velocity and axial turbulence intensity

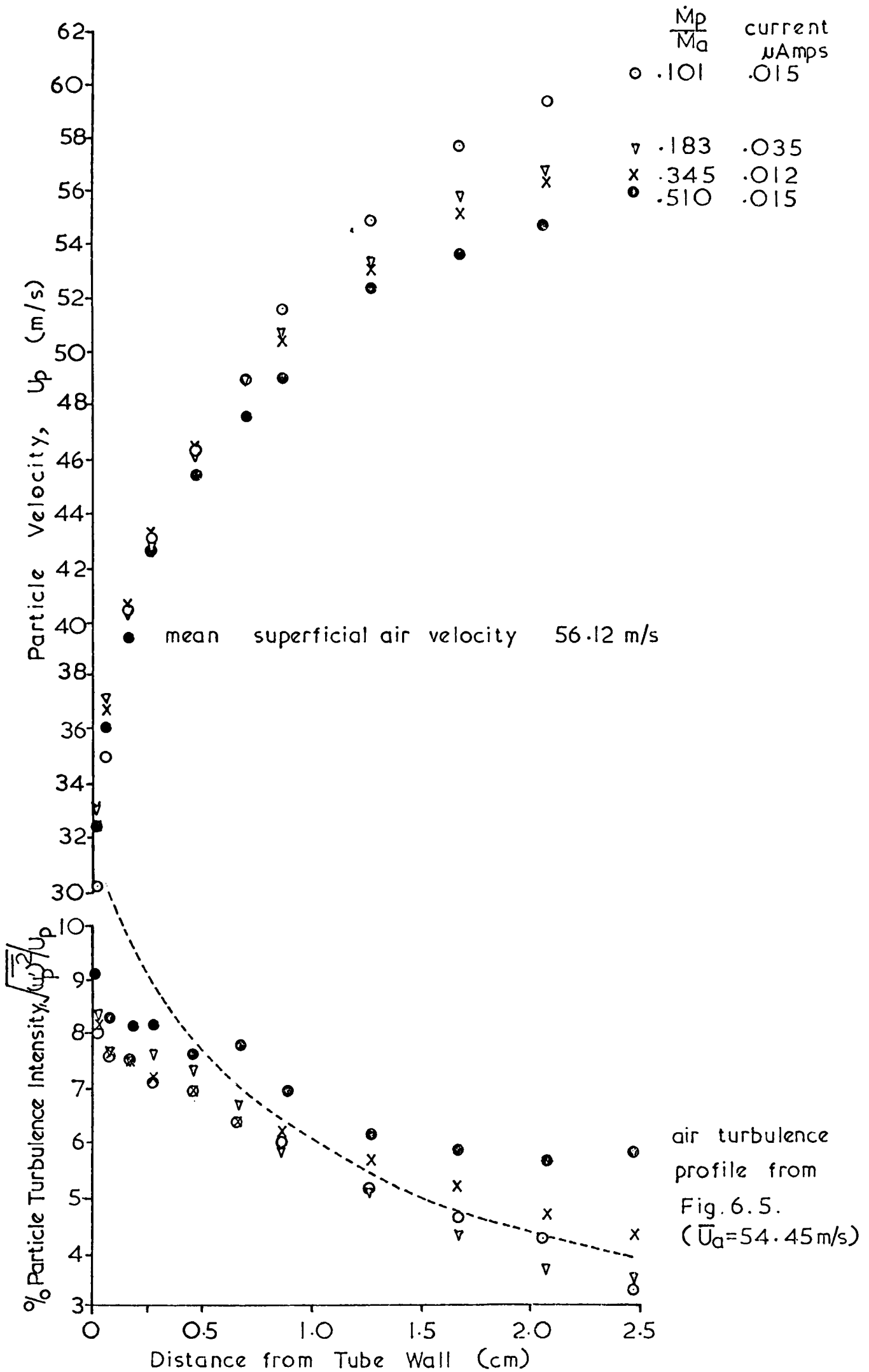


Fig. 8.8.e. Particle velocity and axial turbulence intensity profiles

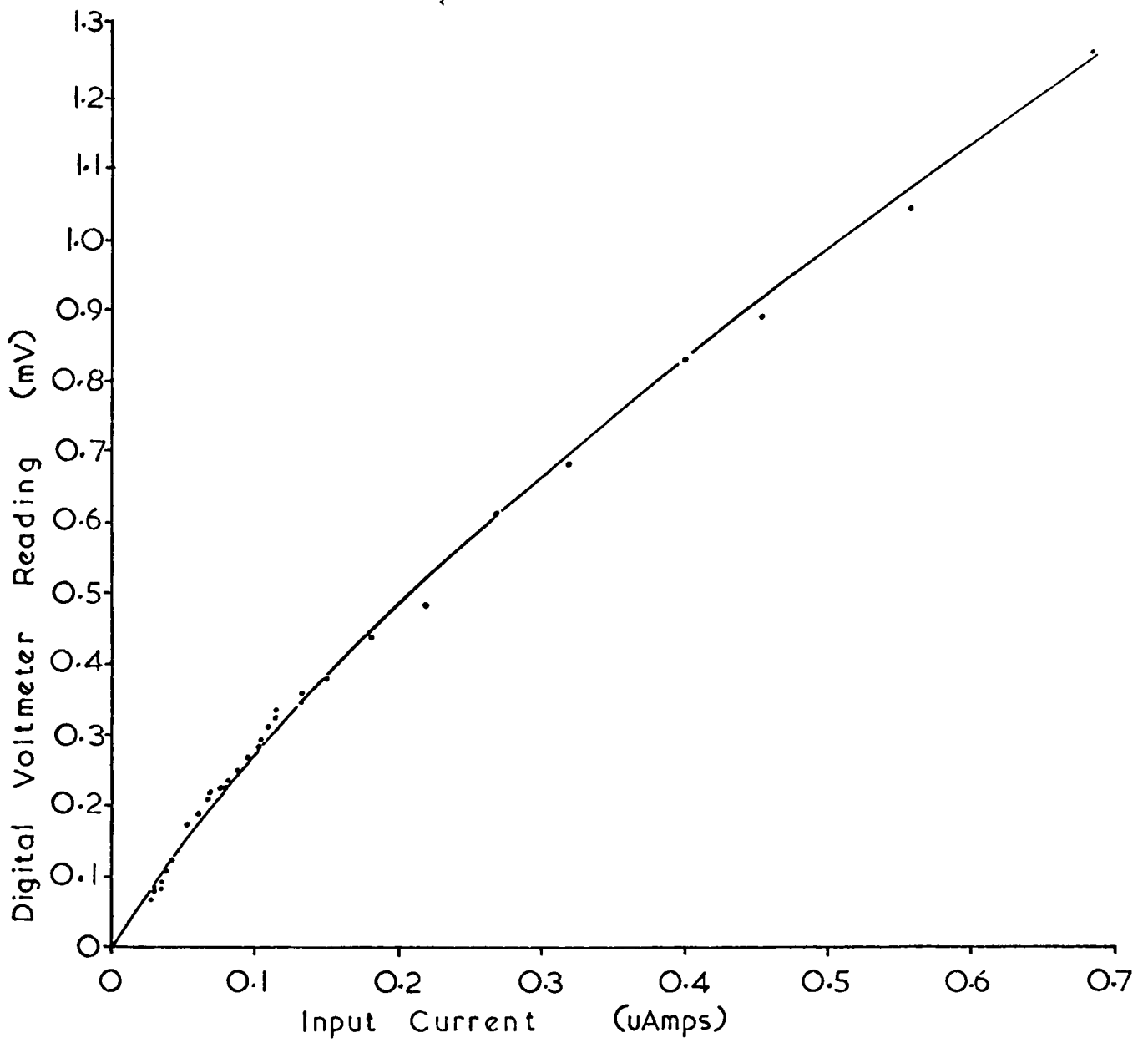


Fig.8.9. Charge Amplifier Calibration Curve

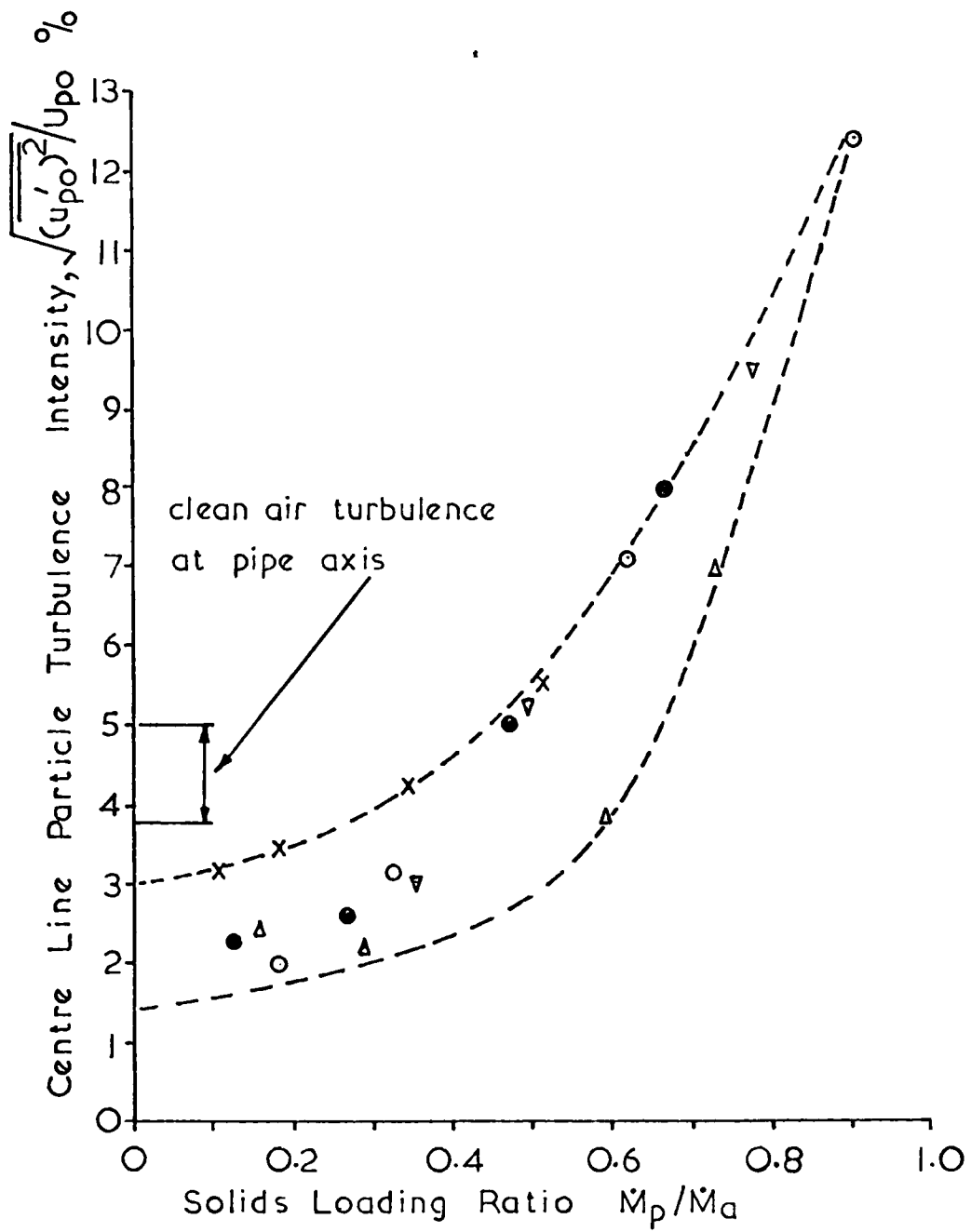


Fig. 8.10. Particle turbulence at the pipe axis

CHAPTER 9

MEAN PARTICLE VELOCITY MEASUREMENT

9.1 Introduction

There have been many previous attempts to measure mean particle velocity since it is of more value to the plant designer than local particle velocity. In general, equations which enable the pressure drop to be predicted include a mean particle velocity term. However, as with the measurement of local particle velocity, suitable instruments for measuring mean particle velocity are not common. During this investigation a technique was developed by which the laser anemometer could be used to measure mean particle velocity in the glass test section. It is hoped that this new procedure will eventually provide industry with a means of continuously monitoring mean particle velocity and hence, the facility may be extended to provide automatic control of a more complex powder handling plant.

9.2 Literature Survey

The measurement of mean solids velocity has been investigated by several researchers. Cramp [119], Mehta [97], and Clark et al [96], used an arrangement in which a section of flowing suspension was trapped by simultaneously closing two valves in a removable part of pipeline.

The mean velocity of the particulate phase was then determined from the solids mass flow rate and the dimensions of the isolated pipe section.

Cramp and Priestly [120], and Cramp [121], described a method of calculating the particle velocity in horizontal pipes. The particles were allowed to discharge from the open end of a pipe, situated at a known height above the floor, and measurement of the horizontal distance of travel enabled the particle velocity to be evaluated.

Richardson and McLeman [122] introduced a solids-free zone by interrupting

the flow for a fraction of a second and electronically timing its travel between two transducers. The zone, which apparently remained stable over 52 ft of the conveying line, was detected by the attenuation of particle noise intensity. Hall [123] used a similar technique to that of Richardson and McLemon, when he timed the passage of radioactively tagged solids instead of a solids free pulse.

The above methods of velocity measurement each have individual drawbacks and accuracy limitations and none provides for the continuous monitoring of particle velocity. Recently, various cross-correlation procedures have been developed [124, 125, 126] which may give a continuous display of mean particle velocity. These include systems in which optical or capacitive transducers are positioned, a fixed distance apart, on the surface of the conveying pipeline. The inherently random flow patterns of the flowing suspension generate random signals which are cross-correlated to enable the transit time of the particles to be automatically tracked.

9.3 Laser Anemometry Arrangement

The probe length, ΔZ , is particularly important here since, by expanding the major axis of the ellipsoid to cover the entire diameter of the flow tube, as shown in fig. 9.1, the mean solids velocity of the flow may be found. However, it is necessary to ensure that the number of fringes across the flow diameter is reasonably constant and so only the central part of the probe length must be used. This requires that ΔZ not only covers the flow tube diameter, but exceeds it considerably. In this investigation the probe length was greater than the pipe diameter by a factor greater than three, as shown in fig. 9.1, where ΔY is exaggerated.

Typical dimensions of the probe volume for an initial laser beam of diameter 0.65 mm, a focussing lens, f_1 , of 600 mm focal length, and a flow tube diameter of 4.94 cm are :-

$$\begin{array}{ll} \Delta X = 0.744 \text{ mm}; & \Delta Z = 170 \text{ mm} \\ \Delta Y = 0.744 \text{ mm} & \delta = 0.0725 \text{ mm} \end{array}$$

In order to obtain the very small value of the beam intersection angle, θ , required for the above dimensions, it was necessary to slightly modify the optical unit. This merely consisted of re-designing to allow the surface mirror to move closer to the beam splitter.

Both reference beam and fringe modes of operation were found to be suitable for the measurement of mean particle velocity. However, the vast majority of measurements were taken in fringe mode. For this the minimum aperture of the collecting optics was not small enough to block out the two beams and so masking tape was used.

9.4 Experimental Procedure

The mean particle velocity for seven sets of superficial air velocity and several loading ratios were obtained using the above arrangement. The measurements were taken in conjunction with those of section 8.3, which enabled the velocities obtained here to be compared with values obtained from the local particle velocity measurements. For each air mass flow rate the initial particle velocity measurements were taken at low solids loading. The solids flow rate was then increased at appropriate intervals until the limit of the laser anemometer penetration was reached. The orifice plate pressure differential and the air temperature at entry to the gas-solids mixing unit were recorded throughout the tests and average values were evaluated.

9.5 Results and Discussion

The experimental results of the mean particle velocity measurements are shown in table 9.1 (method 2). This table includes the results obtained from the particle velocity profiles (method 1). In each case comparison is possible since the air and solids mass flow rates were similar.

It can be seen from the data that it was possible to use the mean measurement technique at higher solids loading ratios than could be obtained for the local velocity measurements. In the lowest velocity range, measurements were taken for solids loading ratios greater than 2.2, whilst at the highest velocity, the maximum solids loading ratio was 0.601. The reduction of maximum solids loading ratio with increase in velocity has been noted in section 8.3, and is due to the faster moving particles scattering less photons of light than the slower particles, so that less light is available for collection at the photomultiplier.

Comparison of the mean particle velocity method with the local velocity method is shown graphically in fig. 9.2. It can be seen that good accuracy was achieved despite the slight variations in solids loading and conveying air velocity for the two methods. Thus, the percentage difference column in table 9.1 is an overestimate and the average is only 2.79%. This variation may be due to the difficulty of measuring the sine of the half angle θ , considering the small values used. $\sin \theta$ was obtained by measuring the length of the beam from the cross-over region to a suitably placed screen (usually at a distance of about 1.5 m), and half the distance between the two beam spots on the screen.

A typical oscilloscope display of the signal to be analysed by the tracking unit is shown in fig. 9.3. This photograph was obtained

during local velocity measurements in very light solids loading conditions. For mean particle velocity measurements and higher solids loading ratios, however, the number of particles which produce a frequency burst is vast and there is also a distinct velocity spread encompassed by the probe volume. The raw signal thus appears as a confused blur with many frequency bursts superimposed upon one another. Only after suitable electronic filtering does the required frequency become apparent and, even then, it is still somewhat indistinct, as shown in fig. 9.4. A small aperture opening, in this case provided by using masking tape, was found to give the best filtered signal, thereby excluding many spurious signals and noise components from the photosensitive cathode. Tracking of the signal frequency became more difficult with increase in both solids loading ratio and superficial air velocity. However, the filtered oscilloscope trace shown in fig. 9.4, though even more indistinct, was still visible at solids loading ratios higher than those reported here. The tracking unit was not capable of following the signal, but the fact that Doppler signals were still penetrating through the flow holds out promise for the measurement of particle velocity in higher solids loading ratios. It may be fruitful to employ spectrum analysis in order to analyse denser flows; however, this technique would not give a continuous analogue of velocity.

The mechanism by which frequency measurements are achieved is difficult to ascertain. The tracking unit must deal with a wide spectrum of frequencies in order to produce an apparently accurate average value. It is suspected that, from the mass of signals available (of the order of 10^4 at any given instant), the processing electronics can accept only the "best quality" signals and uses these to produce a mean velocity

output. Attempts to use the method for the measurement of mean velocity in the seeded flow described in section 6.2 were unsuccessful, perhaps due to the greater velocity spread there. For the two phase flow situation encountered here, the ratio of maximum to minimum velocity in a given profile was typically between 2 and 4. For single phase fluids, because of the wall non-slip condition, the ratio is infinity.

In some chemical reactions strict control of the average solids velocity in a dilute gas-solids flow is essential in order to achieve the required residence time. Since the tracking unit produces a voltage output which is directly proportional to solids velocity, it is evident that the system may be used in a control circuit, opening or closing the conveying air valve in order to automatically regulate the mean particle velocity to a pre-set value.

TABLE 9.1.

solids loading ratio	superficial air velocity m/s	mean particle velocity m/s	method of obtaining mean * particle velocity	ΔZ mm.	δ μ m.	% difference between methods
.583	17.90	17.71	1			3.45
.581	17.78	17.10	2	170	72.5	
1.108	17.85	17.67	1			396
1.089	18.05	17.60	2	170	72.5	
1.641	17.50	16.69	2	170	72.5	
2.262	16.86	16.49	2	170	72.5	
.460	22.62	22.24	1			1.59
.457	22.82	22.60	2	173	73.55	
.664	22.55	21.85	1			.229
.660	22.82	22.80	2	173	73.55	
.866	22.65	21.73	1			3.31
.862	22.82	22.45	2	173	73.55	
1.060	22.85	21.61	1			2.18
1.068	22.82	22.08	2	173	73.55	
1.261	22.75	21.14	1			3.36
1.270	22.82	21.85	2	173	73.55	
1.471	22.82	21.40	2	173	73.55	
1.677	22.82	21.30	2	173	73.55	
1.878	22.82	21.30	2	173	73.55	
.391	26.61	25.51	1			3.29
.392	26.78	26.35	2	168.5	71.65	
.650	26.62	25.41	1			4.53
.655	26.78	26.56	2	168.5	71.65	
.913	26.60	25.29	1			3.20
.914	26.78	26.10	2	168.5	71.65	
1.178	26.50	24.69	1			4.57
1.174	26.78	25.82	2	168.5	71.65	
1.434	26.55	24.36	1			2.96
1.435	26.78	25.08	2	168.5	71.65	
1.607	26.78	24.81	2	168.5	71.65	
1.785	26.78	23.85	2	168.5	71.65	
.335	30.85	29.57	1			5.17
.340	30.22	31.10	2	168	71.5	
.603	31.10	28.92	1			7.53
.612	30.22	31.10	2	168	71.5	
.857	30.92	28.75	1			2.96
.868	30.22	29.60	2	168	71.5	
1.120	30.75	28.25	1			3.71
1.131	30.22	29.30	2	168	71.5	
1.383	30.73	28.02	1			4.56
1.395	30.22	29.30	2	168	71.5	

* method 1 — from velocity profile
 method 2 — mean velocity measurement method

TABLE 91. (Cont'd)

.321	39.60	35.91	1			2.51
.327	38.70	36.00	2	160.2	68.1	
.555	38.80	35.32	1			1.50
.564	38.70	35.85	2	160.2	68.1	
.730	39.00	34.89	1			1.89
.745	38.50	35.55	2	160.2	68.1	
.983	38.50	34.00	1			2.94
.991	38.25	34.10	2	160.2	68.1	
1.112	38.18	33.02	2	160.2	68.1	
.270	48.30	43.50	1			1.15
.274	46.40	43.00	2	160.2	68.1	
.468	46.42	41.43	1			3.78
.473	46.30	43.00	2	160.2	68.1	
.624	46.00	41.15	1			2.92
.623	46.20	42.35	2	160.2	68.1	
.773	45.82	40.83	1			807
.774	46.20	40.50	2	160.2	68.1	
.890	45.60	40.05	1			1.37
.890	45.70	39.50	2	160.2	68.1	
.226	56.02	46.90	1			3.20
.227	56.00	46.85	2	158	65.75	
.350	56.00	46.97	1			2.55
.349	56.00	46.85	2	158	65.75	
.476	55.50	46.40	1			.431
.474	55.85	46.20	2	158	65.75	
.600	55.50	45.79	1			2.60
.601	55.45	44.60	2	158	65.75	

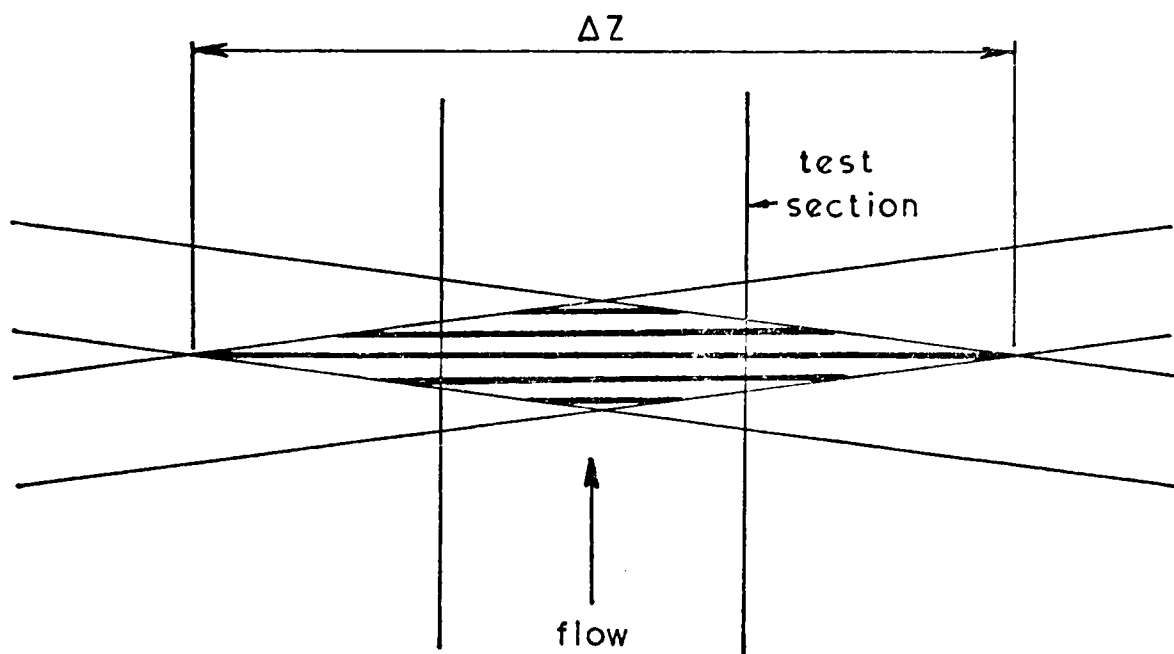


Fig.9.1. Arrangement for mean particle velocity determination

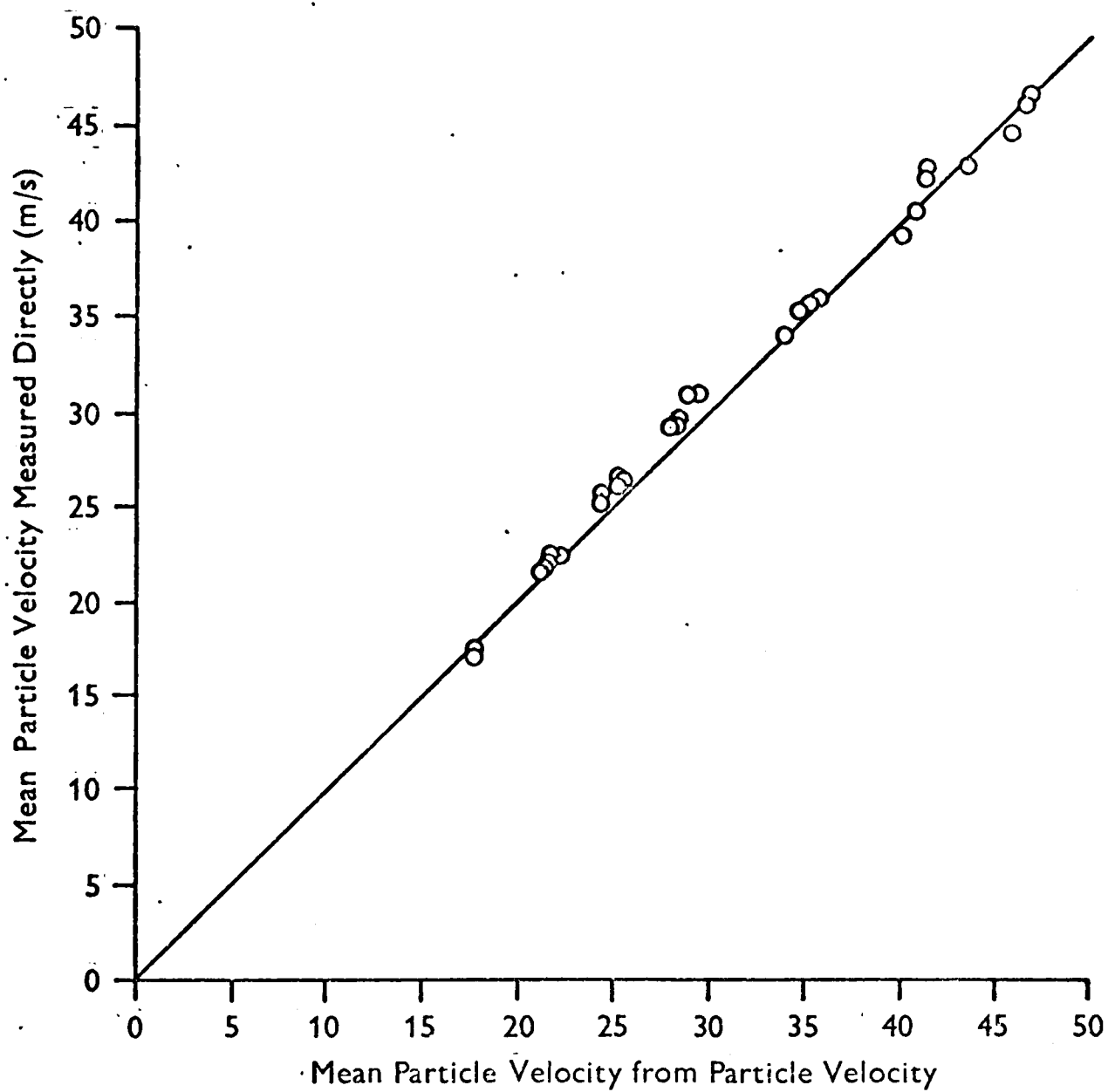


Fig. 9.2. Comparison of the direct and the local particle velocity methods for determination of mean particle velocity

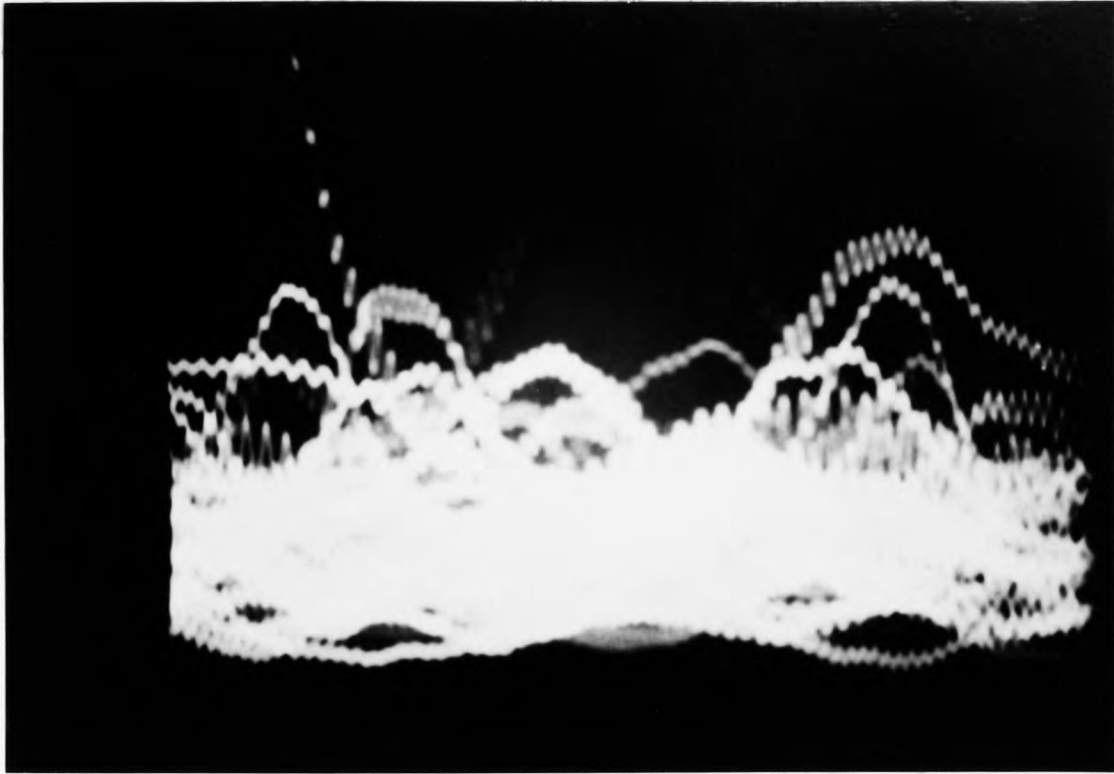


Fig.9.3. Typical oscilloscope display from a gas-solids flow

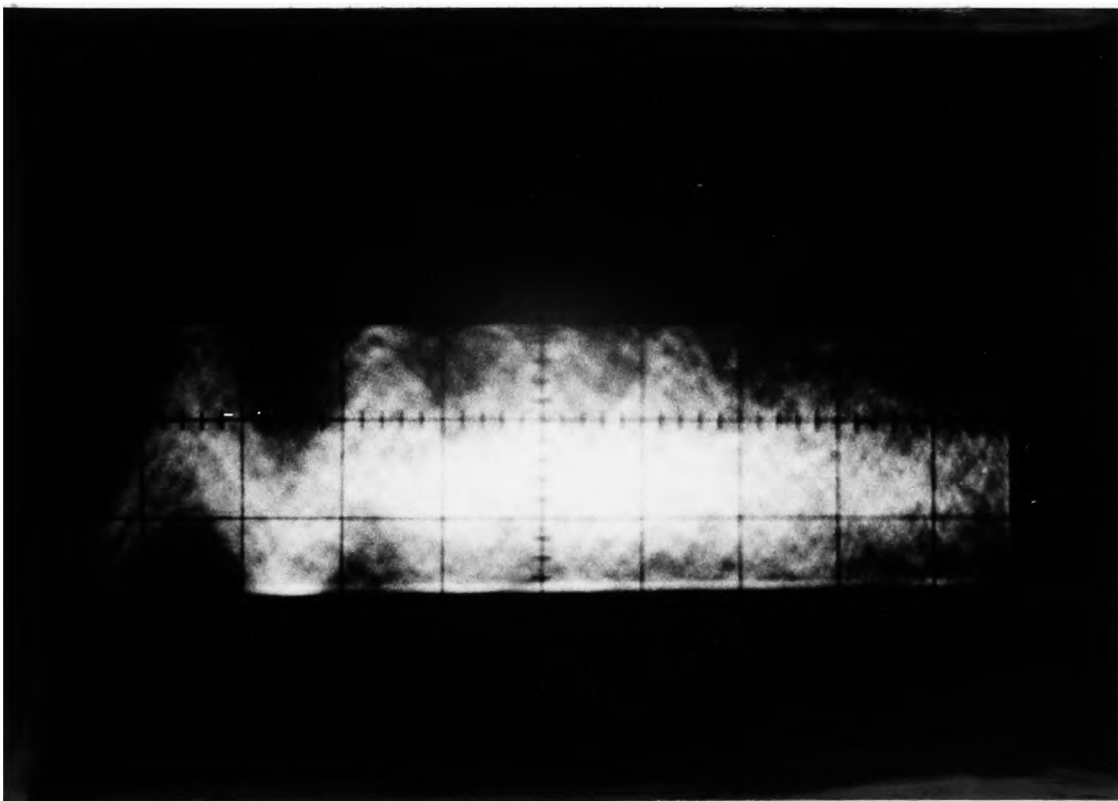


Fig.9.4. Oscilloscope display of processed signal

CHAPTER 10

PARTICLE WALL VELOCITY MEASUREMENTS

10.1 Introduction

Pneumatic conveying systems can be classified into either dilute or dense phase. The distinction between these two forms of transportation is dependent upon a rather arbitrary range of values of the solids loading ratio. However, dilute phase systems normally operate at high conveying velocity, low pressure and small solids loading ratio; whereas the reverse is true for dense phase flow. The transition between dilute and dense phase flows has been represented on a phase diagram by Zenz [127, 128], see fig. 10.1. The diagram is a \log^2 -plot of conveying velocity against pressure drop per unit length of vertical pipework.; The pressure drop for clean gas flow is represented by the line A - B, which is not, however, a true phase boundary since particle laden air flows have been reported in which the pressure drop per unit length was less than that for air alone, [113]. The introduction of solids into the air stream at some conveying velocity corresponding to point B will result in an increased pressure drop, this being indicated by point C. If the conveying velocity at this solids mass flow rate is now gradually reduced, the solids loading ratio will increase and the pressure drop will follow the line C - D which is initially parallel to A -B. Eventually, as the conveying velocity is further decreased, the pressure drop begins to rise rapidly towards position E. The system becomes unstable and the solid particles no longer flow as a dispersed phase, but in 'slugs'. The velocity at which the breakdown of the dispersed solids regime occurs is called the 'choking' velocity. A similar sequence of events could be described for path FGH, which represents the flow behaviour for an increased solids mass flow rate. A pneumatic conveying system which has been designed to work in the dilute phase mode should operate under flow conditions defined by points such as D and G, from considerations of minimum power, minimum

pipe erosion and minimum particle attrition. However, points D and G are close to choking conditions and slight misjudgement can result in blocked pipelines and plant shutdown. It is quite likely that most plants operate at flow conditions considerably different to those for optimum efficiency. This situation arises since correlations for predicting choking conditions are at best "order of magnitude" correlations. For example, Leung et al [129] derived an expression which "correlates to within $\pm 70\%$ the data reported by previous workers".

It is proposed in this chapter that the conditions which exist at the wall of the flow, since this is where the particle and conveying gas velocities are minimum, serve to indicate the onset of choking. Thus, by monitoring the particle wall velocity, the plant can be safely operated close to maximum efficiency positions of fig. 10.1.

10.2 Particle Wall Velocity Measurement Technique

Particle velocity measurements with the laser anemometer have, in previous chapters, been limited to solids loading ratios of about 2, since the scattered laser light was unable to pass through the suspension to the light collecting system at higher loading ratios. In this section, however, a 'backscatter' technique was used which measured the wall velocity only, avoiding the problem of penetration of the scattered light. Thus, the technique does not suffer from loading ratio restrictions. However, the collection of backscattered light presents other difficulties. The light intensity observed in backscatter is very small and close to the wall it is obscured by reflected light from the glass test section. The intensity of the signal carrying light is thus of the order of 1% of the total light received by the photodetector. In order to reduce the difficulties encountered, a laser anemometry system designed specifically for backscatter operation was obtained from Cambridge Consultants together with a signal processor.

The optical arrangement of this totally integrated unit is as shown in fig. 10.2, and consisted of a 5 mW He-Ne gas laser, beam director, beam splitter, focussing lens, collecting lens and photocathode. The non-concentric arrangement of the incident beams, in fringe mode, has been found to reduce flare at the pipe surface and hence to reduce noise collected at the light sensitive photodiode. The fringe spacing, δ , was set at 4.64 microns and a photograph of the system is shown in fig. 10.3. The output from the photodiode passed to the tracking filter unit [130] which gave a digital display of the incoming Doppler frequency, ν_D . The beam intersection region was arranged to protrude into the flow for about half its length, so that the effective $1/e^2$ measurement volume was about 1.7 mm. However, for high solids loading ratios it can be assumed that the depth of view of the anemometer was no more than the depth of the particle being monitored, since penetration is limited with respect to loading ratio. Thus, whilst at low solids loading the measurements were 'near wall' velocities, they can truly be described as particle wall velocities for high solids loading ratios.

10.3 Experimental Procedure

Measurements were limited to the lower velocity range of the pneumatic conveying rig in order to achieve sufficiently high solids loading ratios. Five superficial air velocities were selected, ranging from 11 to 20 m/s, whilst the solids loading ratio for each conveying velocity was increased in increments from about 0.5 to 4.5, the latter limit being imposed by the solids feed system and not by the measurement technique, from which good Doppler signals were observed throughout. The mean particle wall velocity at each solids loading ratio was obtained from the tracking unit digital output. Air flow rate was obtained from the orifice plate differential pressure and air temperature readings.

10.4 Results and Discussion

The experimental results are shown in fig. 10.4, which is a plot of particle wall velocity against solids loading ratio for various 'constant' superficial air velocities. There is inevitably a slight variation of air velocity for each set of results and the figures quoted are average values. Each plot may be considered to be a straight vertical line, similar to that shown dotted in fig. 10.1, except that the situation here is concerned with particle wall velocity and not superficial air velocity. All five curves exhibit a marked reduction in wall velocity for increasing solids loading ratio from 0.5 to about 1.5. However, there will almost certainly be a contribution to this apparent wall velocity because of the finite depth of field of the beam cross-over region at these loading ratios. It may be expected that true particle wall velocity is achieved for loading ratios above about 1.5.

At higher loading ratios and, with reference to the curves representing superficial air velocities of 13.71 m/s, 17.61 m/s and 19.13 m/s, it can be seen that the particle wall velocity is independent of solids loading ratio. Prior to this work it had been envisaged that the particle wall velocity gradually decreased as the solids loading ratio increased, until eventually it attained a negative value at the onset of choking. If this had been so then the particle wall velocity could have been related to mean particle velocity and thus enable the determination of mean flow properties for a given superficial air velocity and solids loading ratio. However, it is apparent from these results that no such gradual reduction in particle wall velocity occurs, but that it comes quickly as choking is approached. It is probable that the two remaining curves, for superficial air

velocities of 12.51 m/s and 11.29 m/s are typical of the eventual form of all such curves, even though the constant wall velocity portion is small due to the compressed nature of these two curves. It can be seen from these curves that two experimental points are included for higher loading ratios; one indicates a positive velocity and the other a negative velocity; that is, flow in the opposite direction to that of the main stream. Even though the laser anemometer cannot distinguish between upward and downward flow without the aid of frequency shifting [131] as was the case here, it was easy to distinguish between the two velocity components since the negative contribution was too low in frequency to register on the same tracking range as the positive component. It was observed that the flow at the wall, for loading ratios above 3 in the case of the lowest velocity curve, fluctuated between positive and negative, the transition being time dependent. The amount of negative flow increased with increase in solids loading, until eventually the whole flow at the wall was negative, even though the mean solids flow was in the upward direction. Slight increase in solids loading beyond this condition, in the case of $\bar{U}_a = 12.51$ m/s, resulted in choking.

It is interesting to note that the positive component of the velocity appeared to remain reasonably constant, as did the negative component, only the relative duration of each determining the position of the curve. Here, the position of the curve is an approximation, but it could have been located accurately by using frequency shifting techniques. The region of changing velocity direction is probably a good indication that the plant operation is close to optimum conditions and, provided that the proportion of time for which negative velocity prevails is small, there is no danger of

choking. It was noticed, however, that negative flow at the wall of the lower part of the glass test section occurred at lighter loading ratios than was experienced in the fully developed region. The collapse of the dilute phase regime is thus probably initiated at such places as pipe restrictions and flow direction changes.

It is conceivable that, since the output from the frequency tracking unit is a voltage proportional to velocity, a feedback system could be devised to control the solids mass flow rate and, therefore, maintain plant operation at optimum solids loading conditions.

Using fig. 10.4, it is possible to construct a graph of particle wall velocity plotted against superficial air velocity for constant solids loading ratio. Unfortunately, some interpolation is necessary since the experimental flow rig allowed only a limited set of results to be obtained and thus only five wall velocity positions are available.

Nevertheless, the possibilities can be seen by reference to fig. 10.5.

If the most efficient air flow rate for a given solids loading ratio is that where the particle wall velocity is just zero, (since a lower loading ratio would still utilise the same air flow rate and a higher one would result in some reverse flow), then the intersections of the constant loading ratio lines with the superficial air velocity axis thus defines the superficial air velocity required for that "most efficient" air flow rate. The inset graph in fig. 10.5 is a plot of optimum superficial air velocity against solids loading ratio and it indicates that the air velocity must be increased steeply in order to avoid choking, as loading ratio is increased. Fig. 10.5 also indicates that wall velocity can be independent of loading ratio well away from choking conditions, since the curves become inseparable at the higher air velocities.

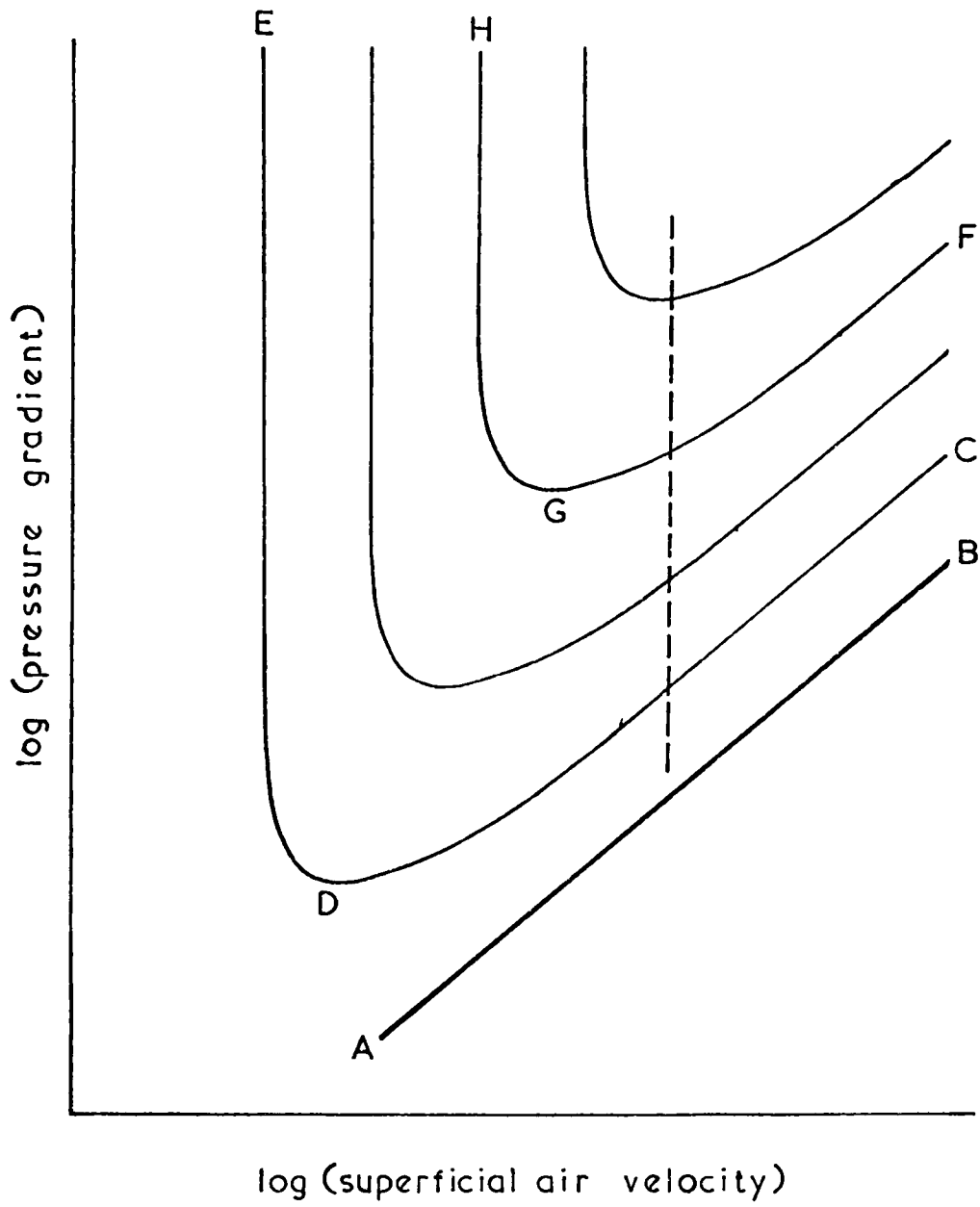


Fig.10.1. Phase diagram for vertical conveying

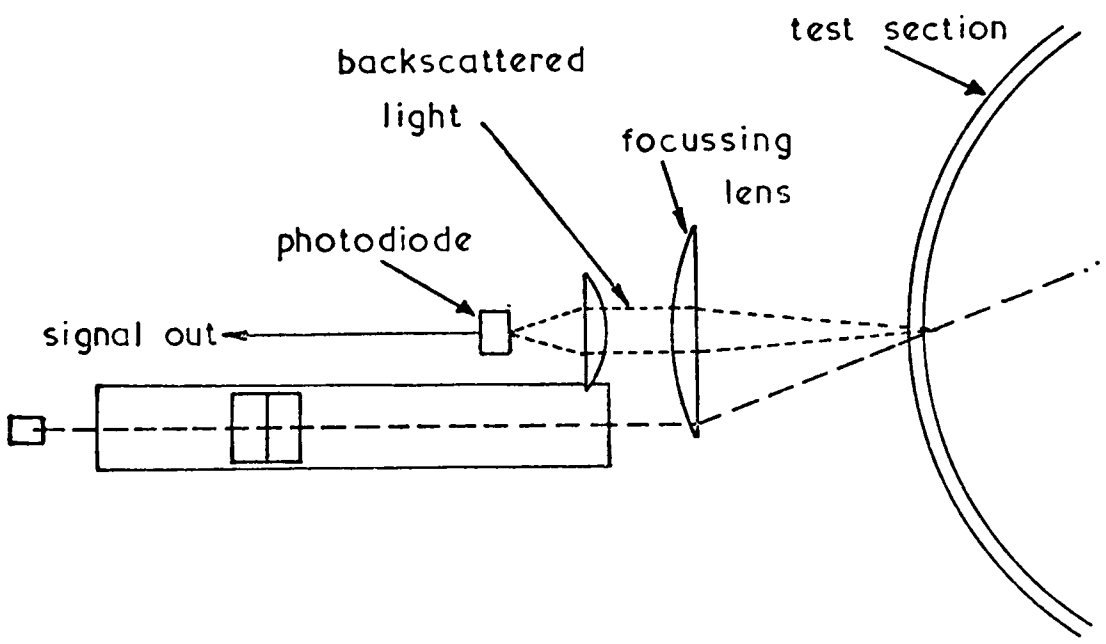
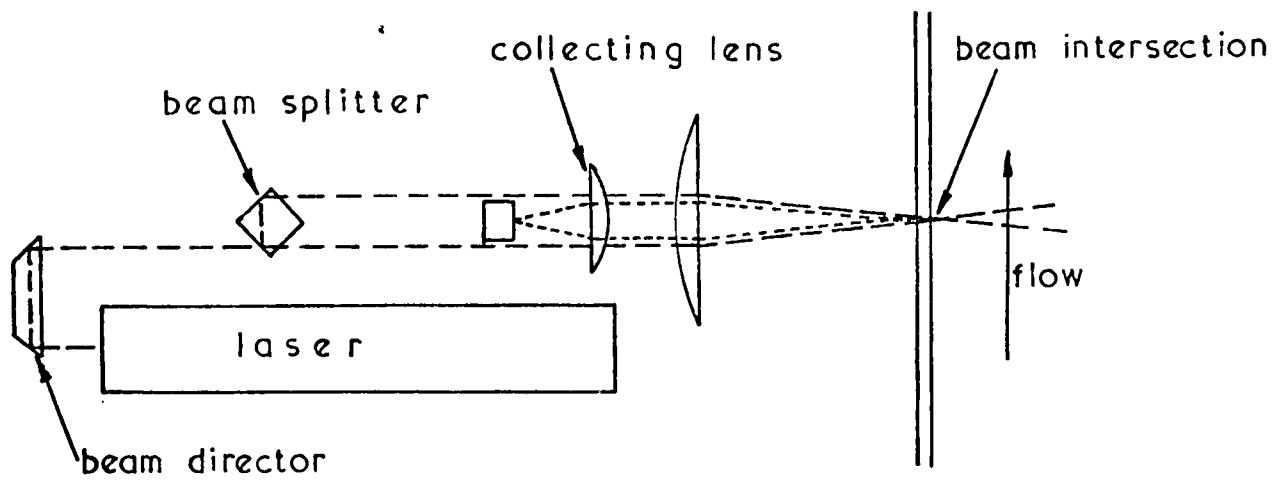


Fig.10.2. Particle wall velocity backscatter arrangement

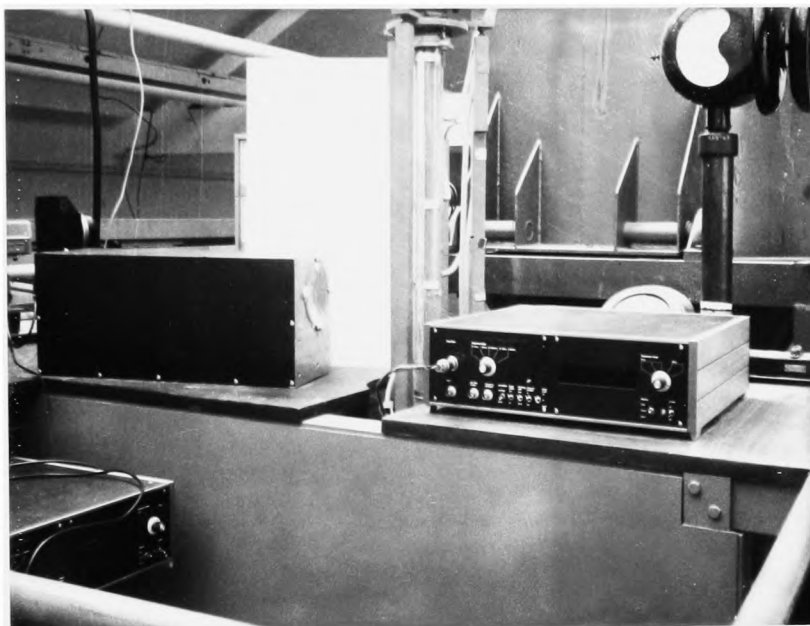


Fig. 10.3. Backscatter laser anemometer

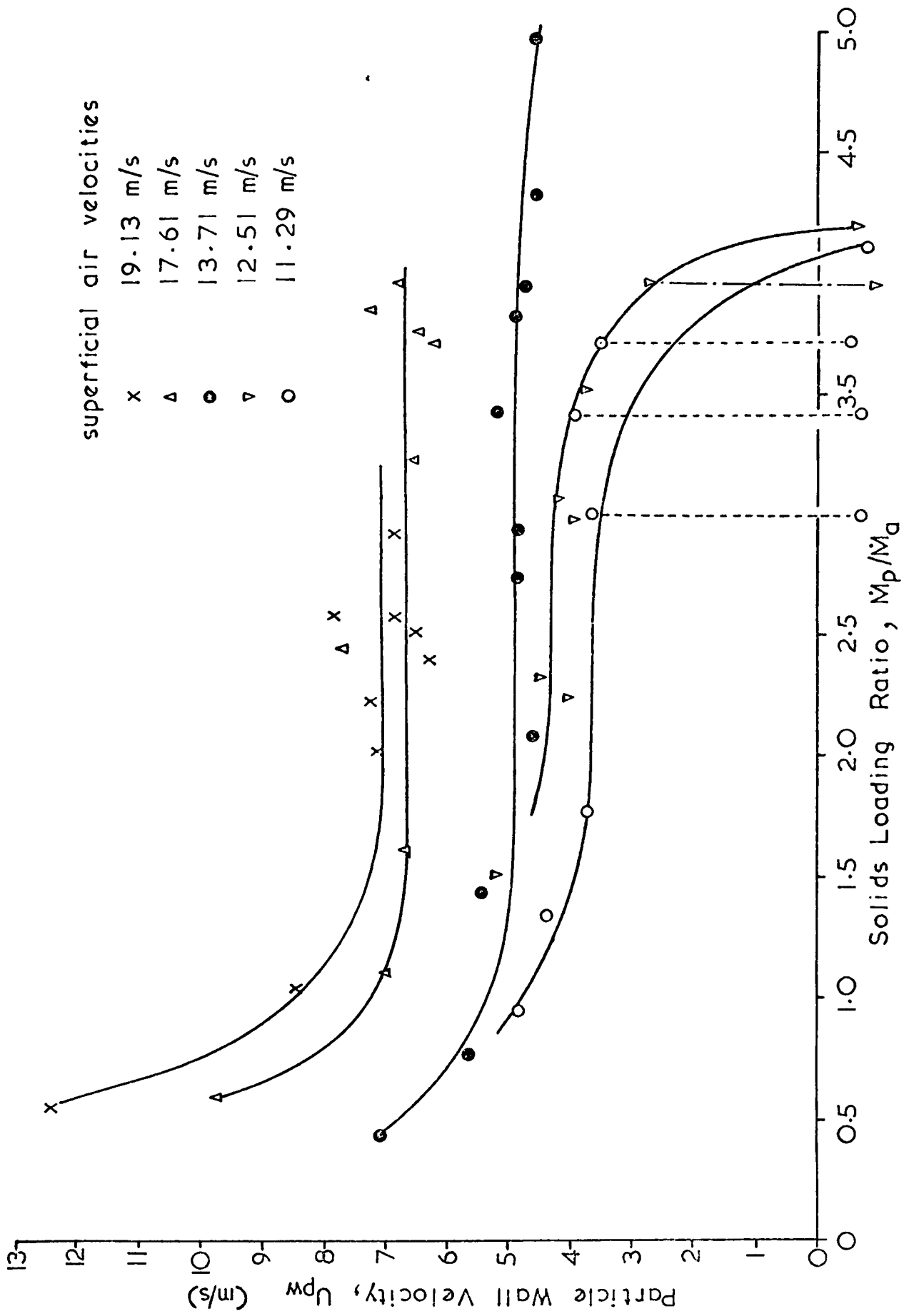
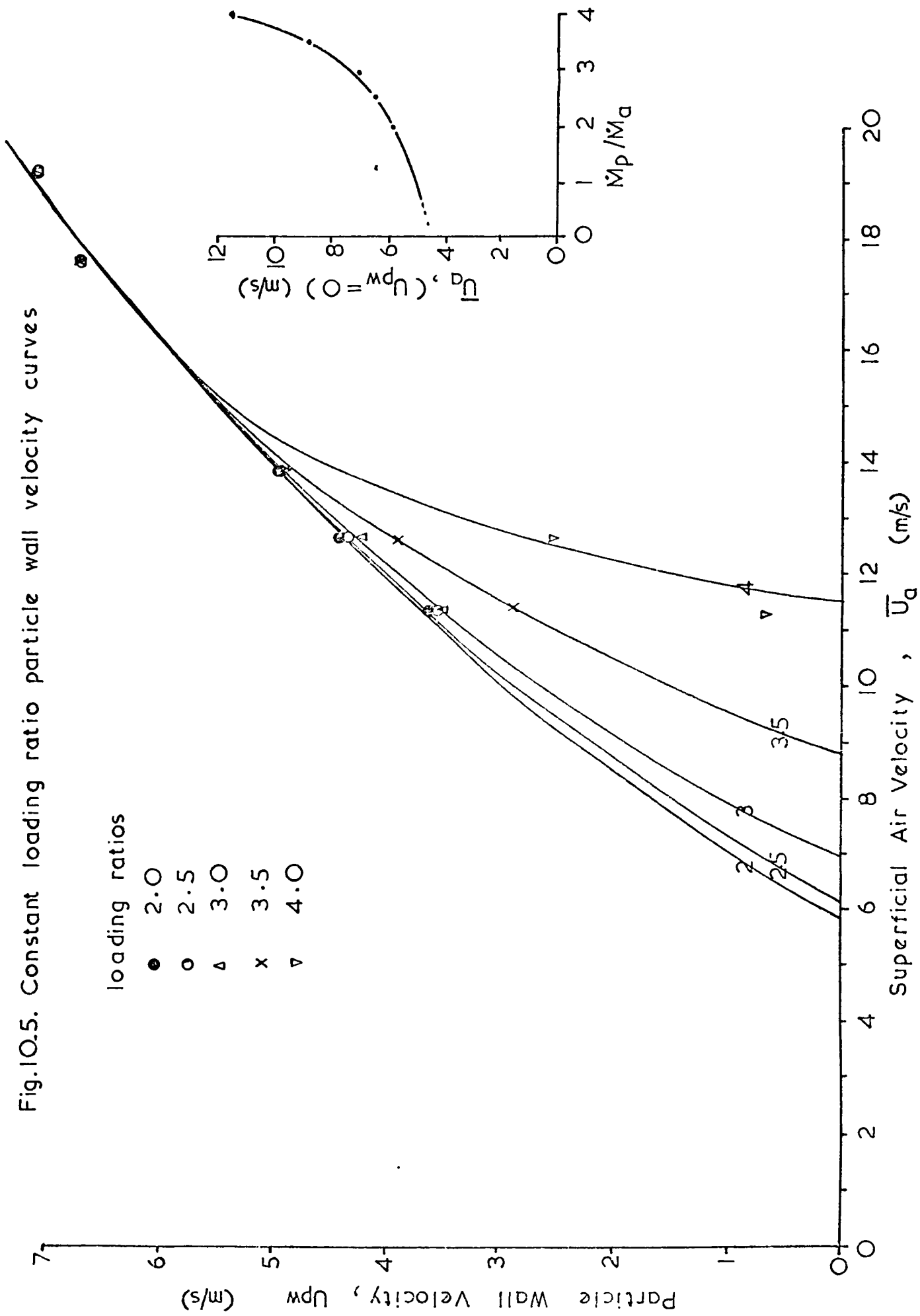


Fig. 10.4. Particle wall velocity curves



CHAPTER 11

PRESSURE DROP MEASUREMENTS

11.1 Introduction

In this chapter pressure drop experiments are described and the proportion of the total pressure drop due to the solids static head is calculated using solids velocities determined with the laser anemometer. The measurements are not meant to be exhaustive since the pneumatic conveying rig was not primarily built for this particular application. However, they are intended to augment the earlier work.

Knowledge of the pressure drop required in the flow of fluids through pipe lines is essential if reliable prediction of overall energy requirements is to be made for plant design. Although it is relatively easy to predict friction losses where single phase fluids are concerned, the procedure for gas-solid flow situations is not yet established. Terms such as density, viscosity and, because of slip between the phases, velocity, have less well defined meanings. A useful way to represent a gas-solids flow is by comparison with similar single phase fluid systems most of which predict pressure drop by reference to a 'friction factor'. An analogous friction factor can be defined for suspension flows.

11.2 Literature Survey

The total measured pressure drop, ΔP_m , for a given length of pipe in which solids are being conveyed pneumatically is due to a number of components, [97, 113] :-

$$\Delta P_m = \Delta P_{aa} + \Delta P_{ap} + \Delta P_{za} + \Delta P_{zp} + \Delta P_{\lambda a} + \Delta P_{\lambda p} \quad (11.1)$$

where ΔP_{aa} is the pressure drop due to acceleration of the air;
 ΔP_{ap} is the pressure drop due to acceleration of the solid particles;
 ΔP_{za} is the pressure drop due to the static head of air;
 ΔP_{zp} is the pressure drop due to the static head of solid particles;
 $\Delta P_{\lambda a}$ is the pressure drop due to air friction at the pipe wall;

and $\Delta P_{\lambda p}$ is the pressure drop associated with the energy required to overcome frictional contact between particles and between particles and the wall.

For horizontal flow, the terms ΔP_{za} and ΔP_{zp} are negligible [97, 132, 133], since the static head is essentially zero.

ΔP_{za} can be shown to be:-

$$\Delta P_{za} = \rho_a g L \quad (11.2)$$

where L is the length of test section over which pressure drop is being measured, and similarly, [113] :-

$$\Delta P_{zp} = \rho_{dp} g L = \rho_a g L \frac{M_p}{M_a} \frac{\bar{U}_a}{\bar{U}_p} = \Delta P_{za} \frac{M_p}{M_a} \frac{\bar{U}_a}{\bar{U}_p} \quad (11.3)$$

Equation (11.3) has sometimes been reduced by assuming $\bar{U}_p \approx \bar{U}_a$, which results in an underestimate of ΔP_{zp} . Boothroyd [134] suggested that the slip velocity could not, in his results, have been so great as to affect ΔP_{zp} by more than a few percent. The work here, however, shows that the error in neglecting the ratio \bar{U}_a/\bar{U}_p is sometimes of the order of 20%. This suggests a significant underestimate in Boothroyd's drag reduction calculations.

The air acceleration term has variously been expressed in the forms:-

$$\Delta P_{aa} = \frac{\dot{M}_a}{A} (\bar{U}_{a2} - \bar{U}_{a1}) \quad (11.4)$$

[10] where \bar{U}_{a1} and \bar{U}_{a2} are the velocities of the air at entry to and exit from the test section and A is the pipe cross sectional area, and from reference [134] :-

$$\Delta P_{da} = R \left(\frac{M_a}{A} \right)^2 \left[\frac{T_2}{P_2} - \frac{T_1}{P_1} \right] \quad (11.5)$$

where $\frac{RT}{P}$ is the gas specific volume, and from [135]

$$\Delta P_{da} = \left[\rho_a \varepsilon \bar{U}_a^2 \right]_0^L \quad (11.6)$$

where ε is the volume fraction of air.

From momentum considerations and considering acceleration from rest in a vertical riser, a common expression for ΔP_{aa} is [136, 97] :-

$$\Delta P_{da} = \frac{\rho_a \bar{U}_a^2}{2} \quad (11.7)$$

There are also equivalent expressions for the solids acceleration pressure drop such as :-

$$\Delta P_{dp} = \frac{M_p}{A} (U_{p2} - U_{p1}) \quad (11.8)$$

[10] where U_{p2} and U_{p1} are the particle velocities at entry to and exit from the test section. A further expression is :-

$$\Delta P_{dp} = 2\pi \left\{ \left[\int_0^{D/2} \frac{r}{\rho_p} U_p^2 dr \right]_2 - \left[\int_0^{D/2} \frac{r}{\rho_p} U_p^2 dr \right]_1 \right\} \quad (11.9)$$

this expression was modified by Boothroyd [134] on account of the difficulty in evaluating U_p and ρ_p , to the approximate relationship :-

$$\Delta P_{dp} = \frac{M_p}{M_a} \cdot \Delta P_{da} \quad (11.10)$$

Alternative expressions are [135] :-

$$\Delta P_{dp} = \left[\rho_p (1 - \varepsilon) \bar{U}_p^2 \right]_0^L \quad (11.11)$$

and from [136, 97] :-

$$\Delta P_{dp} = \frac{\rho_p \bar{U}_p^2}{2} \quad (11.12)$$

for acceleration from rest.

However, most situations considered have been for fully developed flow, where the acceleration terms, ΔP_{aa} and ΔP_{ap} can be eliminated from equation (11.1) to give :

$$\Delta P_m = \Delta P_{za} + \Delta P_{zp} + \Delta P_{\lambda a} + \Delta P_{\lambda p}, \quad \text{for vertical flow.} \quad (11.13)$$

Many authors [137, 138, 139, 143, 122, 101, 136, 133, 135, 111] have assumed that the pressure drop due to the conveying air is the same in the presence of solids as in the clean gas situations, though not always without justification [101], and most have calculated the air pressure drop contribution from the single phase Fanning equation :

$$\Delta P_{\lambda a} = \frac{4 \lambda_a L \bar{U}_a^2}{2D} \rho_a \quad (11.14)$$

where λ_a is the clean gas friction factor. It has then been necessary to find the contribution from the solid phase by subtraction and $\Delta P_{\lambda p}$ has often been expressed in terms of a solids friction factor, [137, 133] :-

$$\Delta P_{\lambda p} = \frac{4 \lambda_p L \bar{U}_p^2}{2D} \rho_{dp} \quad (11.15)$$

This expression varies through the literature, depending upon the measurements taken. Examples are [138]

$$\Delta P_{\lambda p} = \frac{4 \lambda_p L \bar{U}_p \bar{U}_a}{2D} \rho_{dp} \quad (11.16)$$

and from [135] :-

$$\Delta P_{\lambda p} = \frac{4 \lambda_p L \bar{U}_a^2}{2D} \rho_a \quad (11.17)$$

The above approach appears quite acceptable provided that the solids contribution, $\Delta P_{\lambda p}$, increases the total frictional pressure drop. However, where drag reducing flows are encountered [114, 134, 140] this approach will result in negative frictional pressure drops. A more

generally applicable method is to combine the contributions of solids and conveying gas friction into a single term, such as :

$$\Delta R_{\lambda_s} = \Delta R_{\lambda_d} + \Delta R_{\lambda_p} \quad (11.18)$$

giving the Fanning-type equation :-

$$\Delta R_{\lambda_s} = \frac{4 \lambda_s L \bar{U}_d^2}{2D} \rho \quad (11.19)$$

where λ_s is the suspension friction factor.

Amongst the workers who have combined ΔR_{λ_d} and ΔR_{λ_p} , Albright et al [141] found that the suspension friction factor had a negative slope when plotted against the suspension mass velocity, it being a linear function for mass velocities below about 250 lb/s.ft², for coal. They also indicated a distinct pipe diameter effect with the suspension friction factor decreasing with decrease in pipe size for solids loading ratios of about 200.

Boothroyd [134] found that $\Delta R_{\lambda_s} / \Delta R_{\lambda_d}$ showed considerable variation with tube size when conveying 15 micron zinc dust through 1, 2 and 3 inch bore pipes and he concluded that λ_s / λ_d would be expected to increase with increase in $\rho_d D^2 / \rho_p d^2 Re$. Boothroyd also found a distinct minimum, explained in terms of drag reduction, of λ_s / λ_d for $1 < \frac{\dot{M}_p}{\dot{M}_d} < 2.2$ for the 1 inch and 2 inch pipes.

It was suggested that the friction factor was dependent upon :-

$$\frac{\lambda_s}{\lambda_d} = \psi \left[\frac{\rho_d D^2}{\rho_p d^2 Re}, Re, \frac{\dot{M}_p}{\dot{M}_d} \right], \quad (11.20)$$

and a plot of $\frac{\lambda_s}{\lambda_d} \left[\frac{\dot{M}_d}{\dot{M}_p + \dot{M}_d} \right]$ against $\frac{\rho_d D^2}{Re}$ gave a common straight line for all his data.

Segler [6] also used a combined friction coefficient for horizontal transport studies, when conveying wheat and oats in 1.81 to 16.5 inch diameter pipes. He found that for a constant air flow rate the value of λ_s was proportional to the solids flow rate.

Mehta et al [97] used a variation of equation (11.19) by including the particle velocity and dispersed density :-

$$\Delta P_{\lambda_s} = \frac{4 \lambda_s L (\bar{U}_a^2 / \rho_a + \bar{U}_p^2 / \rho_p)}{2 D} \quad (11.21)$$

However, such an expression makes comparison of the suspension friction factor with the clean gas friction factor difficult.

There are, of course, many other publications devoted to pressure drop investigation, [142, 144, 145, 146, 147, 148, 149, 96] and an excellent review was published by Doig and Roper [150].

11.3 Experimental

The pressure drop measurements along the glass test section were taken with a multi-tube manometer inclined at 45° and containing manometer fluid of specific gravity 0.784. The pressure tapings, referred to in section 3.3, were located at distances of 6in., 1 ft.6in., 2ft. 6in., 5ft. 6in., 8ft. 6in., 9ft. and 9ft.6in. from the beginning of the test section. Facility was available for blowing pressurised CO₂ gas through the manometer lines in order to purge them clear of any deposited powder.

The measurements of pressure gradient were taken in conjunction with mean particle velocity determinations using the laser application outlined in sections 8.4 and 9.3. During these experiments the superficial air velocity was maintained approximately constant for

each set of results and the solids loading ratio was increased incrementally to the limit of penetration of the laser system. Pressure gradient readings were also taken for air alone for appropriate air velocities.

11.4 Results and Discussion

A typical set of pressure gradient profiles is shown in fig. 11.1. The curves show that the pressure gradient decreases from a maximum value at entrance to the glass pipe and becomes constant at about half way up the pipe. The large initial pressure gradient is attributable to the acceleration pressure terms ΔP_{aa} and ΔP_{ap} .

The curves will also be affected by the 'hold up' pressure terms

ΔP_{za} and ΔP_{zp} , which should show a linear increase, since for a given loading ratio they are proportional to the distance from entry to the pipe. Having reached a steady velocity, neglecting effects due to expansion of the conveying gas, the constant pressure gradient is largely due to the frictional effects, $\Delta P_{\lambda a}$ and $\Delta P_{\lambda p}$ only, after subtraction of ΔP_{za} and ΔP_{zp} .

For the fully accelerated region, that is where $L > 5$ ft., the total pressure gradients for each superficial air velocity are shown in fig. 11.2. This is a plot of measured pressure gradient $\Delta P_m/L$, against solids loading ratio for each superficial air velocity. As expected, the pressure drop increases with increase in both superficial air velocity and solids loading ratio. Data of this kind is usually presented as pressure gradient versus superficial air velocity for constant solids feed rate. However, the loading ratio is considered to hold more significance than solids feed rate.

Fig. 11.3 shows the ratio of the suspension friction factor to the clean gas friction factor against loading ratio. Each curve is similar to a graph presented by Farbar [146] who represented his experimental points by a single curve. However, his superficial air velocity range was very much smaller than that considered here and his loading ratios were up to 18. Thus, on the scale of his graph the separation of the points would seem negligible. Farbar suggested that his single line representation would be justified when the flow mixture was completely uniform.

The scatter in the experimental points is due mainly to the manometer fluid oscillations which were always present, particularly for the higher loading ratios, making estimation of pressure differentials rather difficult. The friction factor ratio increases with loading ratio and the rate of increase becomes more pronounced with higher superficial air velocities. The friction factor ratio may be represented by:

$$\frac{\lambda_s}{\lambda_d} = \frac{\lambda'_d}{\lambda_d} + \frac{\lambda_p}{\lambda_d} \tag{11.22}$$

where λ_d is the clean gas friction factor, and

λ'_d is the gas friction factor in the presence of particles.

For a given air velocity λ_d is constant, so the increase in λ_s/λ_d at constant air velocity is due to increases in λ'_d and/or λ_p . The effect of λ'_d in the present work is unknown. However, the relationship between λ_d and λ'_d has been explained in terms of both a thickening of the viscous sub-layer [112] and general turbulence suppression [151]. The contributions which make up λ_p are particle/wall and particle/particle collisions. These collisions, if considered non-elastic, produce a conversion of kinetic energy into other energy forms and the particles must thus be

re-accelerated to their former velocities. Particle/particle collisions have been considered to cause negligible pressure drop [150] since the total energy of the travelling particles will remain essentially constant. In addition, Soo [151] found that the shear stress due to collisions with the wall is negligible in comparison with that for the conveying gas and hence this component of friction factor was considered to be small. However, the increase in λ_s/λ_a for a given superficial air velocity must be caused by increased collisions or increased λ'_a or both, with increase in \dot{M}_p/\dot{M}_a . If λ_p is small, then the air friction factor λ'_a must increase with loading ratio due to either turbulence generation by the particles or to a reduction in the viscous sub-layer. Alternatively, if λ'_a remains essentially constant with increase in loading ratio and, as indicated in section 11.3, some authors have considered $\lambda'_a = \lambda_a = \text{constant}$, then particle/particle collisions and particle/wall collisions are important. In view of the particle turbulence intensity discussion in section 8.4.2., at least some contribution from the collisions appears likely. The mechanism of particle collision is discussed in reference [38].

The increase in λ_s/λ_a with increase in superficial air velocity, for constant \dot{M}_p/\dot{M}_a , may be explained in a similar manner. Particle impacts become more energetic and, although the loading ratio is constant, the number of particles will increase with increase in air velocity. In addition, λ_a decreases with increase in Reynolds' number, causing the friction factor ratio to become greater.

The importance of being able to account for the air to particle velocity ratio in equation (11.3) with respect to the solids "hold up" term,

ΔP_{2p} , is shown in fig. 11.4, which was obtained from the results for minimum air velocity.

The significant error in using the approximation :

$$\Delta P_{zp} = \Delta P_{za} \frac{\dot{M}_p}{\dot{M}_a} \quad (11.23)$$

is clearly seen and equation (11.22) differs from equation (11.3) by almost 23%. This produces an overestimate of λ_s/λ_a by 11%, which in some cases would obscure any drag reduction observations

As a final note to this section, some of the pressure drop measurements were taken in conjunction with section 8.4, in which electrostatic effects were monitored. No noticeable difference between pressure drop for the earthed and unearthed systems was observed throughout the tests. It may be of some value to repeat the tests using, for example, a copper pipe, which may have some charge transfer pressure gradient effect, as was observed by Duckworth and Kakka [152] when transporting glass ballotini particles.

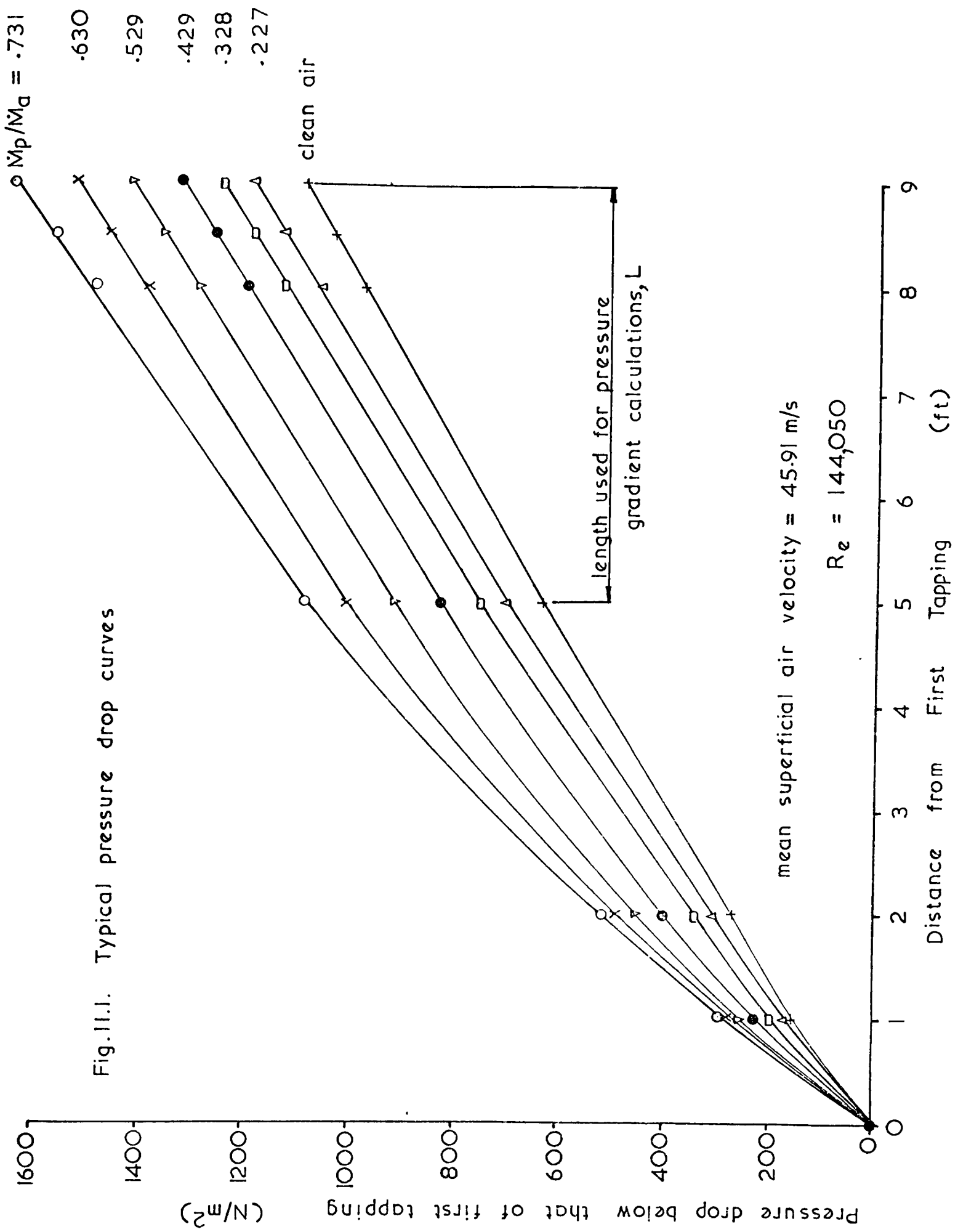


Fig. 11.1. Typical pressure drop curves

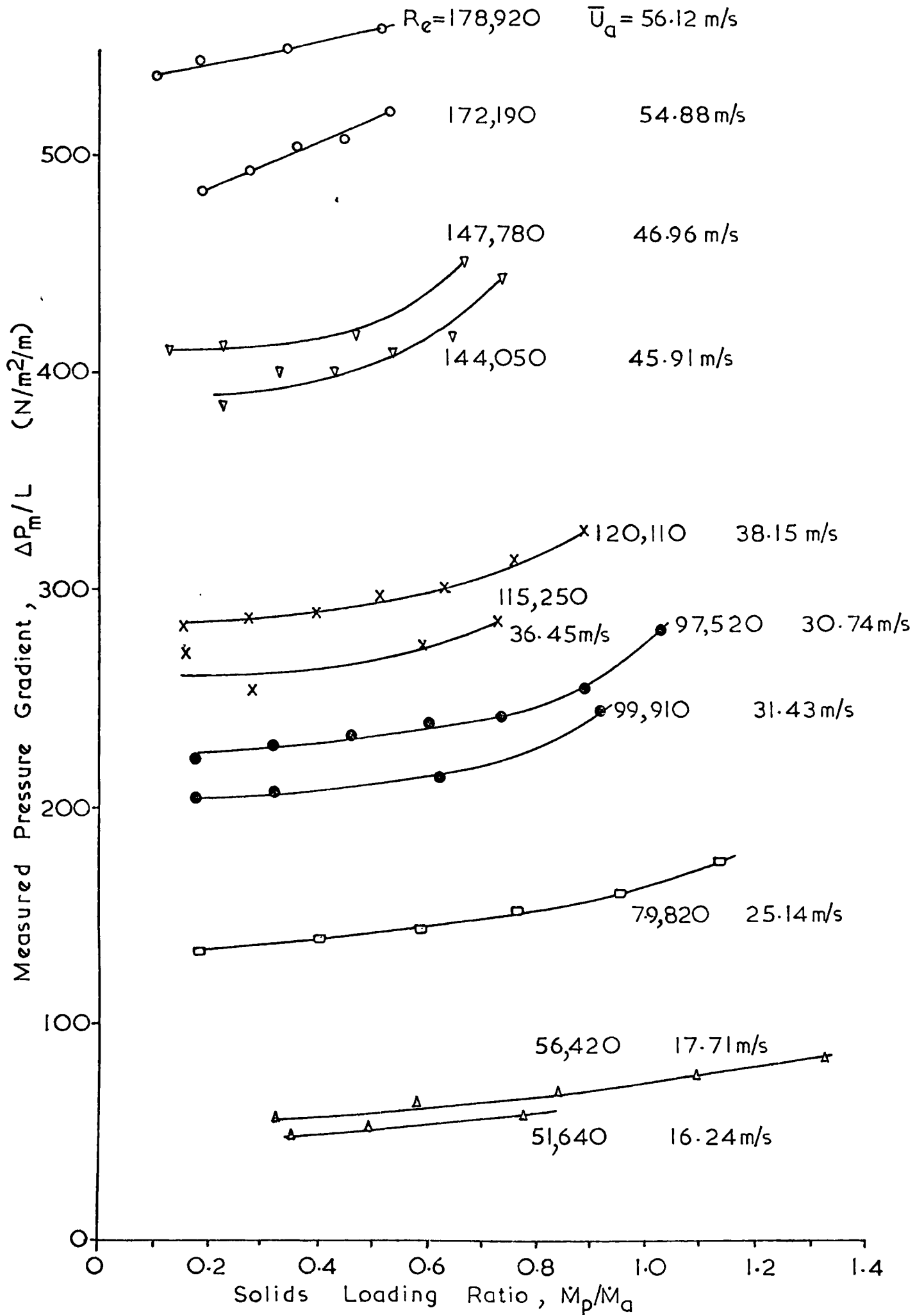


Fig.11.2. Measured pressure gradients

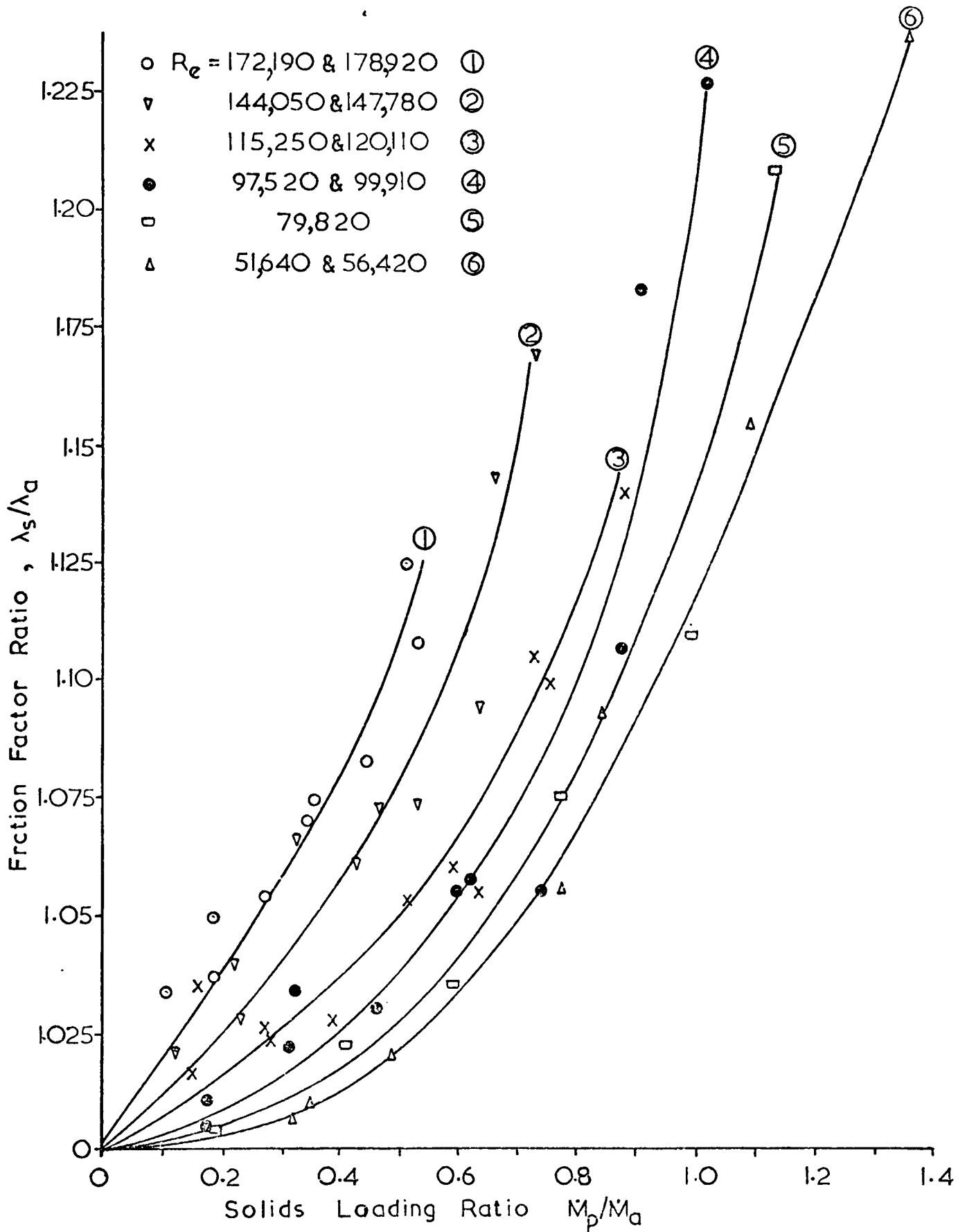


Fig.11.3. Friction factor ratios

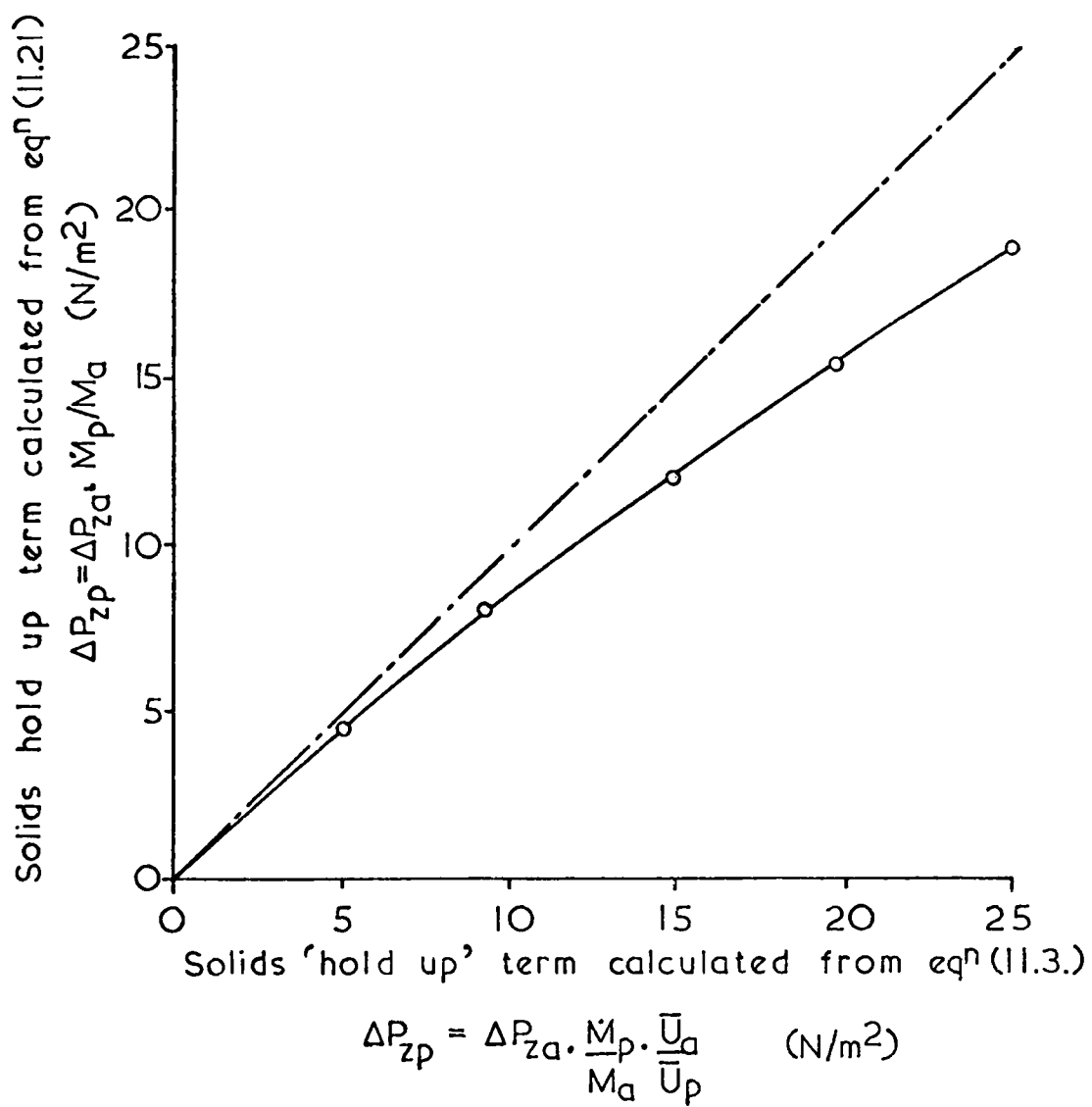


Fig. 11.4. Effect of neglecting velocity ratio from equation(11.3.)

CHAPTER 12

CONCLUSIONS

In this chapter, the more important deductions resulting from this investigation are summarised :-

Chapter 4

The alumina powder size analyses revealed that, although the size distribution of a batch noticeably varied during the first few circuits of the pneumatic conveying rig, thereafter, the powder size spectrum remained essentially the same when compared with that after several months use.

Chapter 5

Derivation of the laser anemometer working equations showed that the observed frequency, although governed by the observation angle for reference beam mode, was independent of the observation angle in differential Doppler mode. It was also shown that these equations could be derived from fringe considerations. It was found useful to distinguish between the probe volume and the volume of measurement, which is modified by the observation angle, θ , and the pinhole diameter.

Velocity gradient broadening was shown to be given by:-

$$\delta \nu_{D_{vg}} = \frac{2 \sin \theta}{\lambda_i} \cdot \frac{dv}{dr} \cdot \delta r$$

for fully developed, axi-symmetric flow and it was also shown that the summation of the remaining broadening terms could be found experimentally by using a rotating disc.

Since the solid angle of light collection is unrestricted in the fringe mode of operation, unlike the reference beam mode case, this arrangement has potentially the higher signal-to-noise ratio.

Chapter 6

The clean air velocity profiles and turbulence intensity measurements barely penetrated the buffer layer; however, the profiles measured approximated closely to accepted standards. Paraffin oil seeding was found to be unsatisfactory for the present flow system, but the T_iO_2 arrangement was quite successful.

Chapter 7

The effect of "large" particle diameter on the probe volume dimensions is to increase the probe volume with respect to that for small particles. The signal strength and signal visibility are not affected detrimentally when velocity measurements of particles greater than 5 microns are concerned; that is, good visibility and signal strength can be achieved for both spherical and irregular large particles. Scattering in this region is governed by reflection, so that small particle scattering theory is not applicable. The choice of fringe spacing for a size spectrum of these particles is largely irrelevant.

Chapter 8

No distinct advantage was found in the use of either mode of operation, apart from the fact that the fringe mode was easier to set up.

Measurements were possible for solids loading ratios up to 1.5 when $\theta = 0$, this figure reducing with increase in conveying velocity, since less photons of light are scattered at higher velocity. The solids loading ratio penetration reduced when θ was made 45° , due to reduction in scattering intensity at this angle. For measurements in flows with higher loading ratios, a more powerful laser may be useful.

None of the particle velocity profiles measured correlated even

approximately, with the relationship suggested by Soo, equation (8.1), and this may have been due to the better spatial resolution and lack of flow disturbance achieved in the present work. The particle velocity profiles were found to flatten with increase in loading ratio, but probably remain stable for a given loading ratio, with increase in conveying velocity. There was negative particle slip at the wall.

Comparison of the clean air profiles with the particle velocity profiles revealed that the velocities of both phases at the flow core could not be the same if the air profile in the presence of solids was to remain the same as the clean air profile. This conclusion is in disagreement with reference [101]. The mean slip velocity was found to increase with loading ratio and with Reynolds' number.

The $1/e^2$ probe length was proved to be a realistic concept and there was uncertainty in the precise measurement position when part of the probe volume was outside the flow boundary.

No difference in the velocity profile or the turbulence intensity profile was apparent in the unearthed system, when compared to the earthed system.

Particle turbulence intensity, which is attributed to air turbulence, particle size distribution, non-axial particle trajectories, particle collisions and local dispersed solids density fluctuations, can be greater than the turbulence intensity of the air. The particle intensity was found to increase with loading ratio and with conveying velocity.

Chapter 9

The laser anemometer can be used for the accurate measurement of average particle velocity in a suspension flow having a solids loading

ratio up to 2.2. Since the system is capable of continuous monitoring, it may be possible to use the anemometer in an automatic control loop.

Chapter 10

The investigation described in this chapter illustrated that the condition of the solids phase flow at the pipe wall gives an indication of the character of the mean particulate phase flow with respect to the proximity of choking conditions. In addition, it was shown that the laser anemometer can be used to achieve useful measurements in conditions of high solids loading and could certainly be used for loading ratios higher than those achieved with the present pneumatic conveying rig. On account of the voltage analogue output, the laser system could be adapted to control the solids flow rate and thus maintain the system at its optimum efficiency.

It was found that the solids velocity at the wall does not decrease gradually with increase in loading ratio, but remains essentially constant and independent of loading ratio until near-choking conditions prevail. For these conditions, both positive and negative wall velocity can exist and the resulting wall velocity decreases relatively rapidly with loading ratio until choking is achieved. The appearance of negative components of wall velocity signifies the close proximity of the optimum solids loading ratio.

Chapter 11

The importance of the velocity ratio, \bar{U}_a/\bar{U}_p for calculation of the solids "hold up" term, ΔP_{zp} , was shown. The suspension friction factor, λ_s , was found to increase with loading ratio and may depend upon Reynold's number, but no drag reduction was observed. Particle collisions are thought to be an important contributory factor to the suspension pressure drop, but electrostatics were shown to have no effect on pressure drop for the present flow system.

CHAPTER 13

SUGGESTIONS FOR FURTHER WORK

The studies outlined below refer to possible future areas of work in which the application of laser anemometry to gas-solids flow would be of benefit. Many of the suggestions originate from the present investigation and these are identified with the relevant chapter.

Throughout this study both fringe and reference beam modes have been used and it would seem reasonable to examine the characteristics of the one beam anemometer mentioned in section 5.3, although it is not envisaged that the technique will be suitable for mean particle velocity measurement. The limit of penetration of the two modes used in this work has not been investigated fully, since this will be partly dependent upon the laser power in the cross-over region; however, the cost of more powerful lasers could prove to be prohibitive. It was suggested in sections 8.3.2 and 9.5 that spectrum analysis might extend velocity measurements into denser flows. This was evident in both cases since there were still signals visible on the filtered oscilloscope trace even when the tracking unit could not follow them.

The logical progression from the study of vertical suspension flows is that for horizontal flow, which would require both horizontal and vertical traverses since some earlier studies, in which gravity was not negligible, have reported non-symmetry about the pipe axis [83, 84]. Developing flows in both horizontal and vertical pipes would be of interest, particular attention being paid to the inlet conditions and the length of pipe required for the establishment of fully developed flow.

A continuation of the work in chapter 10 on the back scatter particle

wall velocity technique is considered highly desirable. Higher solids loading ratios and dense flows in both horizontal and vertical pipes should be examined, preferably with an anemometry system incorporating frequency shifting for directional sensitivity. A pneumatic conveying rig capable of transporting in dense phase is at present under construction at Thames Polytechnic and the facility for back scatter measurements will be provided for horizontal, vertically upwards, vertically downwards and a 45° inclined flow.

It has been mentioned in section 9.5 and 10.4 that there is a possibility of using the laser anemometer for mean velocity and particle wall velocity measurements in a control loop. The tracking unit output would be used to control either the conveying air volumetric flow rate or the solids feed rate. Development of such a system on a pilot scale could be most valuable.

Bend wear is an expensive problem in industry and any further information about the mechanism of wear would be beneficial. Particle velocity is a major cause of bend wear and a study of particle velocity phenomena around bends is desirable. It would, however, be difficult since glass bends of industrial size would be needed and refraction of the laser beams would prove troublesome.

The measurement of particle number density was reported in reference [83] for large particle flows, 500 microns, in which a counting technique noted each particle as it passed through the laser beam cross-over region. This method is acceptable for large particles since relatively high loading ratios can be achieved with relatively few particles in the flow. Generally, there will be no more than a single particle in the probe volume at any instant. For small particles, such as those used in this study, frequency envelope counting cannot be used without

some ambiguity since there may be many particles within the probe simultaneously. However, the intensity of scattered light is proportional to the solids dispersed density and this is perhaps the best alternative to counting [81, 153]. Development of such a technique would give simultaneous velocity and density information.

The measurement of particle velocity and turbulence intensity profiles for two separate mono-sized spherical particle suspensions, and then consideration of a mixture of the two, should improve our understanding of the importance of particle/particle collisions (section 8.4).

Collisions in a suspension of equal finely divided spherical particles should be small in comparison with the flow of mixed particle size, so that any marked change in turbulence for the mixture could be attributable to the increased collisional activity and particle size distribution. The study should be augmented with cinematographic evidence and may include pressure drop tests (section 11.4).

The measurement of air velocity and turbulence intensity in the presence of concurrently transported particles has received some attention by previous researchers [101, 154], but these are difficult measurements to make if flow disturbance is to be avoided. However, if the conveyed particles are large enough to produce considerable slip, then a mixture of sub-micron particles, for air velocity determination, with the larger particles should give two distinct peaks on, say, a spectrum analyser. Alternatively, individual signals could be analysed on a magnetic tape recording. The observations made in section 7.2.2 (fig. 7.4) may be of some value here; however, many problems would need to be resolved. For example, the signal strength of the larger particles will inherently be many times that of the sub-micron particles. The correct balance of small particles, section 6.5, is also important, causing filtration

and feed problems. If the technique proved feasible, however, then it may be possible to measure particle and air velocities and more than one turbulence component for both phases, with the one measuring system.

‘ _____ .

NOMENCLATUREChapter 2

A_p	particle cross-sectional area
C_D	particle drag coefficient
C_L	particle lift coefficient due to Magnus effect
d	particle diameter
d_e	equivalent particle diameter
F_D	drag force
g	acceleration due to gravity
j	contact angle between two colliding spherical particles
m_1, m_2	individual particle masses in two monodispersed particulate clouds
n_1, n_2	number of particles in each of those clouds
p	static pressure
Re_p	particle Reynolds' number
t, ξ	time
\bar{u}	vector fluid velocity (equation 2.1)
U_∞	free stream fluid velocity relative to stationary particle
u_f	instantaneous fluid velocity in turbulent flow field
u_p	instantaneous particle velocity in turbulent flow field
u_p', u_p''	x-direction velocities of two particles before impact
u_p^*, u_p^{**}	x-direction velocities of those particles after impact
$ u_{p1} - u_{p2} $	absolute value of mean difference velocity between two monodispersed particle clouds
V	instantaneous velocity of a sphere in a turbulent flow field, relative to the instantaneous fluid velocity, i.e. $V = (u_f - u_p)$
ρ_f	fluid density

A.1.2.

ρ_p	particle density
μ	fluid dynamic viscosity
ω	particle rotational velocity

Chapter 4

A	manometer reservoir cross-sectional area
a	manometer tube cross-sectional area
D	test section diameter
ΔH	pressure drop across orifice plate
Δh	vertical height of manometer fluid column
l	length of manometer fluid column
M	Mach number
\dot{M}_a	air mass flow rate
\dot{M}_p	solids mass flow rate
M_p	mass of collected solids
P_s	stagnation pressure of airstream
P	static pressure of airstream
P_a	absolute pressure of the air in the test section
R	gas constant
r	radius of measurement position from pipe axis
T_a	air temperature
U_a	local air velocity at radius r
V_a	air volumetric flow rate
γ	ratio of specific heats
ρ_a	air density
ρ_m	manometer fluid density
α	manometer limb inclination

Chapter 5

a, b, c, e	dimensions given in fig. 5.11
$2b$	laser beam diameter
$2b_0$	beam diameter at the waist region of a focussed laser beam
$2b_w$	diameter of image of photomultiplier in plane of probe volume
c	velocity of light in medium considered
D	effective diameter of photodetector surface
d	diameter of beam cross-over region
d_{ph}	photomultiplier pinhole diameter
e	base of natural logarithms
E_1, E_2	amplitude of electric field vectors in the two laser beams
e_1, e_2	electric fields of the two beams
e'	electron charge
f_1, f_2, f_3	focussing lens focal lengths
Δf	detector bandwidth
G	photomultiplier gain
g	discriminator maximum output voltage
h	Planck's constant
$h\nu$	energy of a quantum of radiation of frequency ν
I	light intensity across diameter of laser beam
I_0	maximum light intensity at beam centre
i	photomultiplier output current
i_D	photomultiplier cathode dark current
K	$= \delta / (\delta - 1)$ where δ is the average gain per photomultiplier dynode
k, l	unit direction vectors
m	distance between probe volume and photodetector surface in equation (5.35)

A.1.4.

N	number of fringes in the $1/e^2$ probe volume
P_B	background light power
P_1, P_2	light power of the two laser beams
R_L	amplifier effective resistive load
s	distance defined in fig. 5.8
SNR_{power}	signal-to-noise power ratio
t	time available for velocity measurement
u	discriminator output voltage
\bar{V}	particle velocity vector
v	instantaneous vertical component of \bar{V}
v'	velocity fluctuating component about the mean velocity, V (i.e. $v = V + v'$)
x	radial distance from laser beam centre
$\Delta X, \Delta Y, \Delta Z$	probe volume dimensions in X, Y, Z co-ordinate directions
$\Delta Y'$	dimension of $1/e^2$ probe volume in fig. 5.11
$4kTR_L \Delta f$	mean square thermal photomultiplier noise voltage
β_1, β_2	phase angles
δ	anemometer fringe spacing
ϵ^2	heterodyning efficiency
λ_i	incident laser light wavelength
λ_{sc}	scattered light wavelength
ν_i	incident laser light frequency
ν_p	scattered light frequency relative to moving particle
ν_{sc}	scattered light frequency relative to a stationary observer
ν_D	Doppler shift in frequency
ν'_D	frequency fluctuations about the mean

ν_{osc}	voltage controlled oscillator frequency
ν_0	analyser band pass filter centre frequency
$\delta\nu_{Dt}$	spread in frequency due to finite transit time broadening
$\delta\nu_{Dvg}$	spread in frequency due to velocity gradient broadening
$\delta\nu_{Dd}$	broadening registered by disc experiment, (section 5.9.2)
η	quantum efficiency of photodetector
ψ_1, ψ_2, ψ	angles defined in fig. 5.8
ξ	phase lag
$\delta_1, \delta_2, \delta_3$	angles defined in figs. 5.2, 5.3, and 5.4
θ	half angle between two intersecting laser beams
ω_1, ω_2	circular frequencies
ω_D	circular Doppler frequency
τ	time taken for a particle to cross the probe volume

Chapter 6

n	index in equation 6.1
R	pipe radius
Re	pipe Reynolds' number
U_a	local mean air velocity
$U_{a_{max}}$	maximum air velocity at pipe centre
$U_{a_{mean}}$	average air velocity
u'_a	air velocity fluctuating component about the mean, U_a (i.e. $u_a = U_a + u'_a$) where u_a is the instantaneous component of velocity
U_τ	friction velocity = $\left(\frac{\text{wall shear stress}}{\text{density}} \right)^{\frac{1}{2}}$
Y	distance from pipe wall
ϕ	angle between observation position and optical axis
ν	kinematic viscosity
ν_D	Doppler frequency

A.1.6.

$\delta V_{D_{Vg}}$

spread in frequency due to velocity gradient broadening

δV_{D_d}

broadening registered by disc equipment, (section 5.9.2)

Chapter 7

2b	laser beam diameter
d	particle diameter
e	base of natural logarithms
I_{max}	maximum signal excursion at probe centre
I_{min}	minimum signal excursion at probe centre
ΔI	signal a.c. amplitude
ΔI_{max}	maximum signal a.c. amplitude
$\Delta X, \Delta Y, \Delta Z$	probe volume dimensions
δ	anemometer fringe spacing
ϕ	angle between detector and optical axis
λ_i	laser light wavelength
θ	half angle of beam intersection

Chapter 8

2b	laser beam diameter
$2b_0$	laser beam waist diameter after focussing
$2b_w$	diameter 'seen' by photomultiplier pinhole at the plane of the cross-over region
D	glass pipe diameter
d	particle diameter (mean effective)
e	base of natural logarithms
f_1, f_2, f_3	lens focal lengths
I_p	current due to charge transfer
L	test length for I_p measurement

A.1.7.

m	index in equation (8.1)
\dot{M}_a	air mass flow rate
\dot{M}_p	solids mass flow rate
N	number of particles
p	index in equation (8.2)
Q	electrostatic charge
R	pipe radius
U_p	local mean particle velocity
U_{pw}	local mean particle wall velocity
U_{p0}	local mean particle velocity at pipe axis
\bar{U}_a	average superficial air velocity
\bar{U}_p	average particle velocity
u'_a	fluctuating component of local air velocity
u'_p	fluctuating component of local solids velocity
w_p	weight of average particle
$\Delta X, \Delta Y, \Delta Z$	probe volume dimensions
y	distance from pipe wall
2θ	angle of laser beam intersection
λ_i	laser light wavelength
ρ	air density
ϕ	angle between optical axis and observation position

Chapter 9

\dot{M}_a	air mass flow rate
\dot{M}_p	solids mass flow rate
\bar{U}_p	average solids velocity
$\Delta X, \Delta Y, \Delta Z$	probe volume dimensions
δ	fringe spacing
2θ	angle of laser beam intersection

Chapter 10

U_{pw}	particle wall velocity
\bar{U}_a	average superficial air velocity
ν_D	Doppler frequency shift

Chapter 11

A	pipe cross-sectional area
D	pipe diameter
d	particle diameter
g	acceleration due to gravity
L	length of test section for pressure gradient measurement
\dot{M}_a	air mass flow rate
\dot{M}_p	solids mass flow rate
ΔP_m	measured pressure drop
ΔP_{aa}	pressure drop due to acceleration of the air
ΔP_{ap}	pressure drop due to acceleration of the particles
ΔP_{za}	pressure drop due to the static head of air
ΔP_{zp}	pressure drop due to the static head of particles
$\Delta R_{\lambda a}$	pressure drop due to the air friction at pipe wall
$\Delta R_{\lambda p}$	pressure drop associated with the energy required to overcome frictional contact between particles and between particles and the wall
P	absolute air pressure in the test section
R	gas constant
Re	pipe Reynolds' number
r	radius of measurement
T	air temperature
U_p	local mean particle velocity at radius r
\bar{U}_a	average superficial air velocity
\bar{U}_p	average particle velocity

A.1.9.

ρ_a	air density
ρ_p	particle density
ρ_{dp}	particle dispersed density
ε	air volume fraction
λ_a	clean air friction factor
λ'_a	air friction factor in presence of solids
λ_p	solids friction factor
λ_s	suspension friction factor
ψ	function in equation (11.19)

LIST OF FIGURES

- 3.1 Line diagram of pneumatic conveying system
- 3.2 Plant layout (plan view)
- 3.3 Plant layout (elevation)
- 3.4 Photograph of pneumatic conveying plant
- 3.5 Photograph of pneumatic conveying plant
- 3.6 Ball valve characteristics
- 3.7 Screw feeder
- 3.8 Photograph of screw feeder
- 3.9 Screw feeder extension pieces
- 3.10 Examples of bend wear

- 4.1 Orifice plate details
- 4.2 Photograph of pitot-static tube traverse section
- 4.3 Pitot-static tube traverse results for test no. 10
- 4.4 Graphical analysis of pitot-static traverse for test no. 10
- 4.5 Orifice plate calibration
- 4.6 Screw feeder calibration
- 4.7 Load cell calibration
- 4.8 Alumina size distribution
- 4.9 Electron micrograph of Ti_2O_3 particles
- 4.10 Titanium dioxide size analysis

- 5.1 Doppler shift of scattered light
- 5.2 Analysis of reference beam mode
- 5.3 Analysis of differential Doppler mode

A.2.2.

- 5.4 Analysis of one beam mode
- 5.5 Intersection region
- 5.6 Fringe formation in the $1/e^2$ ellipsoid
- 5.7 Laser anemometry arrangement for fringe mode
- 5.8 Reference beam mode coherence condition
- 5.9 View from photomultiplier pinhole
- 5.10 Measurement volume - fringe mode
- 5.11 Measurement volume - reference beam mode
- 5.12 Broadening determination
- 5.13 Reference beam mode arrangement
- 5.14 Photograph of laser anemometry equipment
- 5.15 Block diagram of tracker

- 6.1 $T_i O_2$ fluidising unit
- 6.2 'Clean air' circuit
- 6.3 Air velocity profiles
- 6.4 Comparison between experimental points and orifice plate calibration curve
- 6.5 Axial turbulence intensity profiles

- 7.1 Signal form variation with ΔZ position
- 7.2 Probe length experiments
- 7.3 Probe length analysis
- 7.4 Effect of wire diameter on signal forms
- 7.5 Signal visibility curve from reference [95]
- 7.6 Irregular particle dimensions and orientation
- 7.7 Photograph of 62 micron particle in 14.4 micron fringe system
- 7.8 Signal strength curves for spherical glass particles in fringe mode
- 7.9 Signal strength curves for spherical glass particles in reference beam mode
- 7.10 Signal visibility curves for spherical glass particles in fringe mode

A.2.3.

- 7.11 Mean experimental signal visibility curves for spherical glass particles in fringe mode
- 7.12 Signal visibility curves for spherical glass particles in reference beam mode
- 7.13 Signal strength curves for irregular alumina particle in fringe mode
- 7.14 Signal visibility curves for irregular alumina particle in fringe mode
- 7.15 Signal strength curves for irregular particle in reference beam mode
- 7.16 Signal visibility curves for irregular particle in reference beam mode

- 8.1 Particle velocity profiles : $\theta = 0^\circ$
- 8.2 Log. plots of dimensionless particle velocity vs. dimensionless distance from the wall
- 8.3 Effect of solids loading on particle velocity profile
- 8.4 Particle velocity profiles for $\Delta Z = 13.9$ mm
- 8.5 a to g Particle and clean air velocity profile comparisons
- 8.6 Mean slip velocities derived from fig. 8.1
- 8.7 a, b and c Comparison of the $1/e^2$ and the measured probe lengths
- 8.8 a to e Particle velocity and axial turbulence intensity profiles
- 8.9 Charge amplifier calibration curve
- 8.10 Particle turbulence at the pipe axis

- 9.1 Arrangement for mean particle velocity determination
- 9.2 Comparison of the direct and local particle velocity methods for determination of mean particle velocity
- 9.3 Typical oscilloscope display from a gas-solids flow
- 9.4 Oscilloscope display of processed signal

A.2.4.

- 10.1 Phase diagram for vertical conveying
 - 10.2 Particle wall velocity backscatter arrangement
 - 10.3 Backscatter laser anemometer
 - 10.4 Particle wall velocity curves
 - 10.5 Constant solids loading ratio vs. particle wall velocity curves

 - 11.1 Typical pressure drop curves
 - 11.2 Measured pressure gradients
 - 11.3 Friction factor ratios
 - 11.4 Effect of neglecting velocity ratio from equation (11.3)
-

REFERENCES

1. Zenz, F.A. and Othmer, D.F. "Fluidisation and Fluid Particle Systems", Reinhold, New York 1960
2. Soo, S.L. "Fluid Dynamics of Multiphase Systems", Blaisdell, 1967
3. Boothroyd, R.G. "Flowing Gas-Solid Suspensions" Chapman-Hall, 1971
4. E.E.U.A. Handbook No. 15 "Pneumatic Handling of Powdered Material", Constable & Co. London, 1963
5. Townsend, A.A. "The Structure of Turbulent Shear Flow", C.U.P., 1956
6. Segler, G. "Pneumatic Grain Conveying" Braunschweig, Germany, 1951
7. Stacey, R.B. Third Pneumotransport Seminar, May, 1975, City University
8. Fischer, J. Chem. Eng., 65, 114, 1958
9. Boothroyd, R.G. Trans. Instn. Chem. Engrs., 44, T306, 1966
10. Rose, H.E. and Duckworth, R.A. The Engineer, 227, 392, 430, 478, 1969
11. Hinz, J.O. Appl. Sci. Res., A11, 33, 1962
12. Soo, S.L. Proceedings of a Symposium on the Interaction between Fluids and Particles, I.Chem. Engrs., London, 50, 1962
13. Stokes, G.G. Trans. Camb. Phil. Soc., 9, part 2, 51, 1851
14. Oseen, C.W. Arkiv. f. Math. Ast. Och. Fys, 6, no. 29, 1910
15. Goldstein, S. Proc. Roy. Soc (London), 128a, 225, 1929
16. Tomotika, S. and Aoi, T. Quart. J. Mech. Appl. Math., 3, 240, 1950

A.3.2.

17. Percy, T. and McHugh, B. Phil. Mag. 7th Ser. 46, no. 378
783, 1955
18. Stewartson, K. Phil. Mag. 8th Ser., 1, no. 4,
345, 1956
19. Kawaguti, M. J. Phys. Soc. Japan, 10, no. 8,
694, 1955
20. Basset, A.B. Treatise on Hydrodynamics, vol.2,
Deighton, Bell & Co., London, 1888
21. Boussinesq, J. "Theorie Analytique de la Chaleur"
Paris, 1903
22. Oseen, C.W. "Hydrodynamik", Leipzig, 1927
23. Hjelmfelt, A.T. and
Mackros, L.F. Appl. Sci. Res., 16, 149, 1966
24. Corrsin, S. and Lumley, J. Appl. Sci. Res., 6, 114, 1956
25. Tchen, C.M. "Mean Value and Correlation Problems
Connected with the Motion of Small
Particles Suspended in a Turbulent
Fluid", Martinus Nijhoff, The Hague,
1947
26. Pearcey, T. and Hill, G.W. Australian J. Phys., 9, 18, 1956
27. Payne, R.B. J. Fluid Mech., 3, 81, 1958
28. Thom, A. Proc. Roy. Soc. (London), Proc.
Camb. Phil. Soc., 32, 392, 1936
29. Irani, R.R. and Callis, C.F. "Particle Size Measurement,
Interpretation and Application",
J. Wiley, 1963
30. Hawksley, P.G.W. Brit. J. Appl. Phys., 5, Suppl.3,
S1, 1954
31. Magnus, G. Abh. der Akad. der Wissensch,
Berlin, 1852
32. Swanson, W.M. J. Basic. Engng., 83, (Trans. ASME,
series D), 461, 1961
33. Maccoll, J.W. J. Roy. Aeronaut. Soc., 32, 777, 1928
34. Rubinow, S.I. and Keller, J.B. J. Fluid. Mech, 11, 447, 1961
35. Soo. S.L., and Tien, C.L. J. Appl. Mech., Trans ASME, 27,
5, 1960
36. Carrier, G.F. J. Fluid. Mech, 4, 376, 1955

A.3.3.

37. Rannie, W.D. "Progress in Astronautics in Rocketry", Academic Press Inc., New York, Vol. 6, 1962
38. Marble, F.E. Phys. Fluids, 7, no. 8, 1270, 1964
39. Corn, M. J. Air Pollution Control Assoc., 11, No. 11, 523 and 11, No.12, 566, 1961
40. Pietsch, W.B. Trans. ASME, paper no. 68 -MH -21
41. Smoluchowski, M.S. Bull. Acad. Sci., Cracow, 1A, 28, 1911
42. Faxen, H. Ark. Mat. Astron. Fys., 19, 13, 1925
43. Coulson, J.M. and Richardson, J.F. "Chemical Engineering" Vol. 2, Pergamon Press, London, 1955
44. Montgomery, D.J. Solid State Physics, 9, 139, 1959
45. Walton, P.J., Arundel, P.A., Mason, J.S., Haque, H. and Boothroyd, R.G. I. Mech. E. Conf. on "Bunker Extraction Gear", Oct. 1971
46. Mason, J.S. PhD Thesis, 1972, Department of Mechanical, Marine and Production Engineering, Liverpool Polytechnic
47. Ower, E. and Pankhurst, R.C. "The Measurement of Air Flow" Pergamon, 1966
48. Schlichting, H. "Boundary Layer Theory" McGraw Hill Book Company, 1968
49. Yeh, Y. and Cummins, H.Z. Appl. Phys. Lett., 4, no. 10, 176, 1964
50. Foreman, J.W., George, E.W., and Lewis, R.D. Appl. Phys. Lett., 7, no. 4, 77, 1965
51. Foreman, J.W., Lewis, R.D., Thornton, J.R. and Watson, H.J. Proc. IEEE, 54, 424, 1966
52. Foreman, J.W., George, E.W., Jetton, J.L., Lewis, R.D., Thornton, J.R. and Watson, H.J. IEEE J. Quantum Electronics, QE-2, 260, 1966
53. Lewis, R.D., Foreman, J.W., Watson, H.J. and Thornton, J.R. Phys. Fluids, 11, 433, 1968
54. Goldstein, R.J. and Kreid, D.K. ASME paper no. 67 -APM -37, 1967

A.3.4.

55. Goldstein, R.J. and Hagen, W.F. Phys. Fluids, 10, 1349, 1967
56. Welch, N.E. and Tomme, W.J. AIAA 5th Aerospace Sciences Mtg., New York, 1967
57. Pike, E.R., Jackson, D.A., Bourke, P.J. and Page, D.I. J. Sci. Insts., J. Phys. E., 1, series 2, 727, 1968
58. Davis, D.T. ISA Trans., 7, no. 1, 43, 1968
59. James, R.N., Babcock, W.R. and Seifert, H.S. AIAA Journal, 6, no. 1, 160, 1968
60. Rudd, M.J. J. Sci. Inst., 2, 55, 1969
61. Angus, J.C., Morrow, D.L., Dunning, J.W., and French, M.J. Indust. and Eng. Chem., 61, no. 2, 8, 1969
62. Berman, N.S. and Santos, V.A. AIChE Journal, 15, no.3, 323, 1969
63. Huffaker, R.M., Fuller, C.E., and Lawrence, T.R. Soc. Automotive Engrs., Inst. Automotive Engrs. Conf., Detroit, Michigan, 1969
64. Mazumder, M.K. and Wankum, D.L. IEEE J. Quant. Electron., QE5, 317, 1969
65. Thew, M.T. and Bedi, P.S. "Flow Visualisation Techniques and Applications", One-day Symposium at Borough Polytech., June 1970
66. Brayton, D.B. "Electro-Optical Systems Design" Conf., New York, Sept. 1969
67. Brayton, D.B. and Goethert, W.H. ISA Trans., 10, 40, 1971
68. Bourke, P.J. and Brown, C.G. Optics and Laser Technol., 3, 23, 1971
69. Denison, E.B., Stevenson, W.H. and Fox, R.W. AIChE Journal, 17, no. 4, 781, 1971
70. Adrian, R.J. and Goldstein, R.J. J. Phys. E., J. Sci. Insts., 4, 505, 1971
71. Morton, J.B. and Clark, W.H. J. Phys.E., J.Sci. Insts., 4, 809, 1971
72. Durst, F. and Whitelaw, J.H. Prog. Heat & Mass Transf., 4, 311, 1971
73. Durst, F. and Whitelaw, J.H. Proc. Roy. Soc. Lond., A324, 157, 1971
74. Durst, F. and Whitelaw, J.H. J. Phys. E., J.Sci. Insts., 4, 804, 1971

A.3.5.

75. Drain, L.E. J. Phys., D., Appl. Phys., 5, 481, 1972
76. Bourke, P.J., Brown, C.G. and Drain, L.E. D.I.S.A. Information no. 12, 21, 1971
77. Pfeifer, H.J. and Vom Stein, H.D. "Electro-Optic Systems in Flow Measurement" Conf., Univ. of Southampton, Sept. 1972
78. Durst, F and Whitelaw, J.H. "Electro-Optic Systems in Flow Measurement" Conf., Univ. of Southampton, Sept. 1972
79. Melling, A. Mech. Eng. Dept., Imperial College, Report ET/TN/B/7, 1971
80. Melling, A. and Whitelaw, J.H. DISA Information no. 15, 5, 1973
81. Humphrey, J.A.C., Melling, A. and Whitelaw, J.H. "Engineering Uses of Coherent Optics" Conf., Strathclyde Univ., Glasgow, April, 1975
82. Barker, R., Reithmuller, M.L., and Ginoux, J.J. Von Karman Institute, TN81, October 1972
83. Reithmuller, M.L. and Ginoux, J.J. "Pneumotransport 2" Conf., Univ. of Surrey, Guildford, Paper no. D3, Sept. 1973
84. Carlson, C.R. PhD. Thesis, Rutgers University, New Jersey, Engng. Dept., 1973
85. Arundel, P.A. First Pneumotransport Seminar, City University, June 1974
86. Temes, C.L. IRE Trans. on Aeronaut. and Navig. Electron., 37, 1959
87. Buchhave, P. DISA Information No. 15, 15, 1973
88. Foreman, J.W. Appl. Optics., 6, no. 5, 821, 1967
89. "Optical Beam Methods for Velocity Measurement". Post experience course at Imperial College, London, Jan. 1973
90. Edwards, R.V., Angus, J.C., French, M.J. and Dunning, J.W. J. Appl. Phys., 42, no. 2, 837, 1971

A.3.6.

91. DISA 55L Laser Anemometer
Instruction Manual
92. Deighton, M.O. and DISA Information no. 12, 5, 1971
Sayle, E.A.
93. Laufer, J. N.A.C.A. Tech. Rept., 1174, 1954
94. Durst, F. PhD. Thesis, Dept. of Mech. Eng.,
Imperial College, London, 1972
95. Farmer, W.M. Appl. Optics, 11, no.11, 2603,
1972
96. Clark, R.H., Charles, D.E., Trans. Inst. Chem. Eng. 30, 209,
Richardson, J.F. and 1952
Newitt, D.M.
97. Mehta, N.C., Smith, J.M., Ind. Eng. Chem., 49, no. 6,
and Comings, E.W. 986, 1957
98. Mason, J.S. and Smith, B.V. Powder Technol. 6, 323, 1972
99. van Zoonen, D. Symposium on Interaction between
Fluids and Particles, paper A54,
I. Chem. E., London, 1962
100. Soo, S.L., Trezek, G.J., I and E.C. Funds, 3, no. 2,
Dimick, R.C. and 98, 1964
Hohnstreiter, G.F.
101. Peskin, R.L. and Dwyer, H.A. A.S.M.E. paper no. 65 - WA/FE - 24,
Feb. 1964
102. Soo, S.L. I and E.C. Funds, 1, no. 1, 33,
1962
103. Eichhorn, R., Shanny, R., Project SQUID, Tech. Rept. PR-107-P,
Navon, U. March, 1964
104. Fulmer, R.D. and Wirtz, D.P. AIAA paper no. 65-11, 1965
105. Finlay, I.C. and Welsh, N. N.E.I. Rept. 331, 1967
106. Ingebo, R.D. N.A.C.A. TN3265, Oct. 1954
107. McCarthy, H.E. and Olson, J.H. I and E.C. Funds, 7, no. 3, 471,
1968
108. Reddy, K.V.S., Van Wijk, M.C., Can. J. Chem. Eng., 47, 85, 1969
and Pei, D.C.T.
109. Reddy, K.V.S., and Pei, D.C.T. I. and E.C. Funds, 8, no. 3,
490, 1969
110. Chandok, S.S. and Pei, D.C.T. "Pneumotransport 1" Conf., Churchill
College, Cambridge, paper no. B5,
Sept. 1971

A.3.7.

111. Jotaki, T. and Tomita, Y. "Pneumotransport 1" Conf., Churchill College, Cambridge, paper no. B3, Sept. 1971
112. Kramer, T.J. and Depew, C.A. A.S.M.E. paper no. 72-FE-29, 1972
113. Kane, R.S. PhD. Thesis, City University, New York, Mech.Eng. Dept., 1973
114. Kane, R.S., Weinbaum, S. and Pfeffer, R. "Pneumotransport 2" Conf., Univ. of Surrey, Guildford, paper no. C3, Sept. 1973
115. Duckworth, R.A. and Chan, T.K. "Pneumotransport 2" Conf. Univ. of Surrey, Guildford, paper no. A5, Sept. 1973
116. Doig, I.D. and Roper, G.H. Aust. Chem. Eng. 4, no. 1, 9, 1963
117. Boothroyd, R.G. Trans. Inst. Chem. Engrs., 45, T297, 1967
118. Wakstein, C. Aerosol Sci., 1, 69, 1970
119. Cramp, W.J. J. Roy. Soc. of Arts, 69, 283, 1921
120. Cramp, W.J. and Priestley, A. The Engineer, pp 34, 64, 89, 112, Jan. 1924
121. Cramp, W.J. J. Soc. Chem. Ind., 44, 207T, 1925
122. Richardson, J.F. and McLeman, M. Trans. Instn. Chem. Engrs., 38, 257, 1960
123. Hall, A.W. U.S. Dept. of Interior, U.S. Bur. of Mines, Inf. Circ., 8314, 55, 1966
124. Beck, M.S., Drane, J., Plaskowski, A. and Wainwright, N. Powder Technol. 2, 269, 1969
125. Mendies, P.J., Wheeldon, J.M. and Williams, J.C. "Pneumotransport 2" Conf., Univ. of Surrey, Guildford, paper no. D1, Sept. 1973
126. Mesch, F. and Kipphan, H. "Electro-Optic Systems in Flow Measurement" Conf. Univ. of Southampton, Sept. 1972
127. Zenz, F.A. Ind. Eng. Chem. 41, 2801, 1949

128. Zenz, F.A. Petroleum Refiner, 36, no. 6, 133, 1957
129. Leung, L.S., Wiles, R.J., and Nicklin, D.J. Ind. Eng. Chem. Process. Des. Develop. 10, no.2, 183, 1971
130. Laser Doppler Velocimeter Manual, Cambridge Consultants
131. Drain, L.E. and Moss, B.A. "Electro-Optic Systems in Flow Measurement" Conf., Univ. of Southampton, Sept. 1972
132. Bannister, H. Chem. and Process. Eng., 40, 241, 1959
133. Chari, S.S. 63rd Annual Mtg. AIChE, Chicago, Illinois, preprint 15j, Nov/Dec 1970
134. Boothroyd, R.G. Trans. Instn. Chem. Engrs., 44, T306, 1966
135. Leung, L.S., Wiles R.J., and Nicklin, D.J. "Pneumotransport 1" Conf., Churchill College, Cambridge, Sept. 1971
136. Jones, J.H., Braun, W.G., Daubert, T.E. and Allendorf, H.D. AIChE Journal, 13, no. 3, 608 1967
137. Hariu, O.H. and Molstad, M.C. Ind. Eng. Chem., 41, 1148, 1949
138. Belden, D.H. and Kassel, L.S. Ind. Eng. Chem., 41, 1174, 1949
139. Pincus, O.J. Appl. Mechanics, 19, 425, 1952
140. Mason, J.S. and Boothroyd, R.G. Proc. 1st Int. Conf. on "Pneumatic Transport of Solids in Pipes" BHRA Fluid Engng., Cranfield, paper no. C1, 1971
141. Albright, C.W., Holden, J.H., Simons, H.P. and Schmidt, L.D. Ind. Eng. Chem., 43, 1837, 1951
142. Boelter, L.M.K. and Kopner, R.H. Ind. Eng. Chem. 31, 426, 1939
143. Rose, H.E. and Barnacle, H.E. Engineer, London, 203, 898, 1957
144. Martinelli, R.C., Boelter, L.M.K., Taylor, T.M., Thomsen, E.G. and Morrin, E.H. Trans. Am. Soc. Mech. Eng., 66, no. 2, 139, 1944
145. Vogt, E.G. and White, R.R. Ind. Eng. Chem, 40, 1731, 1948
146. Farbar, L. Ind. Eng. Chem., 41, 1184, 1949
147. Hitchcock, J.A. and Jones, C. Brit. J. Appl. Phys., 9, 218, 1958

A.3.9.

148. Richards, P.C. and Wiersma, S. "Pneumotransport 2" Conf., Univ. of Surrey, Guildford, paper no. A1, Sept. 1973
149. Stemerding, S. Chem. Eng. Sci., 17, 599, 1962
150. Doig, I.D. and Roper, G.H. Aust. Chem. Eng., 4, 9, 1963
151. Soo, S.L. and Trezek, G.J. I. and E.C. Funds, 5, 338, 1966
152. Duckworth, R.A. and Kakka, R.S. "Pneumotransport 1" Conf., Churchill College, Cambridge, paper no. C3, Sept. 1971
153. Becker, H.A. Hottel, H.C., and Williams, G.C. J. Fluid. Mech. 30, 259, 1967
154. Doig, I.D. and Roper, G.H. I. and E.C. Funds, 6, no. 2, 247, 1967
-

PUBLICATIONS

1. Mason, J.S. and Birchenough, A.
"The Application of a Laser Anemometer in Measuring Parameters Required in the Design of a Pneumatic Conveying System", "Powtech '75" Conference, Harrogate, Feb. 1975.
 2. Mason, J.S. and Birchenough, A.
"The Application of Laser Measurement Techniques to the Pneumatic Transport of Fine Alumina Particles".
"Engineering Uses of Coherent Optics" Conference, Strathclyde University, April 1975
 3. Birchenough, A. and Mason, J.S.
"Local Particle Velocity Measurements with a Laser Anemometer in an Upward Flowing Gas-Solid Suspension", submitted to "Powder Technology" December 1974.
 4. Birchenough, A. and Mason, J.S.
"Velocity and Axial Turbulence Intensity Measurements in a Titanium Dioxide Seeded Airstream Flowing through a Vertical Pipe" submitted to "Particulate Matter", June 1975
 5. Birchenough, A. and Mason, J.S.
"Particle Wall Velocity Measurements in a Densely Flowing Gas-Solid Suspension", summary submitted to "Pneumotransport III" Conference to be held in April, 1976
-